

Unclassified

2

REPORT DOCUMENTATION PAGE

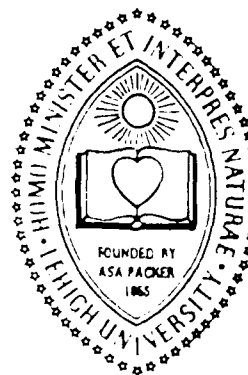
1a. REPORT SECURITY CLASSIFICATION			1b. RESTRICTIVE MARKINGS		
AD-A221 564			3. DISTRIBUTION/AVAILABILITY OF REPORT		
			UNCLASSIFIED/UNLIMITED		
4. AUTHORING OR PERFORMING ORGANIZATION REPORT NUMBER(S) FM-13			5. MONITORING ORGANIZATION REPORT NUMBER(S) AFOSR-TR. 90-0458		
6a. NAME OF PERFORMING ORGANIZATION LEHIGH UNIVERSITY		6b. OFFICE SYMBOL (If applicable)	7a. NAME OF MONITORING ORGANIZATION AFOSR/NA Bolling AFB DC 20332-6448		
6c. ADDRESS (City, State and ZIP Code) DEPARTMENT OF MECHANICAL ENGINEERING LEHIGH UNIVERSITY BETHLEHEM, PA 18015			7b. ADDRESS (City, State and ZIP Code) AFOSR/NA Bolling AFB DC 20332-6448		
8a. NAME OF FUNDING/SPONSORING ORGANIZATION AFOSR		8b. OFFICE SYMBOL (If applicable) NA	9. PROCUREMENT INSTRUMENT IDENTIFICATION NUMBER AFOSR-89-0065		
8c. ADDRESS (City, State and ZIP Code) BOLLING AIR FORCE BASE WASHINGTON, D. C. 20332			10. SOURCE OF FUNDING NOS.		
11. TITLE (Include Security Classification) VORTEX-INDUCED BOUNDARY LAYER SEPARATION			PROGRAM ELEMENT NO. 61102 F	PROJECT NO. 2307	TASK NO. A 2
			WORK UNIT NO.		
12. PERSONAL AUTHOR(S) PERIDIER, VALLORIE J. AND WALKER, JAMES DAVID					
13a. TYPE OF REPORT INTERIM		13b. TIME COVERED FROM 11/88 TO 10/89		14. DATE OF REPORT (Yr., Mo., Day) 1989 OCTOBER	
15. PAGE COUNT 320					
16. SUPPLEMENTARY NOTATION					
17. COSATI CODES			18. SUBJECT TERMS (Continue on reverse if necessary and identify by block number)		
FIELD GROUP SUB. GR.			UNSTEADY BOUNDARY-LAYER SEPARATION, VORTEX, TURBULENT BURSTS, BOUNDARY-LAYER ERUPTIONS; UNSTEADY INTERACTIONS		
19. ABSTRACT (Continue on reverse if necessary and identify by block number) Unsteady boundary-layer separation at high Reynolds numbers, $Re$ , is considered on a theoretical and computational basis. Whenever an external inviscid flow induces a region of adverse pressure gradient near a wall, the development of recirculating eddies in the boundary layer is common. An unsteady viscous-inviscid interaction often follows in the form of a local boundary-layer eruption and abrupt ejection of near-wall vorticity into the external flow. The dynamics of this process, as it develops in an initially thin boundary layer, is considered. As interaction ensues, the flow focuses into a band which progressively narrows in the streamwise direction. The complex flow development is extremely difficult to resolve using conventional Eulerian methods; here the boundary-layer solutions are obtained using Lagrangian methods, wherein trajectories of a large number of fluid particles are computed. The algorithms developed are general but are applied here to the problem of the boundary-layer induced by a two-dimensional vortex above an infinite plane wall. Solutions are obtained for the limit problem $Re \rightarrow \infty$ , and for $Re$ large but					
20. DISTRIBUTION/AVAILABILITY OF ABSTRACT UNCLASSIFIED/UNLIMITED <input type="checkbox"/> SAME AS RPT. <input checked="" type="checkbox"/> DTIC USERS <input type="checkbox"/>			21. ABSTRACT SECURITY CLASSIFICATION Unclassified		
22a. NAME OF RESPONSIBLE INDIVIDUAL DR. JAMES MCMICHAEL		22b. TELEPHONE NUMBER (Include Area Code) 202-767-4935		22c. OFFICE SYMBOL AFOSR/NA	

## 19. Abstract (continued)

finite using an interacting boundary-layer approach.

For the limit problem  $Re \rightarrow \infty$ , the boundary-layer solution develops a singularity at finite time,  $t_s(\infty)$ , as the flow focuses toward an eruption. The multi-structured terminal state<sup>s</sup> is the same as reached for the impulsively-started circular cylinder and found in a recent asymptotic analysis. The interacting boundary-layer solutions are also shown to develop a singularity at finite times  $t_s(Re) < t_s(\infty)$ . Thus, conventional interacting boundary-layer concepts do not alleviate the evolution of a singularity, but promote breakdown at an earlier time that decreases with Reynolds number. The computed results are found to be in excellent agreement with the interactive lengths and time scales predicted by recent asymptotic theories. The present results describe the initial stages of a strong unsteady viscous-inviscid interaction; apparently it is necessary to account for the effect of normal pressure variations to continue the interaction.

# Lehigh University



## **VORTEX-INDUCED BOUNDARY-LAYER SEPARATION**

by

**Vallorie J. Peridier and J. D. A. Walker**

**Report FM-13**

**October, 1989**

**Prepared Under Financial Support of the  
U. S. Air Force Office of Scientific Research  
Contract AFOSR-89-0065**

**Department of Mechanical Engineering & Mechanics  
Lehigh University, Bethlehem, PA 18015**

## VORTEX-INDUCED BOUNDARY-LAYER SEPARATION

by

Vallorie J. Peridier and J. D. A. Walker

**Department of Mechanical Engineering and Mechanics  
Lehigh University, Bethlehem, Pennsylvania 18015**

# Technical Report FM-13

## October, 1989

[illegible]

## Distribution of This Document is Unlimited



## ABSTRACT

Unsteady boundary-layer separation at high Reynolds numbers,  $Re$ , is considered on a theoretical and computational basis. Whenever an external inviscid flow induces a region of adverse pressure gradient near a wall, the development of recirculating eddies in the boundary layer is common. An unsteady viscous-inviscid interaction often follows in the form of a local boundary-layer eruption and abrupt ejection of near-wall vorticity into the external flow. The dynamics of this process, as it develops in an initially thin boundary layer, is considered. As interaction ensues, the flow focuses into a band which progressively narrows in the streamwise direction. The complex flow development is extremely difficult to resolve using conventional Eulerian methods; here the boundary-layer solutions are obtained using Lagrangian methods, wherein trajectories of a large number of fluid particles are computed. The algorithms developed are general but are applied here to the problem of the boundary-layer induced by a two-dimensional vortex above an infinite plane wall. Solutions are obtained for the limit problem  $Re \rightarrow \infty$ , and for  $Re$  large but finite using an interacting boundary-layer approach.

For the limit problem  $Re \rightarrow \infty$ , the boundary-layer solution develops a singularity at finite time,  $t_s(\infty)$ , as the flow focusses toward an eruption. The multi-structured terminal state is the same as reached for the impulsively-started circular cylinder and found in a recent asymptotic analysis. The interacting boundary-layer solutions are also shown to develop a singularity at finite times  $t_s(Re) < t_s(\infty)$ . Thus, conventional interacting boundary-layer concepts do not alleviate the evolution of a singularity, but promote breakdown at an earlier time that decreases with Reynolds number. The computed results are found to be in excellent agreement with the interactive lengths and time scales predicted by recent asymptotic theories. The present results describe the initial stages of a strong unsteady viscous-inviscid interaction; apparently it is necessary to account for the effect of normal pressure variations to continue the interaction.

## ACKNOWLEDGEMENTS

The authors wish to thank the Air Force Office of Scientific Research for providing financial support under contract F49620-85-C-00108 and grant AFOSR-89-0065. Some of the computations of this study were carried out at ICOMP (Institute for Computational Mechanics in Propulsion) at NASA-Lewis Research Center, Cleveland, Ohio, and the Pittsburgh Supercomputer Center. The support of these organizations is gratefully acknowledged. The authors would also like to thank Professor F. T. Smith of University College London for the comments and continuing interest in this work.

The present investigation is part of a larger overall effort which is aimed at developing an understanding of the basic physical processes which occur in a turbulent boundary layer. The eruptions that occur from the near-wall region of the turbulent boundary layer develop abruptly, take place in a very narrow band, and are of the type considered in this study.

## TABLE OF CONTENTS

	Page
ABSTRACT	i
ACKNOWLEDGEMENTS	ii
LIST OF TABLES	v
LIST OF FIGURES	vi
CHAPTER 1 INTRODUCTION	
1.1 Significance and Objectives	1
1.2 Governing Equations	11
1.3 Related Experimental Studies	16
1.4 Interactions	20
1.5 Model Problem	24
CHAPTER 2 THEORETICAL STUDIES OF UNSTEADY SEPARATION	
2.1 Introduction	30
2.2 The Classical Studies	32
2.3 The MRS Model	39
2.4 Lagrangian Methods	48
2.5 The Terminal Boundary-layer Structure	53
2.6 The Onset of Interaction	57
2.7 Conventional Interacting Boundary-layer Theory	64
CHAPTER 3 PROBLEM FORMULATION	
3.1 Introduction	71
3.2 The Eulerian Limit Problem	72
3.3 The Eulerian Interactive Problem	81
3.4 Lagrangian Formulation	84
3.5 An ADI Method for the Boundary-layer Problem	92
3.6 Numerical Solution of the Lagrangian Boundary-layer Problem	105
3.7 The Interaction Problem	111
3.8 The Cauchy Integral	119
3.9 Numerical Solution of the External Flow Problem	127

	Page
CHAPTER 4 THE LIMIT PROBLEM $Re \rightarrow \infty$	
4.1 Introduction	133
4.2 Numerical Methods	136
4.3 Determination of $t_s$	139
4.4 Calculated Results	149
4.5 Discussion	168
CHAPTER 5 INTERACTING BOUNDARY-LAYER RESULTS	
5.1 Introduction	172
5.2 Numerical Considerations Associated with the Interactive Computations	173
5.3 The Boundary-layer Development as $t \rightarrow t_s$	183
5.4 The External Flow Development as $t \rightarrow t_s$	218
5.5 The Streamwise and Temporal Scales for the First Interactive State	247
5.6 Breakdown of the Conventional Interactive Approach	251
5.7 Summary	271
CHAPTER 6 CONCLUSIONS	273
REFERENCES	279
APPENDIX A Lagrangian Variables	289
APPENDIX B Numerical Methods for the Eulerian Boundary-layer Equations	296
APPENDIX C Algorithm for the Cauchy Integral	300
APPENDIX D Evaluation of Physical Quantities from Lagrangian Data	305
D.1 The Normal Distance $\hat{y}(\hat{\xi}, \hat{\eta}, t)$	305
D.2 The Stream Function $\Psi(\hat{x}, \hat{y}, t)$	310
D.3 The Displacement Thickness $\delta^*(\hat{x}, t)$	312
D.4 The Vorticity $\omega(\hat{x}, \hat{y}, t)$	314
D.5 The Wall Shear $\tau_w(\hat{x}, t)$	315
APPENDIX E Determination of $x_s$ , $t_s$ , and $K$	316

# LIST OF TABLES

	Page
Table 4.1. Time steps used in the integrations.	138
Table 5.1. Parameters associated with boundary-layer breakdown for both the limit problem and interacting studies.	181
Table 5.2. Summary of regression study for temporal behavior of wall shear near $\hat{x}_s$ ; $\tau_w = O(t_s - t)^b$ .	253
Table 5.3. Summary of regression study for temporal behavior of pressure gradient near $\hat{x}_s$ ; $dp/dx = O(t_s - t)^b$ .	254
Table 5.4. Summary of regression study for temporal behavior of $v_{max}$ ; $V_d(\hat{x}_s) = O(t_s - t)^b$ .	256
Table C.1. Cauchy integral series coefficients for nodes near the the field point $\hat{x}_i$ .	302

## LIST OF FIGURES

	Page
Figure 1.1.      Schematic diagram showing geometry and coordinates associated with a conventional steady boundary-layer calculation.	3
Figure 1.2.      The triple deck structure for $Re \rightarrow \infty$ near a sharp trailing edge.	5
Figure 1.3.      Schematic diagram of geometry for the model problem.	25
Figure 1.4.      Inviscid streamlines in a frame of reference convecting with the vortex.	25
Figure 1.5.      Streamwise velocity and pressure distributions induced near the wall by the moving vortex.	29
Figure 2.1.      Various stages in the flow development for an impulsively started circular cylinder.	33
2.1(a) Just after the impulsive start	
2.2(b) Just after separation	
2.2(c) Developed separation	
2.2(d) Breakdown	
Figure 2.2.      The Proudman-Johnson problem of unsteady flow near an outflow stagnation point on an infinite plane wall.	37
Figure 2.3.      Schematic of the boundary-layer development at a front stagnation point for a wall moving a constant velocity.	41

	Page
Figure 2.4. Streamline patterns at separation according to Moore, Rott and Sears (reproduced from Sears and Telionis (1975), figure 1).	44
2.4(a) Downstream-moving wall	
2.4(b) Fixed wall	
2.4(c) Upstream-moving wall	
Figure 2.5. A typical velocity profile near $x_s$ as $t \rightarrow t_s$ .	52
Figure 2.6. Schematic of the initial stage of an interaction.	55
Figure 2.7. Schematic diagram of the first interactive state.	60
Figure 2.8. Schematic of the conjectured second stage of interaction.	63
Figure 2.9. Schematic of the three-zone region associated with the terminal state of unsteady, interacting boundary layers (Smith, 1988).	67
Figure 3.1. Schematic diagram of a typical mesh point and four surrounding points in the current and previous time planes.	97
3.1(a) Conventional Crank-Nicholson method	
3.1(b) Upwind-downwind averaging path, for $\bar{P}_{i,j} > 0$	
3.1(c) Upwind-downwind averaging path, for $\bar{P}_{i,j} \leq 0$	
Figure 3.2. Schematic diagram showing the averaging paths used for the approximation of $Q \partial U / \partial \xi$ .	98
3.2(a) Upwind-downwind averaging path, for $\bar{Q}_{i,j} > 0$	
3.2(b) Upwind-downwind averaging path, for $\bar{Q}_{i,j} \leq 0$	

		Page
Figure 3.3.	Schematic diagram of the predictor-corrector algorithm used in the interacting problem.	117
Figure 4.1.	Temporal development of displacement thickness: the limit problem (from Walker, 1978).	135
Figure 4.2.	The evolution of lines of constant $x$ for the limit problem.	
	4.2(a) $t=0.25$ , the start of the Lagrangian calculation	141
	4.2(b) $t=0.45$	142
	4.2(c) $t=0.75$	143
	4.2(d) $t=0.85$	144
	4.2(e) $t=t_s=0.989$	145
Figure 4.3.	Temporal development of the instantaneous streamlines.	
	4.3(a) $t=0.25$	151
	4.3(b) $t=0.45$	152
	4.3(c) $t=0.75$	153
	4.3(d) $t=t_s=0.989$	154
Figure 4.4.	Temporal development of the displacement thickness $\delta^*$ .	
	4.4(a) In a frame of reference convecting with the vortex	156
	4.4(b) In the laboratory frame	157
Figure 4.5.	Evolution of the constant vorticity contours.	
	4.5(a) $t=0.45$	159
	4.5(b) $t=0.75$	160
	4.5(c) $t=0.95$	161
	4.5(d) $t=t_s=0.989$	162



	Page
Figure 4.6. Temporal development of the wall shear plotted for 0.25, (0.10), 0.95 and $t_d=0.989$ .	164
Figure 4.7. Wall shear distribution at selected times.	165
Figure 4.8. Wall shear distribution at $t_s$ using an enlarged scale in $x$ .	166
Figure 4.9. Instantaneous streamlines at $t_s$ using an enlarged scale.	167
Figure 4.10. Velocity profiles near $x=x_s$ at $t=0.9885$ .	170
Figure 5.1(a). Displacement thickness at $t=0.25$ from: (1) a limit problem calculation and, (2) an interacting computation with $Re=10^5$ .	174
Figure 5.1(b). Wall shear at $t=0.25$ from: (1) a limit problem calculation and, (2) an interacting computation with $Re=10^5$ .	175
Figure 5.2. Contours of constant $x$ near the singular time $t_s$ , for two cases of finite $Re$ .	
5.2(a) $Re=10^8$ , $t=t_s-0.020$	177
5.2(b) $Re=10^8$ , $t=t_s$	178
5.2(c) $Re=10^5$ , $t=t_s-0.015$	179
5.2(d) $Re=10^5$ , $t=t_s$	180

Figure 5.3.	Temporal evolution of displacement thickness at times $t_0=0.25, (0.10), t_s$ , in the laboratory frame.	
5.3(a)	$Re=10^8$	184
5.3(b)	$Re=10^7$	185
5.3(c)	$Re=10^6$	186
5.3(d)	$Re=10^5$	187
Figure 5.4.	Displacement thickness at time $t_s$ for $Re=10^5$ in the vortex frame.	188
Figure 5.5.	Typical streamline contours after separation and prior to breakaway ( $Re=10^5, t=0.45$ ).	190
Figure 5.6.	Streamlines at $t_s$ in the vortex frame.	
5.6(a)	$Re=10^8$	191
5.6(b)	$Re=10^7$	192
5.6(c)	$Re=10^6$	193
5.6(d)	$Re=10^6$ on an enlarged scale	194
5.6(e)	$Re=10^5$	195
5.6(f)	$Re=10^5$ on an enlarged scale	196
Figure 5.7.	Temporal evolution of streamline contours for $Re=10^5$ .	
5.7(a)	$t=0.58$	199
5.7(b)	$t=0.60$	200
5.7(c)	$t=0.62$	201
5.7(d)	$t=0.62$ on an enlarged scale	202
5.7(e)	$t=0.63$	203
5.7(f)	$t=0.63$ on an enlarged scale	204

	Page
Figure 5.8. Vorticity field at breakaway time $t_s$ , for $Re=10^8$ .	205
Figure 5.9. Vorticity field for $Re=10^5$ at successive times.	
5.9(a) $t=0.58$	206
5.9(b) $t=0.60$	207
5.9(c) $t=0.62$	208
5.9(d) $t=0.63$	209
5.9(e) $t=0.64$	210
5.9(f) $t=t_s=0.645$	211
Figure 5.10. Temporal evolution of wall shear, at $Re=10^8, 10^7, 10^6$ and $10^5$ .	
5.10(a) $Re=10^8$	213
5.10(b) $Re=10^7$	214
5.10(c) $Re=10^6$	215
5.10(d) $Re=10^5$	216
Figure 5.11. Wall shear for $Re=10^5$ , at $t_s$ .	217
Figure 5.12. Mainstream velocity in the laboratory frame, at $t_s$ .	
5.12(a) limit problem $Re \rightarrow \infty$	219
5.12(b) $Re=10^8$	220
5.12(c) $Re=10^7$	221
5.12(d) $Re=10^6$	222
5.12(e) $Re=10^5$	223

Figure 5.13.	Dynamic pressure at $t_s$ for the limit problem and the interacting cases $Re=10^8, 10^7, 10^6$ .	
5.13(a)	limit problem $Re \rightarrow \infty$	226
5.13(b)	$Re=10^8$	227
5.13(c)	$Re=10^7$	228
5.13(d)	$Re=10^6$	229
Figure 5.14.	Dynamic pressure for $Re=10^5$ as $t \rightarrow t_s$ .	
5.14(a)	at $t_s - 0.015$	230
5.14(b)	at $t_s$	231
Figure 5.15.	Curves of $\partial U / \partial t$ at time $t_s$ .	
5.15(a)	$Re=10^8$	232
5.15(b)	$Re=10^7$	233
5.15(c)	$Re=10^6$	234
5.15(d)	$Re=10^5$	235
Figure 5.16.	Pressure gradient at $t_s$ for the limit problem and the interacting cases $Re=10^8, 10^7, 10^6$ .	
5.16(a)	limit problem $Re \rightarrow \infty$	237
5.16(b)	$Re=10^8$	238
5.16(c)	$Re=10^7$	239
5.16(d)	$Re=10^6$	240
Figure 5.17.	Temporal evolution of pressure gradient as $t \rightarrow t_s$ , $Re=10^5$ .	
5.17(a)	at $t_s - 0.015$	241
5.17(b)	at $t_s$	242

	Page
Figure 5.18. Induced displacement velocity at time $t_s$ .	
5.18(a) $Re=10^8$	243
5.18(b) $Re=10^7$	244
5.18(c) $Re=10^6$	245
5.18(d) $Re=10^5$	246
Figure 5.19. Velocity profiles at equally spaced intervals near $x_s$ for $Re=10^8$ .	
5.19(a) at $t_s-0.004$	258
5.19(b) at $t_s$	259
Figure 5.20. Velocity profiles near $x_s$ for $Re=10^7$ .	
5.20(a) at $t_s-0.01$	260
5.20(b) at $t_s-0.005$	261
5.20(c) at $t_s$	262
Figure 5.21. Velocity profiles near $x_s$ for $Re=10^6$ .	
5.21(a) at $t_s-0.01$	264
5.21(b) at $t_s-0.005$	265
5.21(c) at $t_s$	266
Figure 5.22. Velocity profiles near $x_s$ for $Re=10^5$ .	
5.22(a) at $t_s-0.025$	267
5.22(b) at $t_s-0.015$	268
5.23(c) at $t_s-0.005$	269
5.23(d) at $t_s$	270
Figure A.1. Schematic diagram of characteristic $x=\text{constant}$ in the $\xi, \eta$ plane.	294
Figure D.1. Schematic diagram of integration along a characteristic $\hat{x}=\text{constant}$ .	308

## 1. INTRODUCTION

### 1.1 Significance and Objectives

Fluid flow at high Reynolds number,  $Re$ , is generally observed to exhibit a double structure consisting of: (1) very thin boundary layer-regions near solid walls in which the flow is reduced to relative rest through the action of viscosity, and (2) the remaining "outer" region where the flow is effectively inviscid. In the classical interactive strategy for computing flows at high Reynolds number, it is assumed that the boundary-layer regions remain thin and passive (Smith 1982); the solution of the outer flow is then calculated subject to the condition of vanishing normal velocity at all solid surfaces. The outer solution is not uniformly valid and in order to satisfy the no-slip condition at the wall a thin boundary layer is required. Thus the tangential velocity predicted by the inviscid outer solution serves as the external condition for the boundary-layer calculation. If the boundary-layer solution can be obtained, a description of the entire flow field would then be available. This description is complete to leading order but predicts that the boundary layer induces a small normal velocity  $O(Re^{-1/2})$  on the outer flow which at this stage is unmatched. In principle, the apparent discontinuity in normal velocity can be adjusted by one of two approaches corresponding to consideration of: (1) a limit problem defined by  $Re \rightarrow \infty$ , and (2) interacting boundary-layer theory. In a limit analysis, the boundary layer is considered to induce small  $O(Re^{-1/2})$  second-order velocities in the outer flow; this perturbation velocity field is evaluated subject to the boundary condition that the normal velocity near the solid surface should match that induced by the first-order boundary-layer solution. An entire hierarchy of inner and outer problems may then be considered, and the resulting solutions are anticipated to provide successively higher order approximations in an asymptotic expansion of the solution of the Navier-Stokes equations for large Reynolds number. The second approach corresponds to the classical treatment of interacting boundary layers, wherein a finite (but large) Reynolds number is

adopted in a given calculation procedure. The boundary-layer solution predicts that the outer flow is displaced by an amount  $O(Re^{-1/2})$  and the combination of the body shape plus the boundary-layer displacement thickness is considered to alter the effective body shape. This concept indicates that the outer inviscid flow should then be recomputed and an obvious iteration scheme is suggested.

Unfortunately, the classical interactive strategy for steady flows fails in all but the simplest geometries (for example, flow past a semi-infinite plate at zero incidence). This is because most bodies of practical interest are finite and/or have surface curvature; thus the inviscid solution contains regions of adverse pressure gradient. In a typical numerical solution procedure to compute the steady boundary-layer flow, a calculation is initiated at a frontal stagnation point (where the external inviscid flow attaches to the body along a dividing streamline, as indicated in figure 1.1). The boundary-layer solution is then constructed in a step-by-step numerical procedure moving away from the frontal stagnation point at  $x=0$  along both the upper and lower surface, subject to the pressure gradient predicted by the inviscid solution. In most situations, the numerical integrations cannot be continued beyond certain locations, which are generally located in regions of adverse pressure gradient and have been labelled  $x_{ST}$  and  $x_{SB}$  in figure 1.1. As the numerical integrations approach  $x_{ST}$  and  $x_{SB}$  from upstream the skin friction approaches zero, thus hinting that reversed flow will occur downstream of these locations. In fact, the boundary-layer solution develops a Goldstein singularity (Goldstein, 1948) at such locations and for this reason the integration cannot be continued to downstream locations. It is now well understood that the Goldstein singularity develops as a consequence of imposing the pressure gradient predicted by the outer inviscid solution on the boundary-layer flow. The classical interactive strategy does not allow for the possibility of a significant interaction between the boundary layer and the

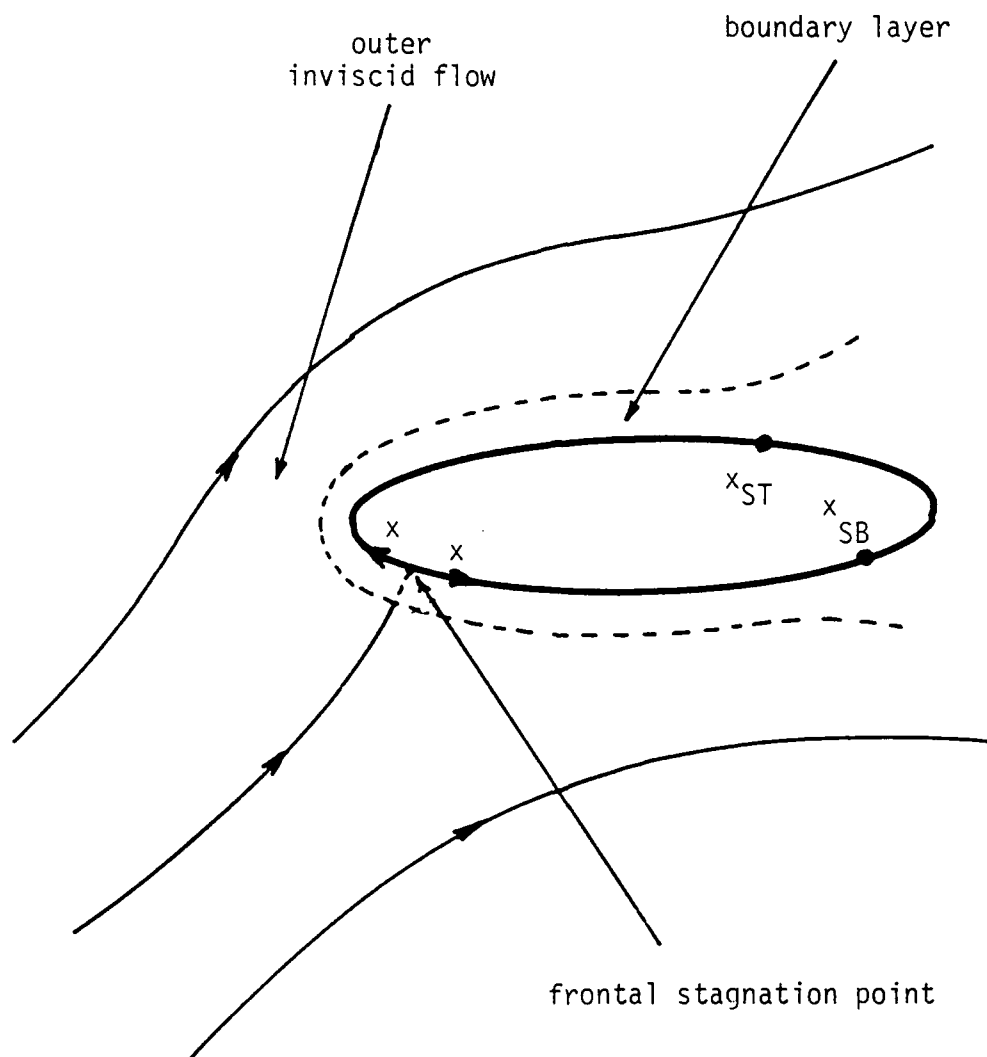


Figure 1.1. Schematic diagram showing geometry and coordinates associated with a conventional steady boundary-layer calculation.



external flow. In physical situations where such an interaction must occur, any attempt to force the pressure distribution prescribed by an external inviscid solution on the boundary layer results in the formation of a Goldstein singularity. As a consequence the entire boundary-layer solution cannot be completed and the classical interactive strategy fails (see Smith, 1982, for a brief discussion of some of the exceptional cases where this strategy is successful).

It is now well established that when viscous shear layers and inviscid regions interact they do so in a manner which is generally much more complex than envisaged in the classical interactive strategy. For steady boundary-layer flows, a viscous-inviscid interaction typically involves the development of a multi-structured region referred to as a "triple deck". This structure was first derived by Messiter (1970) and Stewartson (1969) in connection with the interaction zone near the trailing edge of a flat plate, which is immersed in and aligned with a uniform flow. The asymptotic structure of the flow in the limit  $Re \rightarrow \infty$  is depicted schematically in figure 1.2. A Blasius boundary layer having a thickness  $O(Re^{-1/2})$  develops downstream of the leading edge of the plate toward the trailing edge. At the trailing edge there is an abrupt change in boundary conditions, associated with the streamwise velocity  $u$  changing from the no-slip condition on the plate ( $u=0$ ) to the symmetry condition on the wake centerline ( $\partial u / \partial y = 0$ ). The Goldstein near-wake solution (1930) is double-structured wherein the streamwise velocity is joined onto the upstream Blasius solution. However, the two solutions do not merge smoothly and infinite streamwise gradients are predicted near the trailing edge; furthermore, the normal velocity predicted by the Goldstein near-wake solution is also singular near the trailing edge.

The triple deck occurs in a zone that is intermediate between the Blasius boundary layer and the Goldstein near wake and acts to provide a relatively smooth transition between both regions. A derivation of the thickness in

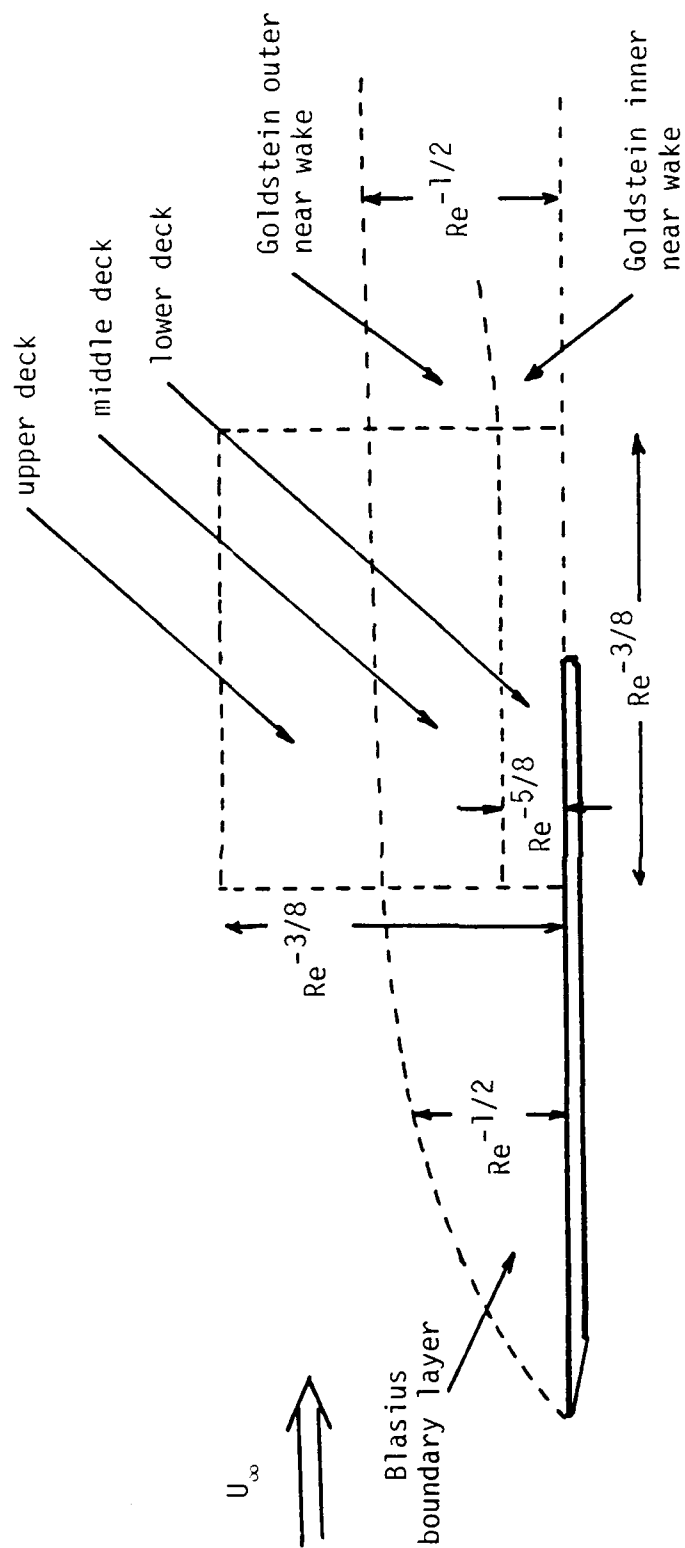


Figure 1.2. The triple deck structure for  $Re \rightarrow \infty$  near a sharp trailing edge (not to scale).

each zone of the triple deck has given by Smith (1982) and here only the main features of each region will be described. Near the wall, a nonlinear viscous response is provoked in the lower deck which has an thickness  $O(\text{Re}^{-5/8})$  and a streamwise extent  $O(\text{Re}^{-3/8})$ . In the lower deck the scaled velocity components satisfy the conventional boundary-layer equations but the pressure gradient is an unknown function of the streamwise variable,  $x$ , which must be computed by means of an interactive calculation involving the upper layers. The middle deck has a thickness  $O(\text{Re}^{-1/2})$  and represents the continuation of the upstream boundary layer. In this region the solution is linearized about the upstream rotational profile and the flow is displaced from the wall by an unknown thickness function which is dependent on the solution of the lower deck. To leading order, the pressure distribution does not vary in the normal direction across the both middle deck and the lower deck. The upper deck is a region above the original boundary layer and centered on the trailing edge; in this zone the problem is linearized about the constant mainstream velocity and the flow is irrotational. The solution of the upper deck equations leads to a relationship between the unknown pressure distribution and the function describing the displacement induced by the lower deck. The pressure-displacement relation that arises from the upper deck solution makes the entire problem in the triple deck elliptic in nature and permits the enforcement of both upstream and downstream conditions, even though the lower deck equations are parabolic.

The discovery of the triple deck structure was an important step in elucidating how information is propagated upstream in a laminar boundary-layer flow. Note that the boundary-layer equations are parabolic and thus disturbances propagate only in the downstream direction. For the situation depicted in figure 1.2 the pressure disturbance due to the trailing edge is transmitted vertically to the upper deck where the governing equations are elliptic; consequently the presence of the trailing edge is propagated upstream through the upper deck, which rides on top of the original boundary layer. Although the triple-deck structure illustrated in figure 1.2 was originally

derived in connection with the trailing edge problem (Stewartson, 1969), the same generic structure occurs in a wide variety of other problems where a "feature" at the wall generates a local interaction. Specific examples include a small hump (or dent) on the wall, having a height  $O(\text{Re}^{-5/8})$  and a length  $O(\text{Re}^{-3/8})$ , a small  $O(\text{Re}^{-1/4})$  change in slope of the wall, a weak injection through a small slot having a length  $O(\text{Re}^{-3/8})$ , and flow near blunt or non-aligned trailing edges; many of these problems are discussed by Smith (1982).

In all cases involving a triple-deck structure, a region of local interaction and a region of upstream influence is generated by the particular "feature" on the wall. Many such problems involve the evolution of regions of reversed flow in the lower deck (for example, the blunt trailing edge or the small bump on the surface). At present, numerical procedures and algorithms for computing the small-scale separation of such flows are approaching a high degree of sophistication, and it is now possible to compute a triple-deck solution to such steady interacting problems fairly routinely. When the flow in the inner region exhibits zones of reversed flow, it is important that the iterative computations be carried out in a specific way in order to avoid the development of a Goldstein singularity in the lower deck solution during the course of the calculation; in general this means that the lower-deck calculation should not be carried out with the pressure distribution specified from the previous iteration. One means of avoiding the evolution of a Goldstein singularity is to carry out the numerical solution of the inner problem using an inverse boundary-layer method (Carter and Wornam, 1975) in which the displacement thickness (from the previous iteration) is specified rather than the pressure gradient.

Triple deck regions also occur in problems involving steady large-scale separation, where a separated boundary layer leads to a massive disturbance of the outer inviscid flow field. The problem of massive separation due to a circular cylinder in a uniform flow was first addressed using limit procedures by Smith (1979) (see also Smith, 1982 and Smith, 1985). In such cases a

triple deck is centered on the location where the separation streamline leaves the body, and it emerges that the dynamics of the triple deck fix the location of the separation point on the body (Rothmayer and Smith, 1985).

The solution of steady flow problems using limit procedures involves the determination of all sub-regions of the flow in the limit  $Re \rightarrow \infty$ ; the solution in each sub-region must be obtained numerically or analytically, and then all solutions are matched asymptotically together. As the complexity of the flow field increases, analysis based on the limit approach becomes increasingly difficult to carry out. One practical alternative that has been developed is steady interacting boundary-layer theory. In this approach a finite, but large, Reynolds number is assumed and the influence of the boundary layer on the outer flow is calculated through an interaction condition. For subsonic flows, this condition requires the evaluation of a Cauchy principal-value integral of the normal velocity induced by the boundary layer on the outer flow. For supersonic flow, the interaction condition relates pressure changes near the wall to the displacement effect induced by the boundary layer. In the limit  $Re \rightarrow \infty$ , interacting boundary-layer solutions must approach the solution predicted by the limit approach, and careful numerical studies generally confirm that this is the case (see, for example: Burggraf, Rizetta, Werle and Vatsa, 1979). For this reason, the steady interacting boundary-layer approach provides a practical (and more efficient) alternative to full numerical solutions of the Navier-Stokes equations. At present, methods based on the interacting boundary-layer concept are fairly well-developed for steady flows (see, for example: Davis and Carter, 1984; Edwards and Carter, 1985; Vatsa and Carter, 1984). It has proven possible to compute flows involving small regions of surface separation and trailing-edge separation using this methodology. In recent times steady interacting boundary-layer theory has been extended to the modeling and calculation of bluff body flows involving massive separation (Rothmayer, 1985).

In summary, the calculation of steady interacting two-dimensional flows,

using either limit procedures ( $Re \rightarrow \infty$ ) or interacting boundary-layer theory ( $Re$  large, but finite) has become fairly commonplace. A number of three-dimensional problems have also been addressed (see, for example: Smith, Sykes and Brighton, 1977; Smith, 1982; Burggraf and Duck, 1982), and although the calculations and structure are more complicated, the basic concepts are similar. In most of these situations, the principal effect of the interaction is to spread the effect of the interaction upstream and to provide a modification of the outer inviscid flow, which essentially consists of to a small displacement effect.

The situation regarding the computation of unsteady interacting boundary-layer flows is much less developed and in general appears to be far more complex. Some work related to unsteady flows has been carried out in the context of the conventional triple deck structure (Smith, 1982); however in these cases the structure of the triple deck is mainly preserved and the unsteadiness does not drastically alter the external flow. In this study, the main interest is in unsteady flows which develop in a conventional boundary layer (having a thickness  $O(Re^{-1/2})$ ) and evolve towards a strong unsteady viscous-inviscid interaction with the external flow. This type of unsteady event has been referred to as unsteady breakaway separation (Smith, 1982; Elliott, Cowley and Smith, 1983) and generally involves a local eruption of the boundary-layer flow near the wall. Some experimental observations of this type of event will be reviewed in §1.3; it is evident from these studies that once a boundary-layer eruption starts to develop it evolves very rapidly and occurs along a very narrow band in the streamwise direction. The event is generally observed to culminate in the discrete ejection of boundary-layer vorticity into the external flow in a complex interaction involving a substantial unsteady disturbance of the outer flow.

The objective of this study is to investigate computational procedures for dealing with unsteady boundary-layer flows which evolve toward a strong unsteady interaction with the external flow field. A rather large body of

literature concerning unsteady boundary layers exists and the relevant parts will be discussed in chapter 2; however it emerges that most attempts to compute the onset of the eruptive behavior have been based on the conventional Eulerian description of the fluid motion and have been largely unsuccessful. The main difficulty is due to the fact that, as the large updrafts begin to develop in the boundary layer, it eventually proves impossible to adequately resolve the locally intense variations in the flow field. In this study, the flow development near the surface will be calculated using Lagrangian variables; this approach differs from the conventional Eulerian methods in that the trajectories of a large number of fluid particles are computed as the flow evolves in time. One advantage is that it proves possible to accurately compute the fluid motion even as the boundary-layer flow focuses into a violent updraft. As the two-dimensional boundary-layer flow develops toward an unsteady interaction, an essentially generic limit structure emerges. The limit problem  $Re \rightarrow \infty$  will be investigated in this study. However, since interacting boundary-layer theory has proved so effective in the calculation of steady flows, the application of this approach to unsteady boundary layers will also be considered; a general interacting boundary-layer formulation is described in §1.4.

The methods developed in this study are general in their application to unsteady flows, but will be employed on a specific model problem described in §1.5. This model problem consists of the unsteady boundary layer induced by a rectilinear vortex in an otherwise stagnant flow above an infinite plane wall, and was originally discussed by Walker (1978). It is considered here because it is the simplest case in which a moving vortex induces a boundary-layer eruption; the nature of this interaction is well-documented by experiment and is non-controversial. As such, the model problem provides a good example involving most of the features of more general unsteady strongly-interacting boundary-layer flows.

## 1.2 Governing Equations

Consider the flow of an incompressible fluid of speed  $U_0^*$  past a body having a representative length  $L^*$ ; if  $\nu$  is the kinematic viscosity of the fluid, the Reynolds number  $Re$  is defined by

$$Re = \frac{U_0^* L^*}{\nu} . \quad (1.1)$$

Let  $x$  and  $Y$  be dimensionless coordinates (with respect to  $L^*$ ) with corresponding dimensionless velocities  $U$  and  $V$ ; the coordinate  $Y$  measures dimensionless distance normal to the body surface and  $x$  measures dimensionless distances in the tangential direction at locations close to the body. The two-dimensional Navier-Stokes equations govern the fluid motion and in vector form these are:

$$\frac{\partial \vec{q}}{\partial t} + \nabla \left( \frac{1}{2} \vec{q} \cdot \vec{q} \right) - \vec{q} \times (\nabla \times \vec{q}) = -\vec{\nabla} p - \frac{1}{Re} \nabla \times (\nabla \times \vec{q}) , \quad (1.2)$$

with an associated equation of continuity

$$\vec{\nabla} \cdot \vec{q} = 0 . \quad (1.3)$$

Here  $t$  is dimensionless time (with respect to  $L^*/U_0^*$ ) and  $p$  is the dimensionless dynamic pressure (with respect to  $\rho U_0^{*2}$ , where  $\rho$  is the fluid density);  $\vec{q} = (U, V)$  is the velocity vector. The boundary conditions are

$$\vec{q} = 0, \text{ at all solid surfaces,} \quad (1.4)$$

in order to satisfy the no-slip and solid surface conditions.

In the classical interactive strategy, the viscous term on the right side of equation (1.2) is neglected in the limit  $Re \rightarrow \infty$  and the unsteady two-dimensional Euler equations are obtained, viz.



$$\frac{\partial \vec{q}}{\partial t} + \nabla \left( \frac{1}{2} \vec{q} \cdot \vec{q} \right) - \vec{q} \times (\nabla \times \vec{q}) = -\vec{\nabla} p, \quad (1.5)$$

$$\vec{\nabla} \cdot \vec{q} = 0. \quad (1.6)$$

These equations are solved subject to the condition of no normal flow through the body surface, i.e.

$$V=0 \quad \text{at} \quad Y=0. \quad (1.7)$$

Since it is not possible to also enforce the no-slip condition at the surface, the resulting inviscid solution will have a slip velocity at the surface denoted by

$$U \rightarrow Ue(x,t) \quad \text{as} \quad Y \rightarrow 0. \quad (1.8)$$

This tangential velocity is reduced to relative rest in a boundary layer having a thickness  $O(Re^{-1/2})$  where the normal velocity is small and  $O(Re^{-1/2})$ . Scaled boundary-layer variables are defined by

$$y = Re^{1/2} Y, \quad v = Re^{1/2} V. \quad (1.9)$$

The boundary-layer equations are an exact subset of the Navier-Stokes equations in the limit  $Re \rightarrow \infty$ , and in Eulerian variables are given by

$$\frac{\partial u}{\partial t} + u \frac{\partial u}{\partial x} + v \frac{\partial u}{\partial y} = -\frac{\partial p}{\partial x} + \frac{\partial^2 u}{\partial y^2}, \quad (1.10)$$

$$\frac{\partial u}{\partial x} + \frac{\partial v}{\partial y} = 0. \quad (1.11)$$

The boundary conditions are

$$u = v = 0 \quad \text{at} \quad y=0, \quad (1.12)$$

and, in order to match to the outer inviscid flow as  $Y \rightarrow 0$  (c.f. equation (1.8))

$$\lim_{y \rightarrow \infty} u(x,y,t) = Ue(x,t). \quad (1.13)$$

In the classical interactive strategy, the pressure distribution is prescribed from the inviscid outer solution and, in this study, this type of scheme will be referred to as the limit problem  $Re \rightarrow \infty$ . The outer solution drives the boundary-layer flow via the imposed pressure gradient, which is evaluated by differentiation of the Bernoulli equation along an external streamline just outside the boundary layer. An equivalent procedure is to take the limit  $y \rightarrow \infty$  in equation (1.10), using the fact that  $\partial u / \partial y \rightarrow 0$  (as well as all higher derivatives); the pressure gradient is given by

$$-\frac{\partial p}{\partial x} = \frac{\partial U_e}{\partial t} + U_e \frac{\partial U_e}{\partial x}. \quad (1.14)$$

In the limit problem, a solution of the external flow problem establishes the tangential velocity distribution  $U_e(x,t)$  once and for all, and the consequent pressure gradient, evaluated from equation (1.14), is imposed on the boundary-layer flow. The differences associated with an interacting boundary-layer formulation will be considered in §1.4.

The Eulerian description of the boundary-layer problem, given in equations (1.10) to (1.13), is the conventional one. Another formulation that will be used extensively in this study is in terms of Lagrangian variables (Van Dommelen, 1981). In this approach, the spatial coordinates  $(\xi, \eta)$  of a large number of individual fluid particles at some initial instant are used as the independent variables. As the motion in the boundary layer evolves, the current streamwise location  $x(\xi, \eta, t)$  and the tangential velocity  $u(\xi, \eta, t)$  of each fluid particle is computed. The boundary-layer equations in Lagrangian variables are derived in Appendix A and these are:

$$\frac{\partial u}{\partial t} = \frac{\partial U_e}{\partial t} + U_e \frac{\partial U_e}{\partial x} + \left( \frac{\partial x}{\partial \xi} \frac{\partial}{\partial \eta} - \frac{\partial x}{\partial \eta} \frac{\partial}{\partial \xi} \right)^2 u, \quad (1.15)$$

$$\frac{\partial x}{\partial t} = u, \quad (1.16)$$

for the dependent variables  $x$  and  $u$ . The boundary conditions for equation (1.15) are

$$u(\xi, 0, t) = 0, \quad (1.17)$$

$$\lim_{\eta \rightarrow \infty} u(\xi, \eta, t) = Ue(x, t). \quad (1.18)$$

Again, the external velocity distribution  $Ue$  must be obtained through a solution of the outer inviscid problem. In Lagrangian variables the fluid particle positions are computed as functions of time (even for a steady external flow) and consequently the streamwise velocity at some initial instant,  $t=t_0$ , must be specified, viz.

$$u = u(\xi, \eta, t), \text{ at } t=t_0, \quad (1.19)$$

at known locations within the boundary layer, viz.

$$x(\xi, \eta, t) = \xi, \quad y(\xi, \eta, t) = \eta, \quad \text{at } t=t_0. \quad (1.20)$$

Upon comparison of equations (1.10) and (1.15) it may be observed that the equations are somewhat similar in form and, in principle, numerical algorithms that have traditionally been developed in connection with unsteady flows for equation (1.10) could be used to solve equation (1.15).

One of the main advantages of the Lagrangian description for unsteady flows is that equations (1.15) and (1.16) do not contain the velocity  $v$  or the coordinate  $y$ ; it is these quantities which become large (and eventually singular) as an unsteady boundary-layer flow evolves toward a strong interaction with the outer flow. By contrast, the streamwise particle positions  $x$  and tangential velocities  $u$  remain regular and bounded, even as the boundary layer develops into an eruptive state. At any stage in the boundary-layer development, the normal distance of each fluid particle from the wall,  $y(\xi, \eta, t)$ , may be computed as a solution of the continuity equation which is

$$\frac{\partial x}{\partial \xi} \frac{\partial y}{\partial \eta} - \frac{\partial x}{\partial \eta} \frac{\partial y}{\partial \xi} = 1 , \quad (1.21)$$

in Lagrangian variables. For a given field of particle positions  $x(\xi, \eta, t)$  at time  $t$ , equation (1.21) is a first order equation for the scaled normal distance  $y(\xi, \eta, t)$  of each particle from the wall. The equations of the characteristics are

$$-\frac{d\xi}{x_\eta} = \frac{d\eta}{x_\xi} = dy , \quad (1.22)$$

and these characteristics are curves of  $x(\xi, \eta, t) = \text{constant}$ ; an integral of equations (1.22) is

$$y(\xi, \eta, t) = \int_{\text{wall}}^{(\xi, \eta)} \frac{ds}{\sqrt{x_\xi^2 + x_\eta^2}} , \quad (1.23)$$

where the integral is taken along a path of constant  $x$  which starts at the wall and passes through the point  $(\xi, \eta)$ . The scaled normal distance from the wall of a particle at time  $t$ , which started at the position  $(\xi, \eta)$  at  $t = t_0$ , is therefore given by equation (1.23). It should be noted that if a stationary point develops in the  $x(\xi, \eta, t)$  field, viz.

$$\frac{\partial x}{\partial \xi} = \frac{\partial x}{\partial \eta} = 0 , \quad \text{at } (\xi, \eta, t) = (\xi_s, \eta_s, t_s) , \quad (1.24)$$

then equation (1.23) predicts that a singularity has evolved in the boundary-layer solution. In physical terms, any fluid particles which lie on a constant  $x$  trajectory close to  $(\xi, \eta) = (\xi_s, \eta_s)$  will be at very large distances from the wall at  $t = t_s$ .

The criterion (1.24) for the evolution of a singularity represents another advantage of the Lagrangian formulation because a well-defined and non-controversial means of determining a breakdown of the boundary-layer solution exists. This is in contrast to the Eulerian formulation, where numerical algorithms eventually fail as a boundary-layer flow begins to

develop strong local updrafts (Walker, 1978); in such situations the question of whether a singularity occurs is always clouded by the severe computational difficulties that are encountered in attempting to retain good numerical resolution as the boundary layer starts to become eruptive.

### 1.3 Related Experimental Studies

Unsteady interactions between an effectively inviscid outer flow and a viscous region near solid surfaces occur in a variety of important applications, such as the flows occurring in turbomachinery and on moving airfoil surfaces. In this section some examples of readily-observable situations, where a boundary layer erupts and thereby induces a viscous-inviscid interaction with the outer flow, will be described. Some of these examples occur in quite different physical environments but nevertheless exhibit a common type of behavior. At a certain stage a viscous layer near a wall, which has been hitherto passive and which to this stage is well-described by conventional boundary-layer theory, begins to develop strong outflows over a zone which is narrow in the streamwise direction. As this eruptive behavior develops, it culminates in the ejection of boundary-layer fluid away from the wall into the outer inviscid flow. This process is known as a strong unsteady viscous-inviscid interaction; it is generally distinguished by the eruptive nature of the phenomena as well as by the fact that discrete "chunks" of vorticity are torn from the region near the surface and abruptly introduced into the outer flow in the process.

An easily observable example of this type of phenomena occurs in flow past bluff bodies at high Reynolds numbers. A geometry which has been observed extensively is the circular cylinder, and the impulsively started circular cylinder is of particular interest. Initially the majority of the flow field is inviscid and irrotational with the viscous effects confined to a thickening (but thin) boundary layer on the surface of the cylinder. However, before the

cylinder has moved a distance equivalent to a diameter  $d$ , symmetric zones of recirculation appear near the rear stagnation point in a phenomenon which has classically been referred to as boundary-layer separation. As time increases the separation point at  $x=x_s$  moves rapidly forward along the cylinder to a position at a angular distance of about  $\theta_s=72^\circ$  from the rear stagnation point. At this stage, the boundary layer is still thin but it is beginning to thicken appreciably in the radial direction. This process, as described, has been documented in a number of flow visualization experiments (see for example Taneda, 1977; Honji and Taneda, 1979; Bouard and Coutenceau, 1980; Ta Phuoc Loc and Bouard, 1985). If  $Re=U_0 d/\nu$  is the Reynolds number, the flow development for Reynolds numbers up to around  $10^4$  appears to consist of a continual thickening of the recirculation zones on the back portion of the cylinder; in this situation, the interaction between the boundary layer and the external flow apparently consists of global displacement of the inviscid flow. Eventually small non-uniformities in the flow field lead to instability, recirculating eddies are shed from the cylinder, and the flow evolves towards the quasi-steady Karman vortex street, with eddies shed alternately from the upper and lower surfaces of the cylinder. However, at Reynolds numbers greater than  $10^4$ , the initial interaction between the boundary layer and the external flow takes on a new characteristic in the form of an intense vortex which begins to evolve near the separation point and starts to move rapidly outward (Ta Phuoc Loc and Bouard, 1985); here the boundary-layer growth is much more rapid than near the rear stagnation point, for example. With increasing Reynolds numbers, this rapidly thickening region will be narrower in the streamwise direction; in the limit of large Reynolds numbers it is expected that the first interaction with the outer flow will consist of an erupting narrow plume (containing intense vorticity) near the separation point (Van Dommelen, 1981). The subsequent nature of the interaction at very high Reynolds numbers is complex and as yet has not been documented in detail by experiment. It is known that shedding of vortices ultimately takes place at high Reynolds numbers (as well as at lower Reynolds numbers). When the vortices are shed from the surface, viscous-inviscid interactions also

but in a periodic manner. As an eddy is shed from the cylinder, the upstream flow sweeps over the cylinder surface and a new unsteady boundary-layer flow begins to evolve on that portion of the cylinder; recirculating eddies then develop and the viscous flow near the surface proceeds toward a strong interaction with the outer flow in the form of the ejection of another vortex into the wake of the cylinder.

Another important example of an unsteady viscous-inviscid interaction occurs in a phenomenon known as "dynamic stall". The process develops on surfaces of highly maneuverable aircraft and is most easily seen in the laboratory on a pitching airfoil (McCroskey, Carr and McAlister, 1976; McAlister and Carr, 1978). When a uniform stream flows past an airfoil at a small angle of attack and the airfoil is suddenly pitched upwards, flow reversal is observed to initiate near the trailing edge on the upper surface of the airfoil. The region of reversed flow grows toward the leading nose of the airfoil and as it approaches the front portion of the airfoil, an eruption of the viscous flow near the surface occurs, wherein a strong vortex is shed. The detailed processes involved are not well understood; however the net result is the formation of an energetic vortex which subsequently convects downstream over the upper surface of the airfoil. The phenomena is of considerable potential technological importance since the aerodynamic lift of the airfoil is observed to increase dramatically (to level up to 250% of the lift value normally associated with the airfoil), while the vortex is above the airfoil surface (Francis and Keese, 1985).

Strong unsteady interactions are also induced whenever a vortex is close to a solid surface. Such interactions are most apparent in situations where the vortex movement is relatively confined within a laboratory frame of reference. Examples include the flow induced near a ground plane by aircraft-trailing vortices (Harvey and Perry, 1971; Walker, 1978), the boundary layer induced by a vortex ring moving toward a plane wall (Walker *et al*, 1987) and the so-called "secondary instability" of Görtler vortices that develop in the boundary

layer on a concave wall (Ersoy and Walker, 1985; Swearingen and Blackwelder, 1987). In all of these situations, recirculating eddies develop in the boundary layer near the wall as a consequence of the pressure distribution induced by the parent vortex. With the evolution of these secondary vortices, strong updrafts begin to develop and the boundary layer evolves rapidly toward interaction with the outer flow. The nature of the interaction is such that a boundary-layer eruption occurs in a band which is narrow in the streamwise direction, with the result that the secondary eddies are ejected from the boundary layer into the external flow (Harvey and Perry, 1971; Walker *et al*, 1987).

A final important example of unsteady interactions is provided by the turbulent boundary layer. For the majority of a given observation period over a fixed position of the wall, the turbulent boundary layer will be seen to be double-structured, consisting of a relatively thick outer layer and a thin wall layer. The outer layer is an effectively inviscid but rotational flow dominated by the motion of vortices; the wall layer is a thin region close to the wall where viscous effects are important. There are two observable features of the wall-layer flow which are crucial. The first of these is the wall-layer streaks; when a visualization medium such as dye or hydrogen bubbles is injected into the wall layer, it will be observed to collect into long streaks in the streamwise direction (Kline *et al*, 1967; Kim, Kline and Reynolds, 1971). The wall-layer streaks are now believed to be the signature of hairpin vortices which are being convected in the outer layer above the wall layer (Acarlar and Smith, 1984; Hon and Walker, 1987). During the period when wall layer streaks are observed, the wall-layer flow is being driven by the outer layer flow (Walker *et al*, 1989). The second important feature is the bursting phenomena, wherein the wall layer is seen to abruptly erupt into the outer region. The process always initiates near a wall-layer streak and results in a strong unsteady interaction between the inner and outer layers. This is the fundamental regenerative process in a turbulent boundary layer wherein new vorticity is continually introduced into the outer part of the boundary layer through the



intermittent eruptions of the wall layer. At present, it appears that the fundamental vortex structure in turbulent boundary layers is the hairpin vortex and that the bursting phenomena is induced by the action of the hairpin vortex on the wall layer (Acarlar and Smith, 1987a, 1987b; Hon and Walker, 1987; Walker *et al*, 1988).

To summarize, unsteady strong interactions occur in a number of technologically important flows. These types of interactions invariably involve a localized eruption of a boundary-layer flow which initially was thin and attached to the wall. The process may be described as a viscous-inviscid interaction and often culminates in the introduction of discrete vortices into the outer flow. The dynamics of these interactions are very complex and at present are not well understood.

#### 1.4 Interactions

It is evident from the experimental studies discussed in the previous section that unsteady interactive flows are common, and in this section an interactive condition will be derived which take into account the influence of a thickening boundary layer on an external flow.

The boundary-layer velocity components may be written in terms of a streamfunction defined by

$$u = \frac{\partial \psi}{\partial y}, \quad v = -\frac{\partial \psi}{\partial x}, \quad (1.25)$$

and it follows from equation (1.13) that

$$\psi \sim Ue(x,t)y + A(x,t), \quad \text{as } y \rightarrow \infty. \quad (1.26)$$

Here, the function  $A(x,t)$  may be related to the dimensionless scaled displacement thickness  $\delta^*$  defined by

$$\delta^* = \int_0^{\infty} \left\{ 1 - \frac{u(x, y, t)}{Ue(x, t)} \right\} dy . \quad (1.27)$$

Upon integration and substitution of equation (1.26) it follows that

$$A(x, t) = - Ue(x, t) \delta^*(x, t) . \quad (1.28)$$

Using equation (1.25), it follows that the normal velocity near the edge of the boundary layer is

$$v \sim -\frac{\partial Ue}{\partial x} y + \frac{\partial}{\partial x} (Ue \cdot \delta^*) , \text{ as } y \rightarrow \infty . \quad (1.29)$$

Re-writing this equation in terms of the outer variables (equations (1.9)) gives

$$V \sim -\frac{\partial Ue}{\partial x} Y + \frac{1}{\sqrt{Re}} \frac{\partial}{\partial x} (Ue \cdot \delta^*) , \text{ as } Y \rightarrow 0 , \quad (1.30)$$

which must be satisfied by the outer solution as  $Y \rightarrow 0$  to match the boundary-layer solution. The first term in equation (1.30) is associated with the leading order solution in the outer region, while the second term is a normal velocity induced by the leading order boundary-layer solution. The form of equation (1.30) suggests that the solution in the inviscid region should be expanded according to

$$\vec{q} = (U, V) = (U_0, V_0) + \frac{1}{\sqrt{Re}} (U_1, V_1) + \dots, \quad (1.31)$$

where  $U_0, V_0$  now denote the leading order inviscid solution and  $U_1, V_1$  are the perturbation velocities induced by the leading order boundary layer solution. It follows from equation (1.30) that

$$V_1 \sim \frac{\partial}{\partial x} (Ue \delta^*) , \text{ as } Y \rightarrow 0, \quad (1.32)$$

where it is understood that  $Ue$  denotes the tangential velocity associated with the outer solution near the surface.

The leading order velocity field  $\vec{q}_0$  and the perturbation field  $\vec{q}_1$  are both irrotational and both satisfy the Euler equations (1.5) and (1.6). By taking the curl of equation (1.5) it follows that

$$\frac{\partial \omega_0}{\partial t} = \frac{\partial \omega_1}{\partial t} = 0 , \quad (1.33)$$

where

$$\omega = \omega_0 + \frac{1}{\sqrt{\text{Re}}} \omega_1 + \dots, \quad (1.34)$$

is the scalar vorticity associated with the outer flow field. An external flow field which is initially irrotational remains so (Kelvin's theorem), and in particular

$$\omega_1 = \frac{\partial U_1}{\partial Y} - \frac{\partial V_1}{\partial x} = 0 . \quad (1.35)$$

Note that in general (x,Y) will be curvilinear coordinates; it will be assumed here for simplicity that (x,Y) are Cartesian coordinates and consequently either the body surface is almost flat or the effects of the interaction are very localized.

The continuity equation (1.6) for the perturbation velocities is

$$\frac{\partial U_1}{\partial x} + \frac{\partial V_1}{\partial Y} = 0 . \quad (1.36)$$

The perturbation streamfunction may be defined by

$$U_1 = \frac{\partial \Psi_1}{\partial Y} , \quad V_1 = - \frac{\partial \Psi_1}{\partial x} , \quad (1.37)$$

and substitution into equation (1.34) yields the Laplace equation

$$\frac{\partial^2 \Psi_1}{\partial x^2} + \frac{\partial^2 \Psi_1}{\partial Y^2} = 0 . \quad (1.38)$$

The solution for which

$$\Psi_1 = -Ue \cdot \delta^* \quad \text{at } Y=0, \quad (1.39)$$

(c.f. equation (1.32)) is

$$\Psi_1 = -\frac{1}{\pi} \int_{-\infty}^{+\infty} \frac{Y Ue \delta^*}{(s-x)^2 + Y^2} ds. \quad (1.40)$$

The distribution for  $U_1$  near the body surface may be obtained by differentiation of equation (1.40) with respect to  $Y$ , viz.

$$U_1 = \frac{\partial \Psi_1}{\partial Y} = -\frac{1}{\pi} \int_{-\infty}^{+\infty} \frac{\{(s-x)^2 - Y^2\}}{\{(s-x)^2 + Y^2\}^2} Ue \cdot \delta^* ds, \quad (1.41)$$

or

$$U_1(x, Y) = \frac{1}{\pi} \int_{-\infty}^{+\infty} \frac{\partial}{\partial s} \left\{ \frac{(s-x)}{(s-x)^2 + Y^2} \right\} Ue \cdot \delta^* ds. \quad (1.42)$$

One integration by parts yields

$$U_1(x, Y) = -\frac{1}{\pi} \int_{-\infty}^{+\infty} \frac{(s-x)}{(s-x)^2 + Y^2} \frac{\partial}{\partial s} \{ Ue \cdot \delta^* \} ds \quad (1.43)$$

and taking the limit as  $Y \rightarrow 0$  gives

$$U_1(x, 0) = \frac{1}{\pi} \int_{-\infty}^{+\infty} \frac{1}{(x-s)} \frac{\partial}{\partial s} \{ Ue \cdot \delta^* \} ds. \quad (1.44)$$

Note that the integral in equation (1.44) is a Cauchy principal value integral.

If, for a given geometry, the leading order inviscid velocity distribution associated with a non-interacting boundary-layer calculation is denoted by  $Ue^0(x, t)$ , then the mainstream velocity distribution at the boundary-layer edge for the corresponding interacting boundary-layer formulation is

$$Ue(x, t) = Ue^0(x, t) + \frac{1}{\sqrt{Re}} U_d(x, t), \quad (1.45)$$

where

$$U_d(x,t) = \frac{1}{\pi} \int_{-\infty}^{+\infty} \frac{V_d(s, t)}{(x-s)} ds, \quad (1.46)$$

and  $V_d$  is the scaled displacement velocity induced by the boundary layer, viz.

$$V_d(x, t) = \frac{\partial}{\partial x} \{ Ue \cdot \delta^* \}. \quad (1.47)$$

The scaled displacement thickness distribution,  $\delta^*$ , is computed from equation (1.27). In interacting boundary-layer (IBL) calculations a finite (but large) Reynolds number is assumed and the external velocity distribution is influenced by the boundary-layer computation through equation (1.45); note that procedure is only justified for situations in which  $Ue^0 \gg Re^{-1/2} U_d$ .

### 1.5 Model Problem

An objective of the present study was to develop algorithms to compute the evolution of strongly interacting boundary-layer flows, and to this end a model problem was considered, namely the unsteady boundary layer due to a rectilinear vortex above a plane wall in an otherwise stagnant fluid. This problem was originally considered by Walker (1978) who showed that the vortex induces an adverse pressure gradient on the boundary layer which leads to the evolution of a secondary vortex in the viscous flow near the wall. Strong updrafts then begin to evolve near the secondary vortex as the boundary layer proceeds toward a strong interaction with the outer flow. Although algorithms for computing the entire interaction are not yet available, a useful advantage of this specific model problem is that the nature of the interaction is well documented by experiment (Harvey & Perry, 1971; Walker *et al*, 1987).

Consider a rectilinear vortex of strength  $\kappa$  which is located a distance  $a$  above an infinite plane wall as depicted in figure 1.3. Inviscid theory (see for example, Milne-Thompson, 1962) predicts that the vortex will remain at

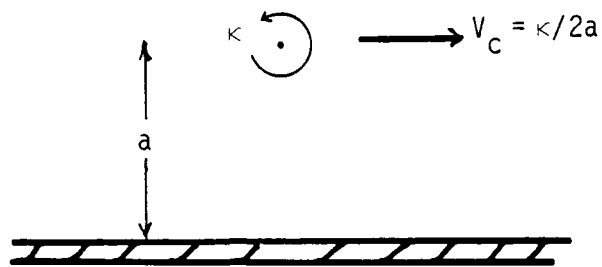


Figure 1.3. Schematic diagram of geometry for the model problem.

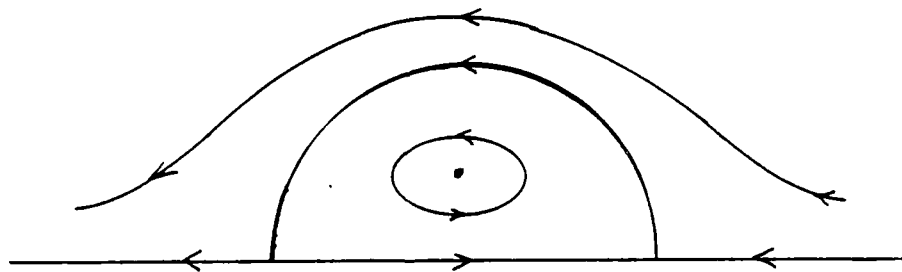


Figure 1.4. Inviscid streamlines in a frame of reference convecting with the vortex.

constant height  $a$  above the wall and convect to the right with constant speed

$$V_c = \frac{\kappa}{2a}. \quad (1.48)$$

These results follow from the fact that a rectilinear vortex does not induce a velocity on itself near the vortex core and consequently the vortex convects only in the field of the image vortex below the plate. This inviscid result is valid in the limit  $Re \rightarrow \infty$ ; note that for interacting boundary-layer theory, described in §1.4, the purely inviscid results described in this section will be modified (c.f §3.7) to reflect the effects of a thickening boundary layer at the wall.

It is convenient to adopt  $a$  and  $V_c$  as the representative length  $L^*$  and velocity  $U_0^*$  used to define dimensionless variables as in §1.2; the Reynolds number is then given by

$$Re = \frac{\kappa}{2\nu} = \frac{aV_c}{\nu}. \quad (1.49)$$

With a streamfunction  $\Psi_0$  defined by

$$U = \frac{\partial \Psi_0}{\partial Y}, \quad V = -\frac{\partial \Psi_0}{\partial x}, \quad (1.50)$$

the streamfunction  $\Psi_0$  due to a vortex whose instantaneous location is at  $(X_v(t), Y_v(t))$  is given by (Milne-Thompson, 1962)

$$\Psi_0 = -\log \left\{ \frac{(x - X_v(t))^2 + (Y - Y_v(t))^2}{(x - X_v(t))^2 + (Y + Y_v(t))^2} \right\}. \quad (1.51)$$

It is easily verified by differentiation that the velocity components at the vortex are

$$U_v(t) = \frac{1}{Y_v(t)}, \quad V_v(t) = 0, \quad (1.52)$$

and the equations of motion of the vortex are therefore

$$\frac{dX_v}{dt} = \frac{1}{Y_v(t)}, \quad \frac{dY_v}{dt} = 0. \quad (1.53)$$

The solution for the convecting vortex trajectory, whose initial location is  $X_v=X_0$ ,  $Y_v=1$  is given by

$$X_v(t) = X_0 + t, \quad Y_v(t) = 1. \quad (1.54)$$

The inviscid flow due to the moving vortex is unsteady in the laboratory frame; however, viewed from a frame of reference which translates uniformly with the vortex, the inviscid motion is steady. If  $x$  is now understood to measure streamwise distance in the moving reference frame of the vortex, the streamfunction describing the inviscid flow is now

$$\Psi_0 = -Y - \log \left\{ \frac{x^2 + (Y-1)^2}{x^2 + (Y+1)^2} \right\}. \quad (1.55)$$

The mainstream velocity at the boundary-layer edge in the moving frame is denoted by  $U_\infty$ ; it may be obtained by differentiation of equation (1.55) and subsequently taking the limit  $Y \rightarrow 0$ , viz.

$$U_\infty = -1 + \frac{4}{x^2 + 1}. \quad (1.56)$$

When the inner viscous problem is posed in the moving reference frame, the wall appears to move to the left with constant velocity and the conventional boundary conditions (1.12) at the wall are replaced with

$$u = -1, \quad v = 0 \quad \text{at } y=0. \quad (1.57)$$

The inviscid flow patterns near the wall are shown in figure 1.4 and describe a Kelvin oval pattern near the vortex center at  $x=0$ . There are two stagnation points near the wall; upstream of the vortex, at  $x=\sqrt{3}$ , there is an



outflow stagnation point while at  $x = -\sqrt{3}$ , behind the vortex, the flow is toward the wall. The pressure distribution near the wall  $p(x)$  may be obtained through substitution of equation (1.56) into (1.14) and integrating to yield

$$p(x) - p_{\infty} = \frac{4(x^2 - 1)}{(x^2 + 1)^2} . \quad (1.58)$$

Here  $p_{\infty}$  is the constant pressure as  $|x| \rightarrow \infty$ . The mainstream velocity and pressure distributions are plotted in figure 1.5. The maximum flow speed occurs under the vortex where the pressure is a minimum; relative maxima in the pressure occur at the stagnation points. The zone between the vortex center at  $x=0$  and the stagnation point,  $0 \leq x \leq \sqrt{3}$ , is a region of adverse pressure gradient; the action of this adverse pressure gradient gives rise to the evolution of a secondary eddy within the boundary layer (Walker, 1978) and it is in this region where the flow ultimately proceeds toward interaction.

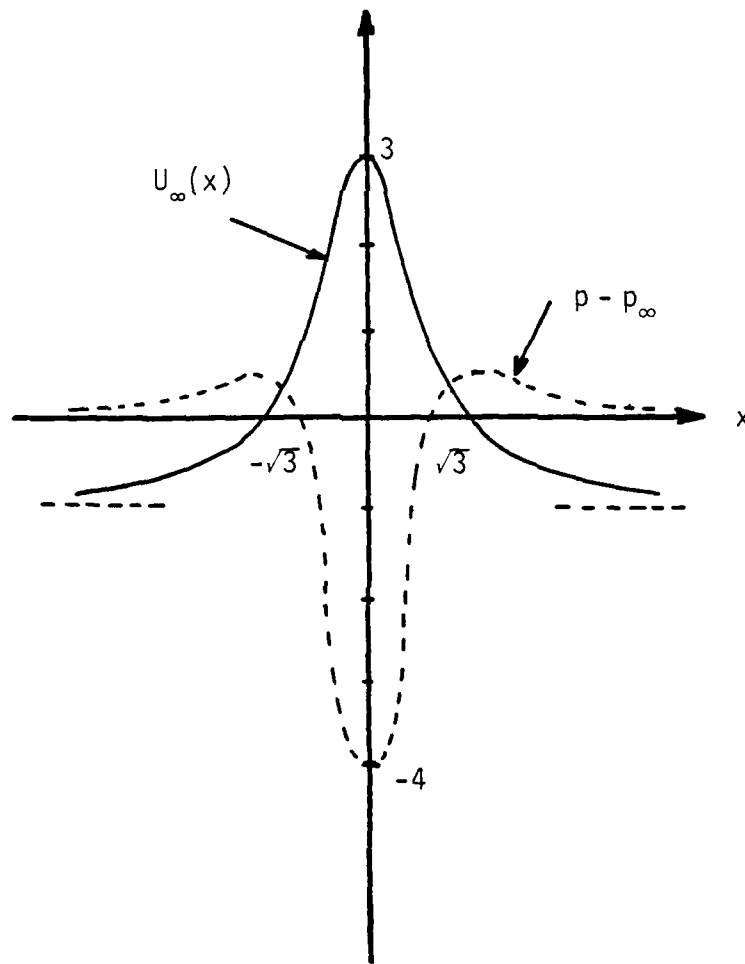


Figure 1.5. Streamwise velocity and pressure distributions induced near the wall by the moving vortex.

## 2. THEORETICAL STUDIES OF UNSTEADY SEPARATION

### 2.1 Introduction

Unsteady flow separation at high Reynolds numbers occurs in a wide variety of important applications, and generally involves complicated evolving flow patterns. Closed-form analytical solutions are rare, and the vast majority of the theoretical investigations have been carried out through numerical integration of the boundary-layer equations. The literature relating to unsteady separation is quite extensive, both with respect to the specific problems investigated and the numerical and analytical approaches utilized; some of these are discussed in review articles by Riley (1975), Williams (1977) and Smith (1982). In many studies of unsteady separation, there is a recurring pattern of experience. For situations where the external flow impresses a region of adverse pressure gradient on the boundary layer, a zone of recirculation was observed to form near the wall. Eventually, rapid boundary-layer growth ensued near the recirculating eddy and *inevitably the numerical scheme failed*. Prior to 1981, a prevalent attitude was that this difficulty in computing unsteady flows was associated with a numerical resolution problem which, in principle, could be rectified by more sophisticated algorithms; some authors still maintain this view (see, for example, Cebeci (1986)). The nature of the difficulty was finally elucidated by Van Dommelen (1981), who showed that a singularity can develop, at finite time, in the solution of the boundary-layer equations in situations where the external pressure distribution is prescribed; this type of non-interactive approach has been the conventional method used to study unsteady boundary-layer separation.

The area of unsteady separation has been controversial and even the definition of the term "separation" has been a matter of debate. In the early classical studies of unsteady boundary layers, the onset of reversed flow in the

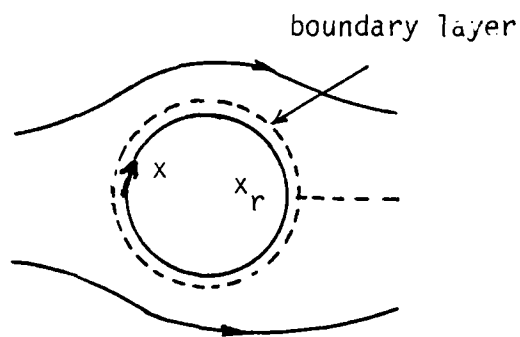
boundary layer was termed separation; these investigations will be discussed in §2.2. In more recent times, Sears and Telionis (1971, 1975) have argued that the term separation should be reserved for the first time a thickening boundary layer has a significant influence on the external inviscid flow field. In 1971 Sears and Telionis postulated a model of unsteady separation known as the "MRS model" which will be discussed in §2.3. Many attempts were made to verify the MRS model through numerical computations, without convincing success, until the matter was resolved by Van Dommelen (1981); this work will be discussed in §2.4.

It is now well known that an unsteady separation singularity can evolve in the solution of the boundary-layer equations at finite time, in all situations where the external pressure gradient is prescribed *a priori*. The boundary-layer equations are exact in the limit  $Re \rightarrow \infty$ , and the evolution of a singularity is simply an indication that the flow has developed to a stage where the assumptions inherent in the boundary-layer equations (namely, that the layer is thin, with thickness  $O(Re^{-1/2})$ ) are breaking down. The breakdown typically occurs along a band which is narrow in the streamwise direction, and should be regarded as the onset of an interaction with the outer inviscid flow. In order to describe the next stage, there are at least two approaches that can be adopted. The first of these is to identify the new length and time scales, in the limit  $Re \rightarrow \infty$ , that evolve as the separation-singularity starts to form. The singularity must eventually be relieved through interaction with the external flow, and the first stage in the process for the limit problem has been discussed by Elliott, Cowley and Smith (1983). This terminal boundary-layer singularity structure is discussed in §2.5, and the structure of the first stage of the interaction will be described in §2.6. The second possible approach is to adapt the interacting boundary-layer concepts that have proven so successful in steady flows (see §1.1) to unsteady problems. Such calculations are carried out for finite but large Reynolds numbers and, as the boundary-layer flow evolves,

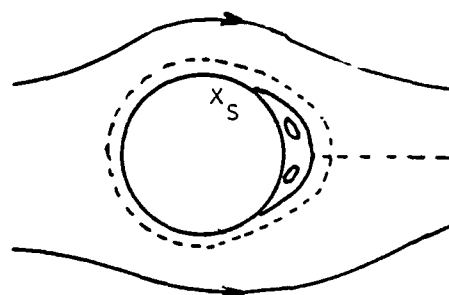
the external field changes via an interaction condition (c.f. §1.4). In this manner, it is hoped that the singularity will be relieved. Some numerical work in this area which is somewhat inconclusive on this last point, is reviewed in §2.7 as well as in a recent paper by Smith (1988). In this last paper, it was concluded that a singularity can develop in finite time in conventional interacting boundary-layer theory, a result which will be confirmed in the present study. Smith (1988) gives analytical predictions of the behavior of skin friction and mainstream pressure distribution; these distributions are detailed in §2.7 to facilitate comparison with the numerical solutions obtained in the present study.

## 2.2 The Classical Studies

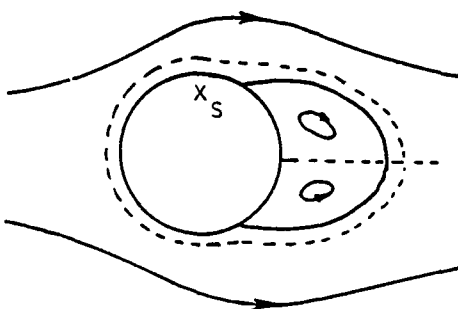
The problem of flow past an impulsively-started circular cylinder has been of considerable interest in the history of research in unsteady laminar separation, for several reasons. First, it is one of the simplest two-dimensional geometries in which the surface curvature gives rise to a zone of adverse pressure gradient in the external flow. Secondly, the initial condition is relatively simple. Immediately following the impulsive start, the flow field is double-structured, consisting of an external potential flow and a thin boundary layer on the cylinder surface, which forms to satisfy the no-slip condition. For  $t=0^+$ , the vorticity diffuses from the cylinder surface and may be imagined to be confined to a thin ring around the cylinder (as depicted in figure 2.1(a)) which is thickening proportional to  $t^{1/2}$ . At this stage the wall shear stress is positive all along the cylinder surface. Shortly after the impulsive start the wall shear at the rear stagnation point (at  $x_r$ ) changes sign. This event heralds the onset of reversed flow in the boundary layer, and the subsequent evolution of two symmetrical regions of recirculating flow which are initially



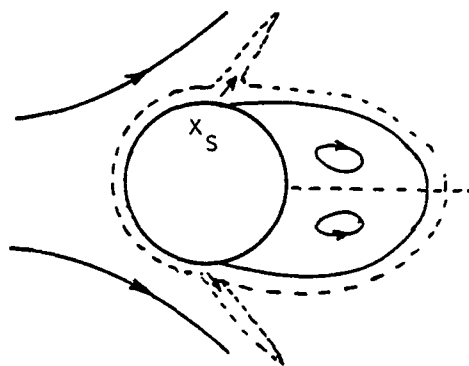
2.1(a) Just after the impulsive start



2.1(b) Just after separation



2.1(c) Developed separation



2.1(d) Breakdown

Figure 2.1. Various stages in the flow development for an impulsively started circular cylinder: the boundary layer and recirculation zone, are grossly exaggerated, and not to scale.

attached to the cylinder. This phenomena has classically been referred to as separation. The situation just after separation has occurred is depicted in figure 2.1(b). After the wall shear vanishes, the separation point (labeled  $x_s$  in figure 2.1(b)) moves rapidly along the cylinder surface, eventually slowing down as it reaches a location about  $72^\circ$  from the rear stagnation point. As the rate of movement of the separation point slows, the region of reversed flow begins to thicken substantially in a direction normal to cylinder, as indicated schematically in figure 2.1(c). It is generally at this stage that severe difficulties are encountered in continuing a numerical integration. The nature of these problems will be discussed subsequently.

The theoretical problem of the flow past an impulsively-started circular cylinder was first considered by Blasius (1908), who expanded the tangential velocity in the boundary layer according to

$$u(x,y,t) = Ue(x) \cdot f_0'(\zeta) + t \cdot Ue(x) \cdot Ue'(x) \cdot f_1'(\zeta) + \dots, \quad (2.1)$$

where  $\zeta = y/2\sqrt{t}$  is a Rayleigh variable which magnifies the initially thin boundary layer that evolves on the surface for  $t=0^+$ . Here  $Ue = 2\sin(x)$  is the mainstream velocity at the boundary-layer edge, where  $x$  is measured in radians from the front stagnation point. The solution for the first term in (2.1) is  $f_0' = \text{erf}(\zeta)$ , and therefore the boundary layer develops initially as if the cylinder were a plane wall. With the passage of time, the second term in equation (2.1) becomes significant; this term represents the initial modifications of the boundary-layer flow from the Rayleigh flow described by the first term of equation (2.1). An ordinary differential equation for  $f_1'(\zeta)$  is readily obtained, which contains  $f_0'(\zeta)$  on the right side as a forcing function, and a solution is available in closed form. If  $t$  is dimensionless time (with respect to  $a/U_0$ , where  $a$  is the cylinder radius and  $U_0$  is the cylinder speed), the Blasius solution predicts a reversal in the wall shear at  $t_s = 0.35$ . Goldstein

and Rosenhead (1936) evaluated the terms  $O(t^2)$  in equation (2.1) analytically, and used these to refine the estimate to  $t_s=0.320$ . Beyond this stage, analytical evaluation of the functional coefficients of the time series is not feasible, and Collins and Dennis (1973a) computed the functional coefficients numerically up to and including those associated with  $t^7$ ; the estimate of the separation time was further refined to  $t_s=0.322$ . Subsequently, Cowley (1983) evaluated terms up to and including those associated with  $t^{50}$ . These series solutions give very accurate representations of the flow field for early times, up to and beyond the time when flow reversal occurs in the boundary layer. Cowley (1983) found that his series failed to converge at about  $t=1.5$ ; however, for time-series calculations of a less heroic nature, the radius of convergence in  $t$  is difficult to estimate with any degree of confidence. For this reason a number of authors have carried out full numerical solutions of the problem, to attempt to extend the solutions to larger times beyond the point when the validity of the time series was in question.

The early numerical solutions of the problem were all carried out using equations based on the Eulerian description of the motion, and include the investigations of Belcher *et al* (1972), Collins and Dennis (1973b), Bar-Lev and Yang (1975) and Cebeci (1978, 1979). A variety of analytical transformations and numerical procedures were employed. However, all of these calculations finally encountered extreme numerical difficulties which are evident by  $t=1$ , and which finally made it impossible to continue the integrations with any degree of accuracy. Although the collective experience of these numerical integrations was suggestive of the development of a singularity in the solution of the boundary-layer equations, a clear demonstration of an irregularity proved elusive due the uncertain level of accuracy in the numerical solutions beyond a certain stage. This situation was further confused (see Riley, 1975) by some misinterpretation of the meaning of a similarity solution



due to Proudman and Johnson (1962); these authors idealized the flow at the rear stagnation point of the circular cylinder by consideration of the boundary layer due to a fixed outflow stagnation point on an infinite plane wall, as indicated in figure 2.2. There is no steady solution available for such a boundary-layer flow, and Proudman and Johnson (1962) considered the evolution of the impulsively-started problem. The tangential velocity in the boundary layer was written as

$$u = -x \cdot \frac{\partial f}{\partial y}(y, t) . \quad (2.2)$$

Shortly after the impulsive start the wall shear changes sign and the solution describes the flow pattern shown schematically in figure 2.2. For large times a similarity solution was found in which  $f$  depends only on the variable

$$\tilde{\zeta} = y \cdot e^{-t} . \quad (2.3)$$

Consequently, the boundary layer thickens exponentially with time. Riley (1975) argues that the boundary-layer equations are valid for all finite time, and that the viscous region will achieve a thickness comparable to the cylinder radius (and thereby alter the external flow) only when  $t = O(\log(Re))$ . The approach was extended subsequently to higher order terms by Robins and Howarth (1972), and has recently been considered by Van Dommelen and Shen (1985). The physical picture of a thickening viscous region which gradually displaces the external flow, as suggested by the Proudman and Johnson (1962) solution, is appealing; experiments relating to the impulsively-started cylinder imply that the boundary layer near the rear stagnation point does eventually lift off the wall. This led some authors to suspect that the common difficulties experienced with numerical integrations of the boundary-layer equations were somehow associated with the expected exponential growth near the rear stagnation point. Cebeci (1979) developed a numerical

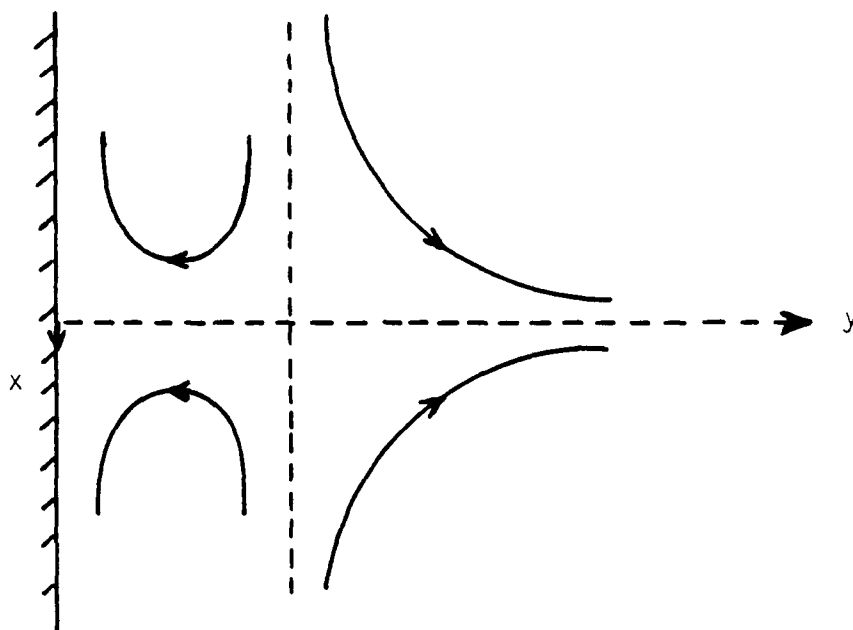


Figure 2.2. The Proudman-Johnson problem of unsteady flow near an outflow stagnation point on an infinite plane wall.

procedure which allowed the calculations to proceed further in time than had been previously accomplished. It was claimed that there was no evidence of a singularity, and although failure of the numerical algorithm occurred again, this was attributed to a rapid increase of the boundary-layer thickness in the reversed-flow region which made "the computations there increasingly uneconomical" (Cebeci, 1979).

A central question in the study of impulsively-started flows is related to the manner in which the developing boundary layer finally interacts with, and influences, the outer external flow. Such an interaction is known as a viscous-inviscid interaction, and it is clear from experiments that such interaction does eventually occur for the circular cylinder, as well as a wide variety of other flows. The fundamental questions are related to: (1) where the interaction starts to develop; (2) the nature of the interaction; and (3) the relevant physical processes involved. At one time, some authors believed that the evolution of recirculating flow somehow invalidated the boundary-layer assumptions (which are simply that the boundary layer remains thin). However, there are a variety of solutions involving steady recirculating flow that have been produced with modern interactive methods (c.f. §1.1) in which the boundary layer remains thin. Riley (1975) points out that a distinction must be made between separation (in the classical sense) and the phenomenon of "breakaway" or "breakdown" (see also Williams, 1977). Following Riley (1975), the term "breakaway" is understood to imply a catastrophic breakdown of the boundary-layer assumptions in which the "notion of a thin boundary layer, embedded within an inviscid flow, fails".

The Proudman-Johnson (1962) solution, and some numerical studies (e.g. Cebeci, 1979), suggested that breakaway for the circular cylinder occurs through a rapid thickening of the reversed-flow region, which leads to a massive displacement of the external flow field. In recent times there has been

considerable interest in developing models of steady, separated flow at high Reynolds numbers. Most of these models (see, for example, Smith, 1985) indicate a physical picture of two very large eddies attached to the cylinder in the steady state. Of course, such solutions are expected to be unstable, since it is well known that cylinder wakes at high Reynolds numbers are characterized by convected vortices that are shed periodically from the cylinder. However, if a steady symmetrical solution, similar to the structure proposed by Smith (1985), exists, it should be reachable as a terminal state of the impulsively started problem. In practical situations, this terminal state can never be achieved because it is not possible to suppress the effects of asymmetric perturbations in the flow field which ultimately trigger vortex shedding. The physical picture of the reversed-flow region gradually thickening, in the impulsively-started cylinder problem, has some appeal because it is easy to extrapolate this evolution to the type of steady state described by Smith (1985). Unfortunately, this simplistic picture of the flow evolution turns out to be incorrect, and the numerical difficulties experienced by many authors are not associated with exponential thickening near the rear stagnation point. On the contrary, the major problem occurs in quite a different region of the flow, near the separation point  $x_s$ . Here, the boundary layer focuses into a narrow needle of erupting fluid, as depicted schematically in figure 2.1(d), in a process that will be described subsequently.

### 2.3 The MRS Model

The impulsively-started circular cylinder is one of many fundamental flows that involve a rich variety of complex, unsteady effects. The study of laminar unsteady separation has been controversial during the past twenty years, and two main points have been debated, namely: (1) how unsteady separation should be defined, and (2) whether or not a singularity evolves at

finite time within the solution of the boundary-layer equations, in all cases of separation. Sears and Telionis (1971) have pointed out that the criteria of vanishing wall shear (which signals the onset of reversed flow for the impulsively-started cylinder problem) and reversed flow itself, are not sufficiently general criteria to describe all cases of unsteady separation. A simple example is due to Rott (1956) and is shown in figure 2.3. Here, the external flow is impinging on the wall at  $x=0$ , and typical boundary-layer profiles for a wall moving with constant velocity to the right are sketched in figure 2.3. To the right of  $x=0$ , the external flow speeds up with increasing distance from the stagnation point but, since the wall speed is constant, a point of zero shear eventually occurs (labeled A in figure 2.3). However, the vanishing of the shear stress is not significant in this case and certainly does not imply that "breakaway" will occur. To the left of the stagnation point, reversed flow (defined here as corresponding to a direction opposite to the local mainstream velocity) is observed immediately in the laboratory reference frame and yet, again, breakaway does not occur. More complex examples are described by Walker (1978) and Ece, Walker and Doligalski (1984). The first of these examples corresponds to the vortex-induced boundary-layer problem described in §1.5, which will be considered in detail in this study. In a frame of reference moving with the vortex, there is flow in both the upstream and downstream directions even in the early stages of the boundary-layer development (Walker, 1978). As the boundary-layer flow develops, a small recirculating eddy forms and starts to grow. Walker (1978) describes this phenomena as separation and suggests that "the first appearance of a closed recirculating eddy in the flow field" is a definition of separation which is in the spirit of the classical view of separation for flow past fixed walls. One potential difficulty with this definition is that whether closed streamlines are seen or not depends on the frame of reference of the observer (Walker, 1978; Doligalski and Walker, 1984). Nevertheless, in many problems there is a natural reference frame. Furthermore, the development of recirculating secondary

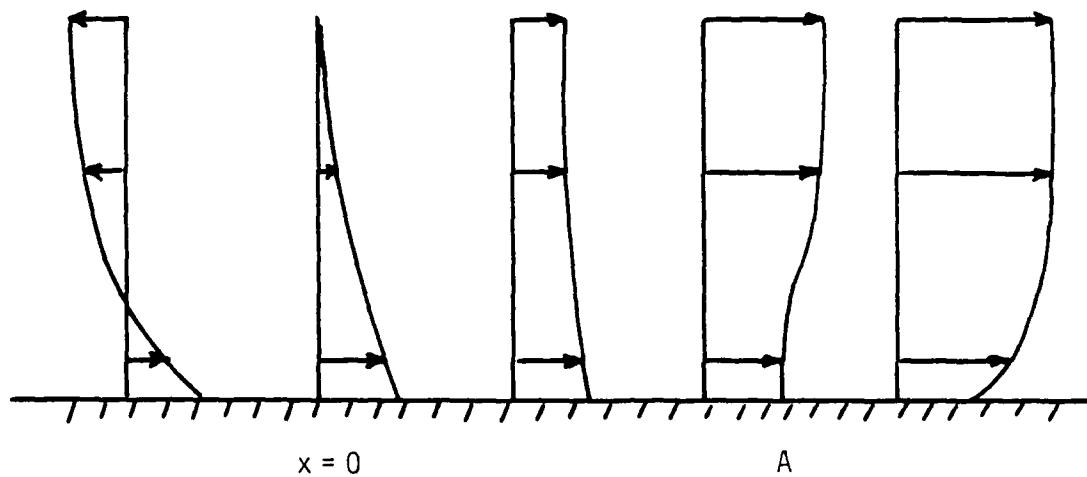


Figure 2.3. Schematic of the boundary-layer development at a front stagnation point for a wall moving at constant velocity.

eddies within the boundary-layer flow is usually the precursor of an interactive event at a later stage (Ersoy and Walker, 1985; 1986); in other words, "breakaway" in the sense described by Riley (1975). The second example of interest here is the impulsively-started translating and rotating cylinder considered by Ece *et al* (1984). Here, closed recirculating eddies appear within the boundary layer shortly after the impulsive start. However, unlike the classical separation problems, these eddies are not attached to the wall and their birth is not associated with a vanishing of the wall shear.

An alternative and rather different view of boundary-layer separation was put forth by Sears and Telionis in 1971. Their model has its basis in a previous study by Moore (1958), who argued that "a singular boundary-layer solution is no doubt a reliable indication of separation". He conjectured that such a singularity would develop along the line of zero vorticity within the boundary layer; in the context of the boundary-layer equations, the vorticity is given by  $\omega = -\partial u / \partial y$ , and it is worthwhile to note that a line of zero vorticity is present whenever regions of recirculating flow occur. Moore (1958) also suggested that the "separation point" should move with the local streamwise flow speed. Sears and Telionis (1971) generalized these ideas and asserted that "separation" should be defined, in all cases, as occurring at the instant of formation of a singularity in the boundary-layer solution. It is useful here to discuss briefly the physical implications of the evolution of a singularity. The boundary-layer equations are an exact subset of the Navier-Stokes equations in the limit  $Re \rightarrow \infty$  and describe an attached flow in a thin layer near the surface with thickness  $O(Re^{-1/2})$ . When a boundary layer remains thin, fluid particles stay near the surface and the scaled variables  $y$  and  $v$  in equations (1.9) continue to be  $O(1)$ . On the other hand, when rapid thickening of the boundary layer occurs and the fluid particles are eventually located at a distance greater than  $O(Re^{-1/2})$  from the wall,  $y$  must become large in order to overcome the infinite limiting value of  $Re$ ; similarly, as normal velocities

having a magnitude greater than  $O(Re^{-1/2})$  develop,  $v$  must become singular (c.f. equation (1.9)). The physical implication of the evolution of a singularity is that an interaction with the external flow is developing and that a new subset of the Navier-Stokes equations is required to describe the next stage in the process. It emerges that unsteady interactions are quite complicated, and the flow field near the "singularity region" develops a multi-layer structure which will be discussed in §2.5 and §2.6. In any event, for impulsively-started problems (as well as other situations where the boundary layer is initially thin and passive) the formation of a singularity may be thought of as the first time at which an erupting boundary layer has a significant effect on the external inviscid flow; put another way, it represents the onset of a viscous-inviscid interaction between the boundary layer and the external flow. Consequently "separation", in the sense defined by Sears and Telionis (1971), refers to the event which Riley (1975) has described as "breakaway"; another equivalent description that has been used by various authors is "breakdown" (Williams, 1977). At present, the Sears and Telionis (1971) definition of separation is not universally accepted and, as Williams (1977) remarks, "only history will determine which terminology will be finally accepted". To some extent, the definition of separation is a matter of personal taste, and in this study the term separation is used to denote the first appearance of recirculating flow, while "breakdown" is used to imply "separation" in the sense suggested by Sears and Telionis (1971).

A more important aspect relates to the nature of the flow field as "separation" or breakdown is about to occur. Sears and Telionis (1971) postulated what is now known as the MRS model (after Moore, Rott and Sears). In the model, they envisaged a moving stagnation point or bifurcation point termed the "center of separation", a sketch of which is shown in figure 2.4(a) (reproduced from Sears and Telionis, 1975). In these sketches, the flow at large distances from the wall is always from left to right, and the frame of



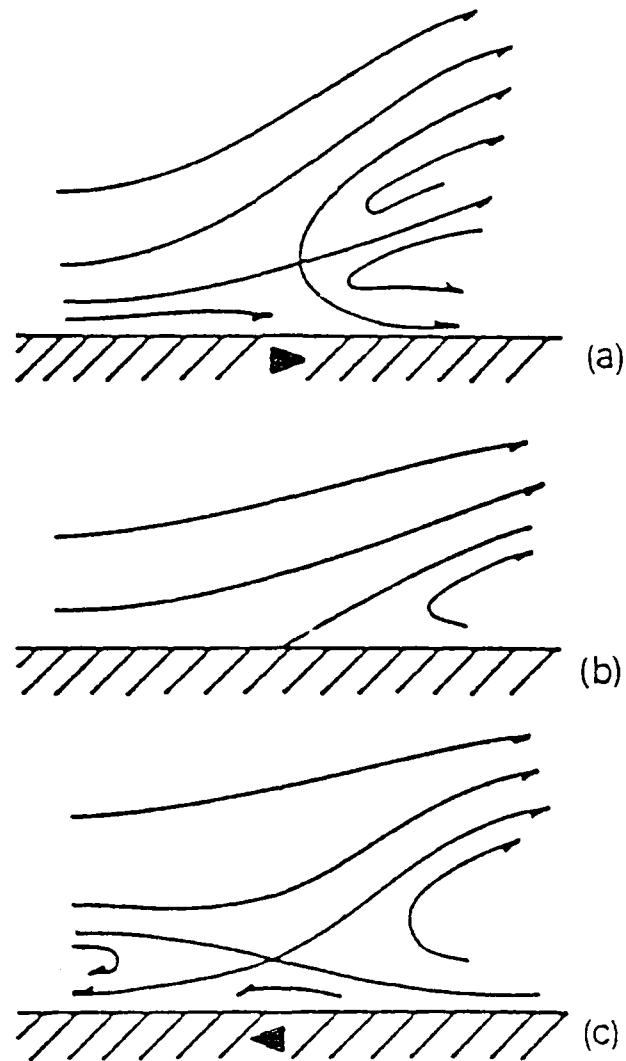


Figure 2.4. Streamline patterns at separation:

- (a) downstream-moving wall,
- (b) fixed wall,
- (c) upstream-moving wall; according to Moore, Rott and Sears

(reproduced from Sears & Telionis, 1975, figure 1)

reference is moving with the "center of separation". The situation depicted in figure 2.4(a) was meant to describe the instantaneous streamlines just before the boundary-layer eruption occurs; in this case the "center of separation" is moving upstream and thus, in a frame of reference moving with the separation, the wall appears to be moving downstream. Most subsequent numerical studies of unsteady separation concentrated on situations involving "downstream-moving walls". However, it is important to note that the terminology does not necessarily imply that the wall is moving in the laboratory frame, but is moving only with respect to the separation; since this "downstream-moving wall" terminology is potentially confusing, Van Dommelen (1981) subsequently refers to such phenomena as "upstream-slipping separation". In any event, let  $(x_0(t), y_0(t))$  denote the coordinates of the moving stagnation point depicted in figure 2.4(a), and let the streamwise velocity of the "center of separation" be  $U_s(t)$  where

$$U_s(t) = \frac{dx_0}{dt}. \quad (2.4)$$

In the MRS model there are two conditions which were conjectured (Sears and Telionis, 1971) to define the necessary conditions for the evolution of a singularity; these are that: (1) the singularity moves with the local flow speed, viz.

$$U_s(t) = u(x_0, y_0, t), \quad (\text{MRS I}), \quad (2.5)$$

and (2) the "separation" point corresponds to a location of zero shear, viz.

$$\frac{\partial u}{\partial y} = 0 \text{ at } x=x_0, y=y_0, \quad (\text{MRS II}). \quad (2.6)$$

Sears and Telionis (1971) also argued that the singularity defining the "separation" was similar to the Goldstein (1948) singularity, which is known

to occur in steady two-dimensional boundary-layer solutions when the mainstream pressure gradient is adverse and prescribed. The following expansions for  $u$  and  $v$  just upstream of separation were proposed:

$$u(x,y,t) = u_0(\psi,t) + A(t) \cdot \chi^{1/2} \cdot \frac{\partial u_0}{\partial y} + O(\chi^{3/4}), \quad (2.7)$$

$$v(x,y,t) = \frac{1}{2} \cdot A(t) \cdot \{u_0(\psi,t) - U_s(t)\} \cdot \chi^{-1/2} + O(\chi^{-1/4}). \quad (2.8)$$

Here,

$$\chi = x_0(t) - x, \quad \psi = y - y_0(t), \quad (2.9)$$

with  $\psi \geq 0$  and  $\chi \ll 1$ ; the function  $A(t)$  is unknown and  $u_0(\psi,t)$  describes the velocity profile at separation. The proposed structure therefore involves a moving singularity in which the boundary-layer velocities are finite; the shear vanishes near the "center of separation" at a point that is, in general, located above the wall. On the other hand, for points above  $y=y_0$ , equation (2.8) indicates that large normal velocities will occur near  $x=x_0(t)$ , thus giving rise to a local bifurcation of the boundary layer.

The MRS model was intended to provide a general description of boundary-layer separation. For a steady two-dimensional flow with a stationary wall (c.f. figure 2.4(b)) the separation point is fixed, and the MRS model reduces to

$$\frac{\partial u}{\partial y} = 0 \text{ at } u=0, \quad (2.10)$$

which is consistent with the classical definition of separation. Furthermore, equations (2.7) and (2.8) become the familiar upstream expansion associated with the Goldstein (1948) singularity (see also Stewartson, 1958). Van Dommelen (1981) subsequently refers to this type of separation as "non-

slipping separation". The third and last type of separation occurs where the separation point moves downstream, and has been referred to by Van Dommelen (1981) as "downstream-slipping separation". The pattern of the instantaneous streamlines near such a point is shown in figure 2.4(c) as envisaged by Sears and Telionis (1971), who generally refer to such situations as the "upstream-moving wall"; this picture was later modified somewhat by Van Dommelen (1981). This situation occurs rather less frequently than "upstream-slipping separation", although a number of examples have been studied (Elliott, Cowley and Smith, 1983; Ece, Walker and Doligalski, 1984); such "separations" did not occur in the present study and consequently will not be discussed further.

The conjectures of Sears and Telionis (1971) were quite controversial, particularly the proposed Goldstein singularity structure in equations (2.7) and (2.8); Riley (1975) has discussed in detail why this aspect of the Sears and Telionis model must be regarded as incomplete and open to question. A large number of attempts to verify this behavior were made through numerical calculations, some of which are described by Williams (1977). An objective of these studies was to confirm the conjectured velocity dependence on the square root of  $(x_0(t) - x)$ . By and large, the numerical studies were not conclusive and were hampered by a number of difficulties. First, as Williams (1977) has noted, the speed at which the "center of separation" moves is unknown in any given problem; the streamline pattern depicted in figure 2.4(a) may be clearly observed only in the moving reference frame of the "center of separation" whose velocity is known *a priori*. Second, all boundary-layer integrations to this stage had been carried out using the conventional Eulerian description of the motion, and although it was evident that severe numerical difficulties were being encountered, it was not possible to definitively pinpoint the reasons for the failures. In regions where the imposed mainstream pressure gradient was adverse, the boundary-layer solutions were

observed to develop relatively large normal velocities in a local zone which was narrow in the streamwise direction. Furthermore, despite a variety of attempts to pack grid points into this zone (see, for example, Cebeci, 1986), eventually it proved impossible to continue the integrations with good accuracy. Since all of these Eulerian computations could not be continued to a time relatively close to the formation of the singularity, it was not possible to infer the nature of the singularity from the numerical results with any degree of confidence.

## 2.4 Lagrangian Methods

In 1980 a major advance occurred with the publication (Van Dommelen and Shen, 1980) of a portion of the Ph.D. thesis of Van Dommelen (1981). In this study, it was pointed out that Lagrangian variables are ideally suited to the computation of unsteady separation phenomena in boundary layers. In the conventional Eulerian formulation, the changes in both  $(u,v)$  velocities are computed at a large number of fixed mesh points in space, as the flow evolves. The Lagrangian viewpoint is fundamentally different, wherein the velocities of a large number of fluid particles are identified at points on a spatial grid at some initial time; as time increases, the subsequent velocity and position of each fluid particle is then computed as a function of time (and initial starting location in the grid). The boundary-layer equations in Lagrangian variables have been given in equations (1.15) and (1.16) and also in Appendix A. One of the main advantages of these equations was first pointed out by Van Dommelen and Shen (1980), and is that (1.15) and (1.16) do not contain the normal velocity  $v$  and the normal coordinate  $y$ , the quantities which become large (and eventually singular) as a boundary layer evolves toward an eruption. By contrast, the quantities which are computed, namely the streamwise particle positions  $x(\xi,\eta,t)$  and their streamwise velocities  $u(\xi,\eta,t)$ ,

will remain finite and well-behaved for all time. The Lagrangian equations provide a natural way to describe the eruptive phenomena of interest in this study; as strong outflows develop, a substantial number of fluid particles move into this zone, thus providing good local resolution of the phenomena.

At any stage in a numerical integration it is possible to compute the normal distance  $y(\xi, \eta, t)$  of each fluid particle from the wall (if this information is desired) through integration of the continuity equation (1.21); the integral is given by equation (1.23) which is repeated here, viz.

$$y(\xi, \eta, t) = \int_{\text{wall}}^{(\xi, \eta)} \frac{ds}{\sqrt{x_\xi^2 + x_\eta^2}}. \quad (2.11)$$

Here, the integral is taken along a path of constant  $x$ , which starts at the wall and passes through  $(\xi, \eta)$ . It is evident that a singularity occurs if the distribution of  $x(\xi, \eta, t)$  develops a stationary point  $S$ , viz.

$$\frac{\partial x}{\partial \xi} = \frac{\partial x}{\partial \eta} = 0, \quad (2.12)$$

at some location  $(\xi_s, \eta_s)$  at time  $t_s$ ; this point will lie on some line of constant  $x$  which will be designated as  $x=x_s$ . It is evident that once a stationary point develops, a singularity occurs in the  $y$ -position. The physical implication of this is that fluid particles which lie along lines of constant  $x$  close to  $x_s$ , at  $t=t_s^-$ , will be located at very large distances from the wall. The condition (2.12) represents another major advantage of the Lagrangian description in that it provides a clear and unambiguous criterion for the evolution of a singularity in the boundary-layer solution. Although it does prove difficult to pinpoint the precise time when (2.12) occurs from numerical studies, there is no doubt when this behavior does develop; the numerical problems associated with determining  $t_s$  will be described in chapter 4. The structure of the singularity will be discussed in more detail in the next section.

Van Dommelen (1981) considered the classical problem of the impulsively-started circular cylinder. Shortly after the initiation of the motion, regions of recirculating flow occur near the rear stagnation point (as discussed in §2.2), and consequently a line of zero vorticity is present. With the passing of time, the reversed flow region thickens and the zero-vorticity line penetrates to the outer regions of the boundary layer, far from the wall where the flow is effectively inviscid. Van Dommelen (1981) argues that in such circumstances the viscous term in the boundary-layer equations becomes negligible, and furthermore that, if a zero-vorticity line is present at some initial time, a stationary point must form in the  $x(\xi, \eta, t)$  field in a finite time. The evolution of a stationary point in  $x$  implies a singularity in  $y$ , and Van Dommelen (1981) rejects the possibility that this singularity can be smoothed out by viscosity. Numerical integrations of the Lagrangian equations were carried out for the impulsively-started cylinder using several sets of mesh sizes, and these confirmed that a stationary point (and a singularity) did form at finite time. The best estimate for this time was  $t_s = 1.500$  after the impulsive start, with the singularity occurring at a location  $110^\circ$  from the front stagnation point. The local flow speed at the stationary point was found to be negative with

$$U_s = -K, \quad K = 0.26, \quad (2.13)$$

and consequently this is a case of "upstream-slipping separation". These numerical solutions were the first calculations completed all the way to the evolution of a singularity, describing the terminal boundary-layer state. Since only regular quantities ( $x$  and  $u$ ) are computed in this approach, there is no difficulty in computing the solution to  $t = t_s$ . In fact, the integrations for  $x$  and  $u$  can, in general, be continued beyond  $t = t_s$ ; it is only through examination of the  $x$  field for stationary points (which lead to a singularity in  $y$ ) that  $t_s$ , and the range of validity of the integrations, may be determined. The nature of the

boundary-layer structure as  $t \rightarrow t_s$ , near  $x = x_s$ , consists of a region which is moving upstream with speed  $K$  and which is thinning in the streamwise direction proportional to  $(t_s - t)^{3/2}$ . The displacement thickness rapidly focuses into a explosively-growing spike as  $t \rightarrow t_s$ . A typical velocity profile for  $t \rightarrow t_s$ , near  $x = x_s$ , is sketched in figure 2.5. In a narrow region which is progressively thinning in the streamwise direction, the boundary-layer flow bifurcates into two layers (regions I and III) separated by a "dead-water zone" (region II), where the vorticity is zero and which is moving upstream with speed  $K$ . For the continuity integral in equation (2.11) along  $x = x_s$ , region I corresponds to the part below the stationary point, while region III corresponds to the part above. The thick "dead-water zone", region II, corresponds to values of  $(\xi, \eta)$  along  $x = x_s$  in the immediate vicinity of the stationary point  $S$ .

Van Dommelen's study also confirmed the two MRS conditions. Since the  $x$  field is regular it may be expanded as a Taylor series about the "separation point"  $S$  at  $(\xi_s, \eta_s)$ , according to

$$x(\xi, \eta, t) = x_s(\xi_s, \eta_s, t) + \frac{\partial x}{\partial \xi} \bigg|_{\xi_s, \eta_s} (\xi - \xi_s) + \frac{\partial x}{\partial \eta} \bigg|_{\xi_s, \eta_s} (\eta - \eta_s) + \dots \quad (2.14)$$

for  $|\xi - \xi_s| \ll 1$  and  $|\eta - \eta_s| \ll 1$ . But using equations (2.12) and differentiating with respect to  $t$ , it follows that the point  $S$  moves with the local flow velocity in the direction of the wall, according to

$$U_s = \frac{\partial x_s}{\partial t} \quad (\text{MRS I}). \quad (2.15)$$

The vorticity in general is given by

$$\omega = -\frac{\partial u}{\partial y} = \frac{\partial x}{\partial \eta} \frac{\partial u}{\partial \xi} - \frac{\partial x}{\partial \xi} \frac{\partial u}{\partial \eta}. \quad (2.16)$$



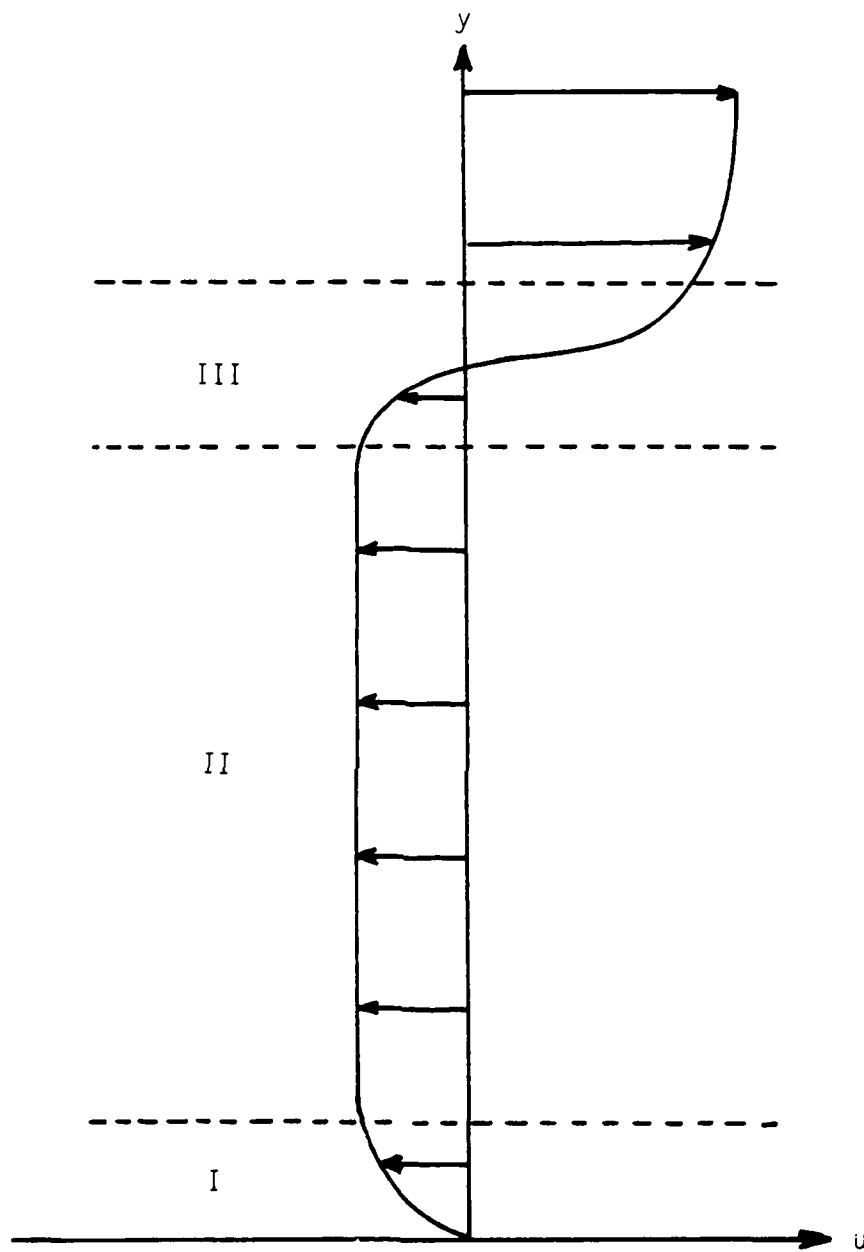


Figure 2.5. A typical velocity profile near  $x_s$  as  $t \rightarrow t_s$ .

Consequently, at the stationary point, where conditions (2.12) hold,

$$\omega_s = 0 \quad (\text{MRS II}), \quad (2.17)$$

which is the second MRS condition.

The details of the flow development obtained by Van Dommelen and Shen (1980) and Van Dommelen (1981) clearly explained the difficulties encountered by other authors who had tried to compute unsteady separation using the conventional Eulerian formulations. In addition, the nature of the phenomena was clearly defined for the first time. As the boundary-layer flow evolves toward eruption, the flow focuses into a narrow band which progressively thins in the streamwise direction, but which grows explosively in the direction normal to the wall. The nature of the flow in this developing spike is complex and will be described in physical terms in the next section. However, it is clear that the Lagrangian formulation is best suited to this type of problem. In any given situation, the location of formation of the singularity is unknown *a priori*. Furthermore, even if  $x_s$  were known approximately (from some previous calculation), a procedure of packing a large number of mesh points into this region (see, for example, Cebeci, 1986) will only give good accuracy for a limited period of time. It is evident that a boundary-layer calculation cannot be carried out with reasonable accuracy on a fixed mesh in the Eulerian frame, as the flow focuses toward an eruption.

## 2.5 The Terminal Boundary-Layer Structure

Once a stationary point occurs in  $x$ , a singularity has developed in the solution of boundary-layer equations. Assume that this occurs at  $x=x_s$  and at time  $t_s$ ; in addition, the case of "upstream-slipping" separation is of interest,

in which the local flow velocity at  $x_s$  {at  $(\xi_s, \eta_s)$ } is  $-K$ , where  $K > 0$ . Both Van Dommelen (1981) and Elliott, Cowley and Smith (1983) have investigated the structure of the singularity and what follows is a description of their results in terms of Eulerian coordinates. As indicated in figure 2.5, when the boundary layer proceeds toward interaction it bifurcates, near  $x_s$ , into three zones which are shown schematically and in more detail in figure 2.6. It should be noted that in the numerical integrations (c.f. Van Dommelen (1981) and the results in chapter 4) this entire region appears as a spike on a scale where  $(x - x_s) = O(1)$ ; in figure 2.6, the scale in the  $x$ -direction has been expanded considerably to show the internal structure of the "erupting spike". Elliott, Cowley and Smith (1983) and Van Dommelen (1981) show that the terminal solution is a function of  $\tilde{X}$  and  $\tilde{Y}$ , where

$$\tilde{X} = \frac{x - x_s - K(t_s - t)}{(t_s - t)^{3/2}}, \quad \tilde{Y} = (t_s - t)^{1/4}. \quad (2.18)$$

The variable  $\tilde{X}$  measures streamwise distance in a coordinate system moving upstream with speed  $K$ , and which arrives at  $x_s$  at  $t = t_s$ ; in physical space, this region thins proportional to  $(t_s - t)^{3/2}$  as  $t \rightarrow t_s^-$ . The variable  $\tilde{Y}$  measures normal distance from the wall in a region which is thickening like  $(t_s - t)^{-1/4}$ . Within zone II in figure 2.6 the flow is inviscid and nonlinear, with the streamwise velocity given by

$$u = -K + (t_s - t)^{1/2} \tilde{U}(\tilde{X}, \tilde{Y}). \quad (2.19)$$

Consequently, zone II is a vorticity-depleted region in which the flow is almost uniform, moving in the upstream direction. A solution for  $\tilde{U}$  may be obtained but complete details will not be given here. The solution is symmetric about a line  $\tilde{Y} = \tilde{Y}_0(\tilde{X})$ , which bisects region II and can be evaluated as a function of  $\tilde{X}$ ; the curve  $\tilde{Y} = 2\tilde{Y}_0(\tilde{X})$  then defines the top of region II. The velocity  $\tilde{U}$  has a minimum value at  $\tilde{Y} = \tilde{Y}_0$  at each  $\tilde{X}$  station, but increases to become large

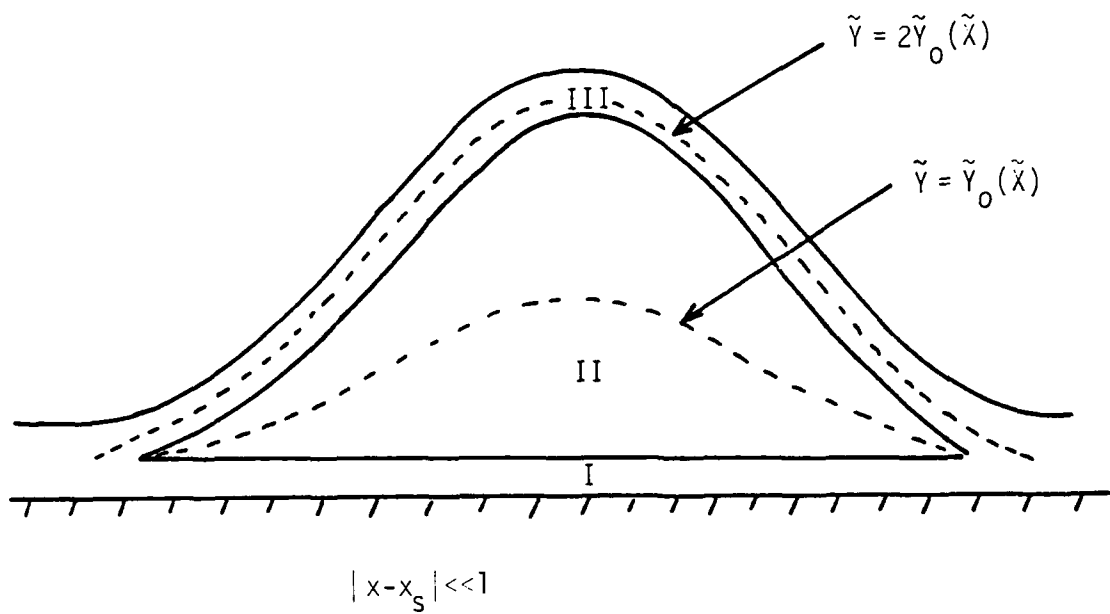


Figure 2.6. Schematic of the initial stage of an interaction (not to scale).

and positive at the bottom and top of region II; in fact

$$\bar{U} \sim \frac{4}{\bar{Y}^2} \quad \text{as } \bar{Y} \rightarrow 0, \quad (2.20)$$

$$\bar{U} \sim \frac{4}{(\bar{Y} - 2\bar{Y}_0)^2} \quad \text{as } \bar{Y} \rightarrow 2\bar{Y}_0. \quad (2.21)$$

Note that, in view of the second of equations (2.19), it may be seen from equation (2.20) and (2.21) that the streamwise velocity starts to deviate progressively from  $-K$  as zones I and III are approached. In I and III,  $y$  and  $y - \bar{Y}_0(t_s - t)^{-1/4}$  are  $O(1)$ , respectively; the velocity is reduced to relative rest on the wall in zone I, and is adjusted across the shear layer III to meet the positive velocity in the upper part of the boundary layer (associated with the external mainstream flow which is from left to right). As  $|\bar{X}| \rightarrow \pm\infty$ , it can be shown (Elliott, *et al*, 1983) that  $\bar{U}$  is  $O(\bar{X}^{1/3})$  and consequently, from (2.18) and (2.19), it may be seen that  $u$  progressively deviates from  $-K$  at the streamwise extremities of the region depicted in figure 2.6, to meet the conventional boundary layer to either side.

Some important features of the terminal solution are:

- (1) The governing equation for  $\bar{U}$  is nonlinear and inviscid, and is independent of the external mainstream pressure gradient. Consequently, at this stage within the erupting zone, the solution has "forgotten" the particular external adverse pressure which initiated the "separation" process. Therefore, the terminal solution appears to be generic for all cases of "upstream-slipping" separation.
- (2) Since the solution in zone I is a function of  $y$  alone, the wall shear near  $x=x_s$  should be regular.
- (3) It follows from the continuity equation and from equations (2.18), (2.19)

that the normal velocity,

$$v = O(t_s - t)^{-5/4} \text{ as } t \rightarrow t_s, \quad (2.22)$$

near  $x = x_s$ .

- (4) The growth of the displacement thickness is given by

$$\delta^* = O(t_s - t)^{-1/4} \text{ as } t \rightarrow t_s^-, \quad (2.23)$$

near  $x = x_s$ .

- (5) Although the MRS conditions were confirmed by Van Dommelen (1981) and Elliott *et al* (1983), the further suggestion of Sears and Telionis (1971), that the singularity in the terminal solution is a Goldstein (1948) singularity displaced from the wall, was shown to be incorrect.

## 2.6 The Onset of Interaction

The solution discussed in §2.5 describes a rapid rise (and eventual spiking) of the displacement thickness on a streamwise scale which is small but  $O(1)$ ; this phase of the process occurs effectively without interaction, and the influence of the mainstream pressure gradient is secondary. It is evident that the rapid local thickening of the boundary layer will induce an interaction with the external flow and that this must occur before  $t = t_s$ , in order to forestall the formation of the singularity. The first stage of interaction has been described by Elliott, Cowley and Smith (1983), and the following discussion is a synopsis of their development.

As the boundary layer thickens locally near  $x = x_s$ , the induced displacement effect is

$$O((t_s - t)^{-1/4} \tilde{Y}_0(\tilde{X})), \quad (2.24)$$

and it follows from equation (1.44) that the induced second-order streamwise velocity

$$U_1 = O\left\{(t_s - t)^{-1/4} \frac{\partial \tilde{Y}_0}{\partial x}\right\}. \quad (2.25)$$

If the pressure is expanded as

$$p = p_0(x) + \text{Re}^{-1/2} p_1 + \dots, \quad (2.26)$$

it follows from the Bernoulli equation that the induced pressure  $p_1$  is proportional to  $U_1$ . Therefore, near  $x = x_s$ , the pressure gradient due to the thickening boundary layer has the following order of magnitude:

$$\frac{\partial p}{\partial x} = O\left(\text{Re}^{-1/2} (t_s - t)^{-1/4} \frac{\partial^2 \tilde{Y}_0}{\partial x^2}\right). \quad (2.27)$$

Using (2.18), it follows that

$$\frac{\partial p}{\partial x} = O\left(\text{Re}^{-1/2} (t_s - t)^{-13/4}\right). \quad (2.28)$$

It may readily be confirmed, using the scalings in equations (2.18) and (2.19), that the equation for  $\tilde{U}$  involves only the convection terms in the boundary-layer equations and that in addition these terms are

$$O((t_s - t)^{-1/2}). \quad (2.29)$$

Consequently, interaction first comes into play when a balance occurs with equation (2.28) for

$$(t_s - t) = O(\text{Re}^{-2/11}). \quad (2.29)$$

From (2.18) and (2.19) it follows that, at this stage,

$$(x-x_s)-K(t_s-t)=O(\text{Re}^{-3/11}), \quad u+K=O(\text{Re}^{-1/11}), \quad (2.30)$$

$$Y = \text{Re}^{-1/2}y = \text{Re}^{-1/2}(t_s-t)^{-1/4}\tilde{Y} = O(\text{Re}^{-5/11}). \quad (2.31)$$

Therefore, a new set of scaled coordinates describing this first interactive state may be defined by

$$X_1=\text{Re}^{3/11}\{(x-x_s)-K(t_s-t)\}, \quad Y_1=\text{Re}^{5/11}Y, \quad (2.32)$$

with the scaled time given by

$$t_1=\text{Re}^{2/11}(t-t_s). \quad (2.33)$$

The streamwise velocity and pressure are scaled according to

$$u = -K + \text{Re}^{-1/11}U_1, \quad p=\text{Re}^{-2/11}p_1, \quad (2.34)$$

and upon substitution in the Navier-Stokes equations it is easily shown that

$$\frac{\partial U_1}{\partial t_1} + U_1 \frac{\partial U_1}{\partial X_1} - \frac{\partial \psi_1}{\partial X_1} \frac{\partial U_1}{\partial Y_1} = -\frac{\partial p_1}{\partial X_1}, \quad U_1 = \frac{\partial \psi_1}{\partial Y_1}, \quad (2.35)$$

$$\frac{\partial p_1}{\partial Y_1} = 0. \quad (2.36)$$

These equations describe a developing inviscid nonlinear flow in the vorticity-depleted region labeled zone II in figure 2.7, which has a transverse thickness  $O(\text{Re}^{-5/11})$ . There are layers above and below region II having thickness  $O(\text{Re}^{-1/2})$  which are labelled zones I and III. If  $Y_1 = \beta_1(X_1, t_1)$  denotes the



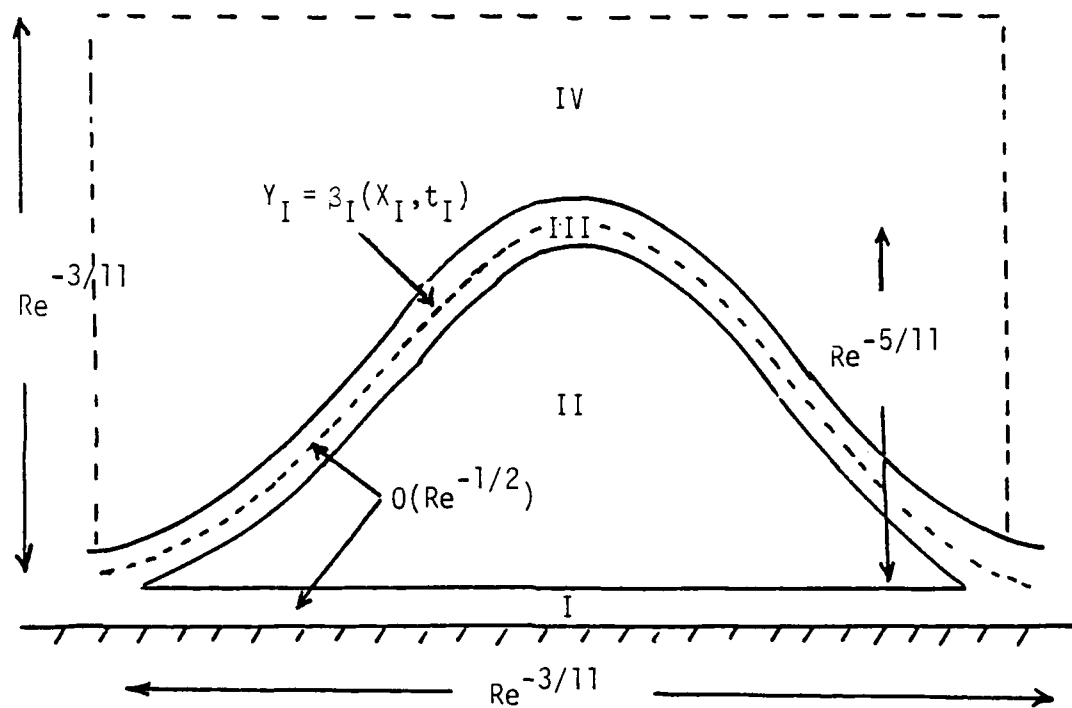


Figure 2.7. Schematic diagram (not to scale) of the first interactive state.

upper extent of zone II, it emerges that the solution in zone II has boundary conditions

$$U_1 \sim \frac{4}{Y_1^2} \quad \text{as } Y_1 \rightarrow 0, \quad (2.37)$$

$$U_1 \sim \frac{4}{(Y_1 - \beta_1)^2} \quad \text{as } Y_1 \rightarrow \beta_1, \quad (2.38)$$

to match the solutions in regions I and III. Note that, in view of equation (2.34),  $U_1$  must become large near regions I and III in order to overcome the small factor  $\text{Re}^{-1/11}$  and thereby change the uniform velocity  $-K$  in the central zone; the specific behavior indicated in equations (2.37) and (2.38) is not immediately obvious and follows from the detailed analysis of Elliott *et al* (1983). As zone II thickens with time, the external flow in an  $O(\text{Re}^{-3/11})$  by  $O(\text{Re}^{-3/11})$  region (which is centered on the point of eruption at  $x=x_s$  and which is labeled zone IV in figure 2.7) is influenced and the pressure response at any stage is given by

$$p_1 = \frac{1}{\pi} \int_{-\infty}^{+\infty} \frac{\partial \beta_1}{\partial \xi} \frac{d\xi}{X_1 - \xi}. \quad (2.39)$$

The problem described by equations (2.35) to (2.39) must be solved numerically, subject to the initial condition that, as  $t_1 \rightarrow -\infty$  the solution should match the boundary-layer terminal state described in §2.5. The numerical problem is complex and as yet has not been solved. At the same time it is possible to speculate on the physical development that is anticipated during this first stage of interaction.

As the boundary layer starts to thicken locally, interaction through the induced pressure gradient in equation (2.39) becomes significant and starts to alter the essentially uniform flow in zone II. However, during this stage the interaction is mainly inviscid and does not influence the flow in regions I and

III. The question then arises as to what happens next. In a recent study, Brown, Cheng and Smith (1988) have considered a similar interactive problem and have determined that a range of singularities can occur within a finite scaled time. In the present context, if a singularity occurs in the solution of equations (2.35) to (2.39) at  $X_{I_s}$  and at  $t_{I_s}$ , the anticipated terminal solution in this state (from Brown *et al*, 1988) is a function of

$$X_{II} = (X_I - X_{I_s})(t_{I_s} - t_I)^{1/2}, \quad (2.40)$$

with  $U_{II}$  and  $p_{II}$  of the form

$$U_I = \frac{1}{(t_{I_s} - t_I)^{1/2}} U_{II}, \quad p_I = \frac{1}{(t_{I_s} - t_I)} p_{II}. \quad (2.41)$$

Consequently, upon comparing (2.34) and (2.41) it may be noted that as  $t_I \rightarrow t_{I_s}$ , then  $u \rightarrow K$  and the pressure  $p$  should rise to become  $O(1)$  during this first interactive stage. Therefore, the velocity profile in region II is expected to be progressively changed away from the uniform profile depicted in figure 2.5; in addition, the vorticity in region II is expected to become progressively non-uniform and different from zero.

It can be argued that this terminal stage of the first interaction leads directly into a second interaction problem with a shorter x-scale  $O(\text{Re}^{-4/11})$  and a still faster time-scale  $O(\text{Re}^{-4/11})$ . A schematic of the conjectured next stage is shown in figure 2.8. The erupting boundary layer has now penetrated a distance  $O(\text{Re}^{-4/11})$  from the wall. At this point, the flows in regions I', II' and III' are all influenced by the induced pressure gradient, and all problems are nonlinear and mainly inviscid. The streamwise velocity profile will then be substantially altered from the flat, uniform distribution depicted in figure 2.5. The second stage of the interaction is also expected to terminate in a singularity at a finite time which is related to a singularity discovered recently

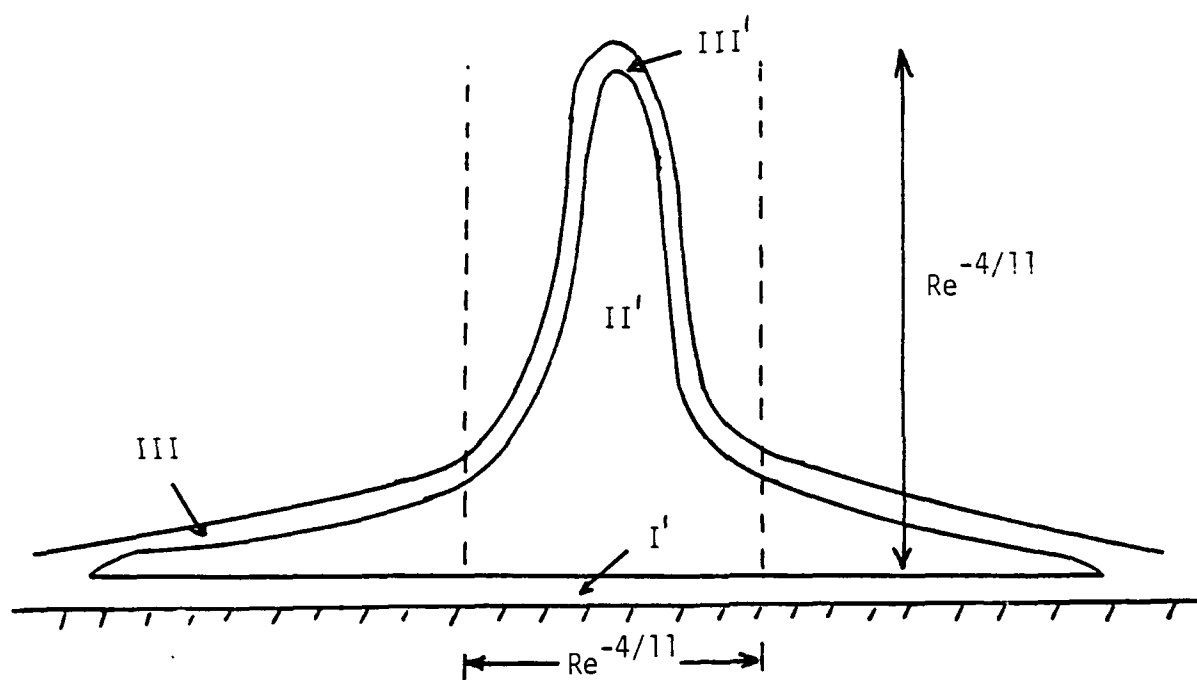


Figure 2.8. Schematic of the conjectured second stage of interaction (not to scale).

by Smith (1988), and which is described in the next section. It should be noted that the second interactive stage discussed here is highly conjectural, and in order to verify the breakdown anticipated in equations (2.40) and (2.41) it will be necessary to obtain numerical solution of the first interactive stage (described by equations (2.35) to (2.39)). Unfortunately, the numerical problem is quite difficult and at this stage has not been carried out. It also is possible that the second interactive stage (depicted in figure 2.8) does not occur and that the solution evolves directly from the first interaction stage to the structure discussed by Smith (1988).

## 2.7 Conventional Interacting Boundary-layer Theory

In the previous two sections the physical characteristics, length scales, and time scale of the first stage (as well as a possible second stage) of a strong interaction have been described for the limit problem  $Re \rightarrow \infty$ . It is evident that the developing flow structure is very complex and can be expected to go through several stages (which terminate in singularities at finite scaled times) before the erupting boundary-layer fluid particles penetrate to an  $O(1)$  distance from the wall. An alternative, potentially simpler, approach to the problem is the interacting boundary-layer method described in §1.4. This approach had been very effective for steady boundary-layer calculations in relieving the Goldstein singularity that occurs whenever the pressure gradient is adverse and prescribed, and the method has enjoyed widespread success in steady flows, as discussed in §1.1. A central question of interest in this study is whether an unsteady erupting boundary layer can be computed using conventional interacting boundary-layer methods, and whether the methodology relieves the singularities that are known to evolve (at least in the early stages of the interaction).

At present the evidence from the few computational studies that have been carried out using interacting boundary-layer methods in unsteady flows presents a mixed and inconclusive picture. Interacting boundary-layer calculations for the impulsively-started circular cylinder have been carried out by Henkes and Veldman (1987) and Riley and Vasantha (1989). Computations were carried out for  $Re=10^4$ ,  $10^5$  and  $10^6$  in both cases. It was concluded that the interacting boundary-layer approach may possibly postpone, and perhaps relieve, the singularity which is known to occur in the limit problem  $Re \rightarrow \infty$ . A similar conclusion was reached by Chuang and Conlisk (1989) in their study of the boundary layer induced by a convected rectilinear vortex; however, in this last study, the eruptive nature of the boundary-layer flow was so strong that, although breakdown of the numerical scheme seemed to be delayed by interaction, failure of the numerical scheme still did ultimately occur. Interacting boundary-layer studies for the flow over a pitching airfoil have been carried out by Cebeci *et al* (1988) with some success; however in this study it was also necessary to terminate the computations at a certain stage for reasons which were not explained. All of these investigations were carried out using the Eulerian formulation for the boundary-layer calculation; in some cases, grid-packing was carried out near the location where eruptive effects were expected. However, some of the authors used low-order numerical algorithms which may smear out important details of the flow, and thereby artificially suppress an important eruptive effect. Consequently, the usefulness of conventional interacting boundary-layer concepts for strongly eruptive flows remains in doubt.

Recently, Smith (1988) has presented an analysis that suggests a singularity can occur at finite time in formulations using the conventional interacting boundary-layer approach. Here, a brief synopsis of the main ideas and results of this paper will be given, since the numerical results obtained in the present investigation will ultimately be compared with Smith's (1988)

predictions. Assume that a singularity can occur at  $x=x_s$  and  $t=t_s$ , and consider a thinning zone which is moving upstream toward  $x_s$  with speed  $C$ ; here,  $C$  is to be found. The streamwise scaling adopted by Smith (1988) is

$$\xi = (x - x_s + CT)T^{-3/2}, \quad T = t_s - t, \quad (2.42)$$

which is similar to the first of equations (2.18) describing the scaled streamwise variable in the first interactive stage of the limit problem; this scaling was also suggested from a previous study of Brotherton-Ratcliffe and Smith (1987) on the stability of flow over a wall that had small surface distortions. The pressure near  $x_s$ , as  $t \rightarrow t_s^-$ , was written in the form

$$p = p_0 + T^{1/2} p_1(\xi) + T^{3/4} p_2(\xi) + \dots, \quad (2.43)$$

which is also a form suggested by the work of Brotherton-Ratcliffe and Smith (1987). Here  $p_0$  is a constant and  $p_1(\xi)$  is to be found through interactive concepts. Smith (1988) argues that the boundary layer splits into three zones as  $t \rightarrow t_s^-$ , which are shown schematically in figure 2.9. If  $y$  denotes the scaled boundary-layer variable then the main zone, zone II, has  $y = O(1)$  and is inviscid. In zone II the flow solution is expanded in the form

$$u = U_0(y) + T^{1/2} U_1(\xi, y) + T^{3/4} U_2(\xi, y) + T U_3(\xi, y) + \dots, \quad (2.44)$$

$$\psi = \psi_0(y) + T^{1/2} \psi_1 + T^{3/4} \psi_2 + T \psi_3 + \dots, \quad (2.45)$$

where  $U_0(y)$  is the velocity profile at  $x=x_s$  for  $T \rightarrow 0$ . It was assumed that, at some  $y_0$ ,  $U_0 = C$ , but the profile is arbitrary otherwise. The  $\psi_n$  satisfy linear equations which are readily solved and, for example, it emerges that

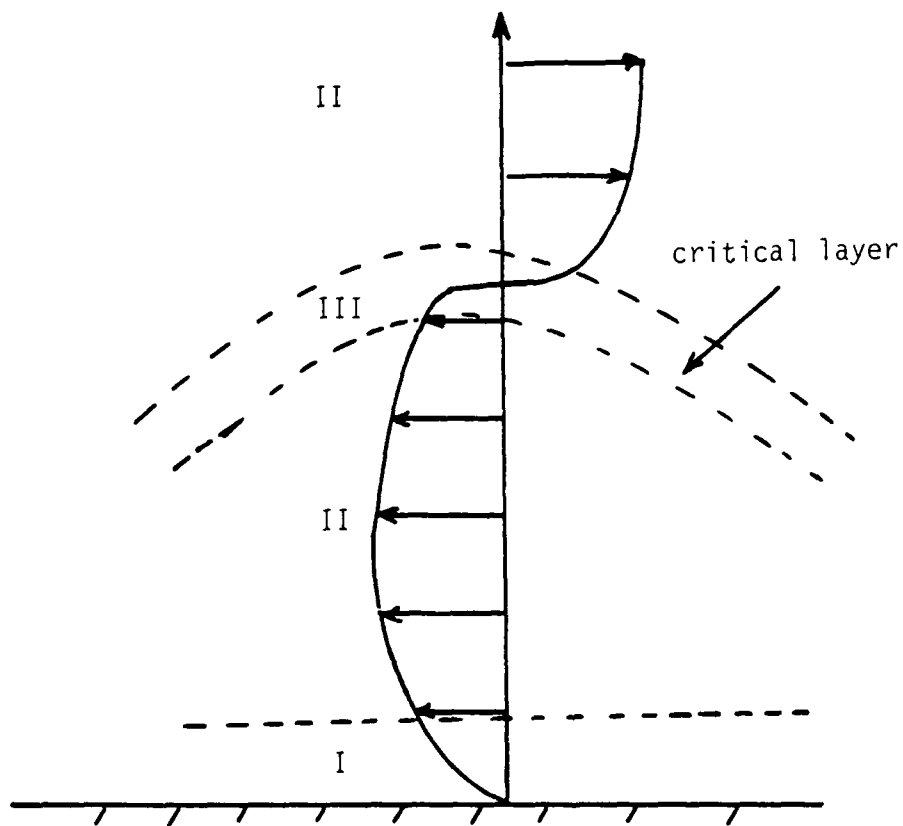


Figure 2.9. Schematic of the three-zone region associated with the terminal state of unsteady, interacting boundary layers (Smith, 1983).



$$\frac{\partial \Psi_1}{\partial \xi} = \{U_0(y) - C\} p_1'(\xi) \cdot \int_y^{+\infty} \{U_0(y) - C\}^{-2} dy, \quad (2.46)$$

in terms of the unknown pressure term  $p_1(\xi)$ . The solution for  $\partial \Psi_2 / \partial \xi$  is similar to equation (2.46), but the next term  $U_3 = \partial \Psi_3 / \partial y$  exhibits a jump in velocity across a critical layer (zone III) centered on  $y = y_0$ , where  $U_0(y_0) = C$ . The other region that is required is a viscous wall layer (zone I), where the inviscid solutions in zone II are adjusted to rest at the wall.

In the wall layer, the scaled variable is defined by

$$\bar{\eta} = T^{-3/4} y, \quad (2.47)$$

and the velocity expands according to

$$u = T^{1/2} \bar{U}_0(\xi, \bar{\eta}) + \dots, \quad (2.48)$$

where  $\bar{U}_0$  satisfies

$$-C \frac{\partial \bar{U}_0}{\partial \xi} = -p_1'(\xi) + \frac{\partial^2 \bar{U}_0}{\partial \bar{\eta}^2}. \quad (2.49)$$

A solution for  $\bar{U}_0$  is readily obtained and predicts the skin friction distribution

$$\tau_w = \left. \frac{\partial u}{\partial y} \right|_{y=0} \sim (t_s - t)^{-1/4} \bar{\tau}_0, \quad (2.50)$$

where  $\bar{\tau}_0 = \partial \bar{U}_0 / \partial \bar{\eta}$  at  $(\xi, 0)$ . Consequently, the shear stress distribution on the wall is expected to develop a singularity and, for example, the local maximum shear stress should behave according to

$$\tau_{w \max} \sim \frac{C}{(t_s - t)^{1/4}}, \quad (2.51)$$

where  $c$  is an unknown constant. This prediction will subsequently be compared with: computed results obtained from interacting boundary-layer methods in chapter 5 of this study.

The critical layer (zone III) is also a region which thins as  $T \rightarrow 0$ , and here the scaled normal coordinate is

$$\eta = \frac{y - y_0}{T^{1/4}}. \quad (2.52)$$

The critical layer is mainly inviscid and nonlinear. Smith (1988) obtains detailed solutions for zone III and determines that the pressure  $p_1$  satisfies the equation

$$a_0 p_1^3 + a_1 p_1 = -\xi, \quad (2.53)$$

where  $a_0$  and  $a_1$  are constants having the same sign. Consequently, as  $\xi \rightarrow \pm\infty$ ,

$$p_1 \sim (\xi/a_0)^{1/3} \quad \xi \rightarrow \pm\infty, \quad (2.54)$$

while, as  $\xi \rightarrow 0$ ,

$$p_1 \sim -\xi/a_1. \quad (2.55)$$

It follows from (2.42) that, near  $x = x_s$ , the pressure should develop a irregular behavior with

$$p - p_0 = O((x - x_s)^{1/3}). \quad (2.56)$$

As the singularity forms, the behavior predicted by equation (2.56) should appear in the computed results as a small local distortion in the pressure

distribution. On the other hand, the predicted behavior of the pressure gradient is more dramatic with

$$\frac{dp}{dx} = O((x-x_s)^{-2/3}) \text{ near } x=x_s. \quad (2.57)$$

The maximum pressure gradient is of the form

$$\left. \frac{dp}{dx} \right|_{\max} \sim \frac{c_1}{(t_s - t)}, \quad (2.58)$$

with  $c_1$  constant. Finally, it follows from (2.42) and (2.45) that the predicted behavior for the maximum normal velocity is

$$v_{\max} \sim \frac{c_2}{(t_s - t)}. \quad (2.59)$$

The results obtained from the numerical solutions in chapter 5 will subsequently be compared to predictions (2.58) and (2.59).

### 3. PROBLEM FORMULATION

#### 3.1 Introduction

In this chapter, a formulation for the model problem described in §1.5 will be developed both for the limit case  $Re \rightarrow \infty$  and for interacting boundary-layer theory. In addition, the algorithms and numerical methods used will be discussed. The boundary-layer calculations were initiated at  $t=0$  using a conventional Eulerian formulation of the governing equations, and this is described in §3.2 and §3.3 for the limit and interacting boundary-layer problems respectively. The main results in this study were obtained using Lagrangian variables for the boundary-layer problem, and the interacting boundary-layer formulation in Lagrangian coordinates is described in §3.4. It was found during the course of this investigation that numerical methods which are known to work well in a conventional Eulerian formulation may perform poorly in Lagrangian coordinates; it proved necessary to develop a new alternating-direction-implicit (ADI) method to efficiently compute the solution of the boundary-layer problem, and this algorithm is described in §3.5. The specific application of this ADI scheme to the Lagrangian boundary-layer equations is described in §3.6. In an interacting calculation, the thickening viscous flow near the wall induces changes in the external flow field as the integration advances in time; a set of equations that describe the time-dependent evolution of the outer flow is given in §3.7. The interaction condition derived in §3.7 involves an integral equation containing a Cauchy principle value integral; an algorithm to compute this integral is described in §3.8. Lastly, it emerges that the outer interaction problem is an integro-differential equation for the mainstream velocity distribution  $U_e(x,t)$  at the boundary-layer edge, and the numerical algorithms used to solve this equation are discussed in §3.9.

### 3.2 The Eulerian Limit Problem

Although one goal of this study was to develop a Lagrangian interacting boundary-layer method, calculations were also carried out using the Eulerian formulation, for two reasons. First, the Eulerian algorithm proved very useful in the initial development process as a means of verifying the results of the Lagrangian calculations, particularly in the early stages of flow evolution where both approaches work well. It should be noted that direct comparison of the unsteady two-dimensional fields that are computed in the Eulerian formulation (i.e.  $u(x,y,t)$  and  $\psi(x,y,t)$ ) with the unsteady distributions obtained in Lagrangian coordinates (i.e.  $x(\xi,\eta,t)$  and  $u(\xi,\eta,t)$ ) is not straightforward or easy to achieve with good accuracy. This is because the spatial coordinates  $(x,y)$  in the Eulerian frame are independent variables, while in the Lagrangian scheme  $x(\xi,\eta,t)$  and  $y(\xi,\eta,t)$  are unsteady dependent variables which are functions of the initial fluid-particle locations  $(\xi,\eta)$ . However, computed distributions such as the wall shear  $\tau_w(x,t)$  or the displacement surface  $\delta^*(x,t)$  may be evaluated easily from calculations carried out in either frame; such distributions serve as a good basis of comparison of the two approaches. In the computations reported in this study the agreement between both sets of results was found to be excellent in the early stages of the motion where both formulations may be used readily.

A second reason for developing the Eulerian calculation method is that it was normally used in this study to produce a "starting solution" for the Lagrangian algorithm. In all cases, the boundary layer was assumed to develop impulsively from rest at  $t=0$ ; for  $t>0$ , a thin unsteady boundary layer develops and grows on the surface. For small  $t$ , the boundary-layer solution is a function of the Rayleigh variable  $\zeta$ , where  $\zeta = \frac{1}{2}y/\sqrt{t}$ , and the boundary layer thickens in proportion to  $\sqrt{t}$ . Consequently the solution varies rapidly in the initial stages of the motion, and to take this behavior into account (as well as

to remove the singularity in the vorticity at  $t=0$ ) it is useful to cast the problem in Rayleigh variables. This can be done in the Eulerian description using the normal variable<sup>1</sup>  $\zeta$  (Walker, 1978). Once the boundary layer thickens to an appreciable extent, the use of the Rayleigh variable  $\zeta$  is not required and it is possible to return to using a conventional normal coordinate  $y$ . In this study, a solution was normally advanced from the impulsive start at  $t=0$  using Rayleigh variables and the Eulerian formulation, until some time  $t_0$ ; at  $t_0$  the resulting solution was used as an initial condition for the calculation carried out using the Lagrangian method. It is worthwhile to note that Rayleigh variables are also readily defined for the Lagrangian problem, and that modifications of the numerical algorithm near  $t=0$  may be considered (Van Dommelen, 1981), with the goal of reducing numerical inaccuracies in the initial stages of the motion. However, in practice it was observed that the solutions at later times are dominated by the effects of the external pressure gradient, and small numerical errors introduced near  $t=0$  are rapidly smoothed out. One basic conclusion of this study is that Lagrangian methods can be very useful in situations where a boundary layer begins to develop strong outflows; in such cases numerical solution of the Eulerian boundary-layer equations generally produce unsatisfactory results. On the other hand, the conventional Eulerian approach can be very efficient for a reasonably well-behaved unsteady boundary layer. Indeed, it was found in this study that the early stages of the boundary-layer flow (up to and including the appearance of zones of recirculation) could be computed much more quickly using the Eulerian method.

In this section the limit problem  $Re \rightarrow \infty$ , first considered by Walker (1978), will be addressed. The model problem of a vortex placed above an infinite plane wall in an otherwise stagnant fluid was described in §1.5, where it was shown that (equation (1.52)) the vortex convects, parallel to the wall,

---

<sup>1</sup>Note that the variable  $\zeta$  is denoted by " $\eta$ " in the original study by Walker (1978).

with a dimensionless velocity

$$U_v = \frac{1}{Y_v}, \quad (3.1)$$

due to the velocity field of the image vortex below the wall; here  $Y_v(t)$  is the instantaneous dimensionless distance of the vortex from the wall. In this analysis the vortex strength and initial distance from the wall are used to define characteristic velocity and length scales, and thus

$$Y_v = 1, \quad \text{at } t = 0. \quad (3.2)$$

For the limit problem  $Re \rightarrow \infty$ , the inviscid flow is assumed to be unaffected by the thin unsteady boundary layer  $O(Re^{-1/2})$  on the wall. Thus, in the limit  $Re \rightarrow \infty$ , the vortex convects with constant velocity parallel to the wall, and

$$U_v = 1, \quad Y_v = 1, \quad \text{for } Re \rightarrow \infty. \quad (3.3)$$

In the interacting formulation (for large but finite values of  $Re$ ) the vortex is gradually displaced by the thickening boundary layer, and both  $U_v$  and  $Y_v$  are functions of time; equations for these quantities will be obtained in §3.7. In the following development  $U_v$  and  $Y_v$  should be regarded as known functions of time given by: (1) equations (3.3) for the limit problem, or (2) the numerical solution of ordinary differential equations that will be obtained in §3.7 for interacting boundary-layer calculations.

Viewed from the laboratory frame, the inviscid motion is unsteady as the vortex moves above the wall. For the limit problem  $Re \rightarrow \infty$ , the inviscid motion is steady to an observer convecting uniformly with the vortex. It is convenient to carry out the analysis in this vortex frame, which convects to the right with speed  $U_v(t)$ . Using equations (1.51) and (3.1) it follows that the

streamfunction associated with the moving vortex in the convected frame is

$$\Psi = -\frac{Y}{Y_v} - \log\left(\frac{x^2 + (Y - Y_v)^2}{x^2 + (Y + Y_v)^2}\right) + O(Re^{-1/2}), \quad (3.4)$$

where  $O(Re^{-1/2})$  indicates that perturbation terms, due to interaction effects, have been omitted (see §1.4). In the moving vortex frame, the wall appears to move to the left with velocity  $-U_v(t)$ . The inviscid velocity near the wall (and at the edge of the boundary layer) in the vortex frame is denoted  $U_\infty$ ; it is determined by differentiating (3.4) with respect to  $Y$ , and taking the limit  $Y \rightarrow 0$ . The result may be written in the form,

$$U_\infty = -U_v + U_e, \quad (3.5)$$

where

$$\left. \begin{aligned} U_v(t) &= \frac{1}{Y_v(t)} + O(Re^{-1/2}), \\ \text{and} \quad U_e(x,t) &= \frac{4Y_v(t)}{x^2 + Y_v^2(t)} + O(Re^{-1/2}). \end{aligned} \right\} \quad (3.6)$$

Here,  $U_e(x,t)$  may be viewed as the instantaneous mainstream velocity as seen in the laboratory frame at the instant the vortex is at the same streamwise position as the observer.

For limit problem  $Re \rightarrow \infty$  (Walker, 1978), the inviscid flow is steady, and is given by

$$U_v = 1, \quad U_e = \frac{4}{x^2 + 1}. \quad (3.7)$$

The boundary-layer equations are



$$\left. \begin{aligned} \frac{\partial u}{\partial t} + u \frac{\partial u}{\partial x} + v \frac{\partial u}{\partial y} &= U_{\infty} \frac{\partial U_{\infty}}{\partial x} + \frac{\partial^2 u}{\partial y^2}, \\ \frac{\partial u}{\partial x} + \frac{\partial v}{\partial y} &= 0; \end{aligned} \right\} \quad (3.8)$$

with boundary conditions

$$\left. \begin{aligned} u &\rightarrow -1 + Ue(x) && \text{as } y \rightarrow \infty, \\ u &= -1 && \text{at } y=0. \end{aligned} \right\} \quad (3.9)$$

It is convenient from a numerical standpoint to deal with variables that are defined on finite intervals, and to this end new variables were taken as follows. First consider the streamwise velocity  $u(x,y,t)$  and define a normalized velocity  $U(x,y,t)$  such that

$$u(x,y,t) = U(x,y,t) Ue(x,t) - 1. \quad (3.10)$$

The boundary conditions (3.9) become

$$\left. \begin{aligned} U &\rightarrow 1 && \text{as } y \rightarrow \infty, \\ U &= 0 && \text{at } y=0, \end{aligned} \right\} \quad (3.11)$$

and it is evident that  $U$  has been normalized for all  $(x,t)$ .

The streamwise independent variable  $x$  has a doubly infinite range,  $-\infty < x < +\infty$ . This variable is mapped onto a finite interval using the following Görtler transformation

$$\hat{x}(x) = \frac{1}{2\pi} \int_x^{\infty} \frac{4}{r^2 + 1} d\tau = 1 - \frac{2}{\pi} \arctan(x). \quad (3.12)$$

Here  $\hat{x}=1$  corresponds to the vortex center (at  $x=0$ ), and  $\hat{x}=2,0$  correspond to downstream and upstream infinity, respectively. In this study the hat (^) convention is used to denote a variable that has undergone a transformation from an infinite range to a finite interval. It is evident that the inverse transformation<sup>2</sup> is

$$x(\hat{x}) = \tan \frac{\pi}{2}(1 - \hat{x}). \quad (3.13)$$

Two additional consequences of this mapping merit comment. The second of equations (3.7) becomes

$$Ue(\hat{x}) = 2(1 - \cos \pi \hat{x}), \quad (3.14)$$

and the transformation law is

$$\frac{\partial}{\partial x} = - \frac{Ue(\hat{x})}{2\pi} \frac{\partial}{\partial \hat{x}}. \quad (3.15)$$

Equation (3.14) indicates that the  $x \rightarrow \hat{x}$  mapping and normalized velocity variable  $U(\hat{x}, y, t)$ , together generate common factors of  $Ue(\hat{x})$  in all terms of the transformed momentum equation; hence it emerges that these transformations yield an elegant and simple form of the governing equations for the limit problem.

The final transformation utilized in the Eulerian method involves defining Rayleigh variables for  $y$  and the streamfunction. A streamfunction  $\bar{\psi}$  may be defined by

$$\left. \begin{aligned} u &= -1 + Ue \frac{\partial \bar{\psi}}{\partial y}, & v &= -\frac{\partial}{\partial x} (Ue \bar{\psi}), \\ \bar{\psi} &= 0 \text{ at } y=0. \end{aligned} \right\} \quad (3.16)$$

---

<sup>2</sup>Note that the variable  $\hat{x}$  corresponds to the variable " $\xi$ " used in the original study by Walker (1978).

Note that this choice for  $\bar{\psi}$  satisfies the continuity equation (1.11) exactly. Define Rayleigh variables by

$$\zeta = \frac{y}{2\sqrt{t}}, \quad \bar{\Psi} = \frac{\bar{\psi}}{2\sqrt{t}}, \quad (3.17)$$

for which the normalized streamwise velocity is given by

$$U = \frac{\partial \bar{\Psi}}{\partial \zeta}, \quad \bar{\Psi}(\hat{x}, 0) = 0, \quad (3.18)$$

and  $U$  satisfies

$$4t \cdot U_t = \left\{ \frac{2t}{\pi} Ue' (1 - Ue) \right\} + \left\{ \frac{2t}{\pi} Ue' (Ue - 1) \right\} U + \\ \left\{ 2\zeta - \frac{2t}{\pi} Ue \frac{\partial}{\partial \hat{x}} (\bar{\Psi} Ue) \right\} \frac{\partial U}{\partial \zeta} + \left\{ \frac{2t}{\pi} Ue (Ue - 1) \right\} \frac{\partial U}{\partial \hat{x}} + \frac{\partial^2 U}{\partial \zeta^2}. \quad (3.19)$$

Here the prime denotes differentiation with respect to  $\hat{x}$ . As  $t \rightarrow 0$  it is seen that equation (3.19) reduces to

$$\frac{\partial^2 U}{\partial \zeta^2} + 2\zeta \frac{\partial U}{\partial \zeta} = 0, \quad (3.20)$$

for which the solution satisfying conditions (3.11) is

$$U = \text{erf}(\zeta). \quad (3.21)$$

Integration of equation (3.18) yields

$$\bar{\Psi} = \zeta \text{erf}(\zeta) + \frac{1}{\sqrt{\pi}} (e^{-\zeta^2} - 1), \quad (3.22)$$

and therefore equations (3.21) and (3.22) are the initial conditions for the system of equations (3.18) and (3.19).

At upstream and downstream infinity ( $\hat{x} \rightarrow 0, 2$  respectively)  $U \rightarrow 0$ , and it is easily verified that equation (3.19) also reduces to equation (3.20); consequently as  $|x| \rightarrow \infty$ , the solution is also given by equations (3.21) and (3.22). For any time  $t > 0$ , the boundary conditions for  $U$  are

$$\left. \begin{aligned} U &\rightarrow 1 && \text{as } \zeta \rightarrow \infty, \text{ all } \hat{x}, \\ U &= 0 && \text{for } \zeta = 0, \text{ all } \hat{x}, \\ U &= \text{erf}(\zeta) && \text{for } \hat{x} = 0, 2, \text{ all } \zeta. \end{aligned} \right\} \quad (3.23)$$

The foregoing formulation of the limit problem was adopted by Walker (1978) to compute the evolution of the vortex-driven boundary layer. The same formulation was used in the present study but with the following difference. The variable  $\zeta$  is defined on the semi-infinite interval  $[0, \infty)$ , and it is convenient in a numerical solution to define a variable on a finite domain. The transformation

$$\hat{\zeta} = \frac{2}{\pi} \arctan(\zeta), \quad (3.24)$$

was used in the present study to map  $\zeta$  onto the interval  $0 \leq \hat{\zeta} < 1$ . The transformation law for this mapping is

$$\frac{\partial}{\partial \zeta} = Z(\hat{\zeta}) \frac{\partial}{\partial \hat{\zeta}}, \quad (3.25)$$

where

$$Z(\hat{\zeta}) = \frac{2}{\pi} \cos^2\left(\frac{\pi \hat{\zeta}}{2}\right). \quad (3.26)$$

Thus the final form of the Eulerian equations integrated in this study is

$$\left. \begin{aligned} 4t U_t &= T \frac{\partial^2 U}{\partial \zeta^2} + P \frac{\partial U}{\partial \zeta} + WU + Q \frac{\partial U}{\partial \bar{x}} + \Gamma, \\ Z(\zeta) \frac{\partial \bar{\Psi}}{\partial \zeta} &= U. \end{aligned} \right\} \quad (3.27)$$

where the coefficients in the momentum equation (3.27) are defined by

$$T = Z^2(\zeta), \quad (3.28)$$

$$P = Z(\zeta) \left( 2 \left\{ \tan \frac{\pi \zeta}{2} - \frac{t}{\pi} Ue \frac{\partial}{\partial \bar{x}} (\bar{\Psi} Ue) \right\} + Z'(\zeta) \right),$$

$$W = \frac{2t}{\pi} Ue'(Ue - 1),$$

$$Q = \frac{2t}{\pi} Ue (Ue - 1),$$

$$\Gamma = \frac{2t}{\pi} Ue'(1 - Ue).$$

The boundary conditions for these equations are

$$\left. \begin{aligned} U &= 0 & \text{at } \zeta=0, \\ U &= 1 & \text{at } \zeta=1, \\ U &= \operatorname{erf}\left(\tan \frac{\pi \zeta}{2}\right) & \text{at } \bar{x}=0, 2, \end{aligned} \right\} \quad (3.29)$$

To calculate the unsteady distributions  $U(\bar{x}, \zeta, t)$  and  $\bar{\Psi}(\bar{x}, \zeta, t)$  the solution was advanced in time increments  $\Delta t$ , and at each successive time plane the solution for  $U, \bar{\Psi}$  was computed throughout the spatial domain  $(\bar{x}, \zeta)$ . This procedure was carried out by first discretizing the above equations using the Crank-Nicolson approximation for the time derivative (Walker, 1978) and standard central-difference approximations for the spatial derivative (see Appendix B). Standard iterative point-by-point relaxation methods were

employed to obtain a converged solution in each time plane (Appendix B); convergence was considered to have occurred when successive iterates in a given time plane agreed to 4 significant figures at each mesh point. At any fixed time, given an estimate of  $U$ , the solution for  $\bar{\Psi}$  was obtained through integration of equation (3.18) along lines of constant  $\hat{x}$ , using Simpson's rule (Appendix B). When the Eulerian method was used as a starting calculation for the Lagrangian scheme, the computations in the Eulerian frame were generally terminated at a "switch-over time"  $t_0$ . A value of  $t_0 = \frac{1}{4}$  is particularly convenient since (from equation (3.17))

$$\zeta(y, t_0) = y. \quad (3.30)$$

and therefore the discretized nodes in both Eulerian and Lagrangian frames occur at the same normal distance from the wall. Other values of  $t_0$  could easily be selected, but then interpolation would have been required to initialize the Lagrangian velocity distribution.

### 3.3 The Eulerian Interactive Problem

When the interaction problem (corresponding to large but finite values of  $Re$ ) is considered, the analysis must reflect the fact that the inviscid solution is unsteady due to interaction effects with the evolving boundary-layer flow. The vortex velocity  $U_v$ , and the mainstream velocity  $U_e$  at the boundary-layer edge, must now be treated explicitly as time-dependent, with the following initial conditions at  $t=0$ :

$$U_v(0) = 1, \quad U_e(\hat{x}, 0) = U_{e0}(\hat{x}) = 2(1 - \cos \pi \hat{x}). \quad (3.31)$$

Here,  $U_{e0}(\hat{x})$  is used to denote mainstream velocity (in the laboratory frame)

associated with the limit problem, which also describes the initial mainstream velocity at the start of the motion in the interacting case. Specific expressions for  $U_v$  and  $U_e$  depend on the mathematical representation of interaction effects (as discussed in §1.4) and will be considered in §3.7; at this stage it is only important to appreciate that the inviscid pressure gradient imposed on the boundary-layer flow is time-dependent in the interacting case. As a practical matter, the variation of the vortex velocity  $U_v(t)$  and distance from the wall  $Y_v(t)$  from the values given by equation (3.3) are only  $O(Re^{-1/2})$  for  $t = O(1)$ . The computed results described in chapter 5 verify that the deviations from (3.3) are small for all values of  $Re$  considered. Thus an analysis in which these functions were assumed constant would be a reasonable approximation in an interacting analysis. However, it emerges that the mainstream distribution  $U_e(x,t)$  may vary considerably from  $U_{e0}(x)$  in a narrow streamwise interval where strong viscous-inviscid interactions take place; consequently, it is important that  $U_e(x,t)$  be explicitly treated as an unsteady distribution for finite values of  $Re$ .

The following generalizations are required when the potential flow is unsteady. The boundary-layer equations (3.8) must reflect that  $U_\infty$  is time-dependent, viz.

$$\left. \begin{aligned} \frac{\partial u}{\partial t} + u \frac{\partial u}{\partial x} + v \frac{\partial u}{\partial y} &= \frac{\partial U_\infty}{\partial t} + U_\infty \frac{\partial U_\infty}{\partial x} + \frac{\partial^2 u}{\partial y^2}, \\ \frac{\partial u}{\partial x} + \frac{\partial v}{\partial y} &= 0. \end{aligned} \right\} \quad (3.32)$$

The boundary conditions for the streamwise velocity  $u(x,y,t)$  now contain the unsteady terms in  $U_e(x,t)$  and  $U_v(t)$  viz.

$$\left. \begin{aligned} u(x,t) &\rightarrow U_\infty(x,t) && \text{as } y \rightarrow \infty, \\ u(x,t) &= -U_v(t) && \text{at } y=0; \end{aligned} \right\} \quad (3.33)$$

where the mainstream velocity (in a frame of reference convecting with the vortex) is given by

$$U_{\infty}(x,t) = -U_v(t) + Ue(x,t). \quad (3.34)$$

The streamwise velocity  $u(x,y,t)$  is again written in terms of the normalized variable  $U(x,y,t)$  according to

$$u(x,y,t) = U(x,y,t) Ue(x,t) - U_v, \quad (3.35)$$

so that the boundary conditions for  $U(x,y,t)$  are again

$$U(x,0,t)=0, \quad U \rightarrow 1 \quad \text{as } y \rightarrow \infty. \quad (3.36)$$

Using the same transformations of independent variables as in the limit problem, including the mapping (3.13), the analog of equation (3.15) is now

$$\frac{\partial}{\partial x} = -\frac{Ue_0(\tilde{x})}{2\pi} \frac{\partial}{\partial \tilde{x}}, \quad (3.37)$$

where  $Ue_0(\tilde{x})$  is defined by (3.31). In the limit problem the mainstream velocity was equal to  $Ue_0$  for all  $t$ , thus the distribution  $Ue_0$  appears in a number of terms in the momentum equation; this leads to the simplified form of equation (3.19). The corresponding interactive equation is somewhat more complicated and contains several terms with the ratio  $Ue_0(x)/Ue(x,t)$ . The interactive coupled unsteady equations are



$$\begin{aligned}
4t \cdot \frac{\partial U}{\partial t} = & \left\{ \frac{2t}{\pi} \frac{\partial U_e}{\partial \tilde{x}} (U_v - U_e) \left( \frac{U_{e0}}{U_e} \right) + 4t \left( \frac{1}{U_e} \frac{\partial U_e}{\partial t} \right) \right\} \\
& + \left\{ \frac{2t}{\pi} \frac{\partial U_e}{\partial \tilde{x}} (U U_e - U_v) \left( \frac{U_{e0}}{U_e} \right) - 4t \left( \frac{1}{U_e} \frac{\partial U_e}{\partial t} \right) \right\} U \\
& + \left\{ 2\zeta - \frac{2t}{\pi} U_{e0} \frac{\partial}{\partial \tilde{x}} (\bar{\Psi} U_e) \right\} \frac{\partial U}{\partial \zeta} \\
& + \left\{ \frac{2t}{\pi} U_{e0} (U U_e - U_v) \right\} \frac{\partial U}{\partial \tilde{x}} + \frac{\partial^2 U}{\partial \zeta^2},
\end{aligned} \tag{3.38}$$

$$\frac{\partial \bar{\Psi}}{\partial \zeta} = U, \tag{3.39}$$

where  $U_v(t)$  and  $U_e(\tilde{x}, t)$  must be evaluated from a set of relations that will be developed in §3.7, which reflect the interaction with the outer flow.

### 3.4 Lagrangian Formulation

A Eulerian description of the interactive vortex-driven boundary layer was developed in the preceding section §3.3, where the problem was posed in terms of the streamwise velocity  $u(x, y, t)$  and streamfunction  $\psi(x, y, t)$ . In principle, equations (3.38) and (3.39) could be discretized and integrated forward in time, once a suitable algorithm to compute  $U_e(x, t)$  and  $U_v(t)$  is available (see, for example, Henkes and Veldman, 1987; Chuang and Conlisk, 1988). However, the strong local updrafts that evolve in unsteady separating boundary layers are known to lead to intense velocity variations along a narrow band in the streamwise direction. Because of this behavior, finite difference schemes on a fixed mesh in the Eulerian formulation eventually encounter severe numerical resolution problems (Chuang and Conlisk, 1988). In problems such as the impulsively started circular cylinder, where the location of local eruptive behavior has been identified from previous work, some authors (e.g. Cebeci, 1979, 1986) have used grid-packing and a highly non-uniform mesh near the eventual location of the boundary-layer eruption.

However, such schemes only postpone the resolution problem or eventually smear it out. Very few interactive boundary-layer calculations in the Eulerian frame were carried out in this study because of the resolution problems that are encountered in this approach. It appears that calculations of eruptive flow development could be feasible in an Eulerian calculation with some type of time-dependent adaptive meshing algorithm, but this possibility was not explored in the present study. The alternative approach adopted was to base all calculations of the boundary-layer flow on the Lagrangian equations (see Appendix A). In this description of the motion, the positions of fluid particles are tracked forward in time. The instantaneous positions of all particles define a mesh in the Eulerian frame; this mesh distorts naturally with time, including those situations where a boundary-layer eruption develops.

In Lagrangian boundary-layer calculations the streamwise displacement  $x(\xi, \eta, t)$  and velocity  $u(\xi, \eta, t)$  of a large number of fluid particles are computed in time. The independent variables in the Lagrangian method are the initial location of the fluid particles, which are given at some initial instant by

$$\left. \begin{aligned} x(\xi, \eta, 0) &= \xi, \\ y(\xi, \eta, 0) &= \eta. \end{aligned} \right\} \quad (3.40)$$

Here,  $\xi$  and  $\eta$  are cartesian coordinates. The Lagrangian representation of the boundary-layer problem is fundamentally different from the Eulerian description, in which  $u(x, y, t)$  and  $\psi(x, y, t)$  are integrated forward in time at fixed spatial stations in  $(x, y)$ . In the following discussion it is important to bear in mind that "x" in the Lagrangian formulation refers to the dependent variable  $x(\xi, \eta, t)$ , corresponding to the current streamwise location of a particle which started at the point  $\xi, \eta$  at  $t=0$ ; this is in contrast to Eulerian methods in which  $x$  is an independent variable describing a fixed streamwise location. Although the momentum equations in both frames are unsteady partial

differential equations of the same order, the behavior of the numerical solutions in the Lagrangian and Eulerian descriptions is fundamentally different. It emerges that numerical integration of the Lagrangian boundary-layer equations requires special procedures, and one such method will be described in §3.5.

From the formal development of the Lagrangian boundary-layer equations in Appendix A, the Lagrangian statement of the interacting Eulerian form of the vortex-driven boundary-layer problem given in §3.3 may be written (in a frame moving with the vortex) as

$$\frac{\partial u}{\partial t} = U_{\infty} \frac{\partial U_{\infty}}{\partial x} + \frac{\partial U_{\infty}}{\partial t} + \left( \frac{\partial x}{\partial \xi} \frac{\partial}{\partial \eta} - \frac{\partial x}{\partial \eta} \frac{\partial}{\partial \xi} \right)^2 u, \quad (3.41)$$

$$\frac{\partial x}{\partial t} = u. \quad (3.42)$$

The boundary conditions for all  $t > 0$  are:

$$u = -U_v(t) \text{ at } \eta = 0, \quad u \rightarrow U_{\infty} \text{ as } \eta \rightarrow \infty, \quad (3.43)$$

where the mainstream velocity  $U_{\infty}$  at the boundary-layer edge is given by

$$U_{\infty} = -U_v(t) + U_e(x, t). \quad (3.44)$$

For the limit problem ( $Re \rightarrow \infty$ ),  $U_v$  and  $U_e$  are given by equation (3.7) for all time  $t$ . In an interactive calculation the vortex velocity  $U_v$  and the external flow speed  $U_e$  change with time, according to relations that will be given in §3.7. The initial conditions for these quantities are

$$\left. \begin{aligned} Ue(x,0) &= Ue_0(x) = \frac{4}{x^2+1}, \\ U_v(0) &= 1. \end{aligned} \right\} \quad (3.45)$$

The initial conditions at  $t=0$  for the viscous boundary-layer problem are:

$$\left. \begin{aligned} u(\xi,\eta,0) &= Ue_0(\xi) - U_v(0), & \text{for } \eta > 0, \\ &= -U_v(0) & \text{for } \eta = 0, \end{aligned} \right\} \quad (3.46)$$

$$x(\xi,\eta,0) = \xi, \quad y(\xi,\eta,0) = \eta. \quad (3.47)$$

The above initial conditions (3.46) apply strictly for an impulsive start condition, wherein the viscosity is assumed to become important at the wall abruptly at  $t=0$ . In the present study, a Eulerian computation was performed up to a time  $t_0$ , and the velocity field at  $t_0$  was used as an initial condition from which to initiate the Lagrangian calculations. Note that the change from the Eulerian to the Lagrangian method may be done at any value of  $t_0$ ; at that instant, the Eulerian solution provides the streamwise velocity at each point in a two-dimensional mesh. These mesh points then mark the starting locations of fluid particles for the Lagrangian calculation. Consequently, the initial conditions for  $x(\xi,\eta,t)$  and  $y(\xi,\eta,t)$  are still given by equation (3.47); the initial condition for  $u$  now corresponds to the value of the streamwise velocity at each point in the Eulerian mesh, rather than equations (3.46). Note that if interactive effects have been considered up to  $t=t_0$ , the external mainstream velocity given by equation (3.44) will have changed with time from the initial values given in (3.45). In the present study, calculations were tried with different values of  $t_0$  and, as expected, the specific switch time has no effect on the subsequent results. However, the value  $t_0 = \frac{1}{4}$  is particularly convenient in this problem for two reasons: (1) it is a time when the flow field is well behaved and calculations in either the Eulerian or Lagrangian descriptions give equal results, and (2) at  $t_0$  (from equation (3.30))  $\eta=y$ , and therefore the

same mesh used in the Eulerian calculation may be used to continue the integration in the Lagrangian frame.

To facilitate the numerical integration, transformed variables were defined on fixed finite intervals. The streamwise velocity was defined in terms of a normalized variable  $U$  in a manner similar to the Eulerian problem in §3.3, viz.

$$u(\xi, \eta, t) = Ue(x, t) U(\xi, \eta, t) - U_v(t), \quad (3.48)$$

with boundary conditions given by

$$U(\xi, 0, t) = 0, \quad U(\xi, \eta, t) \rightarrow 1 \quad \text{as } \eta \rightarrow \infty. \quad (3.49)$$

Note that for an impulsive start at  $t=0$ , the initial condition is  $U=1$ . The streamwise variables  $\xi, x$  are each defined on a doubly-infinite range  $(-\infty, +\infty)$ ; as in the preceding Eulerian development (c.f. §3.2) these variables are mapped onto  $(2, 0)$  using the following transformations:

$$\hat{x}(x) = 1 - \frac{2}{\pi} \arctan(x), \quad \hat{\xi}(\xi) = 1 - \frac{2}{\pi} \arctan(\xi). \quad (3.50)$$

The gradients in equation (3.41) become

$$\frac{\partial}{\partial x} = - \frac{Ue_0(\hat{x})}{2\pi} \frac{\partial}{\partial \hat{x}}, \quad \frac{\partial}{\partial \xi} = - \frac{Ue_0(\hat{\xi})}{2\pi} \frac{\partial}{\partial \hat{\xi}}, \quad (3.51)$$

where  $Ue_0$  is defined as

$$Ue_0(\hat{x}) = 2(1 - \cos \pi \hat{x}). \quad (3.52)$$

The normal coordinates  $\eta, y$  are defined on an infinite range  $[0, \infty)$  and these

variables are mapped onto the finite interval  $[0,1)$ , by

$$\hat{y}(y) = \frac{2}{\pi} \arctan(y), \quad \hat{\eta}(\eta) = \frac{2}{\pi} \arctan(\eta). \quad (3.53)$$

The gradient in  $\eta$  becomes

$$\frac{\partial}{\partial \eta} = Z(\hat{\eta}) \frac{\partial}{\partial \hat{\eta}}, \quad (3.54)$$

where  $Z$  is defined by

$$Z(\hat{\eta}) = \frac{2}{\pi} \cos^2\left(\frac{\pi \hat{\eta}}{2}\right). \quad (3.55)$$

When these above transformations are substituted into the interactive Lagrangian boundary-layer equations (3.41) and (3.42) it is easily shown that

$$\frac{\partial U}{\partial t} = \Gamma + WU + \left( P \frac{\partial}{\partial \hat{\eta}} + T \frac{\partial^2}{\partial \hat{\eta}^2} + S \frac{\partial^2}{\partial \hat{\eta} \partial \hat{\xi}} + R \frac{\partial^2}{\partial \hat{\xi}^2} + Q \frac{\partial}{\partial \hat{\xi}} \right) U, \quad (3.56)$$

$$\hat{x}_t = - \frac{U e_0(\hat{x})}{2\pi} \left( U U e(\hat{x}, t) - U_v(t) \right). \quad (3.57)$$

where the coefficients are defined by

$$\begin{aligned}
\Gamma &= -\left\{ \left( \frac{U_{e0}(\bar{x})}{U_e(\bar{x},t)} \right) \left( \frac{1}{2\pi} \frac{\partial U_e}{\partial \bar{x}} \right) (U_e(\bar{x},t) - U_v(t)) - \left( \frac{1}{U_e} \frac{\partial U_e}{\partial t} \right) \right\}, \\
W &= -\left\{ \left( \frac{U_{e0}(\bar{x})}{U_e(\bar{x},t)} \right) \left( \frac{1}{2\pi} \frac{\partial U_e}{\partial \bar{x}} \right) (U_v(t) - U(\hat{\xi}, \hat{\eta}, t) U_e(\bar{x}, t)) + \left( \frac{1}{U_e} \frac{\partial U_e}{\partial t} \right) \right\}, \\
P &= \bar{\alpha}^2(\bar{x}, \hat{\xi}, \hat{\eta}) \left\{ \frac{\partial \hat{x}}{\partial \hat{\xi}} \left( \frac{\partial^2 \hat{x}}{\partial \hat{\xi} \partial \hat{\eta}} + \beta(\hat{\eta}) \frac{\partial \hat{x}}{\partial \hat{\xi}} \right) - \frac{\partial \hat{x}}{\partial \hat{\eta}} \left( \frac{\partial^2 \hat{x}}{\partial \hat{\xi}^2} + \gamma(\hat{\xi}) \frac{\partial \hat{x}}{\partial \hat{\xi}} \right) \right\}, \\
T &= \bar{\alpha}^2(\bar{x}, \hat{\xi}, \hat{\eta}) \left\{ \frac{\partial \hat{x}}{\partial \hat{\xi}} \right\}^2, \\
S &= \bar{\alpha}^2(\bar{x}, \hat{\xi}, \hat{\eta}) \left\{ -2 \frac{\partial \hat{x}}{\partial \hat{\xi}} \frac{\partial \hat{x}}{\partial \hat{\eta}} \right\}, \\
R &= \bar{\alpha}^2(\bar{x}, \hat{\xi}, \hat{\eta}) \left\{ \frac{\partial \hat{x}}{\partial \hat{\eta}} \right\}^2, \\
Q &= \bar{\alpha}^2(\bar{x}, \hat{\xi}, \hat{\eta}) \left\{ \frac{\partial \hat{x}}{\partial \hat{\eta}} \left( \frac{\partial^2 \hat{x}}{\partial \hat{\xi} \partial \hat{\eta}} + \gamma(\hat{\xi}) \frac{\partial \hat{x}}{\partial \hat{\eta}} \right) - \frac{\partial \hat{x}}{\partial \hat{\xi}} \left( \frac{\partial^2 \hat{x}}{\partial \hat{\eta}^2} + \beta(\hat{\eta}) \frac{\partial \hat{x}}{\partial \hat{\eta}} \right) \right\}.
\end{aligned} \tag{3.58}$$

Here,  $\bar{\alpha}(\bar{x}, \hat{\xi}, \hat{\eta})$ ,  $\beta(\hat{\eta})$  and  $\gamma(\hat{\xi})$  are the following functions:

$$\begin{aligned}
\bar{\alpha}(\bar{x}, \hat{\xi}, \hat{\eta}) &= \left( \frac{U_{e0}(\hat{\xi})}{U_{e0}(\bar{x})} Z(\hat{\eta}) \right), \\
\beta(\hat{\eta}) &= \frac{Z'(\hat{\eta})}{Z(\hat{\eta})}, \\
\gamma(\hat{\xi}) &= \frac{U_{e0}'(\hat{\xi})}{U_{e0}(\hat{\xi})},
\end{aligned} \tag{3.59}$$

where  $Z(\hat{\eta})$  and  $U_{e0}(\hat{\xi})$  are defined in (3.55), (3.52) respectively. The initial condition for equation (3.57) is

$$\hat{x}(\hat{\xi}, \hat{\eta}) = \hat{\xi} \quad \text{at } t=0, \tag{3.60}$$

and for equation (3.56)  $U=1$ , given an impulsive start at  $t=0$ . For a computation initiated from an Euler solution at  $t_0$ , initial values of  $U$  must be

obtained from the corresponding value in equation (3.35) at each node point. The boundary conditions for  $t > 0$  are

$$U(\xi, 0, t) = 0, \quad U(\xi, 1, t) = 1, \quad (3.61)$$

$$\hat{x}(0, \eta, t) = 0, \quad \hat{x}(2, \eta, t) = 2. \quad (3.62)$$

The conditions (3.62) state that fluid particles which are initially at downstream or upstream infinity remain there. The  $\hat{x}$  particle positions along the wall and near the mainstream may be obtained at any value of  $t$  through numerical integration of equation (3.57) using equations (3.61); fluid particles on the wall (or an infinite distance from the wall) remain there but their streamwise location changes with time. For the limit problem  $Re \rightarrow \infty$ , with  $U_e$  and  $U_v$  given by equation (3.7), it is possible to obtain an analytical solution for  $\hat{x}$  on the wall and at infinity; viz.

$$\hat{x}(\xi, 0, t) = 1 - \frac{2}{\pi} \arctan\left\{\tan\frac{\pi(1-\xi)}{2} - t\right\}, \quad \text{for } Re \rightarrow \infty. \quad (3.63)$$

For the interactive problem, a numerical solution of equation (3.57) (with conditions (3.61)) is required to advance the  $\hat{x}$  particle positions in time. At upstream and downstream infinity, the coefficients in equations (3.58) assume limiting forms independent of  $t$ , and it can be shown that

$$U = \operatorname{erf}\left\{\frac{\tan\frac{\pi\eta}{2}}{2\sqrt{t}}\right\}, \quad \text{at } \hat{x} = 0, 2. \quad (3.64)$$

This completes the basic formulation of the boundary-layer problem in Lagrangian variables. However, the interacting problem described by equations (3.56) and (3.57) is not closed at this stage, because the unsteady velocity  $U_e(\hat{x}, t)$  and the vortex velocity  $U_v(t)$  are not known. These functions are dependent on the response of the outer flow to the evolution of the



boundary layer, and must be evaluated in a separate tandem calculation that will be formulated using interactive concepts (c.f. §1.4) in §3.7.

### 3.5 An ADI Method for the Boundary-layer Problem

The numerical method used to compute the solution of the boundary-layer momentum equation will be described in this section. Although the form of the boundary-layer equations in the Lagrangian frame (3.56) bears a resemblance to the form in the Eulerian frame (see for example Walker, 1978; Doligalski and Walker, 1984), in that both are second order time-dependent partial differential equations, the characteristic behavior of the resulting difference equations was found to be rather different. The standard Crank-Nicolson procedure for such equations (see for example Walker, 1978) is to approximate equation (3.56) midway between the previous and current time planes: the spatial derivatives are then approximated using conventional central differences. In this manner, a set of non-linear difference equations is obtained at each internal mesh point. A conventional method of solving these equations consists of a systematic point-by-point sweep of the mesh. This procedure works very well for calculations based on the Eulerian description (Walker, 1978). In the present study, most of the development work on the numerical algorithm was done for the limit problem  $Re \rightarrow \infty$ , and it was found that systematic sweeping of the mesh worked well in the initial stages of the Lagrangian integration but failed to converge as soon as significant updrafts began to develop in the boundary-layer flow. After several trial-and-error approaches to the iteration scheme, it was determined that the integration could be continued somewhat further in time depending upon the pattern in which the mesh was swept; however the method was considered entirely too time-consuming and not suitable as an algorithm to push the computation to the point of significant interaction with the outer flow.

Another approach that was tried is the factored alternating direction method due to Beam and Warming (1978). This method has become quite popular in recent years to produce numerical solutions of the unsteady two-dimensional Navier-Stokes equations. A main feature of the algorithm is that equation (3.56) may be factored into two operators on  $U$ , one in the  $\hat{\xi}$  direction and one in the  $\hat{\eta}$  direction. A sequence of tridiagonal problems, along lines of constant  $\hat{\xi}$  and then along lines of constant  $\hat{\eta}$  (or vice versa) is calculated. The original Beam and Warming method is explicit in that calculations at each time step involve only one sweep in each coordinate direction; iteration is not carried out, and the algorithm continues to move smoothly through each time step. In the early stages of the motion the Beam and Warming method was found to work well, and produced results which were plausible and also consistent with results obtained by point-by-point relaxation methods. At subsequent times the method continued to produce results but, upon examination of either the constant  $\hat{x}$  or  $U$  contours, it became evident that the algorithm was failing to give physically meaningful results. The failure of the method was believed due to the fact that, as strong updrafts begin to evolve in the boundary-layer flow, the tridiagonal problems in each of the coordinate directions eventually lose the property of diagonal dominance, and this results in numerical instability in the method. It is worthwhile to note that the Beam and Warming (1978) algorithm is often applied in situations where a body is impulsively started from rest, and the objective is to compute the flow evolution through to steady state; in this latter type of calculation the level of time dependence in the computed solution is continually diminishing as the solution approaches steady state. The reverse is true in the problems of interest in this study, where variations in time become progressively more intense as the boundary-layer flow evolves toward an eruption.

In view of the failure of conventional numerical procedures it was necessary to develop a new procedure. The method described in this section (see also Peridier and Walker, 1988) is an ADI (Alternating-Direction-Implicit) scheme in which the spatial-derivative operators are factored; in addition the finite-difference approximations to the first-order partial derivatives employ "upwind-downwind" differencing. Although developed in the context of this study, the method is general and may be useful for numerical integration of unsteady second-order systems in which local regions of severe gradients are expected to develop.

The new method is an "upwind-downwind" ADI algorithm which is second-order accurate both in space and time. Consider the momentum equation (3.56)

$$U_t = \Gamma + WU + \left( P \frac{\partial U}{\partial \bar{\eta}} + T \frac{\partial^2 U}{\partial \bar{\eta}^2} + S \frac{\partial^2 U}{\partial \bar{\eta} \partial \bar{\xi}} + R \frac{\partial^2 U}{\partial \bar{\xi}^2} + Q \frac{\partial U}{\partial \bar{\xi}} \right); \quad (3.65)$$

assume that the solution for  $U$  is known in the previous time plane at  $t^*$  and denote such values at a typical point  $(\bar{\xi}, \bar{\eta})$  as  $U^*(\bar{\xi}, \bar{\eta})$ . The objective is to develop a procedure to advance the solution for  $U$  into the current time plane at  $t = t^* + \Delta t$ . Equation (3.65) is first approximated midway between the current and previous time planes at  $\bar{t} = t^* + (\Delta t/2)$ . Quantities evaluated at  $\bar{t}$  are denoted with an overbar and may be related to corresponding values in the previous and current time planes by a simple average; for example

$$\bar{P} = (P + P^*)/2, \quad (3.66)$$

where  $P$  denotes the quantity in the current time plane. Note that the simple average in equation (3.66) is second-order accurate in  $\Delta t$ . When the governing equations are nonlinear in  $U$  (as is the case here) then coefficients such as  $\bar{P}$ ,  $\bar{R}$ , may be functions of both the unknown  $U$  and known  $U^*$  distributions. In

the present approach, the coefficients  $\bar{P}, \bar{R}, \dots$ , etc., are treated as known distributions in a given iteration, which are subsequently updated at the start of each new iteration using the most recent estimates of  $U$ . The Crank-Nicolson approximation to equation (3.65) is

$$\frac{U - U^*}{\Delta t} = \bar{\Gamma} + \left( \bar{P} \frac{\partial}{\partial \hat{\eta}} + \bar{T} \frac{\partial^2}{\partial \hat{\eta}^2} + \bar{S} \frac{\partial^2}{\partial \hat{\eta} \partial \hat{\xi}} + \bar{R} \frac{\partial^2}{\partial \hat{\xi}^2} + \bar{Q} \frac{\partial}{\partial \hat{\xi}} + \bar{W} \right) \bar{U}, \quad (3.67)$$

which is accurate to  $O(\Delta t)^2$ , where

$$\bar{U} = \frac{U + U^*}{2}. \quad (3.68)$$

In a conventional Crank-Nicolson approach, equation (3.67) is rearranged so that the known values of  $U^*(\hat{\xi}, \hat{\eta})$  are on the right side, and it is easily verified that

$$\begin{aligned} \left( 1 - \alpha \left( \bar{P} \frac{\partial}{\partial \hat{\eta}} + \bar{T} \frac{\partial^2}{\partial \hat{\eta}^2} + \bar{S} \frac{\partial^2}{\partial \hat{\eta} \partial \hat{\xi}} + \bar{S} \frac{\partial^2}{\partial \hat{\xi}^2} + \bar{Q} \frac{\partial}{\partial \hat{\xi}} \right) \right) U = \\ \left( 1 + \alpha \left( \bar{P} \frac{\partial}{\partial \hat{\eta}} + \bar{T} \frac{\partial^2}{\partial \hat{\eta}^2} + \bar{S} \frac{\partial^2}{\partial \hat{\eta} \partial \hat{\xi}} + \bar{R} \frac{\partial^2}{\partial \hat{\xi}^2} + \bar{Q} \frac{\partial}{\partial \hat{\xi}} + \bar{W} \right) \right) U^* + 2\alpha \bar{\Gamma}, \end{aligned} \quad (3.69)$$

where

$$\alpha = \frac{\Delta t}{2 - \Delta t \bar{W}}. \quad (3.70)$$

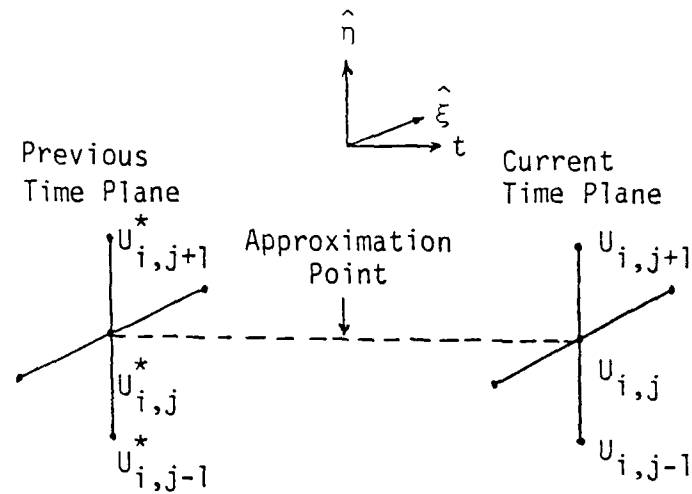
The spatial domain  $(\hat{\xi}, \hat{\eta})$  is generally subdivided in a mesh with  $M$  and  $N$  equal intervals in the  $\hat{\xi}$  and  $\hat{\eta}$  directions, respectively. Thus, in the interior of the computational domain there is a total of  $K = (M-1) \cdot (N-1)$  nodes. In the Crank-Nicolson method, the spatial derivatives in equation (3.69) are approximated by central difference expressions; this leads to a set of difference equations which at any stage are linearized by estimating the coefficients

$\bar{P}, \bar{Q}, \dots$  in (3.69) from the previous iteration. Each difference equation involves  $U$  at the pivotal point  $(\hat{\xi}_i, \hat{\eta}_j)$  and surrounding points (see for example, Appendix B). In situations when the entire system of equations is diagonally dominant, convergence is readily obtained at each time step using standard point-by-point iteration; here the term "diagonal dominance" means that the magnitude of the coefficient of the pivotal element is greater than, or equal to, the sum of the moduli of the coefficients of the surrounding terms. When the system is not diagonally dominant, experience suggests that the iteration will generally fail to converge. Unfortunately, for partial differential equations like (3.69), it is well known that the standard central-difference approximations may generate algebraic systems that lack diagonal dominance if the coefficient of either first derivative term (i.e.  $\bar{P}$  or  $\bar{Q}$ ) is sufficiently large. Doligalski and Walker (1984) have described a differencing approach which overcomes this problem and which will now be described.

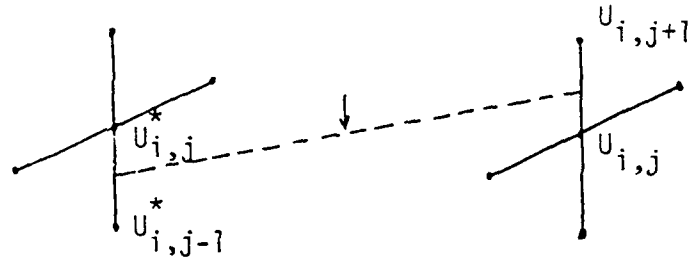
Doligalski and Walker's (1984) "upwind-downwind" finite-differencing scheme is consistent with the Crank-Nicolson evaluation of quantities in the half-time plane  $t=\bar{t}$ ; in addition the method is second-order accurate in both time and space. To appreciate the approach, consider again the approximation to equation (3.65) at  $t=\bar{t}$ . The averaging path for the conventional Crank-Nicolson method is shown in figure 3.1. The averages for the coefficients in equation (3.69) are carried out along this path (c.f. equation (3.66)). For the specific term  $P(\partial U / \partial \hat{\eta})$  in equation (3.65), averaging along this path and the subsequent use of central difference approximations in the current and previous time planes yields the conventional Crank-Nicolson approximation

$$\overline{P \frac{\partial U}{\partial \hat{\eta}}} = \frac{1}{4(\Delta \hat{\eta})} \bar{P}_{i,j} \{ U_{i,j+1} - U_{i,j-1} + U_{i,j+1}^* - U_{i,j-1}^* \}. \quad (3.71)$$

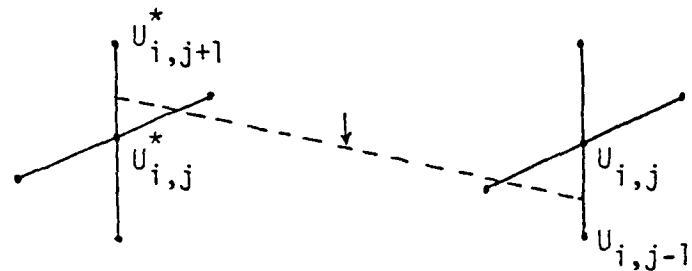
It is evident that this approximation makes contributions to the coefficients of the non-pivotal elements in the final difference equations, but no contribution



(a) Conventional Crank-Nicholson method.



(b) Upwind-downwind averaging path, for  $\bar{P}_{i,j} > 0$ .



(c) Upwind-downwind averaging path, for  $\bar{P}_{i,j} \le 0$ .

Figure 3.1. Schematic diagram of a typical mesh point and four surrounding points in the current and previous time planes; the dotted lines show the averaging paths used for the approximation of  $\frac{\partial U}{\partial \hat{\eta}}$  at  $t = \bar{t}$  and  $(\hat{\xi}_i, \hat{\eta}_j)$ .

to the coefficient of the pivotal element  $U_{i,j}$ . Thus, central differences do not act to enhance the diagonal dominance of the coefficient matrix of the difference equations for  $U_{i,j}$ . To alleviate the problem, first note that it is easily shown that an average along any path passing through  $(\hat{\xi}_i, \hat{\eta}_j, \bar{t})$  connecting the current and previous time planes is second-order accurate in  $\Delta t$ . For  $\bar{P}_{i,j} > 0$ , consider the path depicted in figure 3.1(b) which intersects the current time plane mid-way between the points  $(i, j)$  and  $(i, j+1)$ ; central difference approximations in the current and previous time planes now lead to

$$\bar{P}_{i,j} \frac{\partial \bar{U}}{\partial \hat{\eta}} = \frac{1}{2(\Delta \hat{\eta})} \bar{P}_{i,j} \{U_{i,j+1} - U_{i,j} + U_{i,j}^* - U_{i,j-1}^*\}, \quad \text{for } \bar{P}_{i,j} > 0, \quad (3.72)$$

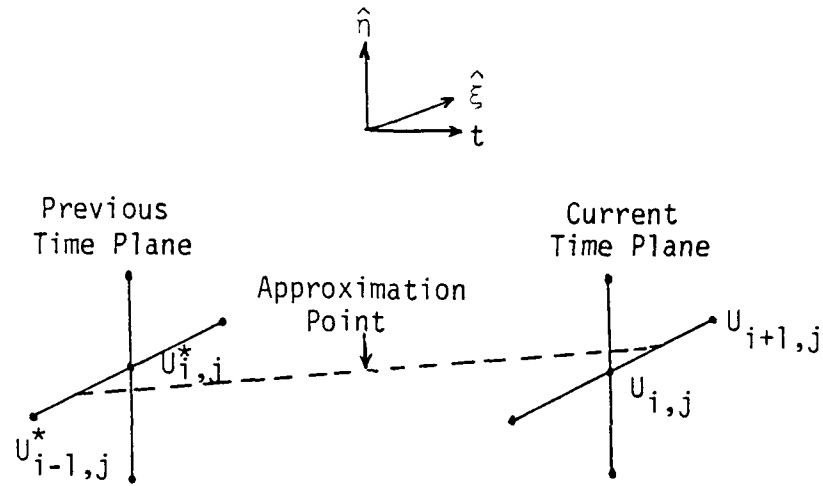
which is second-order accurate in both  $\Delta t$  and  $\Delta \hat{\eta}$ . To appreciate the benefit of this expression, now consider the conventional Crank-Nicolson approximation to  $T(\partial^2 U / \partial \hat{\eta}^2)$  in equation (3.65), which is

$$T \frac{\partial^2 \bar{U}}{\partial \hat{\eta}^2} = \frac{1}{2(\Delta \hat{\eta})^2} \bar{T}_{i,j} \{U_{i,j+1} - 2U_{i,j} + U_{i,j-1} + U_{i,j+1}^* - 2U_{i,j}^* + U_{i,j-1}^*\}. \quad (3.73)$$

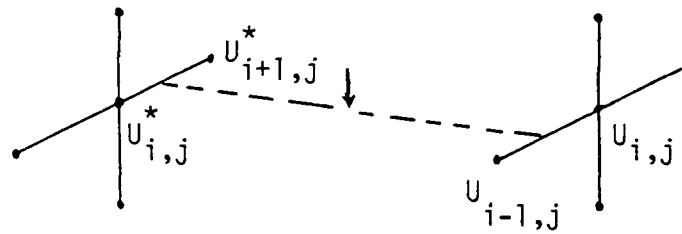
Since  $\bar{T}_{i,j} > 0$  (c.f. equations (3.58)), it follows that the approximation (3.72) acts to increase the magnitude of the coefficient of  $U_{i,j}$ , whereas (3.71) does not. For  $\bar{P}_{i,j} \leq 0$ , the averaging path indicated in figure 3.1(c) is used and

$$\bar{P}_{i,j} \frac{\partial \bar{U}}{\partial \hat{\eta}} = \frac{1}{2(\Delta \hat{\eta})} \bar{P}_{i,j} \{U_{i,j} - U_{i,j-1} + U_{i,j+1}^* - U_{i,j}^*\}, \quad \text{for } \bar{P}_{i,j} \leq 0. \quad (3.74)$$

The other first derivative term in equation (3.65) is  $Q(\partial U / \partial \hat{\xi})$  and a conventional Crank-Nicolson approach for this term leads to the same difficulty as that just described for  $P(\partial U / \partial \hat{\eta})$ . The problem is easily resolved using the averaging paths between the current and previous time planes indicated in figure 3.2. The finite difference approximations are



(a) Upwind-downwind averaging path, for  $\bar{Q}_{i,j} > 0$ .



(b) Upwind-downwind averaging path, for  $\bar{Q}_{i,j} \leq 0$ .

Figure 3.2. Schematic diagram showing the averaging paths used for the approximation of  $Q \frac{\partial U}{\partial \hat{\xi}}$ .



$$\overline{Q \frac{\partial U}{\partial \xi}} = \frac{1}{2(\Delta \xi)} \overline{Q}_{i,j} \left\{ \begin{array}{l} (U_{i+1,j} - U_{i,j} + U_{i,j}^* - U_{i-1,j}^*) \text{ for } \overline{Q}_{i,j} > 0 \\ (U_{i,j} - U_{i-1,j} + U_{i+1,j}^* - U_{i,j}^*) \text{ for } \overline{Q}_{i,j} \leq 0 \end{array} \right\}. \quad (3.75)$$

All other terms on the right side of equation (3.65) are averaged along the conventional Crank-Nicolson path (figure 3.1(a)); the complete set of difference equations is second order accurate in  $\Delta t$ ,  $\Delta \xi$ , and  $\Delta \eta$ .

This set of upwind-downwind approximations was used by Doligalski and Walker (1984) to generate a set of difference equations which were then solved using a point-by-point sweep of the mesh. In the present application, an efficient ADI method was developed which uses these upwind-downwind differencing approximations. In order to set the stage for the method, it is desirable to first write the difference approximations (3.72), (3.74) and (3.75) in a more compact form. Define enlargement operators  $E_{\hat{\xi}}$ ,  $E_{\hat{\eta}}$  in the  $\hat{\xi}, \hat{\eta}$  coordinate directions respectively by

$$\left. \begin{array}{l} E_{\hat{\xi}}^p U(\hat{\xi}, \hat{\eta}, t) = U(\hat{\xi} + p \cdot \Delta \hat{\xi}, \hat{\eta}, t), \\ E_{\hat{\eta}}^p U(\hat{\xi}, \hat{\eta}, t) = U(\hat{\xi}, \hat{\eta} + p \cdot \Delta \hat{\eta}, t), \end{array} \right\} \quad (3.76)$$

which have the effect of shifting the appropriate argument  $p$  mesh lengths. Central difference operators  $\delta$  in each of the coordinate directions are defined by

$$\left. \begin{array}{l} \delta_{\hat{\xi}} = E_{\hat{\xi}}^{+1/2} - E_{\hat{\xi}}^{-1/2}, \\ \delta_{\hat{\eta}} = E_{\hat{\eta}}^{+1/2} - E_{\hat{\eta}}^{-1/2}. \end{array} \right\} \quad (3.77)$$

Now define two difference operators  $\chi_{\hat{\eta}}^+$  and  $\chi_{\hat{\eta}}^-$  by

$$\left. \begin{array}{l} \chi_{\hat{\eta}}^+ = \delta_{\hat{\eta}} E^{+\text{sgn}(\overline{P}_{i,j})/2}, \\ \chi_{\hat{\eta}}^- = \delta_{\hat{\eta}} E^{-\text{sgn}(\overline{P}_{i,j})/2}. \end{array} \right\} \quad (3.78)$$

where

$$\text{sgn}(\bar{P}_{i,j}) = \begin{cases} +1 & \bar{P}_{i,j} > 0, \\ -1 & \bar{P}_{i,j} < 0. \end{cases} \quad (3.79)$$

It may be easily shown that equations (3.72) and (3.74) may be written in the compact form

$$\overline{P \frac{\partial U}{\partial \eta}} = \frac{1}{2(\Delta \bar{\eta})} \bar{P}_{i,j} \{ \chi_{\bar{\eta}}^+ U_{i,j} + \chi_{\bar{\eta}}^- U_{i,j}^* \}. \quad (3.80)$$

In a similar manner, define the operators  $\chi_{\bar{\xi}}^+$  and  $\chi_{\bar{\xi}}^-$  by

$$\left. \begin{aligned} \chi_{\bar{\xi}}^+ &= \delta_{\bar{\xi}} E^{+\text{sgn}(\bar{Q}_{i,j})/2}, \\ \chi_{\bar{\xi}}^- &= \delta_{\bar{\xi}} E^{-\text{sgn}(\bar{Q}_{i,j})/2}, \end{aligned} \right\} \quad (3.81)$$

and it may be shown that equation (3.75) may be written in the compact form

$$\overline{Q \frac{\partial U}{\partial \xi}} = \frac{1}{2(\Delta \bar{\xi})} \bar{Q}_{i,j} \{ \chi_{\bar{\xi}}^+ U_{i,j} + \chi_{\bar{\xi}}^- U_{i,j}^* \}. \quad (3.82)$$

The difference approximations for all other terms in equation (3.65) were developed using the standard Crank-Nicolson method. For the second-order spatial derivatives, finite difference approximations at the typical point in the mesh  $(i,j)$  and at  $\bar{t}$  are given by:

$$\left. \frac{\partial^2 U}{\partial \hat{\eta}^2} \right|_{i,j} = \frac{1}{2(\Delta \hat{\eta})^2} (U_{i,j+1} - 2U_{i,j} + U_{i,j-1} + U_{i,j+1}^* - 2U_{i,j}^* + U_{i,j-1}^*), \quad (3.83)$$

$$\begin{aligned} \left. \frac{\partial^2 U}{\partial \hat{\eta} \partial \hat{\xi}} \right|_{i,j} = \frac{1}{8(\Delta \hat{\eta})(\Delta \hat{\xi})} \{ & (U_{i+1,j+1} - U_{i+1,j-1} + U_{i-1,j-1} - U_{i-1,j+1} \\ & + U_{i+1,j+1}^* - U_{i+1,j-1}^* + U_{i-1,j-1}^* - U_{i-1,j+1}^*) \}, \end{aligned} \quad (3.84)$$

$$\left. \frac{\partial^2 U}{\partial \hat{\xi}^2} \right|_{i,j} = \frac{1}{2(\Delta \hat{\xi})^2} (U_{i+1,j} - 2U_{i,j} + U_{i-1,j} + U_{i+1,j}^* - 2U_{i,j}^* + U_{i-1,j}^*). \quad (3.85)$$

Defining the averaging operators in each of the coordinate directions by

$$\mu_{\hat{\xi}} = \frac{1}{2}(E_{\hat{\xi}}^{+1/2} + E_{\hat{\xi}}^{-1/2}), \quad \mu_{\hat{\eta}} = \frac{1}{2}(E_{\hat{\eta}}^{+1/2} + E_{\hat{\eta}}^{-1/2}), \quad (3.86)$$

the relations (3.83) to (3.85) may be written in operator form

$$\left. \frac{\partial^2 U}{\partial \hat{\eta}^2} \right|_{i,j} = \frac{1}{2(\Delta \hat{\eta})^2} \delta_{\hat{\eta}}^2 (U_{i,j} + U_{i,j}^*), \quad (3.87)$$

$$\left. \frac{\partial^2 U}{\partial \hat{\eta} \partial \hat{\xi}} \right|_{i,j} = \frac{1}{2(\Delta \hat{\eta})(\Delta \hat{\xi})} \{ \mu_{\hat{\eta}} \delta_{\hat{\eta}} \mu_{\hat{\xi}} \delta_{\hat{\xi}} \} (U_{i,j} + U_{i,j}^*), \quad (3.88)$$

$$\left. \frac{\partial^2 U}{\partial \hat{\xi}^2} \right|_{i,j} = \frac{1}{2(\Delta \hat{\xi})^2} \delta_{\hat{\xi}}^2 (U_{i,j} + U_{i,j}^*). \quad (3.89)$$

Using the upwind-downwind approximations (3.80) and (3.82), and the Crank-Nicolson approximations (3.87)-(3.89), a finite difference representation of equation (3.65) may be written (in operator notation)

$$\begin{aligned}
U_{i,j} - \frac{\Delta t}{2} \left\{ \bar{W}_{i,j} + \bar{T}_{i,j} \frac{\delta_{\hat{\eta}}^2}{(\Delta \hat{\eta})^2} + \bar{P}_{i,j} \frac{\chi_{\hat{\eta}}^+}{(\Delta \hat{\eta})} + \bar{S}_{i,j} \frac{\mu_{\hat{\xi}} \delta_{\hat{\xi}} \mu_{\hat{\eta}} \delta_{\hat{\eta}}}{(\Delta \hat{\xi})(\Delta \hat{\eta})} \right. \\
\left. + \bar{R}_{i,j} \frac{\delta_{\hat{\xi}}^2}{(\Delta \hat{\xi})^2} + \bar{Q}_{i,j} \frac{\chi_{\hat{\xi}}^+}{(\Delta \hat{\xi})} \right\} U_{i,j} = \\
U_{i,j}^* + \frac{\Delta t}{2} \left\{ \bar{W}_{i,j} + \bar{T}_{i,j} \frac{\delta_{\hat{\eta}}^2}{(\Delta \hat{\eta})^2} + \bar{P}_{i,j} \frac{\chi_{\hat{\eta}}^-}{(\Delta \hat{\eta})} + \bar{S}_{i,j} \frac{\mu_{\hat{\xi}} \delta_{\hat{\xi}} \mu_{\hat{\eta}} \delta_{\hat{\eta}}}{(\Delta \hat{\xi})(\Delta \hat{\eta})} \right. \\
\left. + \bar{R}_{i,j} \frac{\delta_{\hat{\xi}}^2}{(\Delta \hat{\xi})^2} + \bar{Q}_{i,j} \frac{\chi_{\hat{\xi}}^-}{(\Delta \hat{\xi})} \right\} U_{i,j}^* + \Delta t \bar{\Gamma}_{i,j}. \quad (3.90)
\end{aligned}$$

Here the overbar indicates that a coefficient is evaluated midway between the current and previous time planes and is evaluated at the typical mesh point  $(i,j)$  using a simple average analogous to equation (3.66). A set of algebraic equations, similar to that obtained in Appendix B for the Eulerian boundary-layer problem, may be obtained by letting the operators in (3.90) operate on  $U_{i,j}$ ; this set of simultaneous equations could be solved at any time step using point-by-point iteration. An attractive alternative is an ADI approach in which the the operators on the left side of equation (3.90) are factored into separate operators in each of the  $\hat{\xi}$  and  $\hat{\eta}$  coordinate directions. The factored form of equation (3.90) is

$$\begin{aligned}
\left( 1 - \frac{\alpha_{i,j} \cdot \Delta t}{(\Delta \hat{\xi})^2} \left( \bar{R}_{i,j} \delta_{\hat{\xi}}^2 + (\Delta \hat{\xi}) \cdot \bar{Q}_{i,j} \chi_{\hat{\xi}}^+ \right) \right) \left( 1 - \frac{\alpha_{i,j} \cdot \Delta t}{(\Delta \hat{\eta})^2} \left( \bar{T}_{i,j} \delta_{\hat{\eta}}^2 + (\Delta \hat{\eta}) \cdot \bar{P}_{i,j} \chi_{\hat{\eta}}^+ \right) \right) U_{i,j} \\
= D_{i,j}, \quad (3.91)
\end{aligned}$$

where

$$\alpha_{i,j} = \frac{1}{2 - (\Delta t) \cdot \bar{W}_{i,j}}, \quad (3.92)$$

and

$$D_{i,j} = 2\alpha_{i,j}U_{i,j}^* + \alpha_{i,j}\Delta t \left( \bar{W}_{i,j} + \bar{P}_{i,j} \frac{\chi_{\bar{\eta}}^-}{(\Delta \bar{\eta})} + \bar{T}_{i,j} \frac{\delta_{\bar{\eta}}^2}{(\Delta \bar{\eta})^2} + \bar{R}_{i,j} \frac{\delta_{\bar{\xi}}^2}{(\Delta \bar{\xi})^2} \right. \\ \left. + \bar{Q}_{i,j} \frac{\chi_{\bar{\xi}}^-}{(\Delta \bar{\xi})} \right) U_{i,j}^* + \alpha_{i,j}\Delta t \left( 2\bar{\Gamma}_{i,j} + \bar{S}_{i,j} \frac{\mu_{\bar{\xi}} \delta_{\bar{\xi}} \mu_{\bar{\eta}} \delta_{\bar{\eta}}}{(\Delta \bar{\xi})(\Delta \bar{\eta})} (U_{i,j} + U_{i,j}^*) \right). \quad (3.93)$$

There are two important points related to this factorization. First, equations (3.90) and (3.91) are not completely equivalent and differ by a term  $O(\{\alpha_{i,j}\Delta t\}^2)$ . However, since  $\alpha_{i,j}$  is  $O(1)$ , the difference between (3.90) and (3.91) is  $O(\{\Delta t\}^2)$ , the same level of error that was associated with the original approximations to equation (3.65) at  $t=\bar{t}$ . Consequently, equation (3.91) may also be regarded as a second-order accurate approximation to equation (3.65). The second point is that the second-order accurate finite-difference approximation to the term  $S(\partial^2 U / \partial \bar{\xi} \partial \bar{\eta})$  cannot be easily factored. Therefore, the term has been placed on the right side of equation (3.91), and appears as the last part of equation (3.93) for  $D_{i,j}$ ; since  $D_{i,j}$  contains values of  $U$  in the current time plane, it is necessary to recompute  $D_{i,j}$  after each complete iteration at a given time step.

The set of equations defined by (3.91) can be solved as a sequence of tri-diagonal matrix problems, in each of the coordinate directions. In view of the upwind-downwind approximations (3.80) and (3.82), each tri-diagonal problem is diagonally dominant and direct solution by the Thomas algorithm yields a stable procedure. Define an intermediate variable  $\tilde{U}_{i,j}$  such that

$$\left( 1 - \frac{\alpha_{i,j}\Delta t}{(\Delta \bar{\xi})^2} \left( \bar{R}_{i,j} \delta_{\bar{\xi}}^2 + (\Delta \bar{\xi}) \cdot \bar{Q}_{i,j} \chi_{\bar{\xi}}^+ \right) \right) \tilde{U}_{i,j} = D_{i,j}, \quad (3.94)$$

and then it follows that equation (3.91) becomes

$$\left( 1 - \frac{\alpha_{i,j}\Delta t}{(\Delta \bar{\eta})^2} \left( \bar{T}_{i,j} \delta_{\bar{\eta}}^2 + (\Delta \bar{\eta}) \cdot \bar{P}_{i,j} \chi_{\bar{\eta}}^+ \right) \right) U_{i,j} = \tilde{U}_{i,j}. \quad (3.95)$$

Assume that estimates of the coefficients  $\bar{R}_{i,j}$ ,  $\bar{Q}_{i,j}$ , and the right side of

equation (3.94),  $D_{i,j}$ , are known from values of  $U_{i,j}$  from a previous iteration at a given time step; then equation (3.94) defines a set of tri-diagonal matrix problems along lines of constant  $\hat{\xi}$  for the intermediate values  $\tilde{U}_{i,j}$  which are easily solved using a direct method. With  $\tilde{U}_{i,j}$  defined at each point in the mesh, equation (3.95) defines a set of tri-diagonal matrix problems along lines of constant  $\hat{\eta}$ , which are readily solved to find  $U_{i,j}$ . The details of the method are described in the next section.

### 3.6 Numerical Solution of the Lagrangian Boundary-layer Problem

The boundary-layer problem in Lagrangian coordinates consists of the coupled system of equations (3.56) and (3.57), and it is necessary to define a numerical procedure which can advance the solution for  $\hat{x}$  and  $U$  simultaneously from the previous time plane at  $t^*$ , to the current time plane at  $t=t^*+\Delta t$ . In section §3.5, difference approximations were derived for the momentum equation (3.56) which were based on approximating the momentum equation for each  $(i, j)$  node at time  $\bar{t}=t^*+(\Delta t)/2$ ; the resulting equations were factored to produce equations (3.94) and (3.95). In this section, the detailed procedure for advancing the solution of equations (3.56) and (3.57) is described.

Consider first equation (3.57), which describes the evolution of the  $\hat{x}$  particle positions and which is also approximated at  $\bar{t}$  at the point  $(i,j)$  viz.

$$\hat{x}_{i,j} = \hat{x}_{i,j}^* - \frac{\Delta t}{2\pi} \cdot \overline{Ue_0(\hat{x}_{i,j})} \cdot \left\{ \overline{U}_{i,j} \cdot \overline{Ue(\hat{x}_{i,j}, t)} - U_v(\bar{t}) \right\}. \quad (3.96)$$

Here, the overbar indicates that a quantity is evaluated at  $\bar{t}$ . The quantity  $Ue_0(\hat{x})$  is the analytic steady distribution given by equation (3.52) and is evaluated at  $\bar{t}$  at the mesh point  $(i,j)$  according to

$$\overline{Ue(\tilde{x}_{i,j})} = Ue_0(\tilde{x}_{i,j}). \quad (3.97)$$

Here the particle positions at  $\tilde{t}$  are computed as a simple average between the current and previous time planes by

$$\tilde{x}_{i,j} = (\hat{x}_{i,j} + \hat{x}_{i,j}^*)/2. \quad (3.98)$$

For the limit problem  $Re \rightarrow \infty$ ,  $Ue(\hat{x}_{i,j}, t) \equiv Ue_0(\hat{x}_{i,j})$  and  $U_v(t) \equiv 1$ . It may be inferred that for a given estimate of the fluid particle speed  $U_{i,j}$ ,

$$\bar{U}_{i,j} = (U_{i,j} + U_{i,j}^*)/2, \quad (3.99)$$

and equation (3.96) defines a non-linear equation for the single unknown  $\hat{x}_{i,j}$ . For the interacting boundary-layer problem, the mainstream velocity changes with time and  $Ue$  at  $\tilde{t}$  was calculated from

$$\overline{Ue(\tilde{x}_{i,j}, t)} = \{Ue(\tilde{x}_{i,j}, t^*) + Ue(\tilde{x}_{i,j}, t)\}/2. \quad (3.100)$$

Note that the particle positions in equation (3.100) are evaluated at  $\tilde{t}$  according to equation (3.99); an alternative method of approximation to the right side of equation (3.100) is

$$\overline{Ue(\tilde{x}_{i,j}, t)} = \{Ue(\hat{x}_{i,j}^*, t^*) + Ue(\tilde{x}_{i,j}, t)\}/2, \quad (3.101)$$

which differs from equations (3.100) by an amount  $O(\{\Delta t\}^2)$ . Both methods were used in the present study and both give essentially the same results. However, equation (3.100) is more efficient since the distributions of  $Ue$  in the current and previous time planes can be summed according the right side of equation (3.100) to obtain a single distribution; for a given value  $\tilde{x}_{i,j}$

(obtained from equation (3.99)) one interpolation is the required to find the left side of equation (3.100).

The solution for  $\hat{x}_{i,j}$  was obtained in a general iterative procedure in the following manner. Assume that an iteration for the streamwise velocity distribution  $U_{i,j}$  (using a procedure that will be described below) has just been completed. At this stage, new estimates of  $U_{i,j}$ , as well as estimates of  $\hat{x}_{i,j}$  from the previous iteration, are available at every point in the mesh; these are used to compute  $\bar{x}_{i,j}$  and  $\bar{U}_{i,j}$  from equations (3.98) and (3.99). The right side of equation (3.96) may then be evaluated using equation (3.100) to define a new iterate for  $\hat{x}_{i,j}$ .

It remains to discuss the numerical procedure used to obtain the streamwise velocity at each time step. In §3.5 a factored ADI algorithm was derived and is given in equations (3.94) and (3.95). The algorithm was used to advance the solution for  $U_{i,j}$  from the previous to the current time plane and the details will now be discussed. The coefficients  $\bar{P}$ ,  $\bar{Q}$ ,  $\bar{R}$ ,  $\bar{S}$ , and  $\bar{T}$  in equations (3.93)-(3.95) correspond to the quantities defined in (3.58) but evaluated midway between the current and previous time planes, at  $t=\bar{t}$ . The quantities  $P$ ,  $Q$ ,  $R$ ,... in equations (3.58) involve first and second order partial derivatives of  $\hat{x}$ , and the coefficients were evaluated as simple averages between the current and previous time planes, using central differences. For example, the gradient  $\partial\hat{x}/\partial\bar{\eta}$  at  $\bar{t}$  was approximated by

$$\frac{\partial\hat{x}_{i,j}}{\partial\bar{\eta}} = \frac{1}{2} \left\{ \frac{\hat{x}_{i,j+1} - \hat{x}_{i,j-1}}{2(\Delta\bar{\eta})} + \frac{\hat{x}_{i,j+1}^* - \hat{x}_{i,j-1}^*}{2(\Delta\bar{\eta})} \right\}, \quad (3.102)$$

which is equivalent to

$$\frac{\partial\hat{x}_{i,j}}{\partial\bar{\eta}} = \left\{ \frac{\bar{x}_{i,j+1} - \bar{x}_{i,j-1}}{2(\Delta\bar{\eta})} \right\}, \quad (3.103)$$



using equation (3.98). The approximations for  $\partial\hat{x}/\partial\hat{\xi}$ ,  $\partial^2\hat{x}/\partial\hat{\xi}^2$ ,  $\partial^2\hat{x}/\partial\hat{\xi}\partial\hat{\eta}$ , and  $\partial^2\hat{x}/\partial\hat{\eta}^2$  at  $\bar{t}$ , were also obtained using a simple average in  $t$  and central differences in a manner analogous to equation (3.102).

A converged solution for the streamwise particle positions  $\hat{x}_{i,j}$  and velocities  $U_{i,j}$  is obtained in the current time plane as follows. To initiate the iteration,  $U_{i,j}$  and  $\hat{x}_{i,j}$  were first set equal to their known values  $U_{i,j}^*$  and  $\hat{x}_{i,j}^*$  in the previous time plane at  $t=t^*$ . The coefficients  $\bar{P}_{i,j}$ ,  $\bar{Q}_{i,j}$ ,  $\bar{R}_{i,j}$ ,  $\bar{S}_{i,j}$ , and  $\bar{T}_{i,j}$  were then evaluated using relations analogous to equation (3.102). The coefficients  $\bar{F}_{i,j}$  and  $\bar{W}_{i,j}$  (as defined in equations (3.58)) depend on the outer mainstream velocity distribution  $Ue(\hat{x},t)$ , as well as the gradients of  $Ue$  with respect to  $\hat{x}$  and  $t$ . For the interacting calculations,  $Ue$  is time-dependent and to evaluate  $\bar{F}_{i,j}$  and  $\bar{W}_{i,j}$ ,  $Ue$  and its gradients must be evaluated at  $\bar{t}$ . The distributions of  $\bar{Ue}$ ,  $\partial\bar{Ue}/\partial\hat{x}$ , and  $\partial\bar{Ue}/\partial t$ , were evaluated at any time step through consideration of the interaction problems which will be discussed in the next section. These distributions were therefore available at any stage (defined on a mesh in the streamwise direction) and for a given fluid particle at  $\bar{t}$  (whose streamwise position is given by (3.98)) values of  $\bar{Ue}$ ,  $(\partial\bar{Ue}/\partial\hat{x})$ , and  $(\partial\bar{Ue}/\partial t)$ , may be obtained through interpolation. In this manner, values of  $\bar{F}_{i,j}$  and  $\bar{W}_{i,j}$  were computed at each point in the mesh.

In the mesh, there are  $M$  equal intervals in the  $\hat{\xi}$  direction and  $N$  equal intervals in the  $\hat{\eta}$  direction. With the estimated coefficients of equation (3.94) and (3.95), a new iterate was produced for  $U_{i,j}$  using two successive computational phases. Consider first equation (3.94), which defines a set of tri-diagonal matrix problems along lines of constant  $\hat{\eta}$  for the streamwise variable  $\hat{U}_{i,j}$ . Let  $j=1$  and  $j=(N+1)$  denote the boundaries  $\hat{\eta}=0$  and  $\hat{\eta}=1$ ; and let  $i=1$  and  $i=(M+1)$  denote the boundaries  $\hat{\xi}=0$  and  $\hat{\xi}=2$ , respectively. On  $i=1$  and  $i=(M+1)$  the coefficients  $R$  and  $Q$  are zero since  $\hat{x}=\hat{\xi}$  for all  $t$ ; therefore equation (3.94) reduces to

$$\tilde{U}_{i,j} = D_{i,j}, \quad (3.104)$$

where  $D_{i,j}$  here denotes the limiting form of equation (3.93) as  $\hat{\xi} \rightarrow 0, 2$ . Since  $U_e$ ,  $\partial U_e / \partial \hat{x}$  and  $\partial U_e / \partial t$  tend to zero as  $\hat{\xi} \rightarrow 0, 2$ , then  $\Gamma = W = S = 0$  at  $\hat{\xi} \rightarrow 0, 2$ ; thus the special form of equation (3.93) at upstream and downstream infinity is

$$D_{i,j} = \left\{ 1 + \frac{\Delta t}{2} \left( \frac{\bar{P}_{i,j} \chi_{\hat{\eta}}^-}{(\Delta \hat{\eta})} + \frac{\bar{T}_{i,j} \delta_{\hat{\eta}}^2}{(\Delta \hat{\eta})^2} \right) \right\} U_{i,j}^*, \quad \text{for } i=1, i=M+1. \quad (3.105)$$

Consequently, equation (3.104) provides boundary values for the tri-diagonal matrix problems defined by (3.94) which are of the general form

$$b_i \tilde{U}_{i+1,j} + a_i \tilde{U}_{i,j} + c_i \tilde{U}_{i-1,j} = D_{i,j}, \quad (3.106)$$

for  $i=2, M$ . With  $\tilde{U}_{i,j}$  at  $i=1$  and  $(M+1)$  given by equation (3.104), equations (3.106) ..., were solved for  $\tilde{U}_{i,j}$  for  $j=2$  to  $j=N$  using the Thomas algorithm. In the second phase of the procedure, the computed values of  $\tilde{U}_{i,j}$  were used on the right side of equation (3.95) which defines tri-diagonal matrix problems along lines of constant  $\hat{\xi}$  that are of the form

$$b_j U_{i,j+1} + a_j U_{i,j} + c_j U_{i,j-1} = \tilde{U}_{i,j}, \quad (3.107)$$

for  $j=2$  to  $N$ . The boundary values are

$$U_{i,1} = 0, \quad U_{i,N+1} = 1. \quad (3.108)$$

The sequence of tri-diagonal problems was then solved along lines on constant  $\hat{\xi}$  for  $i=1$  to  $(M+1)$ . Note that the distribution of  $U$  at  $\hat{\xi}=0, 2$  is calculated at each time step as part of the overall algorithm; the values of  $U$  are also given

by equation (3.64) which could be incorporated as an alternative solution procedure.

Once the second phase of the ADI solution procedure is complete, a full iteration for  $U_{i,j}$  was considered to have occurred. At this stage, equation (3.96) was used to calculate the new particle positions  $\hat{x}_{i,j}$  at time  $t$ . It is evident from equation (3.98) that the coefficients  $\bar{P}$ ,  $\bar{Q}$ ,  $\bar{R}$ , ... in equations (3.94) and (3.95) will change as the estimates of  $\hat{x}_{i,j}$  and  $U_{i,j}$  are refined at each iteration. Consequently, at every time step, the factored ADI solution for  $U_{i,j}$  and a following recalculation of  $\hat{x}_{i,j}$ , was repeatedly carried out, until successive estimates of  $U_{i,j}$  differed by less than four significant digits. It is worthwhile to note that this procedure is implicit, in contrast to the Beam and Warming (1978) type of ADI algorithm in which only one sweep in the  $\hat{\xi}$  and  $\hat{\eta}$  directions is carried out before proceeding to the next time step; the latter type of method is sometimes referred to as an explicit method. Some calculations in this study were attempted using the explicit Beam and Warming ADI method; however these computations soon became unstable when the boundary-layer calculation was carried on beyond separation, at  $t=0.28$ . The observed instability is believed to be due to a gradual loss of diagonal dominance in the tri-diagonal matrix problems associated with the Beam and Warming (1978) method. The ADI method of this study is numerically stable since the upwind-downwind approximations guarantee diagonal dominance. For the limit problem  $Re \rightarrow \infty$  the calculation typically moved through each time step in 5-10 iterations. For the interactive problem a second set of iterations is required since the external flow distribution  $U_e(\hat{x},t)$  changes with the evolution of the boundary-layer flow; the calculation of the fully interacting problem is considered in the next section.

### 3.7 The Interaction Problem

The boundary-layer problem was formulated (c.f. §3.3, §3.4) assuming that the vortex velocity  $U_v(t)$  and the mainstream velocity distributions  $U_e(\bar{x},t)$  and  $U_\infty(\bar{x},t)$  could be computed at any time  $t$  during the course of the numerical integration. Recall that  $U_\infty(\bar{x},t)$  is the mainstream velocity in a frame of reference moving with the vortex, while  $U_e(\bar{x},t)$  is the instantaneous velocity at the boundary-layer edge in the laboratory frame of reference; the two distributions are related by

$$U_\infty(\bar{x},t) = -U_v(t) + U_e(\bar{x},t). \quad (3.109)$$

A solution procedure to evaluate the outer velocities is required to close the interacting boundary-layer problem; this will be developed in this section, where a set of equations to compute  $U_e$  and  $U_v$  will be derived.

The vortex is convected in the velocity field induced by the image vortex as well as the local flow velocity above the wall. The thickening boundary layer induces velocities  $O(Re^{-1/2})$  in the potential flow above the wall. Therefore, the velocity components of the vortex  $U_v(t)$  and  $V_v(t)$  are of the form

$$U_v(t) = U_{v0}(t) + \frac{1}{\sqrt{Re}} U_{v1}(t) + \dots, \quad (3.110)$$

$$V_v(t) = V_{v0}(t) + \frac{1}{\sqrt{Re}} V_{v1}(t) + \dots. \quad (3.111)$$

Similarly, the mainstream velocity function is of the form

$$U_e(\bar{x},t) = U_e^0(\bar{x},t) + \frac{1}{\sqrt{Re}} U_e^1(\bar{x},t) + \dots. \quad (3.112)$$

Consider first the leading order terms for  $U_v$ ,  $V_v$ , and  $U_e$ . The leading order vortex velocity components are obtained from equations (1.52) and

$$U_{v0} = \frac{1}{Y_v(t)}, \quad V_{v0} = 0, \quad (3.113)$$

where the initial position of the vortex is described by

$$Y_v = Y_{v0} = 1 \quad \text{at } t=0. \quad (3.114)$$

The external streamfunction describing the inviscid flow due to the vortex in the laboratory frame is given by equation (1.51). Differentiating (1.51) with respect to  $Y$  and taking the limit  $Y \rightarrow 0$  yields the leading order term for  $U_e$ , viz.

$$U_e^0(\bar{x}, t) = \frac{4Y_v}{x^2 + Y_v^2}, \quad (3.115)$$

and the corresponding mainstream velocity in a frame of reference which convects with the vortex may be obtained from (3.109) and (3.111) according to

$$U_\infty^0(\bar{x}, t) = \frac{4Y_v}{x^2 + Y_v^2} - \frac{1}{Y_v}. \quad (3.116)$$

The perturbation velocity terms in equations (3.110)-(3.111) are  $O(\text{Re}^{-1/2})$  and are obtained according to the interaction principles discussed in §1.4. The perturbation velocities  $(U_1, V_1)$ , may be determined by differentiating the streamfunction given by equation (1.40) according to

$$\Psi_1 = -\frac{1}{\pi} \int_{-\infty}^{+\infty} \frac{Y \cdot U_e \cdot \delta^*}{(s-x)^2 + Y^2} ds. \quad (3.117)$$

Here  $\delta^*$  is the boundary-layer displacement thickness, and the coupling between the external flow and the evolving boundary layer is accounted for

through equation (3.117). The displacement thickness<sup>3</sup>  $\delta^*$  is defined in terms of velocities in the laboratory frame and

$$\delta^*(x,t) = \int_0^{\infty} (1-U) dy, \quad (3.118)$$

where  $y$  is the scaled boundary-layer variable and  $U$  is the normalized velocity given by (3.48). Because the displacement thickness is calculated from the boundary-layer solution it depends implicitly on the external mainstream velocity. Consequently, an inner-outer iteration is (in general) required at each time step. For the present purpose, assume that  $\delta^*(x,t)$  is known or, alternatively, may be computed in the course of a general iterative procedure at time  $t$ . The perturbation velocity components may be obtained by differentiating  $\Psi_1$  in equation (3.117) and subsequently integrating by parts (c.f. equation 1.43); the results are

$$U_1 = -\frac{1}{\pi} \int_{-\infty}^{+\infty} \frac{(s-x) \cdot V_d(s)}{(s-x)^2 + Y^2} ds, \quad (3.119)$$

$$V_1 = \frac{1}{\pi} \int_{-\infty}^{+\infty} \frac{Y \cdot V_d(s)}{(s-x)^2 + Y^2} ds, \quad (3.120)$$

where  $V_d(x,t)$  is the scaled displacement velocity (1.47) given by

$$V_d = \frac{\partial}{\partial x} (Ue \cdot \delta^*). \quad (3.121)$$

In a frame of reference convecting with the vortex, the vortex coordinates are  $(0, Y_v)$ ; thus, from equations (3.119) and (3.120), the perturbations to the vortex velocity are given by

$$U_{v1} = -\frac{1}{\pi} \int_{-\infty}^{+\infty} \frac{s \cdot V_d(s)}{s^2 + Y_v^2} ds, \quad (3.122)$$

---

<sup>3</sup>The numerical procedure used to compute  $\delta^*$  in Lagrangian variables is discussed in Appendix D.

$$V_{v1} = \frac{1}{\pi} \int_{-\infty}^{+\infty} \frac{Y_v \cdot V_d(s)}{s^2 + Y_v^2} ds. \quad (3.123)$$

The perturbation term for  $U_e$  is found by taking the limit  $Y \rightarrow 0$  in equation (3.119) and is

$$U_e^1 = \frac{1}{\pi} \int_{-\infty}^{+\infty} \frac{V_d(s)}{(x-s)} ds, \quad (3.124)$$

where in equation (3.124) the Cauchy principal value is indicated.

It is worthwhile at this stage to summarize the key quantities and governing equations associated with the external flow pattern. The vortex velocity components are computed at any stage from

$$U_v(t) = \frac{1}{Y_v(t)} - \left( \frac{1}{\sqrt{Re}} \right) \cdot \frac{1}{\pi} \int_{-\infty}^{+\infty} \frac{s \cdot V_d(s,t)}{s^2 + Y_v^2} ds, \quad (3.125)$$

$$V_v(t) = \left( \frac{1}{\sqrt{Re}} \right) \cdot \frac{Y_v(t)}{\pi} \int_{-\infty}^{+\infty} \frac{V_d(s,t)}{s^2 + Y_v^2} ds, \quad (3.126)$$

where the normal velocity induced by the boundary layer,  $V_d(x,t)$ , is given in terms of  $\delta^*$  and  $U_e$  by equation (3.121). The normal coordinate of the vortex,  $Y_v$ , is calculated from

$$\frac{dY_v}{dt} = V_v, \quad Y_v(0) = 1, \quad (3.127)$$

with  $V_v$  given by equation (3.126). The mainstream velocity in the laboratory frame  $U_e$  is given by

$$U_e(x,t) = \frac{4Y_v(t)}{x^2 + Y_v^2} + \left( \frac{1}{\sqrt{Re}} \right) \cdot \frac{1}{\pi} \int_{-\infty}^{+\infty} \frac{\frac{\partial}{\partial s} (U_e(s,t) \cdot \delta^*(s,t))}{(x-s)} ds, \quad (3.128)$$

where the interaction velocity  $V_d$  has been written explicitly in terms of  $U_e$  and  $\delta^*$ . The mainstream velocity in the convected frame is

$$U_{\infty}(x,t) = U_e(x,t) - U_v(t), \quad (3.129)$$

with  $U_v$  defined by equation (3.125). In the interacting boundary-layer method,  $U_e$  changes with time and is to be determined as part of the solution. Since  $U_e$  appears in the integrand on the right side of equation (3.128), it is evident that it is necessary to compute the solution of a singular integro-differential equation (3.128) at each time step in the integration.

The basic scheme used to integrate the interacting equations through one time step will now be described. In general, the calculations were carried out in terms of the variable  $\bar{x}$ , defined on the finite domain (0,2) by equation (3.50). The formulation of the boundary-layer problem in Lagrangian coordinates has been described in §3.4, where it was assumed that the distributions of  $U_e(\bar{x},t)$ ,  $U_v(t)$ ,  $\partial U_e/\partial \bar{x}$  and  $\partial U_e/\partial t$  were known functions of  $t$ ; note that these quantities are the only distributions associated with the external flow which influence the boundary-layer problem defined in equations (3.56)-(3.59). However, in the interacting boundary-layer formulation  $U_e(\bar{x},t)$  and  $U_v(t)$  are affected by the thickening boundary-layer flow and must be constructed during the course of the integration. A solution of the boundary-layer problem may be produced for a given distribution of  $U_e$  and  $U_v$ , thus yielding an estimate of the displacement thickness distribution  $\delta^*(\bar{x},t)$  at time  $t$ , which is the critical information required to compute the changes in the external flow distributions  $U_e(\bar{x},t)$  and  $U_v(t)$ . The detailed numerical solution procedures for the external flow problem will be described in §3.8 and §3.9. However, it is evident that once an estimate of  $\delta^*(\bar{x},t)$  is available, the displacement velocity  $V_d$  may be computed from equation (3.121) and it follows, from equations (3.125) to (3.128), that the external flow quantities depend only on  $V_d$  and  $\delta^*$ .



As in §3.5 and §3.6, let  $t^*$  denote the previous time plane where the solution is known; all quantities evaluated at  $t^*$  are denoted by an asterisk. The objective is to advance the solution to the current time plane at  $t=t^*+\Delta t$ . There is a variety of ways in which the iteration between the external flow problem and the boundary-layer solution could be carried out. The method used in this study is a "predictor-corrector" scheme depicted schematically in figure 3.3, where it is assumed that a converged interactive solution is known at  $t=t^*$ . The iteration to determine the solution at time  $t$  was started by first computing a "predicted" boundary-layer solution at time  $t$ . As discussed in §3.4, §3.5 and §3.6 the boundary-layer equations were approximated midway between the current and previous time planes at  $\bar{t}=t^*+\Delta t/2$ , and the coefficients in equations (3.56) and (3.57) were evaluated at  $\bar{t}$  using a simple average between these two time planes (see, for example, equations (3.66) or (3.100)). To calculate  $\bar{\Gamma}$  in equation (3.93), for example, it is evident from equations (3.58) that the distributions of  $U_e$ ,  $\partial U_e/\partial \bar{x}$  and  $\partial U_e/\partial t$ , as well as  $U_v$ , are required at  $\bar{t}$ ; however,  $U_v$  and  $U_e$  are not known at  $t$  in the predictor phase of the calculation and consequently are initially taken equal to their values at  $t=t^*$  (as indicated in figure 3.3). In addition,  $\partial U_e/\partial \bar{x}$  is estimated from the distribution  $U_e^*(\bar{x},t)$ . The time derivative  $\partial U_e/\partial t$  was normally calculated as a central difference according to

$$\frac{\partial \bar{U}_e}{\partial t}(\bar{x}_{i,j},t) = \frac{1}{\Delta t} \{U_e(\bar{x}_{i,j},t) - U_e^*(\bar{x}_{i,j},t)\}, \quad (3.130)$$

where  $\bar{x}_{i,j}$  is the average particle position between the current and previous time planes given by equation (3.98). In the predictor phase, where  $U_e$  is estimated to be  $U_e^*$ , the estimate of the time derivative from equation (3.130) gives  $\partial \bar{U}_e/\partial t=0$ ; this was considered to be a poor approximation and consequently, in the predictor phase,  $\partial \bar{U}_e/\partial t$  at  $\bar{x}_{i,j}$  was estimated from the known distribution of  $U_e$  at  $t^*$  and  $t^*-\Delta t$ . Thus, in the predictor phase, the estimate of the time derivative of  $U_e$  is "lagged" a full time step.

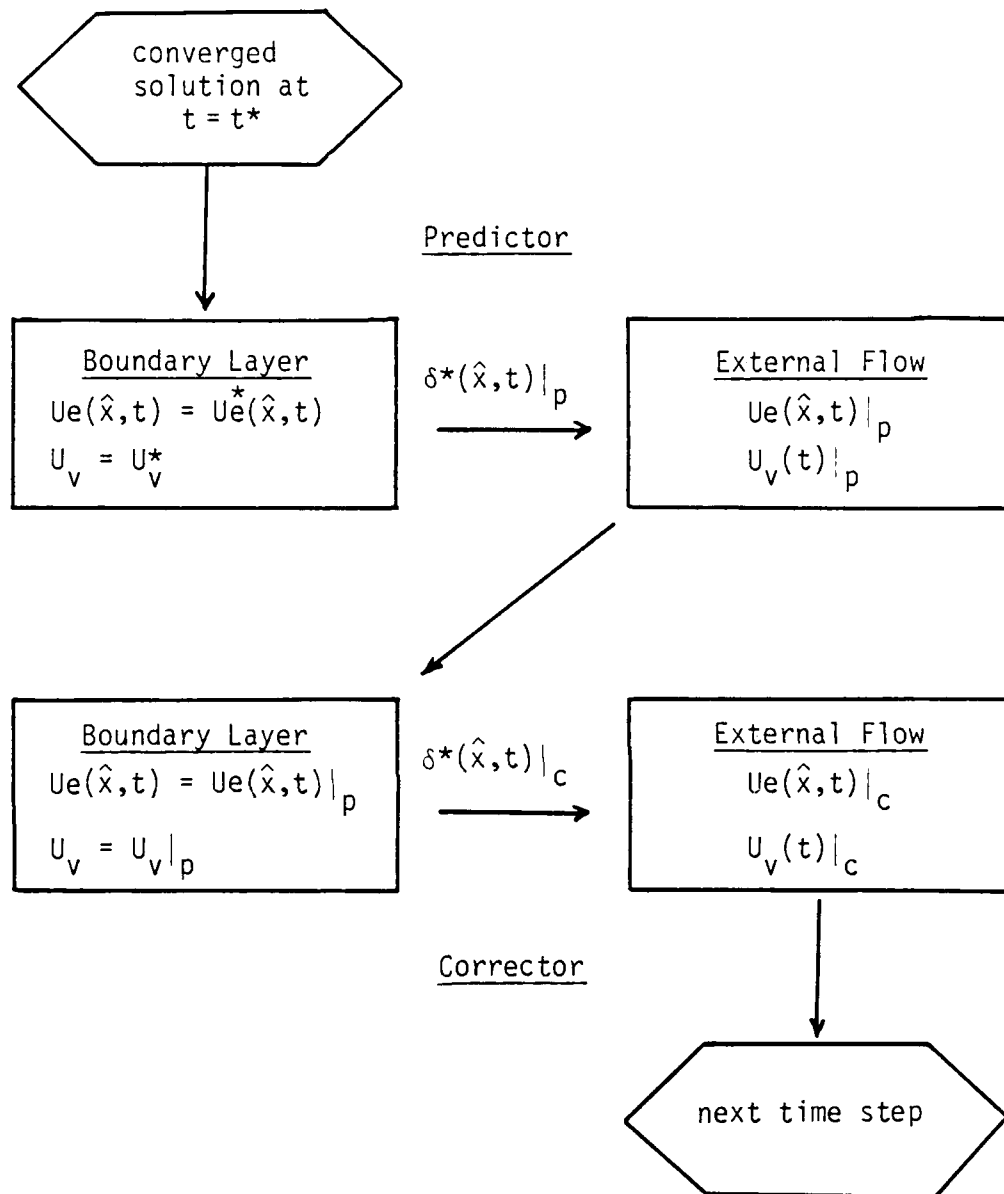


Figure 3.3. Schematic diagram of the predictor-corrector algorithm used in the interacting problem.

An iteration of the boundary-layer problem was carried out using the procedure outlined in §3.6 until convergence occurred, typically in 7-10 full sweeps through the mesh. This calculation thus generated a predicted distribution of  $U$  and  $\bar{x}$  at time  $t$ . In addition, a predicted displacement surface is produced at this stage (as indicated in figure 3.3) which was then used to generate "predicted" distributions of the external flow quantities as follows. A scaled displacement velocity  $V_d$  was obtained by differentiation from equation (3.121) (using  $U_e = U_e^*(\bar{x}, t)$ ). With  $Y_v$  set equal to  $Y_v^*$ , integration of the right sides of equations (3.125) and (3.126) produced "predicted" values of the vortex velocity components  $U_v(t)$  and  $V_v(t)$ . A "predicted" value of  $Y_v(t)$  was then obtained through the following second-order accurate approximation to equation (3.127)

$$Y_v(t) = Y_v^* + \frac{\Delta t}{2}(V_v^* + V_v). \quad (3.131)$$

The final phase of the external calculation used the predicted values of  $Y_v$  and  $\delta^*$  to solve the integro-differential equation (3.128) to obtain a predicted distribution of the mainstream velocity function  $U_e(\bar{x}, t)$ . This equation involves a Cauchy principal-value integral, and the numerical method used to discretize the integral will be described in §3.8, while the algorithm to compute  $U_e$  will be discussed in §3.9.

Once the predicted solution for the external flow was obtained, it was then used to calculate a "corrected" boundary-layer solution as indicated in figure 3.3. This computation is similar to that associated with the predictor phase. However, since good estimates of  $U_e(\bar{x}, t)$  and  $U_v(t)$  were available at this stage, refined estimates of the coefficients in (3.56) and (3.57) were obtained at  $t = \bar{t}$ . One main difference from the predictor phase is that the time-derivative in equation (3.130) was the estimated using the predicted

values of  $U_e$ , so that  $\partial \overline{U_e} / \partial t$  was no longer "lagged" a time step. Typically, another 7-10 iterations were required to produce a converged "corrected" boundary-layer solution and, as indicated in figure 3.3, the net result of this computation was a new "corrected" displacement thickness  $\delta^*(\bar{x}, t)$ . Finally, this distribution of  $\delta^*$  was used to compute a "corrected" solution of the external flow problem, obtaining new estimates of  $U_e(\bar{x}, t)$ ,  $U_v(t)$ ,  $V_v(t)$  and  $Y_v(t)$ . At this stage, a time step was considered to have been completed and the computation was advanced to the next time step.

The computational time associated with the solution of the boundary-layer problem was found to be roughly equal to the time required to compute the displacement surface and the unsteady external-flow velocities. Convergence was generally decided by insisting the  $U$  must agree with the previous iterate at every mesh point to within four significant figures; the  $\bar{x}$  field was not tested in order to reduce the computational time and because it generally exhibits less variation than the  $U$  field. The size of the time step has a major influence on the rate of convergence, and  $\Delta t$  was selected during the calculations so that the number of iterations associated with the boundary-layer problem was less than ten. In a typical calculation,  $\Delta t$  was started at 0.005 and reduced during course of the computation to values as low as  $\Delta t = 0.0005$ . The interacting boundary-layer calculations all terminate in a singularity and thus small time steps were used as  $t \rightarrow t_s$  to obtain an accurate estimate of  $t_s$  (and not because the numerical algorithm experienced convergence problems).

### 3.8 The Cauchy Integral

The integral equation (3.128) contains a Cauchy principal value integral, and the accurate numerical evaluation of this integral is not a simple matter.

In this study several methods of evaluating the Cauchy integral were tried before the second-order method (that will subsequently be described in this section) was adopted. Previous unsteady interacting boundary-layer calculations were discussed in §2.7, and it was remarked that there is no clear consensus as to whether the effect of interaction relaxes the separation singularity. As a result of experience obtained during this study, it is believed that part of the apparent confusion on this point may be associated with the use of low-order numerical methods for the Cauchy integral. Therefore, before discussing the second-order method used in this study, it is worthwhile to recount the experience when a first-order method was used.

Define a general Cauchy integral by

$$C(x,t) = \frac{1}{\pi} \int_{-\infty}^{+\infty} \frac{F(s)}{x-s} ds, \quad (3.132)$$

where in this study  $F$  is given by

$$F(x) = \frac{\partial}{\partial x} \{ Ue(x,t) \cdot \delta^*(x,t) \}. \quad (3.133)$$

Equation (3.128) may now be written in the form

$$Ue(x,t) = \frac{4Y_v}{x^2 + Y_v^2} + \frac{1}{\sqrt{\text{Re}}} C(x,t). \quad (3.134)$$

The integral in equation (3.132) is defined on a doubly infinite domain, and it is convenient to use the same mapping to the finite range (0,2) that was used in the boundary-layer problem; this is particularly convenient since the mapping emphasizes the region near the vortex where the effects of interaction are most important. Under this mapping, equation (3.132) becomes

$$C(\bar{x},t) = \frac{1}{\pi} \sin\left(\frac{\pi\bar{x}}{2}\right) \int_0^2 \frac{H(\bar{s})}{\sin\left\{\frac{\pi}{2}(\bar{x}-\bar{s})\right\}} d\bar{s}, \quad (3.135)$$

where  $\hat{s}$  is a dummy variable of integration and  $H(\hat{x})$  is given by

$$H(\hat{x}) = \sin\left(\frac{\pi\hat{x}}{2}\right) \cdot \frac{\partial}{\partial \hat{x}} \{Ue(\hat{x},t) \cdot \delta^*(\hat{x},t)\}. \quad (3.136)$$

Here, and in all subsequent equations in this section, the functional argument  $t$  has been omitted on the left side of equation (3.136) since the integrations are generally performed at fixed  $t$ .

If the interval  $(0,2)$  is split into  $N$  equal parts of length  $\Delta\hat{x}$ , equation (3.135) may be written according to

$$C(\hat{x}_i) = \frac{1}{\pi} \sin\left(\frac{\pi\hat{x}_i}{2}\right) \cdot \sum_{j=1}^N \int_{\hat{x}_{j-1}}^{\hat{x}_j} \frac{H(\hat{s})}{\sin\left\{\frac{\pi}{2}(\hat{x}_i - \hat{s})\right\}} d\hat{s}, \quad (3.137)$$

at  $\hat{x}=\hat{x}_i$ ; here  $\hat{x}_0=0$  and  $\hat{x}_N=2$ . A common approach to the evaluation of the Cauchy integral is to compute the integrals in equation (3.137) by taking the integrand to be constant in each interval and equal to the value at the midpoint of the interval. Thus if

$$\bar{\hat{x}}_j = \frac{\hat{x}_j + \hat{x}_{j-1}}{2}, \quad \bar{H}_j = \sin\left(\frac{\pi\bar{\hat{x}}_j}{2}\right) \{Ue_j \cdot \delta^*_{j-1} - Ue_{j-1} \cdot \delta^*_j\}, \quad (3.138)$$

then the approximation to equation (3.136) is

$$C(\hat{x}_i) = \frac{1}{\pi} \sin\left(\frac{\pi\hat{x}_i}{2}\right) \cdot \sum_{j=1}^N \frac{\bar{H}_j}{\sin\left\{\frac{\pi}{2}(\hat{x}_i - \bar{\hat{x}}_j)\right\}}. \quad (3.139)$$

An iterative scheme was then formulated for  $Ue(\hat{x}_i)$ ; if a superscript "k" denotes successive iterates, the scheme that was initially used is (from equation (3.134))

$$Ue_i^{k+1} = \frac{4Y_v}{\cot^2(\frac{\pi\bar{x}_i}{2}) + Y_v^2} + \frac{1}{\pi\sqrt{Re}} \sin(\frac{\pi\bar{x}_i}{2}) \cdot \sum_{j=1}^N \sin(\frac{\pi\bar{x}_j}{2}) \cdot \frac{\{Ue_j^k \delta_j^* - Ue_{j-1}^k \delta_{j-1}^*\}}{\sin\{\frac{\pi}{2}(\bar{x}_i - \bar{x}_j)\}}. \quad (3.140)$$

At each time step for a given estimate of  $J^*(\bar{x}, t)$ , equation (3.140) was iterated until convergence was obtained.

The algorithm (3.140) was used in the initial phases of this study with apparent success. The computed flow fields seemed plausible, and the results tended to support the notion that the effect of interaction was to at least delay the occurrence of a singularity, and perhaps relax it altogether (see, for example, Henkes and Veldman 1987; Chuang and Conlisk, 1989; Riley and Vasantha, 1989). However, the difficulty with equation (3.140) is the low-order accuracy of the scheme used to approximate the Cauchy integral. Formula (3.138) is basically a trapezoidal rule and although the accuracy should be  $O(\Delta\bar{x}^3)$ , it is, in fact, far less accurate. The Cauchy integrator (3.139) was tested on functions such as  $F(x)=1/(1+x^2)$  and  $F(x)=x/(1+x^2)$  in equation (3.132), whose exact Cauchy integrals are known. These tests revealed that the error was unacceptably high (and much worse than  $O(\Delta\bar{x}^3)$ ). Consequently, the approach was abandoned in favor of a more accurate algorithm. At the same time, it is worthwhile to note that the inaccurate Cauchy integrator appeared to be very effective at smoothing the computed distributions of  $\delta^*$  and, in effect, at artificially smearing the eruptive portion of the boundary-layer flow.

The integration scheme that was finally used for all the interactive calculations reported in this study is a second-order accurate method similar to that described by Napolitano, Werle and Davis (1978). The Cauchy integral (3.132) is first split into two parts according to

$$C(x_i) = S(x_i) + L(x_i), \quad (3.141)$$

where  $S_i$  is the main part of the integral given by

$$S_i = S(x_i) = \frac{1}{\pi} \int_{-R}^{+R} \frac{F(s)}{x_i - s} ds, \quad (3.142)$$

and  $R$  is a large value of  $x$  to be selected. The asymptotic tails of the integral are

$$L_i = L(x_i) = \frac{1}{\pi} \left\{ \int_{+R}^{+\infty} \frac{F(s)}{x_i - s} ds + \int_{-\infty}^{-R} \frac{F(s)}{x_i - s} ds \right\}. \quad (3.143)$$

Note that the decomposition (3.141) was carried out because the mapping (3.50) to transform the entire interval (as in equation (3.135)) generated significant error near  $\hat{x}=0,2$  in using the trial functions that were used to test the algorithm. For this reason, the tail portions of the integral  $L_i$  were treated separately from the main part  $S_i$ .

Consider first  $S_i$  and again introduce the mapping (3.50). If the interval (0,2) is assumed to be divided into  $N$  equal parts of length  $\Delta\hat{x}$ , the value of  $R$  selected was

$$R = \tan\left\{ \frac{\pi}{2} \left(1 - \frac{\Delta\hat{x}}{2}\right) \right\}. \quad (3.144)$$

Then,  $S_i$  may be written as the sum of integrals

$$S_i = \frac{1}{\pi} \sin\left(\frac{\pi}{2} \hat{x}_i\right) \sum_{j=1}^{N-1} \int_{\hat{x}_j - \Delta\hat{x}/2}^{\hat{x}_j + \Delta\hat{x}/2} \frac{H(\hat{s})}{\sin\left\{ \frac{\pi}{2} (\hat{x}_i - \hat{s}) \right\}} d\hat{s}, \quad (3.145)$$

where  $H(\hat{x})$  is defined by equation (3.136). Note that the nodes at  $\hat{x}_j$  are at the midpoints of the corresponding interval of integration. One method of evaluating the integrals in equation (3.145) is to assume that  $H(\hat{s})$  is constant over the  $j$ th interval and equal to the value at the nodal point  $\hat{x}_j$ . This approach is similar to that used by Henkes and Veldman (1987), and Riley



and Vasantha (1989); however, as Napolitano, Werle and Davis (1978) have shown, this approach yields results which are only first order accurate in  $\Delta\hat{x}$ . A second-order accurate algorithm is obtained by taking

$$H(\hat{x}) = H_j + (\hat{x} - \hat{x}_j)H_j' + O(\Delta\hat{x}^2), \quad (3.146)$$

on the  $j$ th interval  $[\hat{x}_j - \Delta\hat{x}/2, \hat{x}_j + \Delta\hat{x}/2]$ ; here  $H_j'$  denotes the first derivative of  $H$  evaluated at the node  $\hat{x}_j$ . An approximation to equation (3.145) is

$$S_i = \frac{1}{\pi} \sin\left(\frac{\pi}{2}\hat{x}_i\right) \sum_{j=1}^{N-1} \{\alpha_{i,j}H_j + \beta_{i,j}H_j'\}, \quad (3.147)$$

where

$$\alpha_{i,j} = \Delta\hat{x} \int_{-1/2}^{+1/2} \frac{d\mu}{\sin\left\{\frac{\pi}{2}(r_{i,j} - \mu\Delta\hat{x})\right\}}, \quad (3.148)$$

$$\beta_{i,j} = \Delta\hat{x}^2 \int_{-1/2}^{+1/2} \frac{\mu d\mu}{\sin\left\{\frac{\pi}{2}(r_{i,j} - \mu\Delta\hat{x})\right\}}, \quad (3.149)$$

with

$$r_{i,j} = \hat{x}_i - \hat{x}_j = (i-j)\Delta\hat{x}. \quad (3.150)$$

Expression for the coefficients  $\alpha_{i,j}$  and  $\beta_{i,j}$  are given in Appendix C.

For the Cauchy integral of interest in the present study,  $H$  is given by equation (3.136) and the following second-order accurate formulae were used to approximate  $H_j$  and  $H_j'$ :

$$H_j = \frac{\sin(\frac{\pi}{2}\hat{x}_j)}{2(\Delta\hat{x})} \cdot \{\delta_{j+1}^* U_{e_{j+1}} - \delta_{j-1}^* U_{e_{j-1}}\}, \quad (3.151)$$

$$H_j' = \frac{\pi \cdot \cos(\frac{\pi}{2}\hat{x}_j)}{4(\Delta\hat{x})} \cdot \{\delta_{j+1}^* U_{e_{j+1}} - \delta_{j-1}^* U_{e_{j-1}}\} \\ + \frac{\sin(\frac{\pi}{2}\hat{x}_j)}{(\Delta\hat{x})^2} \cdot \{\delta_{j+1}^* U_{e_{j+1}} - 2 \cdot \delta_j^* U_{e_j} + \delta_{j-1}^* U_{e_{j-1}}\}. \quad (3.152)$$

Other second-order accurate finite-difference representations of  $H_j$  and  $H_j'$  are possible, and several alternatives were tried in the present study. However, no significant differences were observed in the computed results. Note that a singularity-induced displacement-thickness spike eventually occurred in all the interacting cases, and that the difference formula used in equations (3.151) and (3.152) were potentially applied across the "spike". A number of attempts were made to isolate the current streamwise location of the "spike" and to implement sloping difference formulae on either side in preference to (3.151) and (3.152). However, the procedure did not significantly change the results and since it involved much more computation (including recomputing the  $\alpha_{ij}$  and  $\beta_{ij}$  coefficients at each iterate) the algorithm was discontinued.

Next, consider the tail portions of the Cauchy integral in equation (3.143) which were evaluated in terms of the variable  $x$ . Often the tail portion of the Cauchy integral is ignored, but in tests of this procedure on functions such as  $1/(1+x^2)$  this omission was judged to lead to unacceptable error. Consequently, the tail portions of the integral were evaluated in this study analytically using an asymptotic expansion of the integrand. Suppose that the asymptotic expansion for  $F$  in equation (3.143) is given by

$$F \sim \sum_{k=1}^{\infty} \frac{u_k}{x^k} \text{ as } x \rightarrow +\infty, \quad (3.153)$$

and

$$F \sim \sum_{k=1}^{\infty} \frac{l_k}{x^k} \text{ as } x \rightarrow -\infty. \quad (3.154)$$

Upon substitution in equation (3.143) it is easily shown that

$$L_i \sim \sum_{k=1}^{\infty} (u_k a_{i,k} + l_k b_{i,k}), \quad (3.155)$$

where  $a_{i,k}(x_i)$  and  $b_{i,k}(x_i)$  are given by

$$a_{i,k} = \frac{1}{\pi x_i^k} \int_{+R/x_i}^{+\infty} \frac{d\tau}{\tau^k(1-\tau)}, \quad b_{i,k} = \frac{1}{\pi x_i^k} \int_{-\infty}^{-R/x_i} \frac{d\tau}{\tau^k(1-\tau)}, \quad (3.156)$$

for  $x_i \neq 0$  and by

$$a_{i,k} = -\frac{1}{\pi} \int_{+R}^{+\infty} \frac{ds}{s^{k+1}}, \quad b_{i,k} = -\frac{1}{\pi} \int_{-\infty}^{-R} \frac{ds}{s^{k+1}}, \quad (3.157)$$

for  $x_i = 0$ . Expressions for  $a_{i,j}$  and  $b_{i,k}$  are given in Appendix C. Note that it is assumed here that  $|x_i| < R$  and that  $R$  is large enough so that the asymptotic expansions (3.153) and (3.154) give a good representation of  $F(x)$  for  $|x| > R$ .

In the present problem,  $F(x)$  is given by equation (3.133). As  $|x| \rightarrow \infty$ , the solution for  $U$  approaches that Rayleigh solution given by equation (3.64), and therefore  $\delta^*$  will approach a constant value (for fixed  $t$ ) denoted by  $\delta_{\infty}^*$ , i.e.

$$\delta^*(x,t) \rightarrow \delta_{\infty}^* \text{ as } |x| \rightarrow \infty. \quad (3.158)$$

The dominant form of  $Ue$  is

$$Ue(x,t) = \frac{4Y_v}{x^2 + Y_v^2} + O(Re^{-1/2}) \quad (3.159)$$

from equation (3.128), and consequently from equation (3.133)

$$F \sim -\frac{8xY_v(t)\delta_{\infty}^*(t)}{(x^2 + Y_v^2)^2} \text{ as } |x| \rightarrow \infty. \quad (3.160)$$

From this equation it is easily shown that

$$F \sim -8Y_v(t)\delta_{\infty}^*(t)\left\{\frac{1}{x^3}-\frac{2Y_v^2}{x^5}+\dots\right\}, \quad (3.161)$$

and the tail contribution for the present problem is given by equation (3.155), with  $u_1=u_2=u_4=l_1=l_2=l_4=0$ , and

$$u_3 = l_3 = -8Y_v(t)\delta_{\infty}^*(t), \quad u_5 = l_5 = -2Y_v(t)^2 u_3. \quad (3.162)$$

This completes the description of the treatment of the Cauchy integral in equation (3.128), which may now be written

$$\begin{aligned} \frac{1}{\pi} \int_{-\infty}^{+\infty} \frac{1}{(x_i-s)} \frac{\partial}{\partial s} (Ue \cdot \delta^*) ds = \\ \frac{1}{\pi} \sin\left(\frac{\pi}{2} \hat{x}_i\right) \sum_{j=1}^{N-1} \{\alpha_{ij} H_j + \beta_{ij} H_j'\} + u_{i,3}(a_{i,3} + b_{i,3}) + u_{i,5}(a_{i,5} + b_{i,5}). \end{aligned} \quad (3.163)$$

Here,  $H_j$  and  $H_j'$  depend on  $Ue$  and  $\delta^*$  and are given by equations (3.151) and (3.152);  $u_{i,3}$  and  $u_{i,5}$  are given by equation (3.162), and  $\alpha_{ij}$ ,  $\beta_{ij}$ ,  $a_{ij}$  and  $b_{ij}$  are given in Appendix C. The coefficients developed in Appendix C are independent of  $F(x)$  in equation (3.143) and therefore need to be computed only once. On the other hand,  $H_j$ ,  $H_j'$ ,  $u_{i,3}$  and  $u_{i,5}$  depend on time and must be recomputed each time step.

### 3.9 Numerical Solution of the External Flow Problem

The numerical procedures used to solve the four equations (3.125) to (3.128) associated with the external flow problem (developed in §3.7) will be discussed in this section. The solutions of equations (3.125) and (3.126) for

the vortex components  $U_v$  and  $V_v$  and equation (3.127) for the vortex displacement  $Y_v$  were obtained using methods based on the conventional trapezoid rule. The solution of the integro-differential equation (3.128) for the mainstream velocity  $Ue(x,t)$  is more involved and requires use of the second-order method developed in §3.8 to evaluate the Cauchy principal value integral.

The boundary-layer problem is calculated in terms of the streamwise variable  $\hat{x}$  defined by equation (3.50) on the finite interval (0,2), and it is convenient to carry out the solution for the external flow quantities in terms of this same variable. The same discretization was used as for the boundary-layer problem and, with the range (0,2) divided into  $N$  equal intervals of length  $\Delta\hat{x}$ , the mesh points are at

$$\hat{x}_i = i \cdot (\Delta\hat{x}), \quad i=0,1,2, \dots, N. \quad (3.164)$$

Note that the mesh for the outer problem may be selected independently from the choice for the boundary-layer problem, and either a coarser or finer mesh is possible; this point will be discussed subsequently.

At a given time step the first distribution that was calculated was the scaled displacement thickness  $\delta_i^*$ , at each point in the mesh, where

$$\delta_i^* = \delta^*(\hat{x}_i). \quad (3.165)$$

The procedure for the contour integration of  $\delta_i^*$  on contours of constant  $\hat{x}_i$ , using Lagrangian data, is described in Appendix D; note at least  $(N+1)$  contour integrations must be carried out, one for each point in the mesh (3.164). The velocity components and displacement of the vortex were computed next using a method based on the trapezoid rule. Equations (3.125)

and (3.126) may be expressed in terms of the variable  $\hat{x}$  with the results

$$U_v = \frac{1}{Y_v} + \frac{1}{\sqrt{\text{Re} \pi}} \cdot \int_0^2 \tan\left(\frac{\pi}{2}\{1-\hat{x}\}\right) \frac{(\delta^* U_e)'}{\tan^2\left(\frac{\pi}{2}\{1-\hat{x}\}\right) + Y_v^2} d\hat{x}, \quad (3.166)$$

$$V_v = -\frac{Y_v}{\sqrt{\text{Re} \pi}} \cdot \int_0^2 \frac{(\delta^* U_e)'}{\tan^2\left(\frac{\pi}{2}\{1-\hat{x}\}\right) + Y_v^2} d\hat{x}, \quad (3.167)$$

where the prime indicates differentiation with respect to  $\hat{x}$ . The numerical approximations used are of the form:

$$U_v = \frac{1}{Y_v} + \frac{1}{\sqrt{\text{Re} \pi}} \cdot \sum_{i=1}^N \tan\left(\frac{\pi}{2}\{1-\bar{\hat{x}}_i\}\right) \cdot \Phi_i, \quad (3.168)$$

$$V_v = -\frac{Y_v}{\sqrt{\text{Re} \pi}} \cdot \sum_{i=1}^N \Phi_i, \quad (3.169)$$

where

$$\Phi_i = \frac{\delta_i^* \cdot U_{e_i} - \delta_{i-1}^* \cdot U_{e_{i-1}}}{\tan^2\left(\frac{\pi}{2}\{1-\bar{\hat{x}}_i\}\right) + Y_v^2}, \quad (3.170)$$

$$\bar{\hat{x}}_i = (\hat{x}_i + \hat{x}_{i-1})/2, \quad (3.171)$$

and

$$U_{e_i} = U_e(\hat{x}_i). \quad (3.172)$$

The vortex displacement was obtained at any stage by integration of equation (3.127) using a trapezoid rule in time as indicated in equations (3.131).

To obtain the solution of equation (3.128) for  $U_e(\hat{x}_i, t)$ , the integral was approximated using the method described in §3.8, and it is easily shown that a the second-order accurate expression for  $U_{e_i}$  at the  $i$ th internal node is given by

$$\begin{aligned}
Ue_i = & \frac{4Y_v}{\tan^2(\frac{\pi}{2}\{1-\hat{x}_i\}) + Y_v^2} + \frac{1}{\sqrt{Re}\pi} \cdot \sum_{k=1}^5 (a_{i,k} \cdot u_k + b_{i,k} \cdot l_k) \\
& + \frac{\sin(\pi \hat{x}_i/2)}{\sqrt{Re}\pi} \cdot \sum_{j=1}^{N-1} \left( \alpha_{ij} \left( \frac{\sin(\pi \hat{x}_j/2)}{2(\Delta \hat{x})} \{ \delta_{j+1}^* \cdot Ue_{j+1} - \delta_{j-1}^* Ue_{j-1} \} \right) \right. \\
& + \beta_{ij} \left( \frac{\pi \cos(\pi \hat{x}_j/2)}{4(\Delta \hat{x})} \{ \delta_{j+1}^* Ue_{j+1} - \delta_{j-1}^* Ue_{j-1} \} \right. \\
& \left. \left. + \frac{\sin(\pi \hat{x}_j/2)}{(\Delta \hat{x})^2} \{ \delta_{j+1}^* Ue_{j+1} - 2\delta_j^* Ue_j + \delta_{j-1}^* Ue_{j-1} \} \right) \right). \quad (3.173)
\end{aligned}$$

Here, the coefficients  $\alpha_{ij}$ ,  $\beta_{ij}$ ,  $a_{i,k}$ , and  $b_{i,k}$  are the constants given in Appendix C which depend only on the selected mesh. The coefficients  $u_k$  and  $l_k$  are given by (3.162) and depend on  $Y_v$  and  $\delta_\infty^*$ . In equation (3.173) it may be noted that each nodal quantity in  $Ue$  depends on all of the others in the mesh. In addition, the values of  $Ue$  at the endpoints of the interval are given by

$$Ue_0 = Ue_N = 0. \quad (3.174)$$

In principle, equation (3.173) could be solved for the  $Ue_i$  in an iterative manner similar to that discussed in connection with equation (3.134). However, the variations in  $Ue$  eventually become substantial in the narrow region of strong interaction, and iteration was found to be very time-consuming. The alternative approach that was used is a direct inversion procedure. Equations (3.173) define a set of linear algebraic equations for the unknown values of  $Ue_i$  at each mesh point. The problem may be written in matrix form according to

$$(I - M)(\vec{Ue}) = (\vec{F}), \quad (3.175)$$

where  $I$  is the identity matrix.  $M$  is the coefficient matrix defined on the

interior nodes  $0 < (i,j) < N$  by

$$\begin{aligned} M_{i,j} = & \frac{\sin(\pi \hat{x}_i/2)}{\sqrt{\text{Re} \pi}} \cdot \delta_j^* \cdot \left( \alpha_{i,j-1} \left( \frac{\sin(\pi \hat{x}_{j-1}/2)}{2(\Delta \hat{x})} \right) - \alpha_{i,j+1} \left( \frac{\sin(\pi \hat{x}_{j+1}/2)}{2(\Delta \hat{x})} \right) \right. \\ & + \beta_{i,j-1} \left( \frac{\pi \cos(\pi \hat{x}_{j-1}/2)}{4(\Delta \hat{x})} \right) - \beta_{i,j+1} \left( \frac{\pi \cos(\pi \hat{x}_{j+1}/2)}{4(\Delta \hat{x})} \right) + \\ & \left. + \beta_{i,j-1} \left( \frac{\sin(\pi \hat{x}_{j-1}/2)}{(\Delta \hat{x})^2} \right) - 2\beta_{i,j} \left( \frac{\sin(\pi \hat{x}_j/2)}{(\Delta \hat{x})^2} \right) + \beta_{i,j+1} \left( \frac{\sin(\pi \hat{x}_{j+1}/2)}{(\Delta \hat{x})^2} \right) \right). \end{aligned} \quad (3.176)$$

The right side vector  $\vec{F}$  has components

$$F_j = \frac{4Y_v}{\tan^2(\frac{\pi}{2}\{1-\hat{x}_j\}) + Y_v^2} + \frac{1}{\sqrt{\text{Re} \pi}} \cdot \sum_{k=1}^5 (a_{j,k} \cdot u_k + b_{j,k} \cdot l_k), \quad (3.177)$$

again for  $0 < j < N$ , since  $Ue_0 = Ue_N = 0$ . This matrix problem was solved to evaluate  $Ue_i$ ,  $i=1, \dots, N-1$  using LU decomposition with scaled partial pivoting.

In this approach, the number of subdivisions  $N$  is an important practical factor in the computation of  $Ue$ , since an  $(N+1) \cdot (N+1)$  matrix is evaluated and inverted in every iteration of the outer problem. A second feature of the algorithm which becomes computationally burdensome for large  $N$  is the  $(N+1)$  contour integration calculations for  $\delta_i^*$ , since these calculations require a considerable degree of interpolation and many function evaluations. Both of these aforementioned considerations provide incentive to use an increased value of  $\Delta \hat{x}$  (and reduce  $N$ ) in the mesh selected for the external calculation. However, as strong interactions begin to take place it is desirable to have as much resolution in the outer problem as is practical. It is important to realize that there is no "natural" discretization of the outer problem when the boundary-layer problem is computed in Lagrangian variables. In parallel test studies of  $\text{Re}=10^6$ , the discretization of the outer problem was set to  $\Delta \hat{x} = \Delta \hat{\xi}$



in a first test and  $\Delta\tilde{x}=2\cdot\Delta\hat{\xi}$  in the second; here  $\Delta\hat{\xi}$  denotes the mesh length associated with the calculation of the boundary-layer problem. The results for these two test studies were virtually indistinguishable. For all the results presented in this study, the mesh length associated with the outer problem was

$$\Delta\tilde{x}=\Delta\hat{\xi}. \quad (3.178)$$

It was not possible to use smaller mesh lengths for the outer problem because there was not sufficient computer memory to invert a larger matrix.

## 4. THE LIMIT PROBLEM $Re \rightarrow \infty$

### 4.1 Introduction

Calculated results for the vortex-driven boundary layer for the limit problem  $Re \rightarrow \infty$  will be discussed in this chapter. Results obtained using interacting boundary-layer theory for finite, but large, Reynolds numbers will be discussed in Chapter 5. There are several reasons why the limit problem merits a separate discussion. First, numerical solutions have previously been obtained by Walker (1978) using a Eulerian formulation up until a time of about  $t=0.75$ , at which point it proved difficult to continue the integrations with good accuracy; these results provided a good check on the accuracy of the Lagrangian algorithm developed in this study. A second objective of the limit calculation was to determine the subsequent flow evolution beyond  $t=0.75$  when the Eulerian computation failed (Walker, 1978). Finally, it is of interest to confirm that a separation singularity does evolve, and to identify the time  $t_s$  and the location  $x_s$  at which it occurs; this information is required in Chapter 5 to compare the interacting results with the asymptotic structure of the onset of interaction indicated by the work of Elliott, Cowley and Smith (1983).

The principal difference between the limit problem discussed in this Chapter and the interacting boundary-layer analysis to be discussed in Chapter 5 is that in the former the pressure distribution is steady while in the latter the pressure changes with time, due to the evolving boundary-layer displacement thickness  $\delta^*(x,t)$ . With the evolution of a recirculating eddy in the boundary-layer flow, a rapidly-growing "hill" having thickness  $O(Re^{-1/2})$  develops in the displacement surface  $\delta^*$ ; in an interactive calculation this growth induces a localized unsteady pressure response in the external flow which then subsequently influences the boundary-layer development. On the

other hand, for the limit problem  $Re \rightarrow \infty$ , the boundary layer appears as a region of zero thickness which does not influence the external flow; thus the vortex convects with constant speed and at constant height above the wall, and the imposed pressure-gradient distribution is invariant with time.

Numerical integrations of the limit boundary-layer problem have been carried out using an Eulerian formulation by Walker (1978), and a similar approach (described in §3.2) was used in the present study to advance the solution from  $t=0$  to  $t=0.25$ . The separation time of  $t_s \simeq 0.28$  found by Walker (1978) (defined as the first appearance of a closed recirculating eddy) was confirmed by the present Lagrangian calculations. The subsequent growth and motion of the eddy has been described in some detail by Walker (1978), who noted that the eddy first grows rapidly in the streamwise direction and then experiences pronounced growth normal to the wall. There is a consequent rise in the boundary-layer thickness and the temporal development of displacement thickness is shown in figure 4.1 which has been reproduced from Walker (1978). It is evident that by  $t=0.7$ ,  $\delta^*$  is approaching a vertical variation near  $\hat{x}=1$ , which corresponds to a streamwise location directly beneath the vortex.<sup>1</sup> Calculations in the Eulerian frame became progressively more difficult for  $t>0.6$  (Walker, 1978) owing to the severe variations that developed in the velocity field near  $x=0$ ; eventually, for  $t>0.75$ , sharp "spikes" were observed in the streamlines and displacement thickness near  $x=0$ . At the time, it was remarked (Walker, 1978) that "whether or not this is a real feature of the flow development for  $t>0.75$  is not known." The work of Van Dommelen and Shen (1980) and Van Dommelen (1981) on the impulsively-started circular cylinder subsequently showed that the "spiking" observed by Walker (1978) is likely to be attributable to the

---

<sup>1</sup>Note that, in figure 4.1, the transformed coordinate defined by equation (3.12) is used. This has the effect of emphasizing the region immediately under the vortex ( $-\sqrt{3}<x<\sqrt{3}$ ). In this study, the results will generally be presented in terms of the physical coordinate  $x$ .

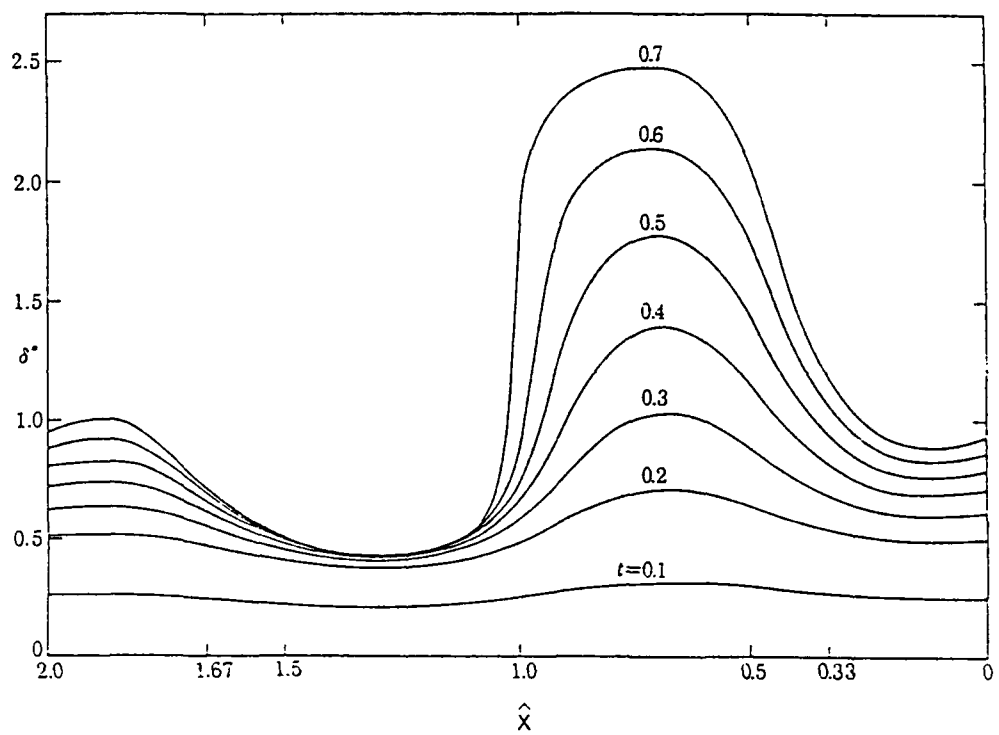


Figure 4.1. Temporal development of displacement thickness:  
limit problem (from Walker, 1978).

onset of a singularity at finite time; furthermore, it is the signature of the start of a boundary-layer eruption. At the same time, it is evident that the Eulerian calculation cannot be carried on with good accuracy anywhere near the terminal state (except, perhaps, using some kind of adaptive grid that changes with time as the boundary layer focuses toward an eruption). Consequently, the integrations were continued in the present study using a Lagrangian algorithm; specific details of the calculations are described in §4.2. It was found that a separation singularity does form in finite time, and the method used to estimate this time  $t_s$  is discussed in §4.3. The computed results are presented in §4.4 and a discussion of these results follows in §4.5.

## 4.2 Numerical Methods

The computational algorithms for the limit problem have been discussed in Chapter 3 (see, for example, §3.2 and §3.4). In this section the values of the numerical mesh sizes used in the integration will be described, as well as the convergence criterion. Three sets of mesh sizes were used as a check on the accuracy, having the following number of points: [61x41], [101x61] and [201x101], which will be denoted here as mesh (1), (2), and (3); here, the first number denotes the number of points in the streamwise direction while the second corresponds to points across the boundary. The mesh was uniform in the variables  $\hat{x}$  and  $\hat{\zeta}$ , defined by equations (3.13) and (3.24) respectively, and consequently for the smallest mesh size used, there were 200 equal intervals in  $\hat{x}$  and 100 in  $\hat{\zeta}$ . Note that in physical space (i.e.  $x$  and  $\zeta$ ) the mesh is highly non-uniform and that the transformations (3.13) and (3.24) generally tend to concentrate the mesh in the immediate vicinity of the vortex and close to the wall, respectively. As discussed in §3.2, the Eulerian calculation was continued to  $t_0=0.25$ , at which point the Lagrangian algorithm, described in §3.4, was implemented. Note that  $t_0=0.25$  is a time that is convenient to switch from

one formulation to another; however, the value of  $t_0$  is arbitrary and a number of test runs using different values of  $t_0$  confirmed that the particular value of  $t_0$  used has no effect on the subsequent results. At the switchover to the Lagrangian method, the new independent variables  $(\hat{\xi}, \hat{\eta})$  defined by equations (3.50) and (3.51) are readily obtained from the Eulerian mesh; the calculation continues on in Lagrangian variables defined on a uniform mesh.

The calculations were carried out in double precision on a VAX/8350 computer. The ADI method described in §3.5 was used to advance the solution forward in time, and at each time step an iteration was carried out until the solution for  $U$  had converged to four significant figures at each point in the mesh. If  $U_{ij}^k$  is the  $k$ th iterate for velocity at the  $(ij)$  node in the mesh, the convergence criterion used was

$$\left| \frac{U_{ij}^k - U_{ij}^{k-1}}{U_{ij}^{k-1}} \right| < 10^{-4}, \quad (4.1)$$

for all  $(ij)$ . In a typical calculation, three to seven iterations of the ADI method are required (an iteration consists of one sweep along lines of constant  $\hat{\eta}$  and another along lines of  $\hat{\xi}$ ) before convergence was considered to have occurred in the current time plane. As the iteration proceeded, the displacements  $\hat{x}(\hat{\xi}, \hat{\eta}, t)$  were evaluated concurrently as described in §3.6 and, in principle, a convergence test could also be carried out for the  $\hat{x}_{ij}$ . A convergence check similar to equation (4.1) was initially used for the  $\hat{x}_{ij}$ ; however this additional precaution was found to be unnecessary and, because it requires additional computational time, convergence testing on  $\hat{x}_{ij}$  was eventually abandoned. The reason for this may be inferred from equation (3.57). If  $\Delta U_{ij}$  denotes the change in  $U_{ij}$  at node  $(ij)$  in a given time interval  $\Delta t$ , the corresponding change in  $\hat{x}_{ij}$  is  $O(\Delta U_{ij} \cdot \Delta t)$ ; since the time step  $\Delta t$  was always selected to be very small, the changes in  $\hat{x}$  at any given node are always much smaller than the corresponding variations in  $U$  during a specific

time step. Consequently the test (4.1), which in any case is a rather restrictive test for  $U$ , was considered to be more than adequate as an overall convergence criterion.

In the initial stages of the integrations, the time step was taken equal to 0.001 and was then reduced during the course of a calculation (and in particular near  $t=t_s$ ) in order to keep the total number of iterations to a moderate level. The time steps used in the three mesh sizes are summarized in table 4.1.

time	Mesh 1 (61X41)	Mesh 2 (101X61)	Mesh 3 (201X101)
0.2500	0.0100	0.0010	0.0010
0.5500	0.0010	0.0010	0.0010
0.7500	0.0010	0.0010	0.0005
0.8250	0.0010	0.0010	0.0002
0.8600	0.0005	0.0005	0.0002
0.9000	0.0005	0.0005	0.0002
0.9500	0.0005	0.0005	0.0001

Table 4.1. Time steps used in the integrations. Up to  $t=0.25$  the Eulerian method was used; beyond  $t=0.25$  all integrations were based on the Lagrangian method. To interpret the table note, for example, that for Mesh 3 the time step until  $t=0.55$  was 0.001. and for  $0.55 \leq t \leq 0.75$  the time step  $\Delta t=0.0005$ .

The calculations were terminated when it was believed that a singularity had evolved in the boundary-layer solution (c.f. §2.4). The best estimate of this time is  $t_s=0.989$  and the means of determining  $t_s$  will be discussed in the next section. It is worthwhile to note that no catastrophic instability or

breakdown of the numerical scheme used to integrate the Lagrangian boundary-layer equations occurs as  $t \rightarrow t_s^-$ . In fact, because the distributions of  $\hat{x}$  and  $U$  are regular, the integrations for these quantities may be carried on without complication beyond  $t_s$ .

### 4.3 Determination of $t_s$

A singularity in the  $y$ -position develops (as discussed in §2.4 and §2.5) when a stationary point develops in the  $x$ -position field. In this study, a norm of the gradient was defined by

$$|\nabla x|^2 = \left(\frac{\partial x}{\partial \xi}\right)^2 + \left(\frac{\partial x}{\partial \eta}\right)^2, \quad (4.2)$$

and the location  $(\xi_s, \eta_s)$  and the time of formation of the singularity was estimated by determining where and when

$$|\nabla x| \rightarrow 0, \quad (4.3)$$

for the first time. To understand how the stationary point forms, it is useful to plot the development of the level curves in  $x$  for the model problem. The variable  $\xi$  is defined as the streamwise location  $x$  of each fluid particle at the start of the calculation at  $t=t_0$  (in this case,  $t_0=0.25$ ). Thus, at the start of any Lagrangian computation, since  $x(\xi, \eta, t_0)=\xi$ , it follows that

$$|\nabla x| = 1, \quad t = t_0, \text{ all } \xi, \eta \quad (4.4)$$

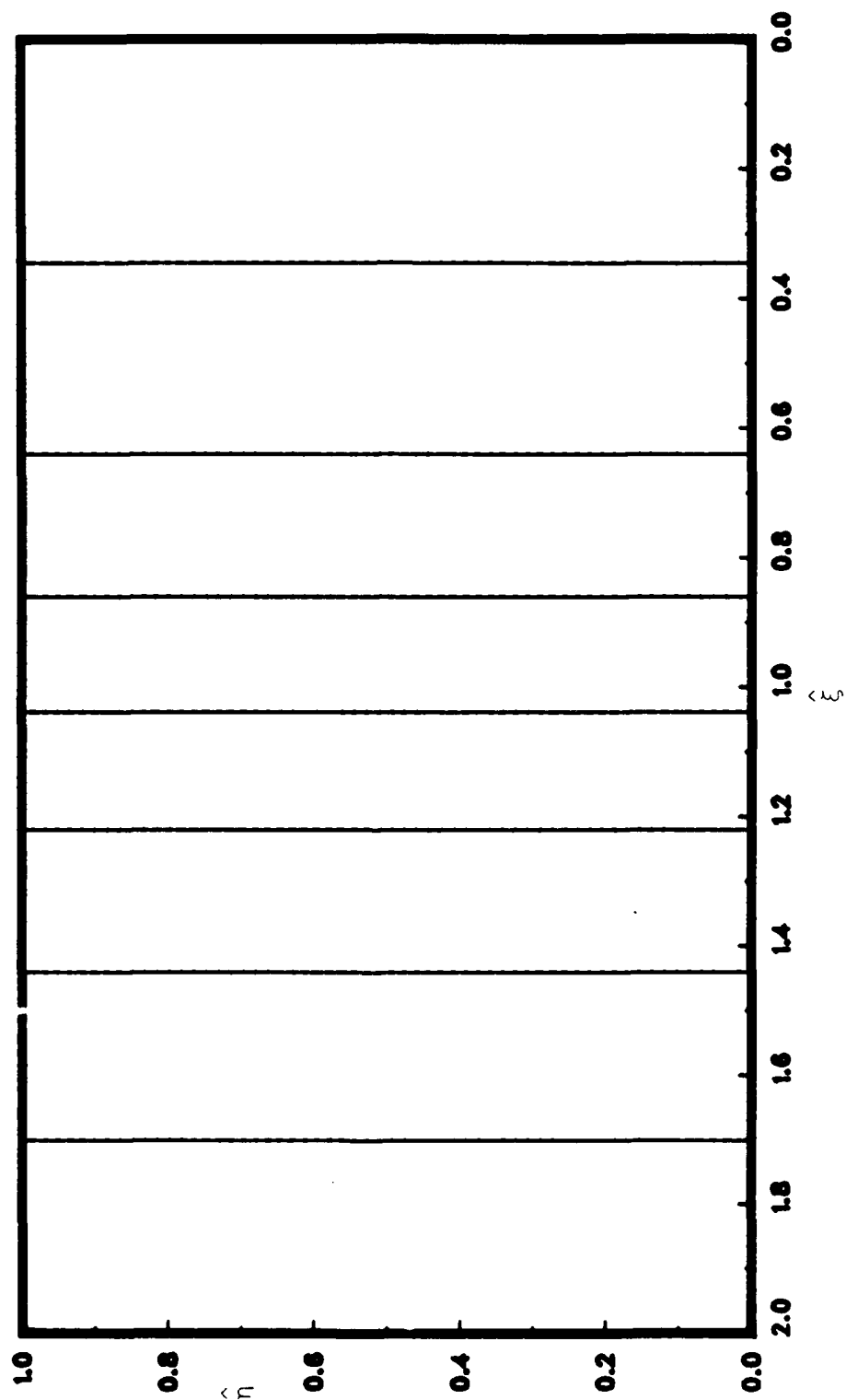
and curves of constant  $x$  appear as vertical straight lines; these initial contours are shown in figure 4.2(a). As  $t$  increases the lines of constant  $x$  distend, as shown in figure 4.2(b) at  $t=0.45$ . It should be noted that the physical



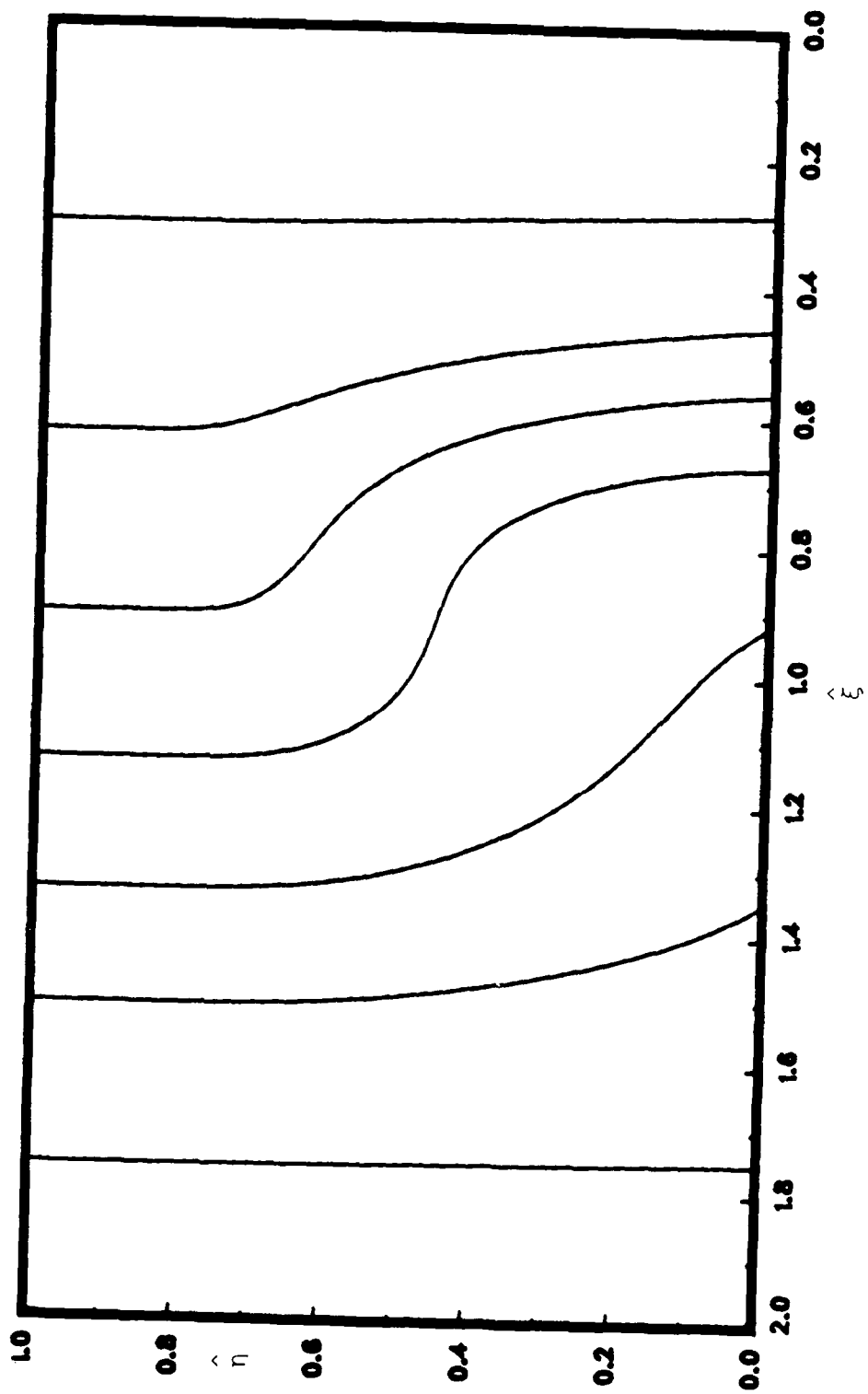
interpretation of these contours in that they represent the initial starting location of a line of fluid particles which have now all arrived at constant  $x$ . In the model problem, the one location where the displacement of the fluid particles is known *a priori* is the wall; fluid particles initially on the wall remain there and are transported to the left with constant velocity  $-1$  in the vortex frame. Near upstream and downstream infinity ( $\hat{\xi}=0,2$ )  $Ue \rightarrow 0$ , and the fluid particles experience an almost constant drift to the left; thus the constant  $x$  contours are therefore almost straight lines. On the other hand, in the region under the vortex, substantial distension in the constant  $x$  lines may be noted. In this region, it is evident that the fluid particles have experienced a drift to the right which is most pronounced in the upper part of the boundary layer; this is consistent with the anticipated action of the mainstream velocity given by equation (1.56).

As  $t$  increases, the trend observed in figure 4.2(b) persists and may be observed in figures 4.2(c) and 4.2(d) at  $t=0.75$  and  $t=0.85$ , respectively. By  $t=0.85$ , a small "thumb-like" region has formed in the constant  $\hat{x}$  contours, which may only be accessed by constant  $\hat{x}$  contours in a small range near  $\hat{\xi}=0.75$ . It is within this "thumb" that a stationary point finally develops at  $t_s=0.989$  in the location indicated on figure 4.2(e).

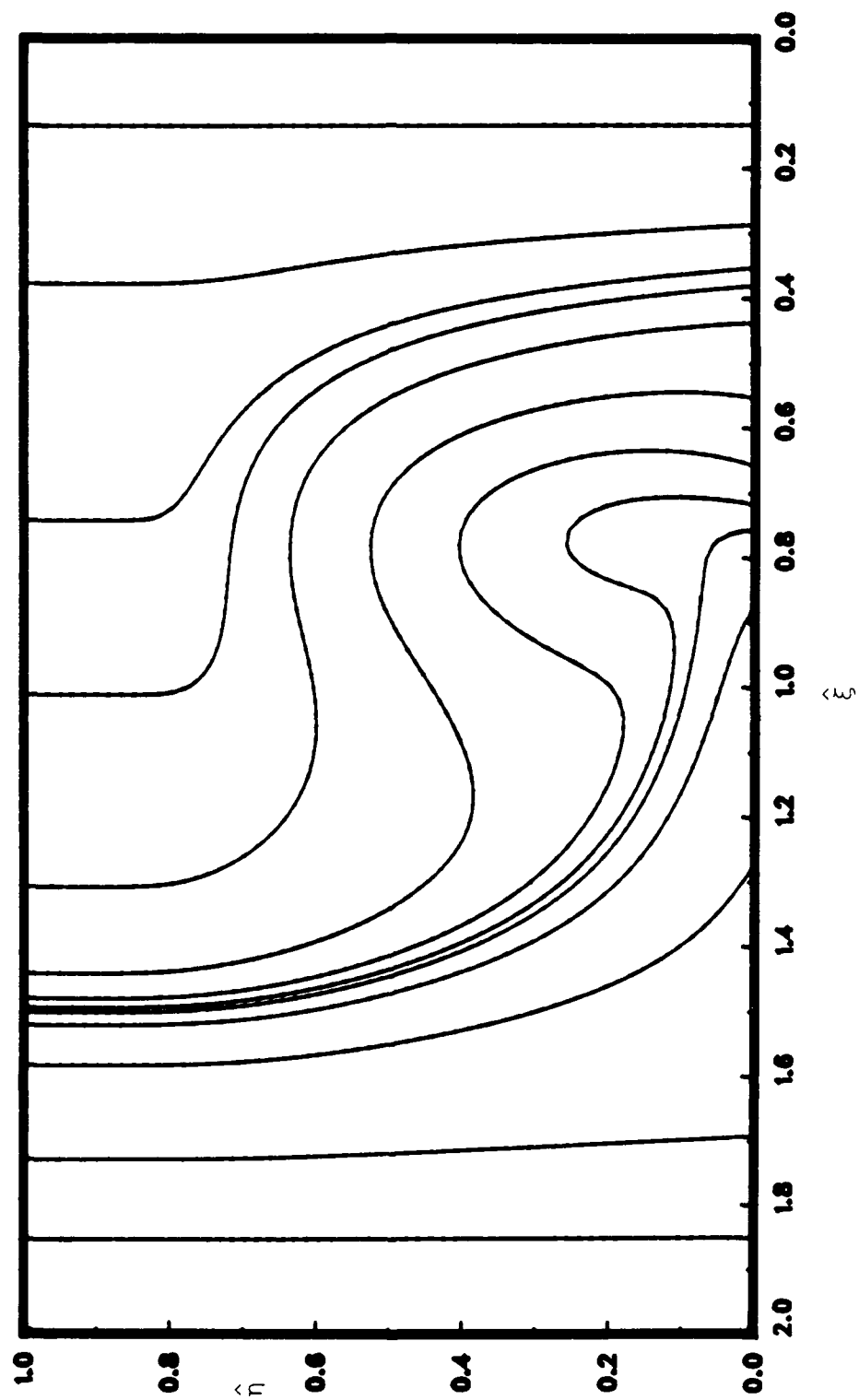
Although the criterion (4.3) for the occurrence of a singularity is well defined, there are a number of practical numerical difficulties associated with estimating where and when in  $(\xi, \eta)$ -space the singularity actually occurs. In this study three methods were used to estimate  $t_s$ , two of which were based (in part) on tracking the point where the norm of the gradient of  $x$  is a



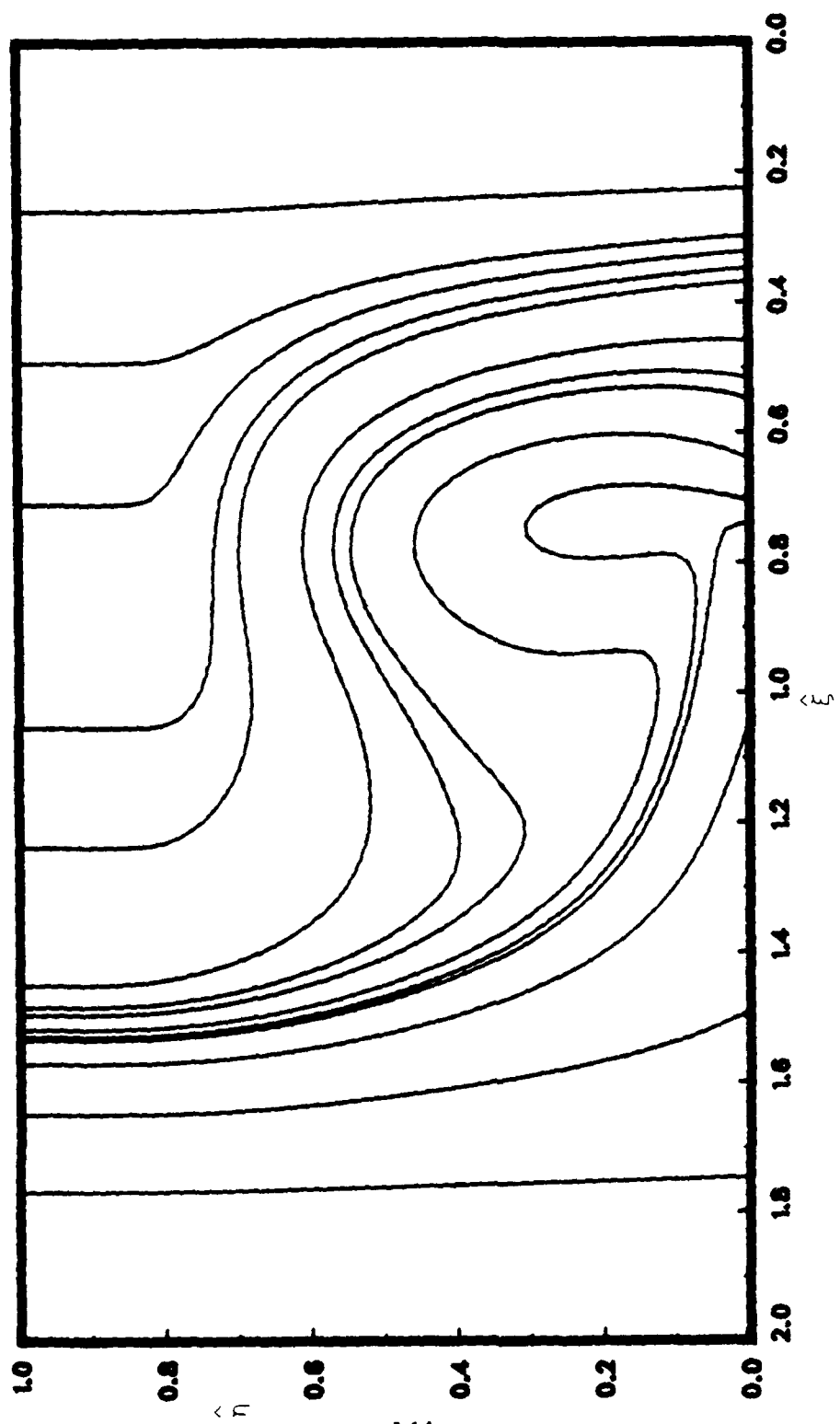
4.2(a)  $t = 0.25$ , the start of the Lagrangian calculation  
 Figure 4.2 The evolution of lines of constant  $x$  for the limit problem.



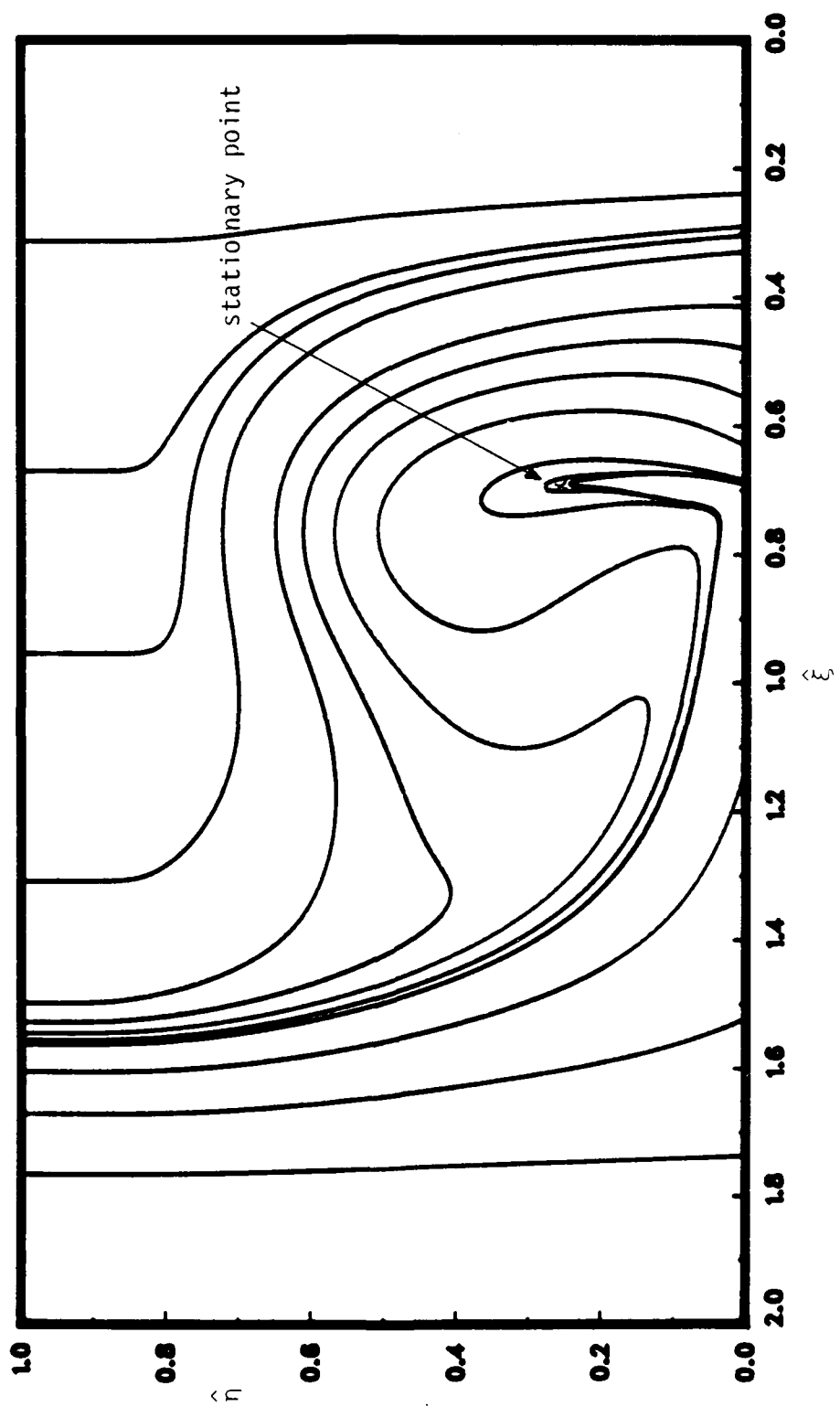
4.2(b)  $t = 0.45$



4.2(c)  $t = 0.75$



4.2(d)  $t = 0.85$



4.2(e)  $t = t_s = 0.989$

minimum. The calculations were carried out in terms of the transformed variables  $\hat{\xi}$ ,  $\hat{\eta}$ , and  $\hat{x}$  defined by equation (3.50) and (3.53), and it proved convenient to work in terms of a gradient-norm function  $\mathcal{N}$  defined by

$$\mathcal{N} = \left( \frac{\partial \hat{x}}{\partial \hat{\xi}} \right)^2 + \left( \frac{\partial \hat{x}}{\partial \hat{\eta}} \right)^2. \quad (4.5)$$

It is easily verified that  $\partial x / \partial \xi = 0$  and  $\partial x / \partial \eta = 0$  when

$$\frac{\partial \hat{x}}{\partial \hat{\xi}} = \frac{\partial \hat{x}}{\partial \hat{\eta}} = 0, \quad (4.6)$$

and vice versa; thus  $|\nabla x| \rightarrow 0$  as  $\mathcal{N} \rightarrow 0$ . At any fixed value of  $t$  during the course of the computation, the first derivatives of  $\hat{x}$  with respect to  $\hat{\xi}$  and  $\hat{\eta}$  were evaluated at all interior mesh points using conventional central-difference approximations; a value of  $\mathcal{N}$  was then computed at each mesh point. A search through the mesh located the minimum value of  $\mathcal{N}$  and the associated mesh point at say,  $(I, J)$ . As the  $\hat{x}$ -field develops a stationary point

$$\min(\mathcal{N}) \rightarrow 0 \quad \text{as } t \rightarrow t_s, \quad (4.7)$$

and consequently the exact location of the minimum is of interest (at any  $t$ ) as well as the value of  $\mathcal{N}$  at that stage. Since  $\hat{x} = \hat{\xi}$  at  $t = t_0$  for all  $(\hat{\xi}, \hat{\eta})$ ,  $\mathcal{N}$  is initially unity everywhere; as  $t$  increased an absolute minimum developed in the distribution of  $\mathcal{N}$ , which subsequently was observed to decrease monotonically. It is noted in passing that initially the calculations were also carried out in which the minimum of the function on the right hand side of equation (4.2) was found at each time step; however this requires a transformation back to the variables  $(\xi, \eta)$  and  $x$  and was finally judged to be less accurate, as well as less convenient, than seeking the minimum of the function  $\mathcal{N}$  defined by equation (4.5).

In general the minimum value of  $N$  will not occur exactly at a mesh point, and to refine the estimate of the location of the minimum, the function  $N$  was represented near the minimum node in the grid at  $(I,J)$  by a local quadratic surface. The formula used for this purpose involves the functional value of  $N$  at  $(I,J)$  and five surrounding points, and is given in Appendix E. This procedure represents the surface for  $N$  as a local Taylor series about the point  $(I,J)$  and contains terms through second order; in effect the surface is represented locally as a paraboloid. This method accurately identifies the  $(\hat{\xi}, \hat{\eta})$  location where  $N$  is a minimum at any time  $t$ , and eventually gives the location of the singularity  $(\hat{\xi}_s, \hat{\eta}_s)$  as  $t \rightarrow t_s$ . However, it is difficult to estimate  $t_s$  precisely with this approach for the following reason. The quantity  $N$  is, by definition, non-negative for all  $t$  and the singularity occurs when  $N$  first touches the plane  $N=0$ . The gradients in equation (4.5) were evaluated numerically and because of discretization error will never be exactly zero. Consequently, although this procedure was found to be useful for indicating an approximate value of  $t_s$ , a refined estimate is not possible with this method.

A second technique for estimating  $t_s$  was used in this study, and is based on a graphical approach wherein the value of  $t_s$  was bracketed within a range of  $t$ . At any time, contours of constant  $\hat{x}$  may be evaluated using the integration procedures discussed in Appendix D. As the minimum in  $N$  approaches zero, a stage is reached where the minimum does not show further decrease and at this point the surface for  $N$  begins to flatten and spread; thus an expanding region where  $N$  is almost zero begins to develop. This zone shows up in a plot of contours of constant  $\hat{x}$  as an area near the tip of the "thumb" in figure 4.2(e), which is very difficult to enter along a characteristic curve of  $\hat{x}$  constant. As  $t$  increases, this zone of "flat" but small  $N$  expands; this is an indication that the singularity has evolved at a previous time and that now  $t > t_s$ . In general the identification of a "flat" zone is somewhat subjective; in addition, the process is necessarily interactive and involves



examination of graphs of several closely-space time planes of data in order to bracket the value of  $t_s$  within a range of  $t$ . This method of estimating  $t_s$  is extremely tedious, and since it not highly accurate was used basically as a check on a third (and more reliable) method for computing  $t_s$ .

The final method used in this study to estimate  $t_s$  is based on computing the distance between the location in the minimum in  $N$ , at any stage, and the zero vorticity line. As discussed in §2.3 and §2.4 in connection with the MRS model, the singularity forms on the zero-vorticity line at finite time and consequently the minimum in  $N$  is expected to eventually move to a location where  $\partial u / \partial y = 0$ . This expectation was confirmed in the present study and this approach is regarded as the best and most reliable method for determining  $t_s$ . The details of the numerical procedure are described in Appendix E. The algorithm was found to produce results for  $t_s$  which were entirely consistent with the graphical method described earlier.

The best estimate of  $t_s$  is based on the smallest mesh size used (c.f. table 4.1) and is

$$t_s = 0.989, \quad (4.8)$$

which is also consistent with the values obtained on the other two meshes. The best estimate of the location of the singularity is  $\hat{x}_s = 1.134$ , and this corresponds to a streamwise location in the physical coordinate  $x$  of

$$x_s = -0.214. \quad (4.9)$$

The drift velocity of the "dead-water zone" associated with the terminal boundary-layer solution described in §2.5 may be calculated by evaluation of  $U(\hat{\xi}, \hat{\eta}, t)$  at  $(\hat{\xi}_s, \hat{\eta}_s, t_s)$ . The details are given in Appendix E and the best estimate for  $K$  (c.f. equation (2.19)) is

$$K = 0.521 . \quad (4.10)$$

Since  $K > 0$ , the "dead-water region" is moving from right to left and in a direction opposite to the local mainstream velocity. Consequently, this situation corresponds to what Van Dommelen (1981) has referred to as "upstream-slipping separation".

#### 4.4 Calculated Results

The early flow development for the limit problem has been described in detail by Walker (1978) and, for completeness, a brief synopsis will be given here. The nature of the flow evolution may be understood through examination of the instantaneous streamline patterns as time progresses. In order to plot the streamlines in a frame of reference which convects with the vortex, define an unsteady streamfunction by

$$u = \frac{\partial \Psi}{\partial y}, \quad (4.11)$$

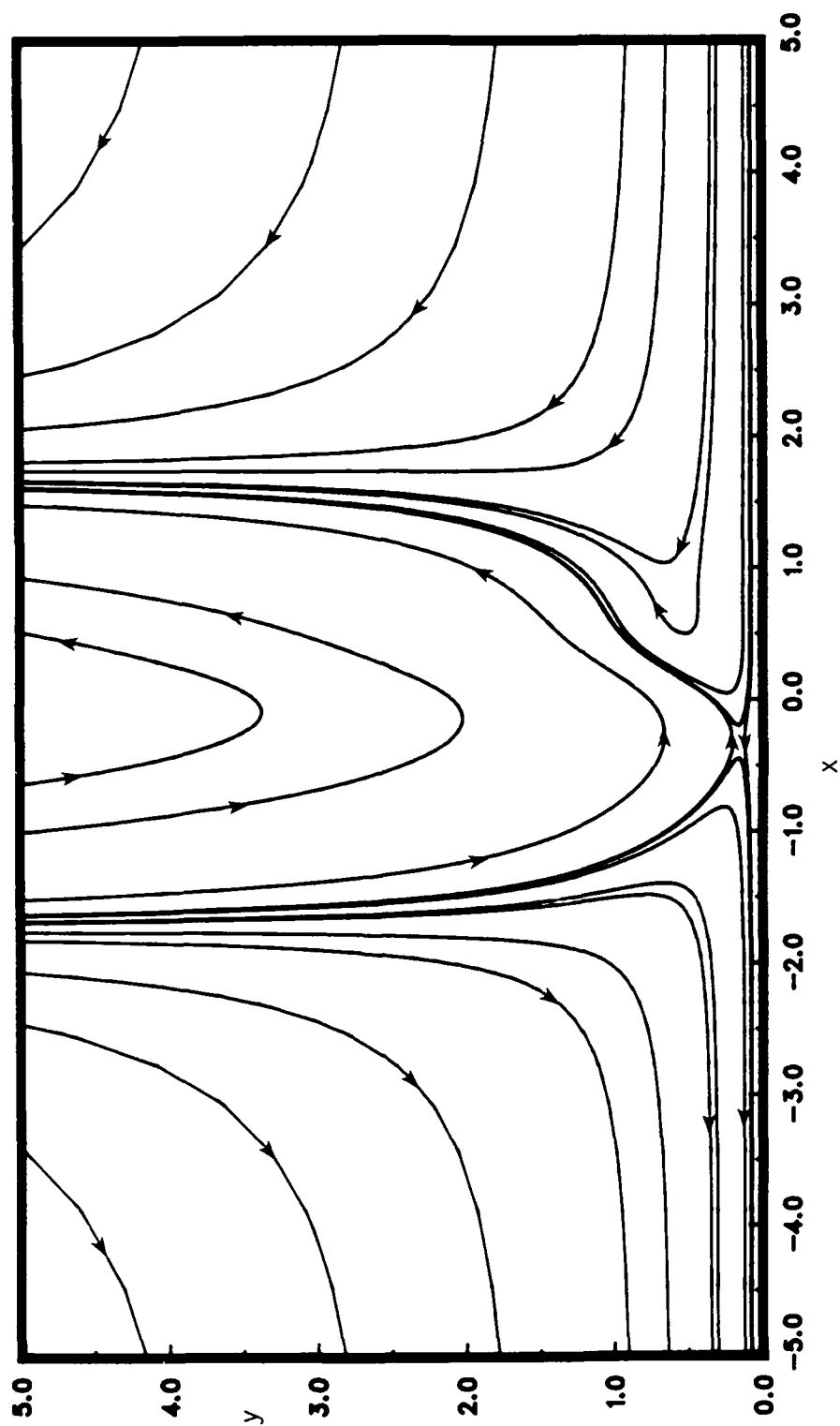
where  $u$  in the moving vortex frame is given by

$$u = -1 + Ue(\hat{x}) \cdot U(\hat{\xi}, \hat{\eta}, t), \quad (4.12)$$

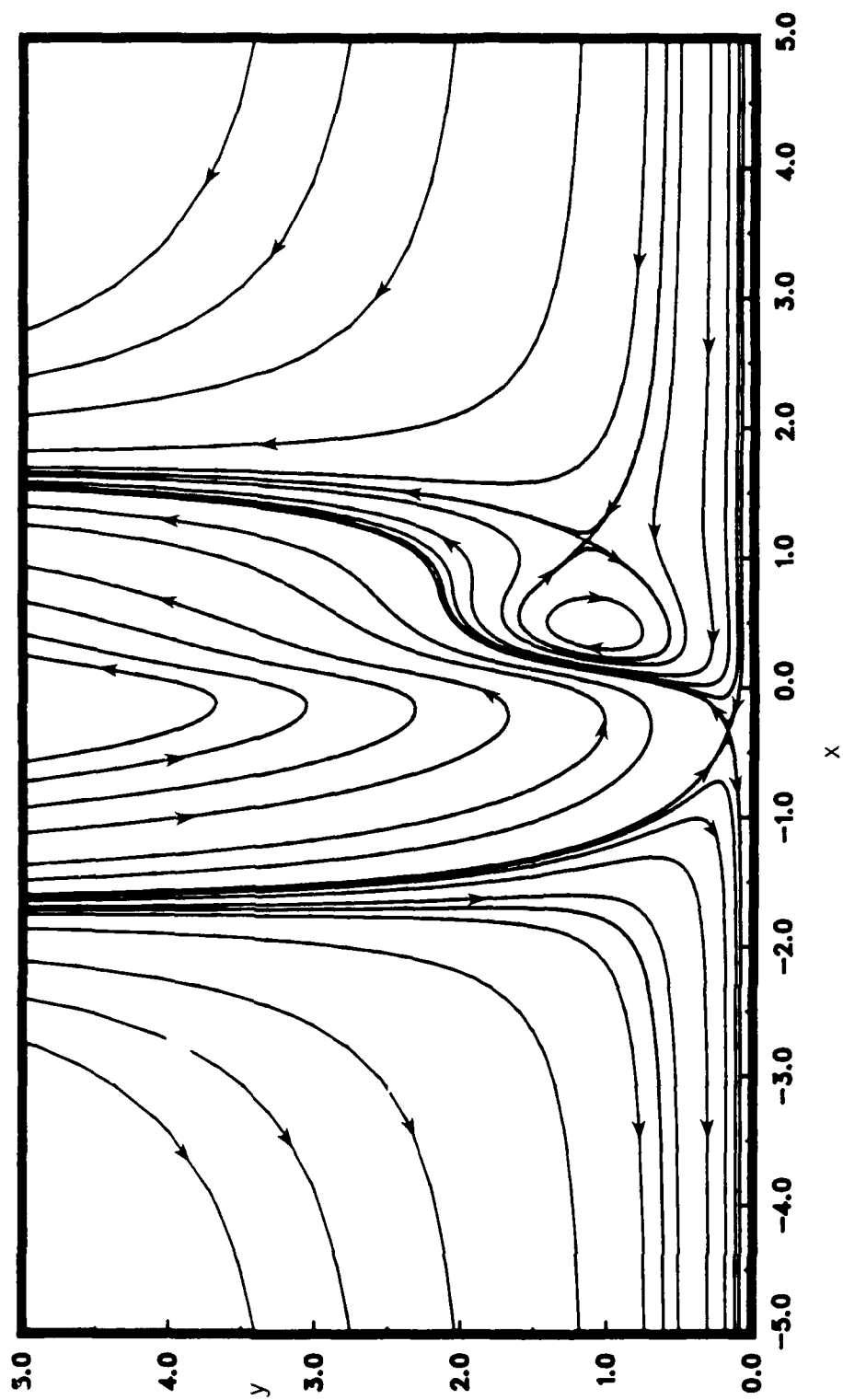
and  $Ue$  is given by equation (3.14). Here it is assumed that  $U$  is known at any time  $t$  as a function of the Lagrangian variables  $(\hat{\xi}, \hat{\eta})$ . In order to compute  $\Psi$  at points in the flow field it is necessary to integrate equation (4.12) along a contour of constant  $\hat{x}$ ; the numerical method used for this is described in Appendix D. To plot the instantaneous streamlines, values of  $\Psi$  were obtained at each point in a selected mesh in  $(\hat{x}, \hat{y})$  using the procedure

outlined in Appendix D; from this information contours of constant  $\Psi$  were evaluated.

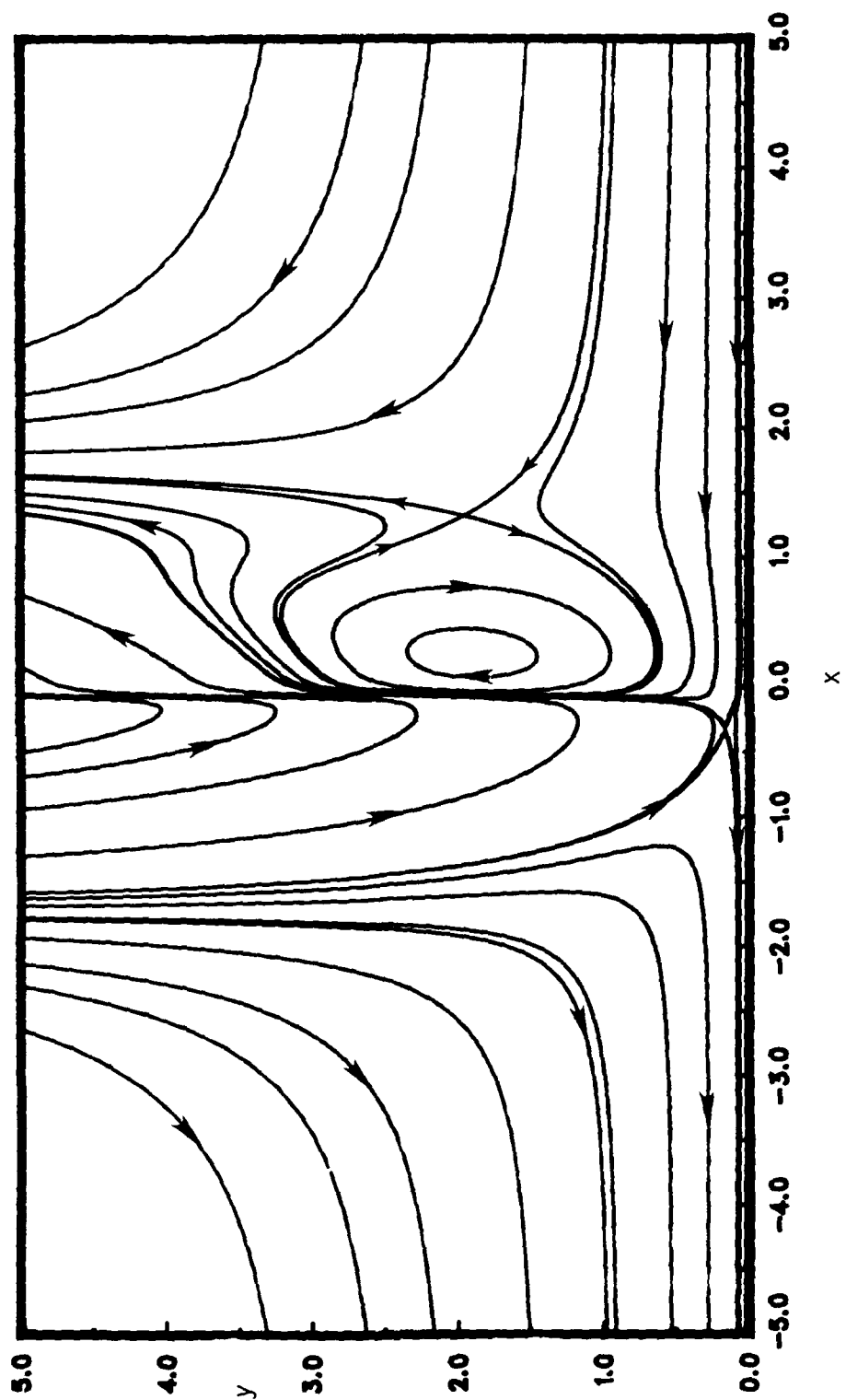
The instantaneous streamlines at  $t=0.25$  are shown in figure 4.3(a) in a frame of reference convecting with the vortex. Note that the results are presented in terms of the physical coordinate  $x$  and the boundary-layer coordinate  $y$ . At this stage the flow patterns are almost symmetrical, consisting of: (1) motion from upstream infinity upward and toward the outflow stagnation point at  $x=\sqrt{3}$ ; (2) motion downward and away from the inflow stagnation point at  $x=-\sqrt{3}$ ; and (3) an inflow, then outflow, underneath the vortex itself. The wall is moving to the left in this frame with a constant speed of unity and there is one stagnation point in the boundary layer near  $x=-0.3$  just above the wall. A recirculating eddy appears in the boundary-layer streamline patterns at  $t=0.281$  (Walker, 1978) and may be observed at a later stage of development at  $t=0.45$  in figure 4.3(b). Once the eddy forms at  $t=0.281$ , it grows rapidly in the streamwise direction and then starts to thicken in a direction normal to the wall. This trend may be observed in figure 4.3(c) at  $t=0.75$ . Note that the streamlines on the left side of the eddy run very close together and this is an indication of an intense variation that is developing in the flow field there. From a physical standpoint, the recirculating eddy produces a blocking effect in the boundary-layer flow. The external pressure gradient below the vortex continually forces the boundary-layer fluid from left to right; eventually, the flow is deflected upward as it is forced to pass over the expanding zone of recirculation. This "blocking" effect gives rise to increasing normal velocities near the left side of the eddy and the progressive formation of what appears to be a developing vertical shear layer on a scale where  $x$  is  $O(1)$ . This is consistent with the generic terminal boundary-layer structure described in §2.5. The streamlines at  $t=t_s=0.989$  are shown in figure 4.3(d), where a continuation of the aforementioned trends should be noted. Note that in the interval from  $t=0.45$



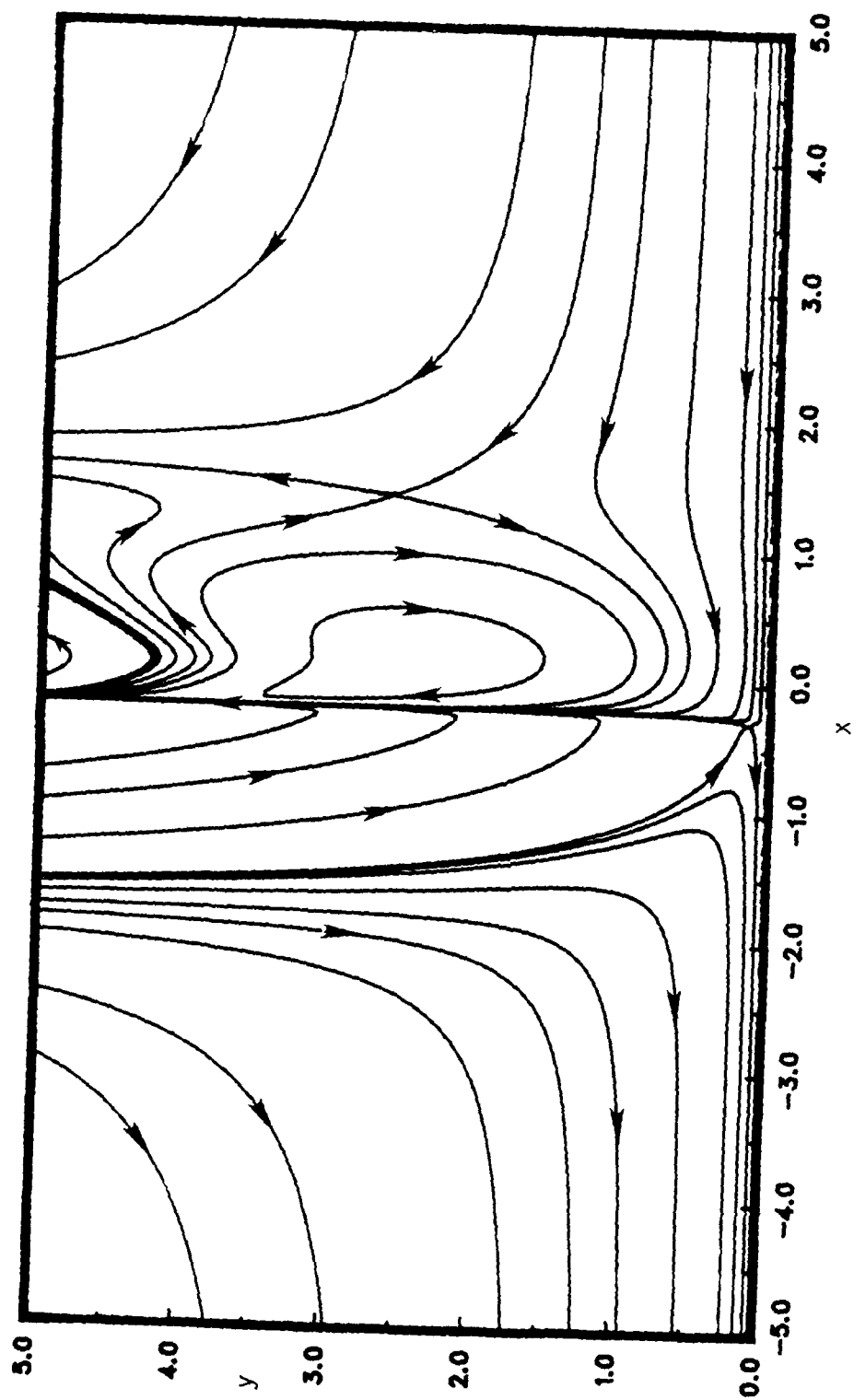
4.3(a)  $t = 0.25$   
 Figure 4.3. Temporal development of the instantaneous streamline patterns.



4.3(b)  $t = 0.45$



4.3(c)  $t = .75$



4.3(d)  $t = t_s = 0.989$

to  $t=0.989$  the eddy has doubled in width but is almost four times thicker in the vertical direction; the eddy is also lifting off the wall with the center moving from  $y_c \simeq 1.0$  to  $y_c \simeq 2.5$ . A new feature that has developed somewhat before this stage is that the streamlines at the top of the eddy have developed a "spike" as the recirculation zone is being drawn into the region of intense variation near  $x_s = -0.214$ .

A displacement thickness  $\delta^*$  may be defined in terms of the instantaneous velocity distributions in laboratory frame of reference according to

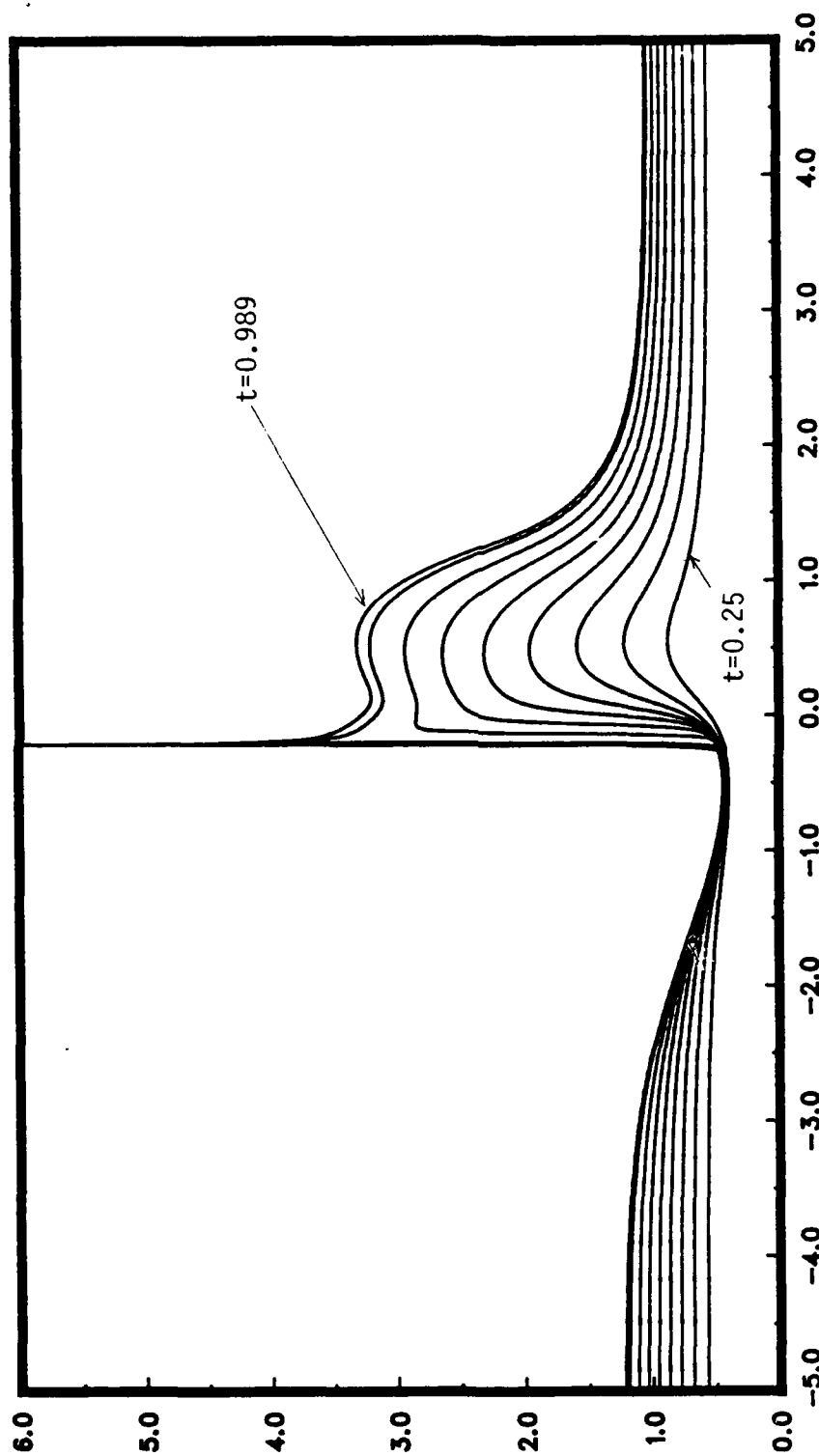
$$\delta^* = \int_0^{+\infty} \left\{ 1 - \frac{u+1}{Ue(x)} \right\} dy, \quad (4.13)$$

and it follows from equation (3.48) that

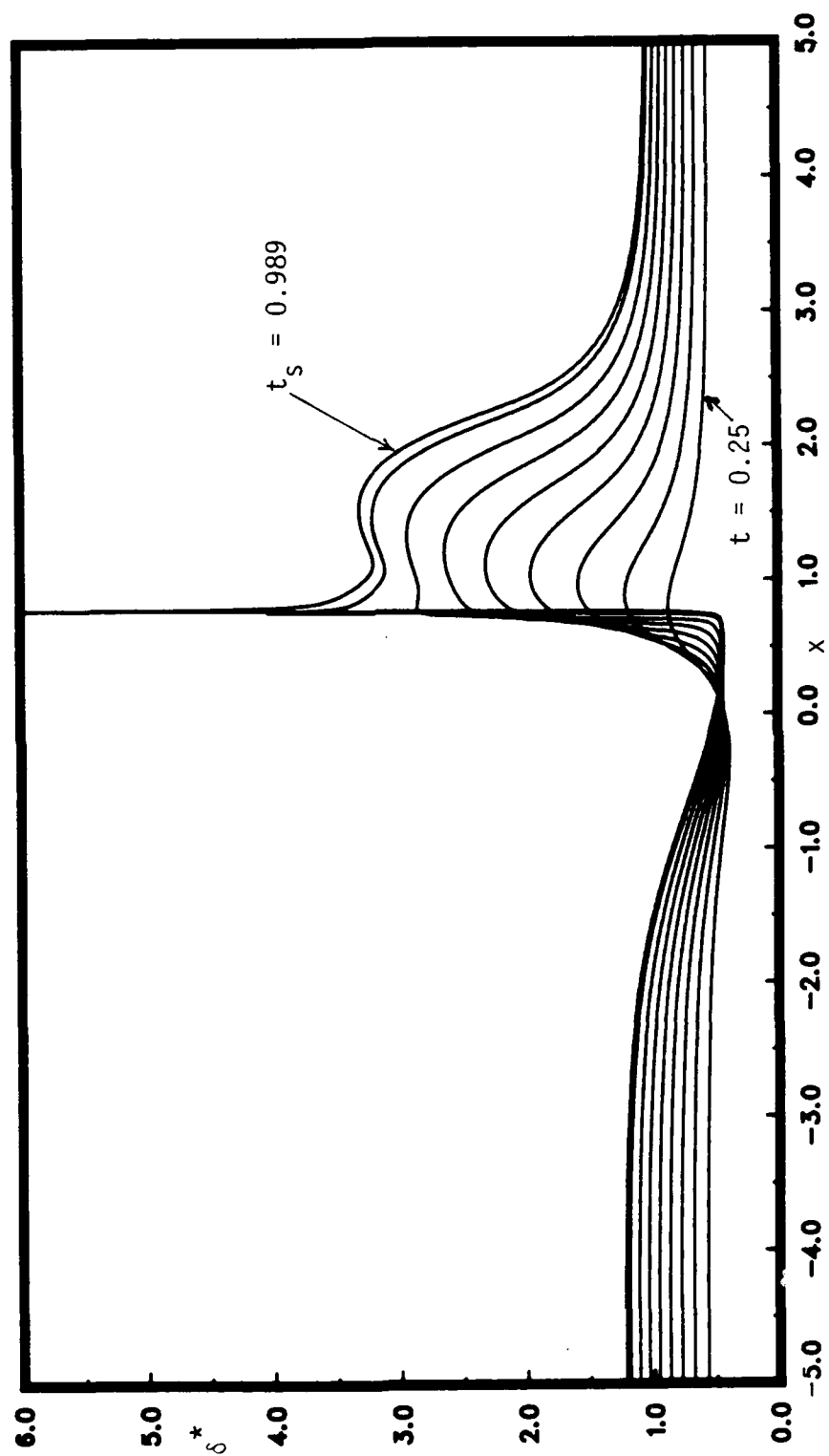
$$\delta^*(x,t) = \int_0^{+\infty} \{ 1 - U(\xi, \eta, t) \} dy. \quad (4.14)$$

Here it is understood that the integration on the right side of equation (4.15) is carried out for fixed  $t$  along a line of constant  $x(\xi, \eta, t)$ . The procedure used to calculate  $\delta^*$  from Lagrangian data is described in Appendix D. The temporal development of  $\delta^*$  is shown in figure 4.4(a) in the frame of reference moving with the vortex, where it may be observed that explosive boundary-layer growth finally occurs near  $x = -0.214$ . The rather abrupt nature of this phenomena should be noted. Up until  $t=0.85$ , the growing recirculating eddy has caused significant but unremarkable thickening of the boundary layer over a streamwise extent  $O(1)$ . However, in the interval between  $t=0.85$  and  $0.989$  the boundary-layer flow abruptly focuses into a band which is very narrow in the streamwise direction. The maximum displacement thickness more than doubles during this interval and, on a scale where  $x=O(1)$ , the local displacement surface appears as a spike. The phenomena develops and takes place in a frame of reference moving with the vortex; an observer in this frame





4.4(a) In a frame of reference convecting with the vortex;  
 Figure 4.4 Temporal development of the displacement thickness  $\delta^*$ ; plotted curves are  
 at  $t = 0.25$ ,  $(0.10)$ ,  $0.95$  and  $t_s = 0.989$ .



4.4(b) In the laboratory frame

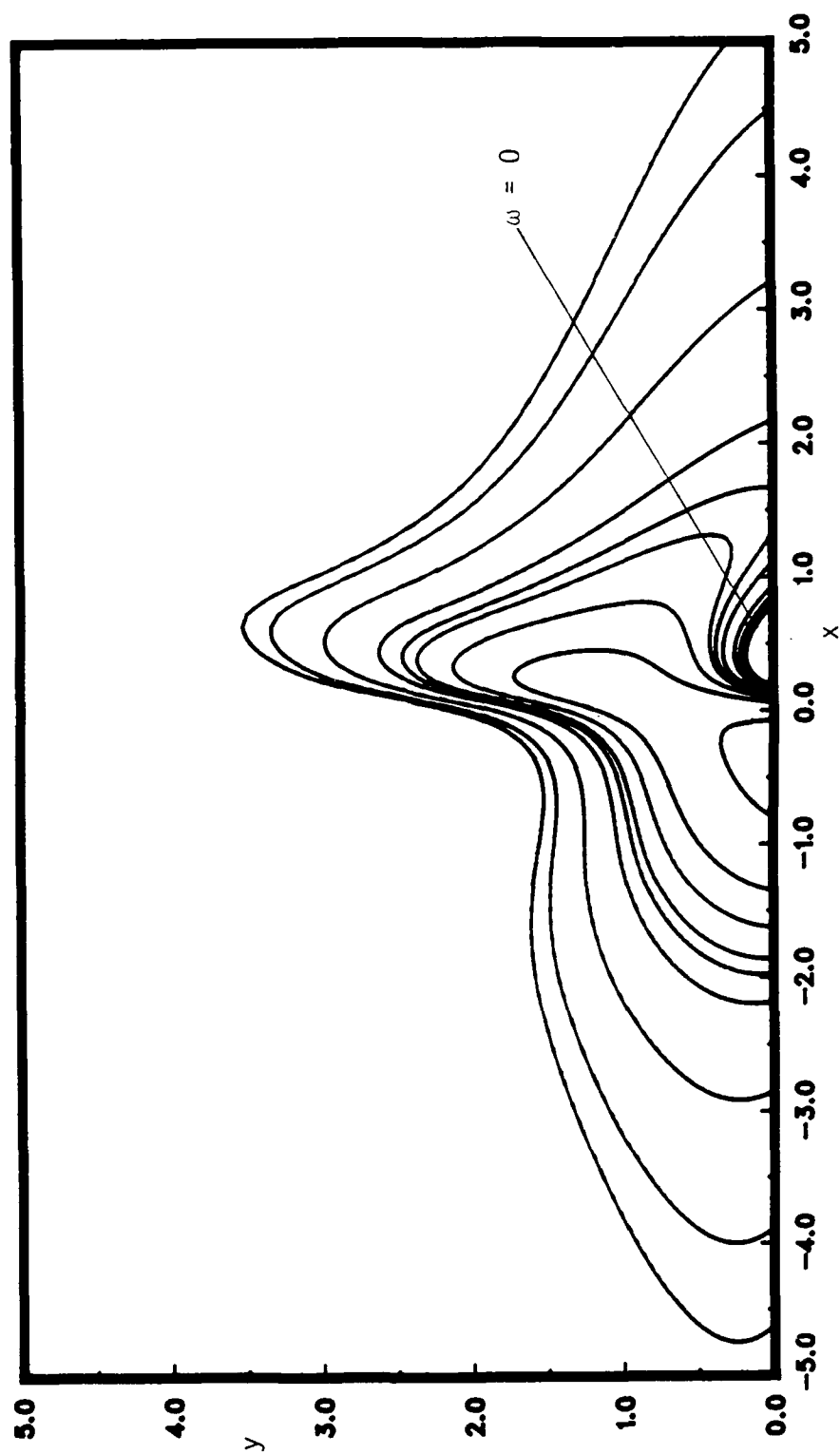
sees a localized region of abrupt boundary-layer growth which appears to be moving upstream in its final stages. Again, this is a case of "upstream-slipping separation". On the other hand, an observer in the laboratory frame of reference would see a strengthening region of outflow which moves downstream; for comparative purposes, the temporal development of  $\delta^*$  in the laboratory frame is shown in figure 4.4(b).

Using the interactive theory discussed in general terms in §1.4, it is easily shown that the scaled displacement velocity (with respect to  $Re^{-1/2}$ ) induced on the external flow is

$$V_d = \frac{\partial}{\partial x} \{ Ue(x) \cdot \delta^*(x,t) \} . \quad (4.15)$$

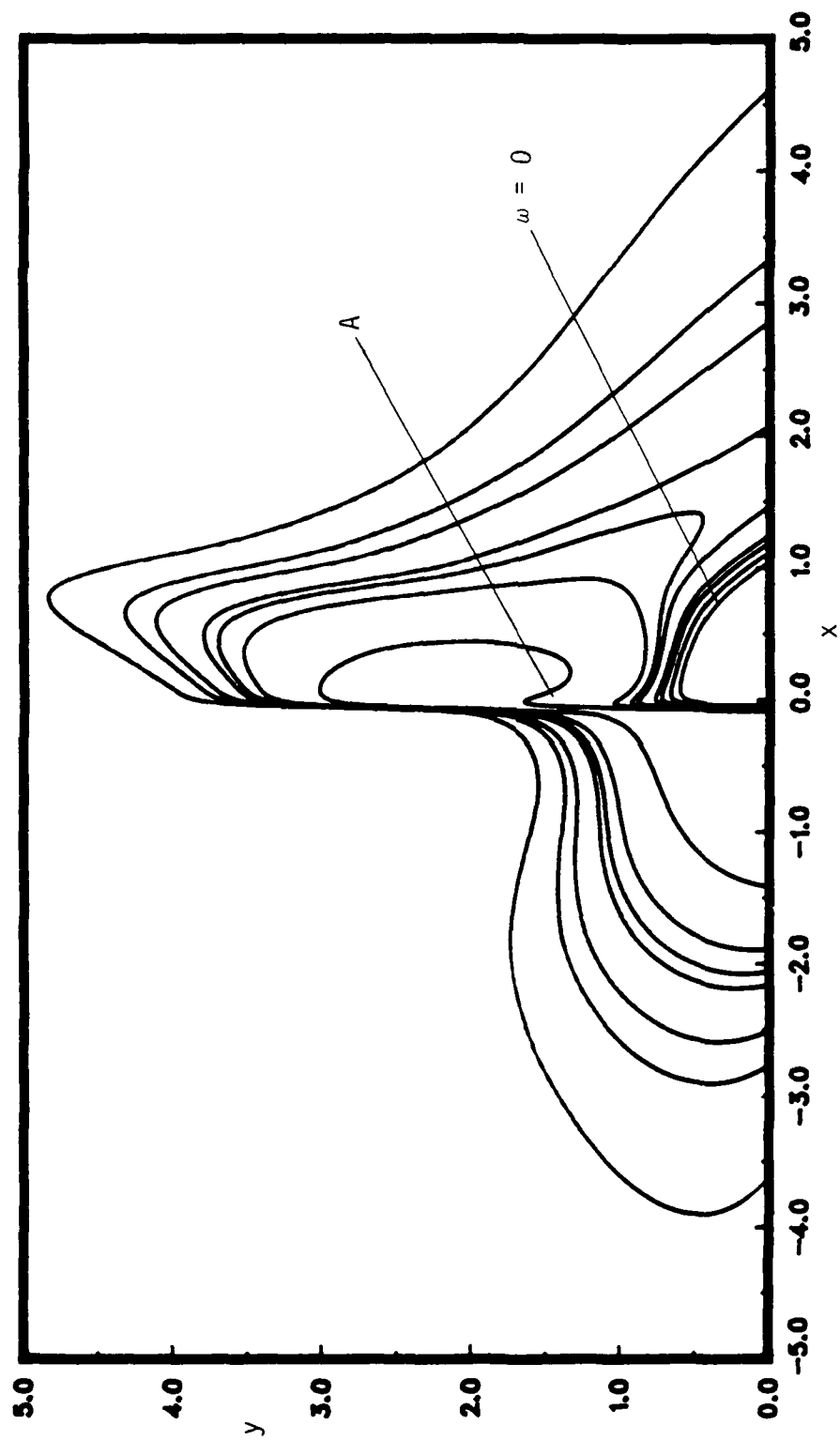
It is evident from figure 4.4(a) that  $V_d$  becomes large as  $t \rightarrow t_s$ , and eventually singular in accordance with the theory reviewed in §2.5.

The vorticity is defined as  $\omega = -\partial u / \partial y$ , and a method for calculating  $\omega$  from Lagrangian data is described in Appendix D. Contours of constant vorticity at  $t=0.45, 0.75$  and  $0.95$  and at  $t_s=0.989$  are shown in figures 4.5(a)-4.5(d) respectively. In these figures the zero-vorticity contour is labeled. In figure 4.5(a) at  $t=0.45$  the zero-vorticity line touches the wall at about  $x=0.25$  and  $0.75$ . Between the wall and the zero-vorticity line, the vorticity is positive. Elsewhere the vorticity is negative and actual magnitudes may be inferred from the plots of wall shear (that will be discussed subsequently), since all equi-vorticity lines begin and end on the wall. The maximum magnitude of vorticity in figure 4.5(a) occurs, for example, near  $x=-0.5$ , and the magnitude of the vorticity decreases progressively for contours which start at values of  $x$  moving progressively to the left. The evolution of the constant vorticity contours is instructive in developing an appreciation of the dynamics of an erupting boundary layer. It may be seen that by  $t=0.75$ , the constant  $\omega$

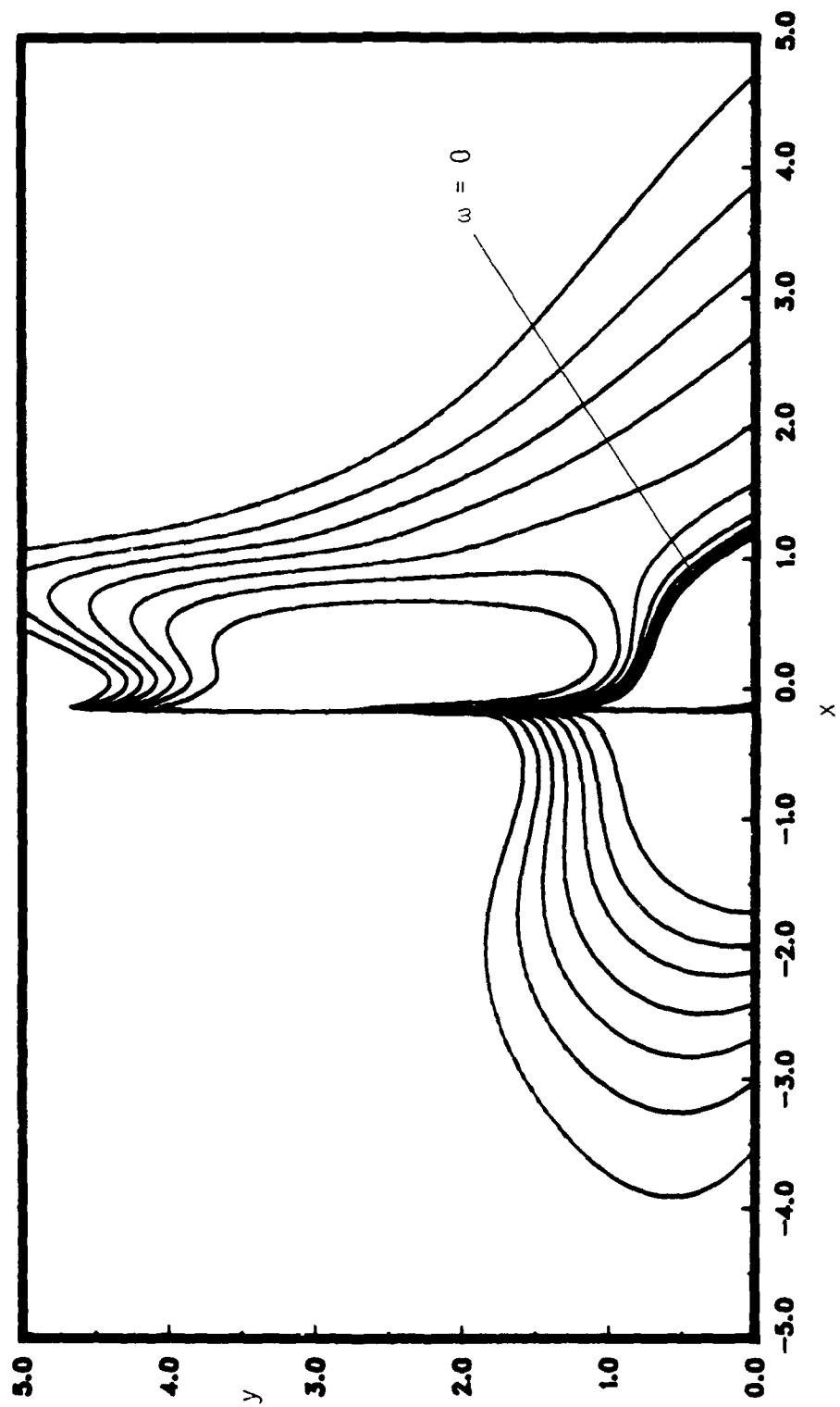


4.5(a)  $t = 0.45$

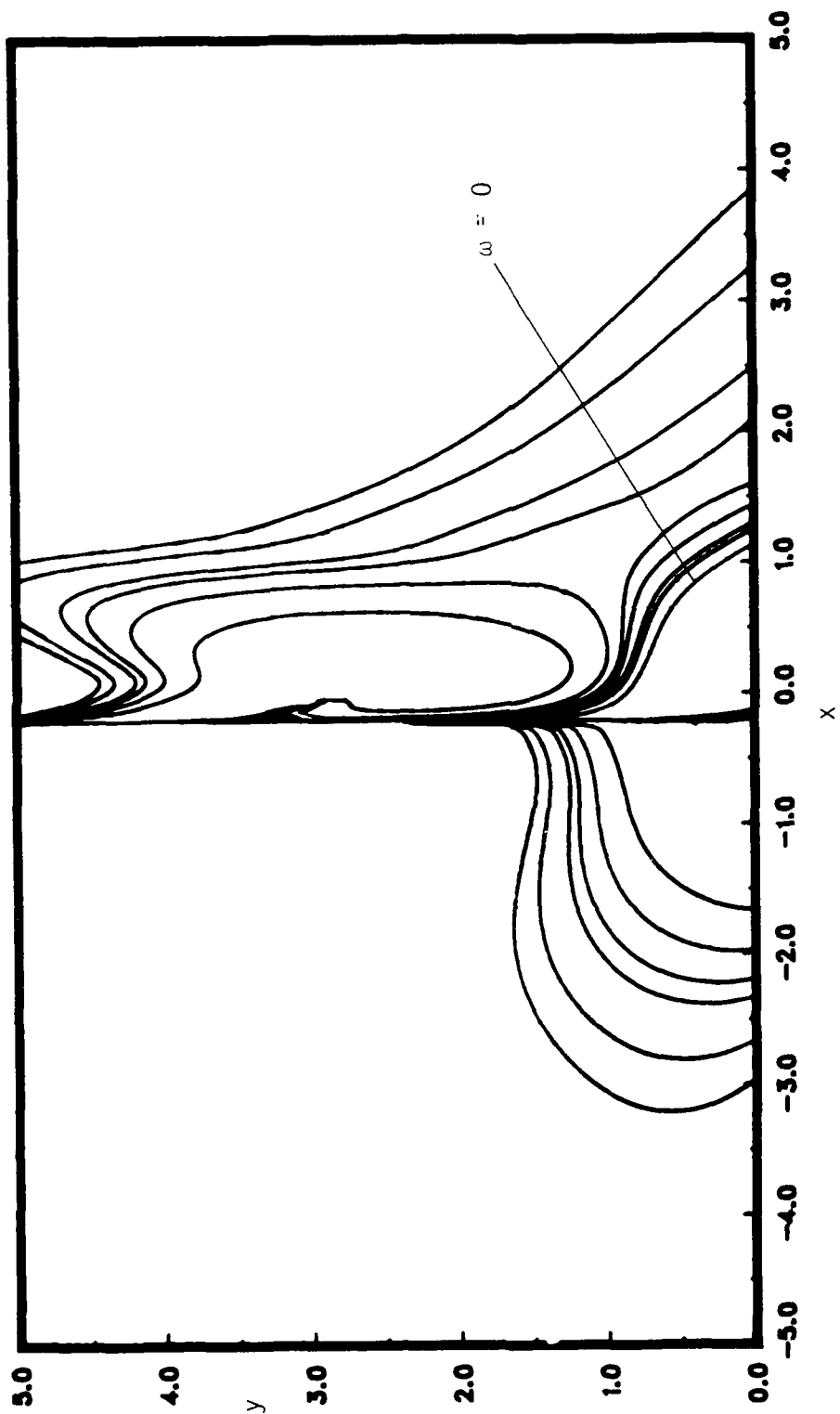
Figure 4.5. Evolution of the constant vorticity contours.



4.5(b)  $t = 0.75$



4.5(c)  $t = 0.95$



4.5(d)  $t = t_s = 0.989$

contours have begun to deform, and develop an inverted "V" near  $x=0$ ; this may be seen, for example, at the location on the contour labeled "A" in figure 4.5(b). By  $t=0.95$ , most of the equi-vorticity contours above  $x=-0.20$  have developed this inverted "V" pattern which is now becoming considerably stretched in the vertical direction. This development is consistent with the theoretical description of the terminal boundary-layer structure discussed in §2.5. The two sides of the "inverted V" pattern, where the equi-vorticity lines are congregating, form the moving shear layer denoted in figures 2.6 and 2.7 as region III; recall that these figures represent exploded views of the structure within the "spike" of figure 4.4(a). Inside the "V" there is a vorticity-depleted region (region II in figure 2.6). The constant vorticity contours at  $t=t_s$  are shown in figure 4.5(d) where the trends noted in connection with figure 4.5(c) may be observed to have continued.

The wall shear is defined by

$$\tau_w(x,t) = \left. \frac{\partial u}{\partial y} \right|_{y=0}, \quad (4.16)$$

and using equation (3.48) it is readily shown (see Appendix D) that

$$\tau_w(x,t) = Ue(x) \left. \frac{\partial U}{\partial \eta} \right|_{\eta=0}. \quad (4.17)$$

The derivative of  $U$  was evaluated using a four-point forward difference formula (Appendix D) and the temporal development of wall shear is shown in figure 4.6. It may be observed that during the course of the integration the wall shear distribution remains smooth and regular, with the possible exception near  $t=t_s$  when the wall shear near  $x=-0.30$  appears to rise abruptly. This behavior is illustrated more clearly in figure 4.7 where the wall shear is plotted at three selected times. At first glance this behavior is disturbing since the implication of the theory of Van Dommelen (1981) and



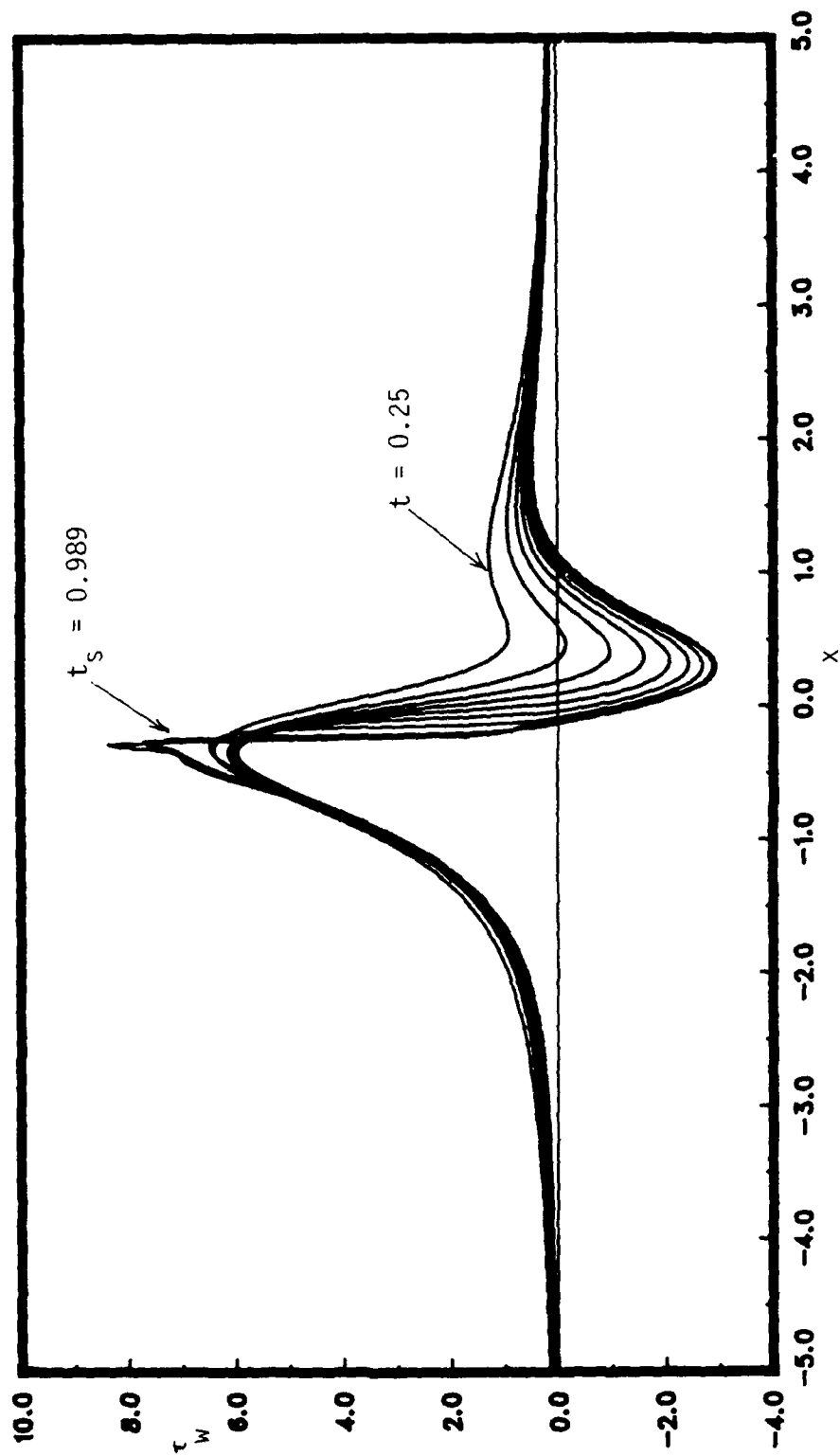


Figure 4.6. Temporal development of wall shear; the distributions are plotted for  $t = 0.25$  (0.10) 0.95 and at  $t_s = 0.989$ .

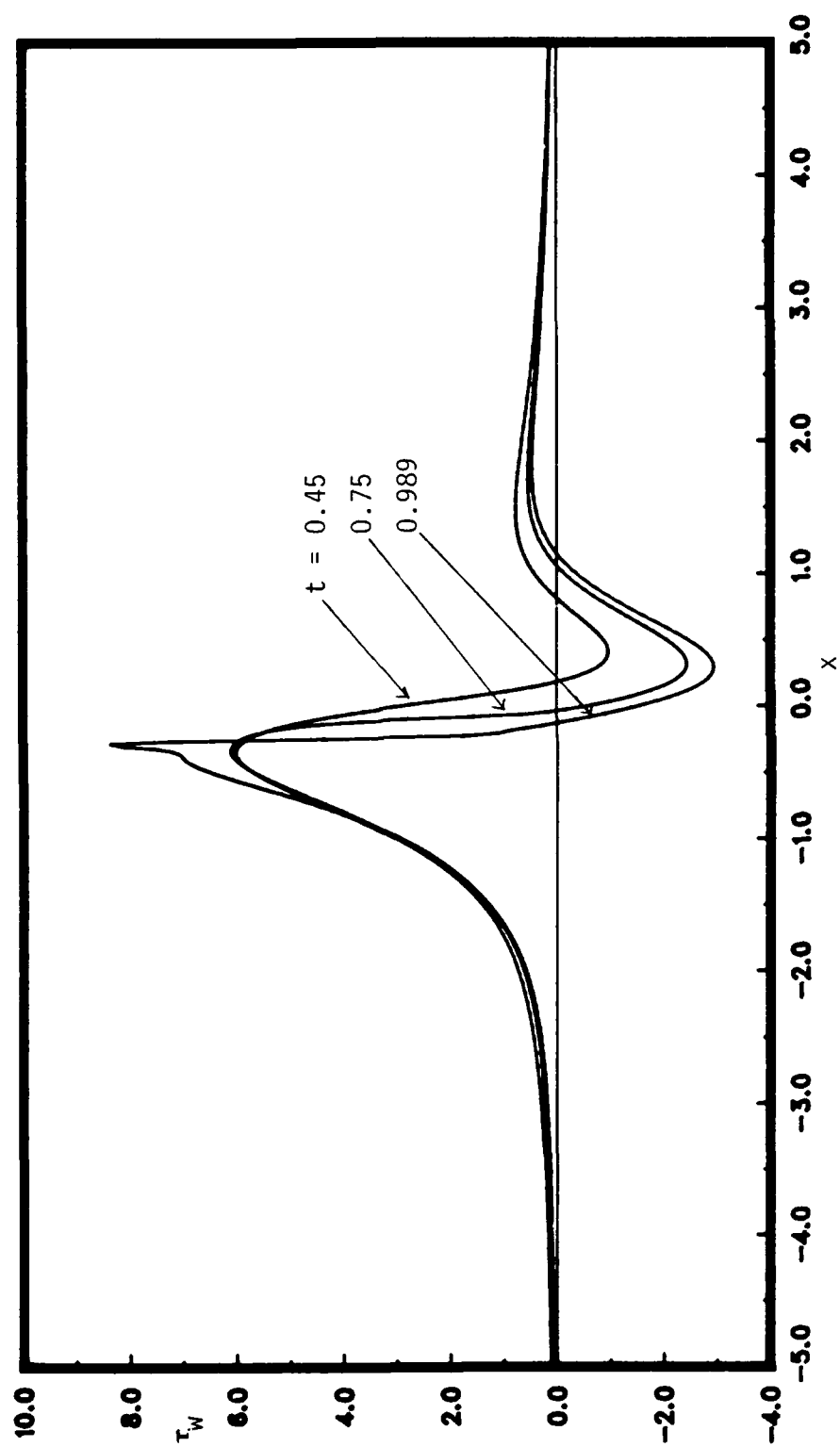


Figure 4.7. Wall shear distributions at selected times.

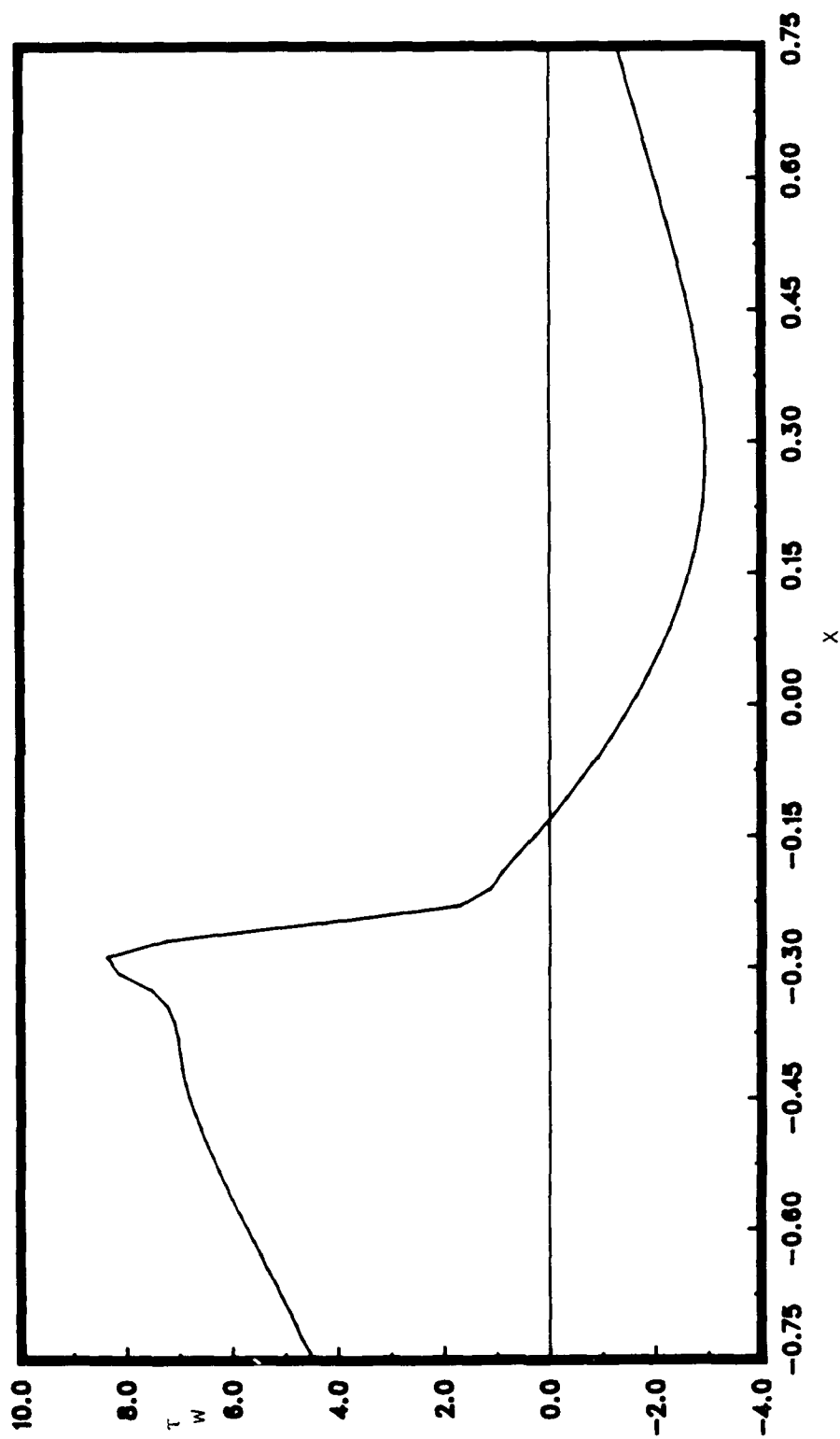


Figure 4.8 Wall shear distribution at  $t_s$  using an enlarged scale in  $x$ .

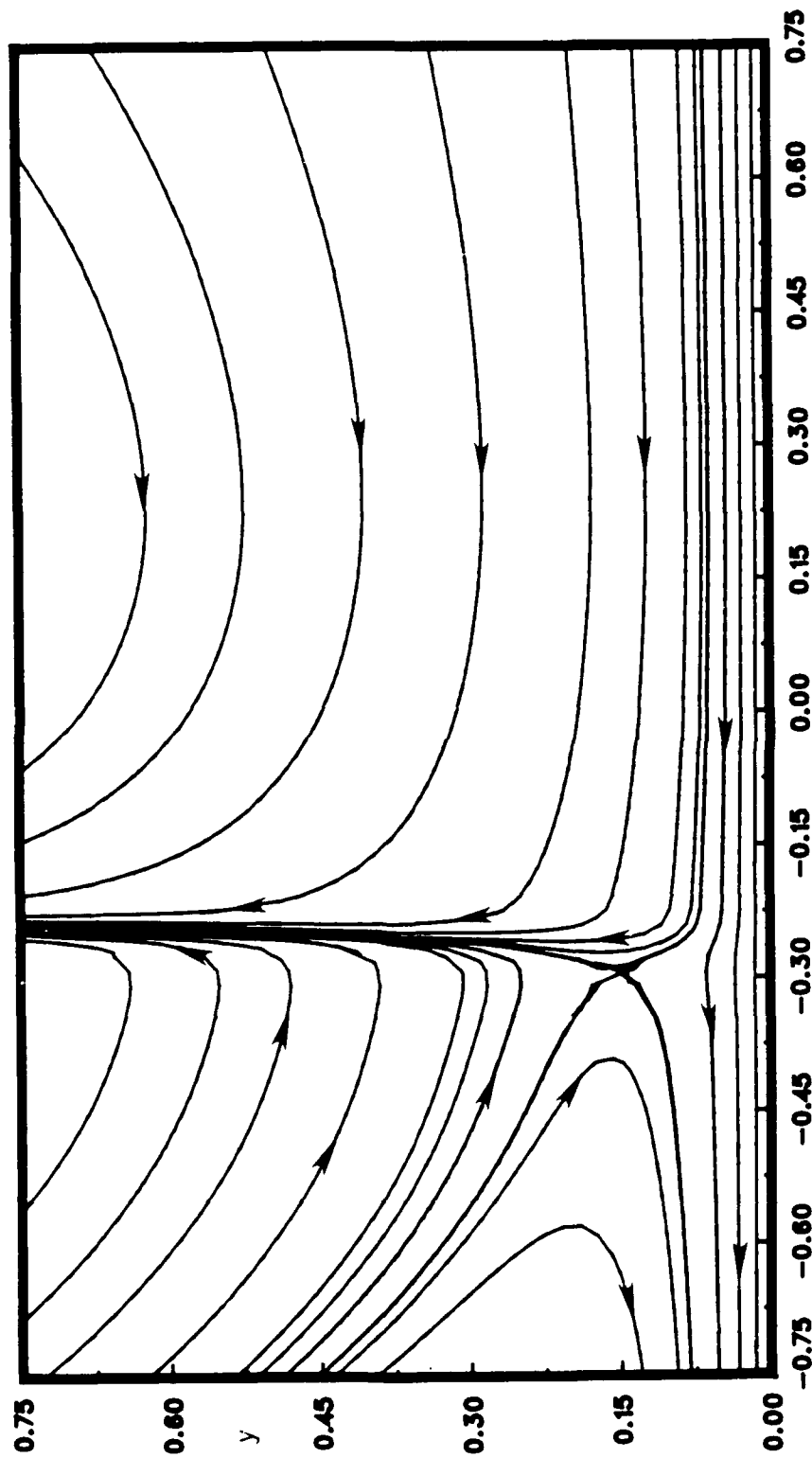


Figure 4.9. Instantaneous streamlines at  $t_s$  using an enlarged scale near the wall.

Elliott, Cowley and Smith (1983) is that the wall shear should remain regular as  $t \rightarrow t_s$ , near  $x = x_s$ . The first point of interest is that, for the present case,  $x_s = -0.214$  and it may be confirmed from figure 4.7 that  $\tau_w$  is regular there. The location where the apparent "spike" in  $\tau_w$  is developing in near  $x = -0.30$ , in figure 4.7, just to the left of  $x_s$ . As previously indicated, results were obtained on three sets of mesh sizes and this behavior was found in all cases. To appreciate the physical reason for this distribution of  $\tau_w$ , the results for  $\tau_w$  and the instantaneous streamlines were plotted on a magnified scale near  $x = -0.30$  in figures 4.8 and 4.9 respectively. Note that no attempt was made in figure 4.8 to smooth the computed results and the plotter has connected the values of  $\tau_w$  at each mesh point with straight lines. It may be noted that on the scale of the figure 4.8, the distribution of  $\tau_w$  appears reasonably well-behaved. The maximum in wall shear (which appears as the tip of the small spike in figure 4.7) coincides very closely with the streamwise location of the stagnation point in figure 4.9. With the evolution of large updrafts near the singularity at  $x_s = -0.214$  the stagnation point depicted in figure 4.9 has been lifted somewhat away from the wall; this gives rise to a pinching of the streamlines near the wall as fluid particles pass by the stagnation point. For this reason, the wall shear exhibits a mildly intense variation at  $t_s$  near the stagnation point.

#### 4.5 Discussion

The present results were found to agree well with the structure of the singularity and terminal boundary-layer solution given by Van Dommelen (1981) and Elliott, Cowley and Smith (1983) which were discussed in §2.5. In particular, results obtained here were compared to the predicted behavior in the maximum value of the displacement thickness

$$\delta^*_{\max} = \frac{C}{(t_s - t)^M}, \quad (4.18)$$

where Elliott *et al* (1983) predict  $M=1/4$ . The method used to compute  $\delta^*$  is described in Appendix D; due to the nature of the computation it is difficult to calculate  $\delta^*_{\max}$  with a high degree of confidence. Nevertheless, a least squares curve fit of equation (4.18) to the computed results for  $\delta^*_{\max}$  in the time interval  $0.900 < t < 0.986$  produced the following values:

$$C = 1.71 \pm 0.02, \quad M = 0.253 \pm 0.003. \quad (4.19)$$

This closely confirms the growth rate of the boundary layer predicted by Elliott, Cowley and Smith (1983) near  $t=t_s$ .

In figure 4.10, velocity profiles near  $x_s$  are plotted across the boundary layer and these also confirm the structure described in §2.5. At  $x=x_s$ , the profile is very flat and the boundary-layer is thick; a shear layer is present near the wall and in the upper part of the boundary layer to adjust the velocity from the uniform value of  $u=-K$ . The location  $x=x_s$  is within the vorticity-depleted zone inside the evolving spike in displacement thickness. To the left and right of  $x_s$  it may be noted that the upper shear layer is returning toward the wall, and that a significant portion of the profiles are flat (c.f. figures 2.5 and 2.6).

Finally, this phenomena has been referred to here as "upstream-slipping separation" after Van Dommelen (1981), in the sense that the singularity is moving upstream in a direction opposite to that of the mainstream flow. There has been a tendency in the past (see, for example, Sears and Telionis (1971)) to classify the "separation" relative to the motion of the wall. In the present situation the wall is moving upstream but plays a minor role in the

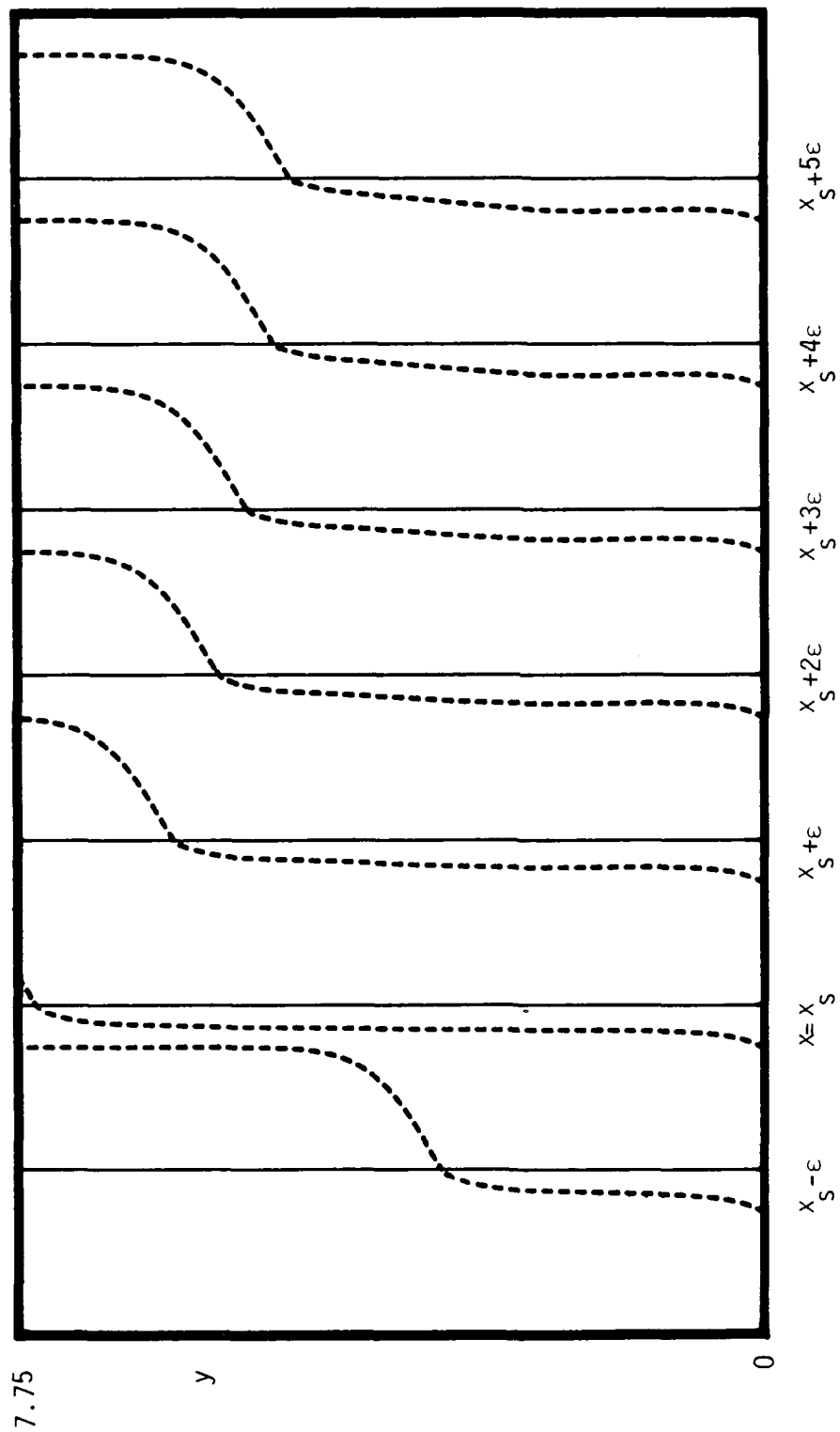


Figure 4.10. Velocity profiles near  $x = x_s$  at  $t = 0.9885$ ;  $\epsilon = 1.05 \times 10^{-3}$ .

evolution of the eruption that finally develops. Consequently, it would seem useful to classify such eruptions as either "upstream-" or "downstream-slipping" separation on the basis of the motion of the singularity relative to the local mainstream flow.



## 5. INTERACTING BOUNDARY-LAYER RESULTS

### 5.1 Introduction

The results obtained from interacting calculations of the model problem for  $Re=10^8, 10^7, 10^6$  and  $10^5$  are discussed in this chapter. The evolution of the boundary-layer flow for all cases of  $Re$  considered was virtually indistinguishable from the flow development of the limit problem (described in Chapter 4), until the point at which strong interactions with the outer flow began to take place. With the onset of strong interaction, an immediate departure from the limit-problem solution was observed and the solution proceeded rapidly toward an eruptive state, developing a singularity at  $t=t_s(Re)$ . The time when strong interaction initiates, as well as  $t_s$ , varies with  $Re$ ; both times were found to *decrease* with decreasing Reynolds number. Consequently, an important conclusion of this study is that interaction does not postpone or mitigate the evolution of a singularity; on the contrary, the effect of interaction is to hasten the breakdown of the boundary-layer solution. These results confirm the conclusion of Smith (1988) that any interacting formulation of unsteady separation can generate breakdown in finite time.

Initially, for all the interacting cases of  $Re$  considered, the smooth and regular boundary-layer flow evolution is indistinguishable from that of the limit-case problem. Even in the terminal stages of the calculation, when strong interactive effects dominate the flow development, the effect of interaction is largely confined to a very narrow streamwise region centered on the breakdown location  $x_s$ . The boundary-layer flow outside the strong interaction zone continues to develop smoothly, as if interaction effects were absent and almost as if unperturbed by the explosive phenomena occurring

near  $x_s$ . Although visual examination of the results can be used to estimate  $x_s$  and  $t_s$ , more precise numerical estimates of these quantities may be obtained, and these procedures are explained in §5.2. In §5.3 computed results for the boundary layer in the terminal stages of the calculation will be presented for all cases of  $Re$  considered. The external mainstream flow problem, like the boundary-layer, does not depart significantly from the steady distribution of the limit problem until strong interaction ensues. However, once  $t \rightarrow t_s$ , the variations in the outer solution for  $x \rightarrow x_s$  become quite severe. The behavior of the external flow in the terminal stages of the calculation will be considered in §5.4. The results obtained in this study are compared with two recent asymptotic investigations. The present results confirm the singularity structure given by Elliott, Cowley and Smith (1983), and this is discussed in §5.5. In addition, the present investigation supports the recent theoretical study of Smith (1988); a detailed comparison with the predicted asymptotic structure is presented in §5.6, and summarized in §5.7.

## 5.2 Numerical Considerations Associated with the Interactive Computations

Calculations for each interacting case at finite  $Re$  were initiated at  $t_0=0.25$  from velocity data generated by an Eulerian calculation for the limit problem  $Re \rightarrow \infty$ . (c.f. §3.4). The use of a limit-problem starting calculation was based on the assumption that interaction effects are negligible prior to boundary-layer separation, which occurs at  $t \sim .28$  (Walker, 1978). The experience of this study indicates that this is a reasonable assumption, and to confirm that interaction effects are negligible prior to  $t_0=0.25$ , an interactive Lagrangian calculation for  $Re=10^5$  was initiated at  $t=0$  and continued to  $t=0.25$ . In each plot of figures 5.1 there two curves, one generated from the  $Re=10^5$  (Lagrangian) data, and the other generated from the limit-problem

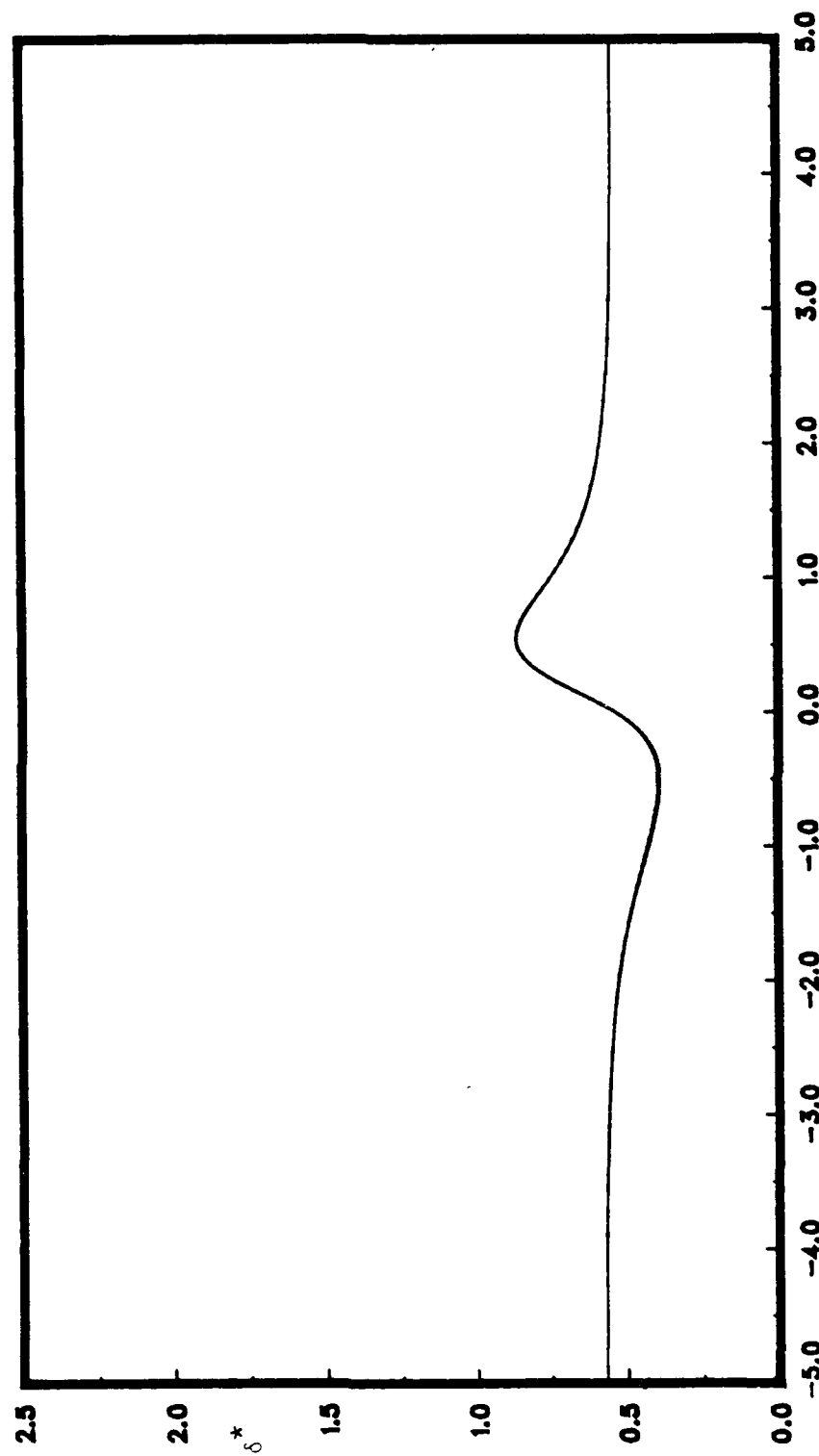
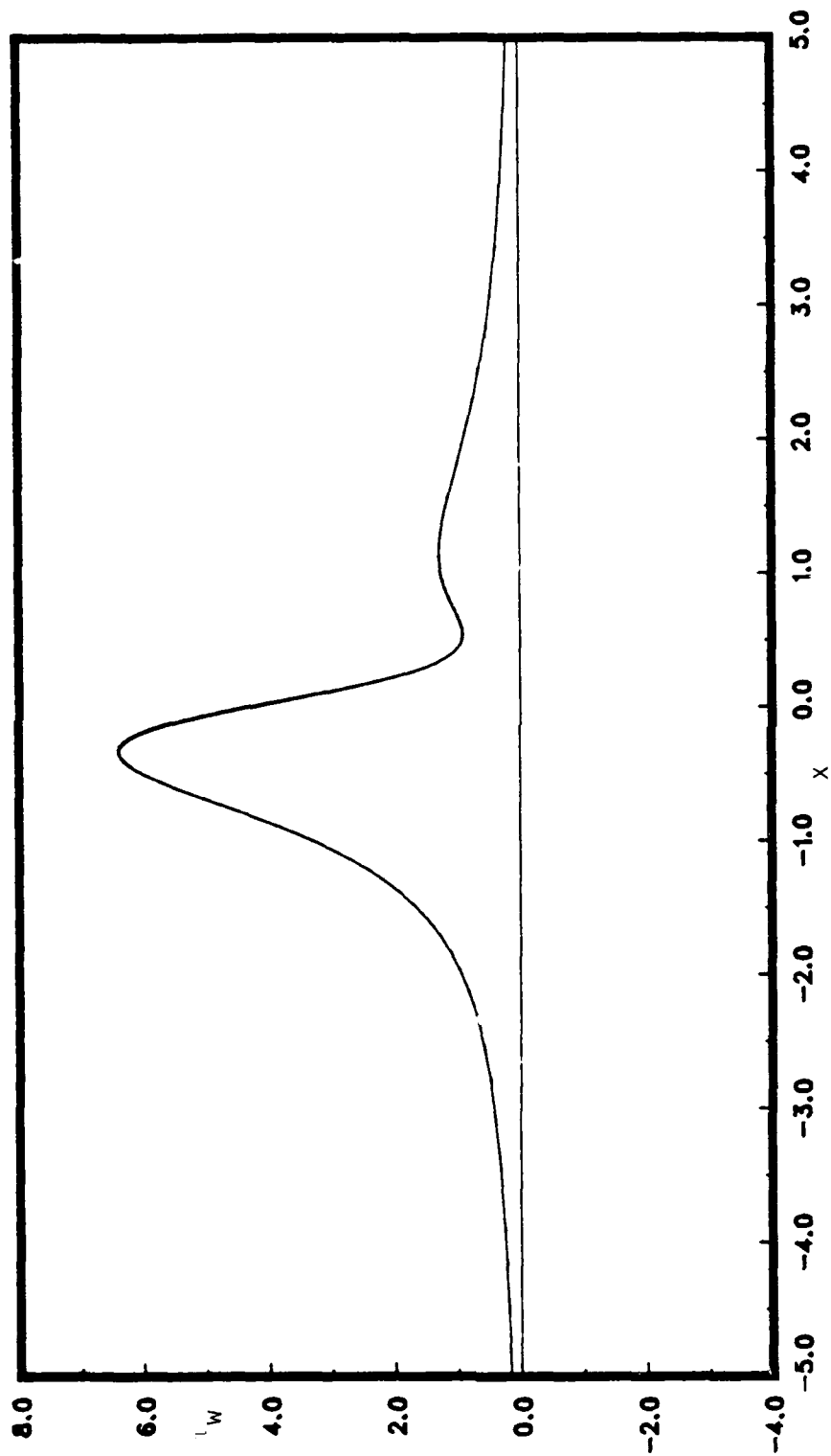


Figure 5.1. (a) Displacement thickness at  $t=0.25$  from (1) a limit problem calculation and (2) an interacting computation with  $Re=10^5$ ; the curves are indistinguishable.



5.1(b) Wall shear at  $t=0.25$  from (1) a limit problem calculation and (2) an interacting computation with  $Re=10^5$ ; the curves are indistinguishable.

(Eulerian) results; figure 5.1(a) depicts the displacement thickness  $\delta^*$  for both cases, and figure 5.1(b), the wall shear  $\tau_w$ . It is evident that in both cases the plotted results are indistinguishable.

When the singularity forms in the boundary-layer problem, a stationary point develops in the streamwise fluid-particle distribution  $\hat{x}(\hat{\xi}, \hat{\eta})$ . The contours of constant  $\hat{x}(\hat{\xi}, \hat{\eta})$  provide qualitative visual evidence of the onset of boundary-layer breakdown, just as it does in the limit problem, where a "thumb region" forms in the neighborhood of the stationary point (c.f. §4.3). However, with decreasing Reynolds number the evolution of interaction is much more abrupt and the "thumb" forms much more quickly. Contours of constant  $\hat{x}(\hat{\xi}, \hat{\eta})$  at two times as  $t \rightarrow t_s$  for the largest and smallest Re considered ( $Re=10^8, 10^5$ ) are illustrated in figures 5.2. Figure 5.2(a) shows contours of constant  $\hat{x}$  for  $Re=10^8$  at  $t_s-0.02$ ; the "thumb" contour feature is easily identified and, overall, the plot at  $t_s-0.02$  does not appear much different than figure 5.2(b), which depicts constant  $\hat{x}$  contours for  $Re=10^8$  a short time later at  $t_s$ . By contrast, consider figure 5.2(c) for  $Re=10^5$  at  $t_s-0.015$ ; there is no "thumb" region. However, as may be seen in figure 5.2(d), by time  $t_s$  the "thumb" is seen to have abruptly deformed the otherwise smooth contours.

Estimates of  $t_s$ ,  $x_s$ , and the drift velocity of the first interactive state ( $-K$ ) are given in table 5.1 for each case of finite Re considered. An additional parameter given in this table is the time at which strong interactive effects emerge,  $t_{01}$ ; here,  $t_{01}$  is defined to be the time at which the boundary-layer thickness "spike" is first detected in the numerical results.

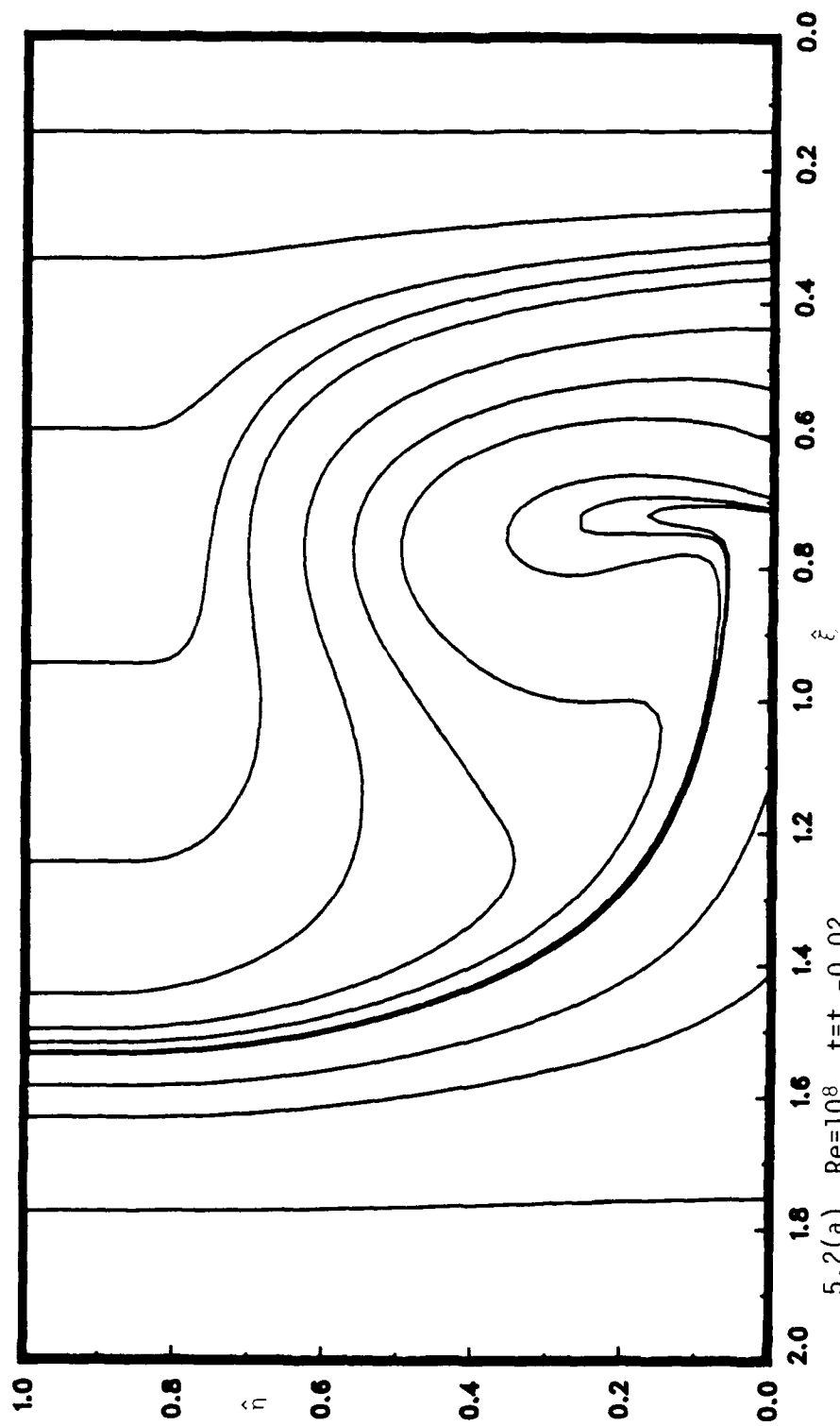
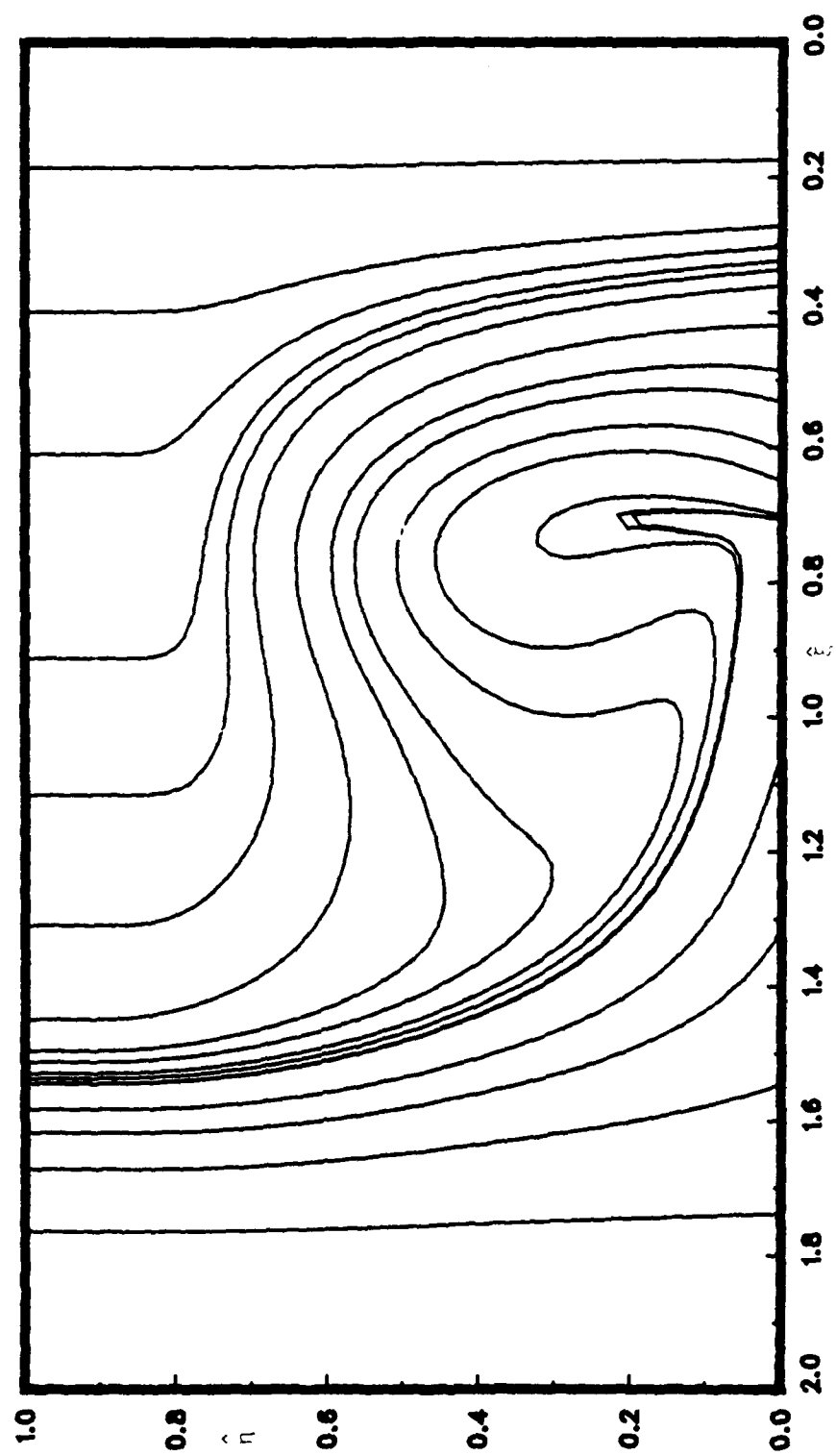
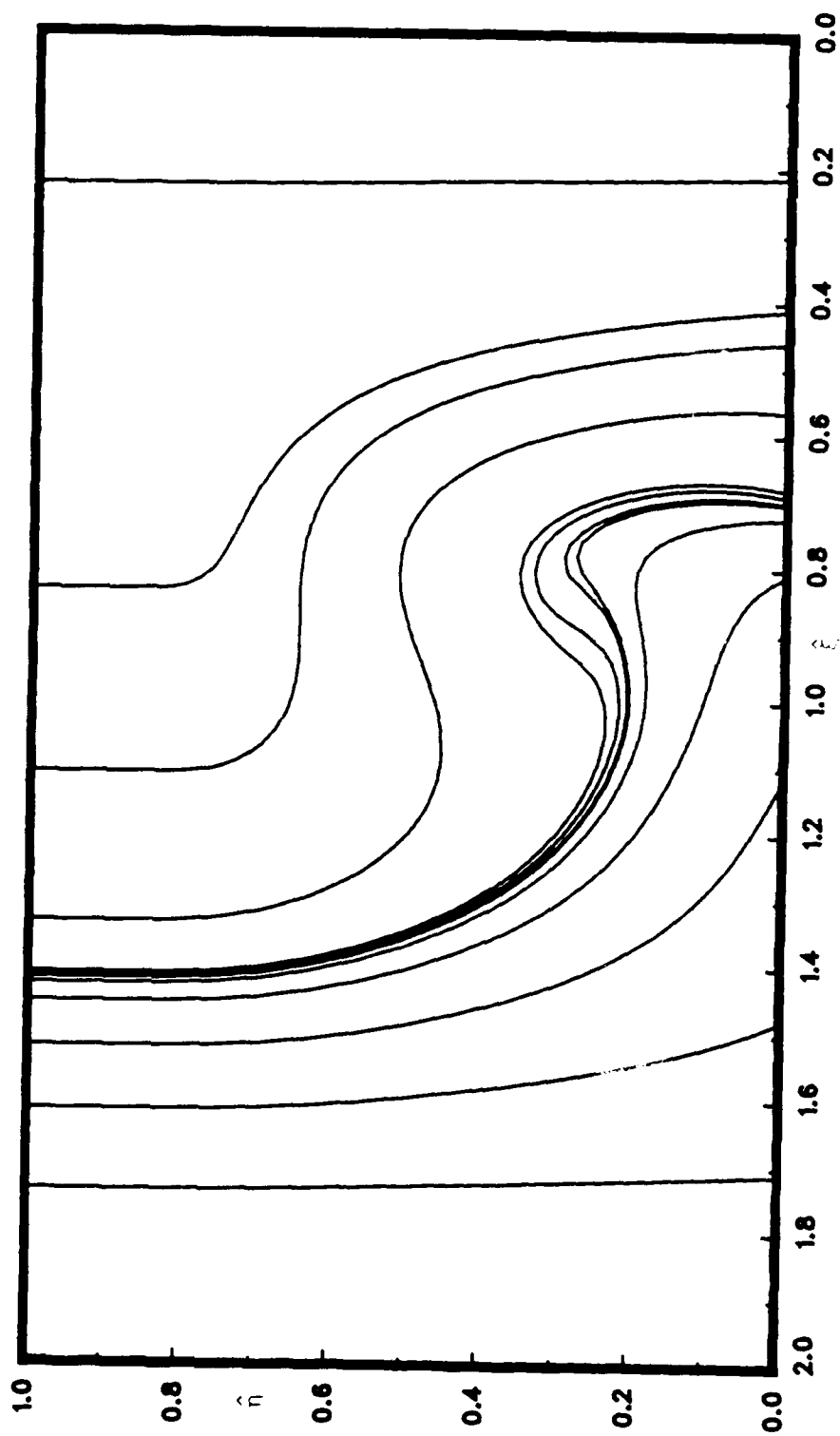


Figure 5.2. Contours of constant  $x$  near the singular time  $t_s$ , for two cases of finite  $\text{Re}$ .

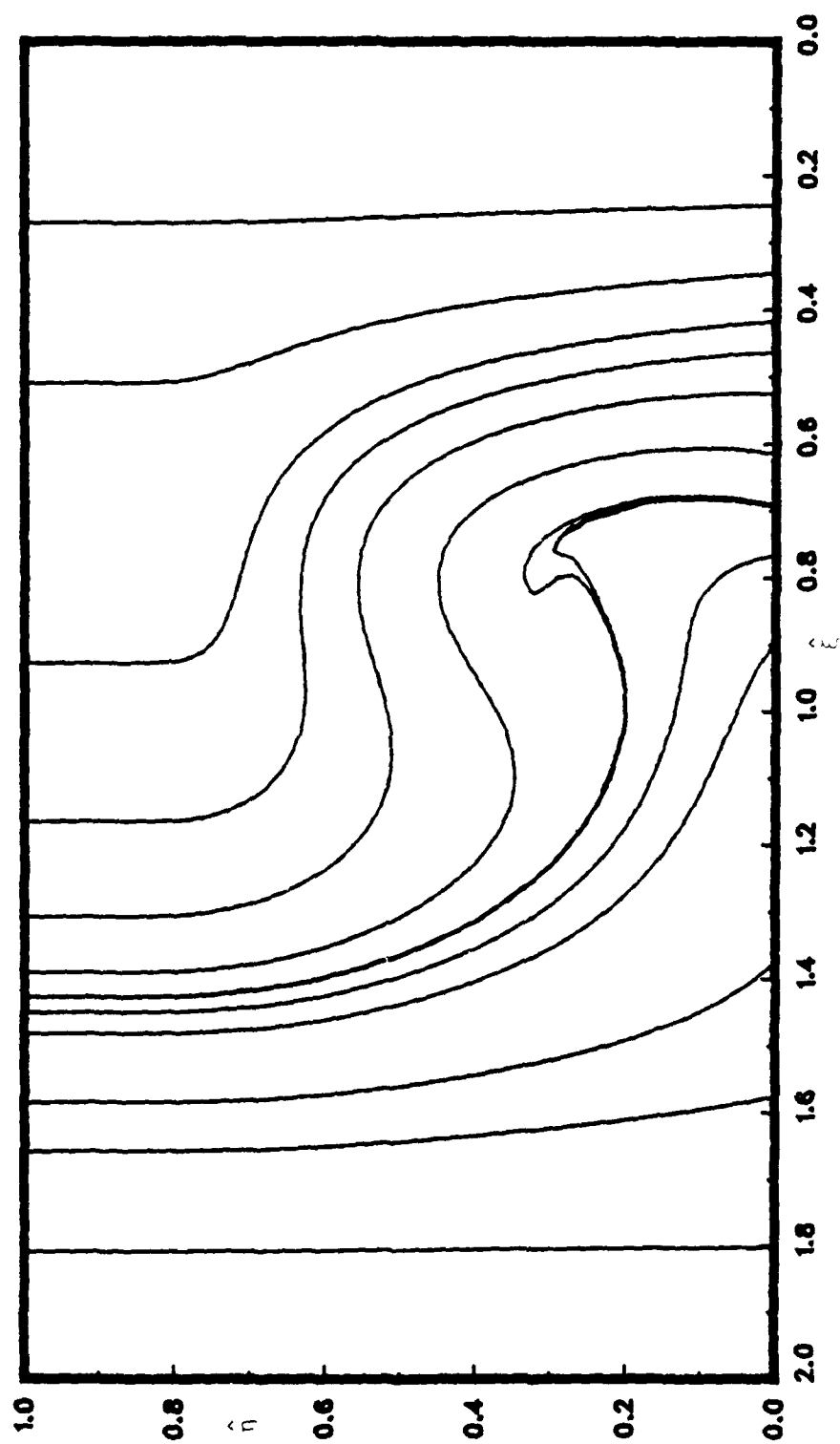


5.2(b)  $\text{Re}=10^8$ ,  $t=t_s$



5.2(c)  $\text{Re}=10^5$ ,  $t=t_S-0.015$





Re	$t_{01}$	$t_s$	$x_s$	$(-K)$
$\infty$	0.8900	0.9885	-0.214	-0.521
$10^8$	0.8200	0.8965	-0.152	-0.686
$10^7$	0.7520	0.8185	-0.091	-0.671
$10^6$	0.6800	0.7240	0.000	-0.321
$10^5$	0.6230	0.6445	0.126	-0.035

Table 5.1. Parameters associated with boundary-layer breakdown, for both the limit problem and interacting studies. Note that  $x_s$  and  $(-K)$  are in a frame of reference moving with the vortex.

The values of  $t_s$  given in table 5.1 were estimated using the procedure described in §4.3. Values for  $x_s$  and  $(-K)$  for the limit problem and all cases of finite Re, except  $Re=10^5$ , were interpolated at  $(\hat{\xi}_s, \hat{\eta}_s)$  as described in Appendix E. The estimated values of  $x_s$  and  $t_s$  for the  $Re=10^5$  case were determined using an alternate approach for reasons which will now be described.

The tip of the spike that was found to develop in displacement surface  $\delta^*$  is located at  $x_s$ . Another method for locating  $x_s$  is to carry out a search through the distribution of  $\delta^*$  using a process of interval-halving to find the maximum value; however, in all cases but  $Re=10^5$  the six-point interpolation method of Appendix E finds  $x_s$  with better accuracy and fewer calculations. The interpolation method of computing  $x_s$  was found to locate the tip of the "spike" in displacement thickness  $\delta^*$  with considerable precision in all cases except  $Re=10^5$ ; for this case the estimates of  $\hat{x}_s$  produced by the interval-halving method were slightly different from those produced by the interpolation method of Appendix E during the last 0.012 time units before  $t_s$ .

The reason for the discrepancy was traced to six-point interpolation scheme described in Appendix E. As indicated in §5.1 the present results tend to corroborate the asymptotic structure proposed by Smith (1988) in which the boundary layer bifurcates into three zones (c.f. figure 2.9). In the case of  $Re=10^5$ , it emerged that the fluid particle  $(\hat{\xi}_s, \hat{\eta}_s)$  was located close to the top of the inviscid region (zone II, figure 2.9). Consequently, the six-point interpolation in the calculation for  $Re=10^5$  was carried out over a region of intense variation in the flow, namely the critical layer (zone III). The value of  $(-K)$  computed in the last few time steps for the case  $Re=10^5$  was also felt to be significantly in error because the velocity variation across the critical layer is quite large. Because the interpolation procedure was considered to be an unreliable method for estimating  $x_s$  for the  $Re=10^5$  case, the value for  $x_s$  given in table 5.1 was determined by finding the streamwise location of the maximum value of  $\delta^*$  as  $t \rightarrow t_s$ . Up until  $t_s - 0.012$  the estimates of  $(-K)$  for  $Re=10^5$  seemed to be approaching an almost constant value and it is this value which is reported in table 5.1; the interpolation method of Appendix E produced positive values  $O(1)$  for  $(-K)$  as  $t \rightarrow t_s$  but, for reasons that have been discussed, these estimates of  $(-K)$  were not considered reliable.

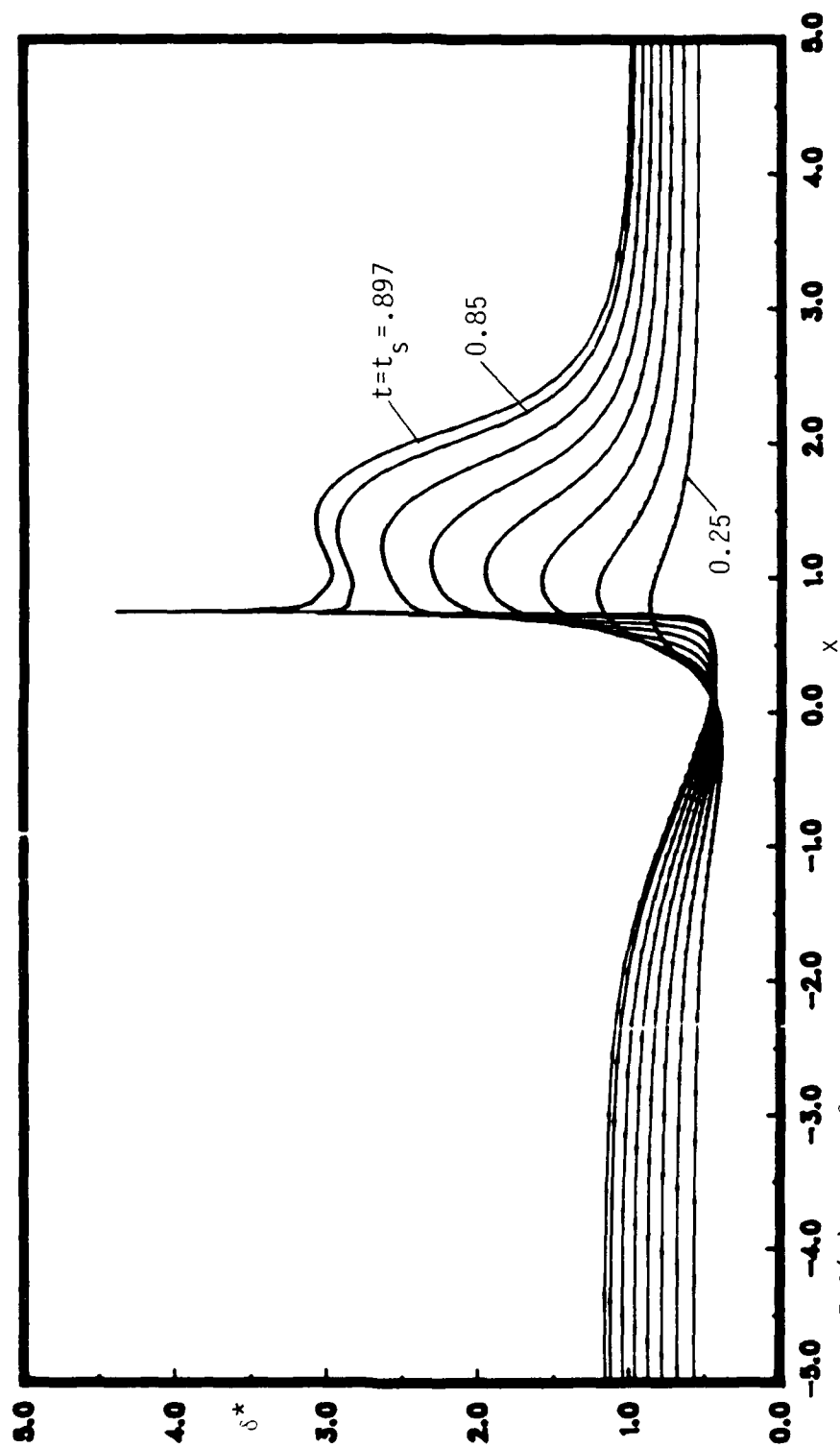
There are several general features in table 5.1 that are worthy of note. First, it is evident that the boundary-layer breakdown time,  $t_s$ , occurs at progressively earlier stages in time as  $Re$  is decreased. Second, the time interval (after strong interaction ensues at  $t_0$ ), over which the boundary layer proceeds toward an eruption, decreases with decreasing  $Re$ . Finally, recall that  $x_s$  and  $(-K)$  are values in a frame of reference moving with the vortex; since  $K > 0$  for all four interacting studies, each situation corresponds to an upstream-slipping singularity (i.e. in a direction opposite to that of the mainstream flow).

### 5.3 The Boundary-layer Development as $t \rightarrow t_s$

The boundary-layer flow development as  $t \rightarrow t_s$ , for each case of finite  $Re$ , will be examined in this section. As noted in §5.1, the boundary-layer flow evolves initially in all cases just as for the limit problem until strong interactions ensue, at which point the interactive problem proceeds rapidly toward an eruptive state. Because the flow evolution prior to interaction follows that of the limit problem discussed in Chapter 4, only the terminal stages of the flow shall be discussed in this section. In each case of finite  $Re$ , the boundary layer developed an eruptive interaction zone, centered on  $x_s$ , as  $t \rightarrow t_s$ . This eruptive character of this phenomena is graphically illustrated in the four plots of figures 5.3 which depict the temporal evolution in displacement thickness  $\delta^*$ , for  $t_0 \leq t \leq t_s$ , all in the laboratory reference frame.<sup>1</sup> The spike is quite needle-like at  $Re=10^8$  (figure 5.2(a)) and thickens slightly with decreasing  $Re$ , giving qualitative evidence that the streamwise-scale of the eruptive region varies inversely according to some power of  $Re$  (this will be confirmed more precisely in §5.5). The displacement thickness curve at  $t_s$  for  $Re=10^5$ , shown in 5.3(d), is unique among these four cases because not one, but two "spikes" develop; one of these is associated with the unsteady singularity and the second "spike" evolves further to the left;  $\delta^*$  for  $Re=10^5$  is depicted again in figure 5.4 at  $t=t_s$ , this time in the vortex frame. In this section it will be shown that the second spike near  $x=0$  is associated with a tertiary vortex formation in the boundary layer. The case  $Re=10^5$  is particularly complex and interesting because two independent regions develop that start to interact with the outer flow.

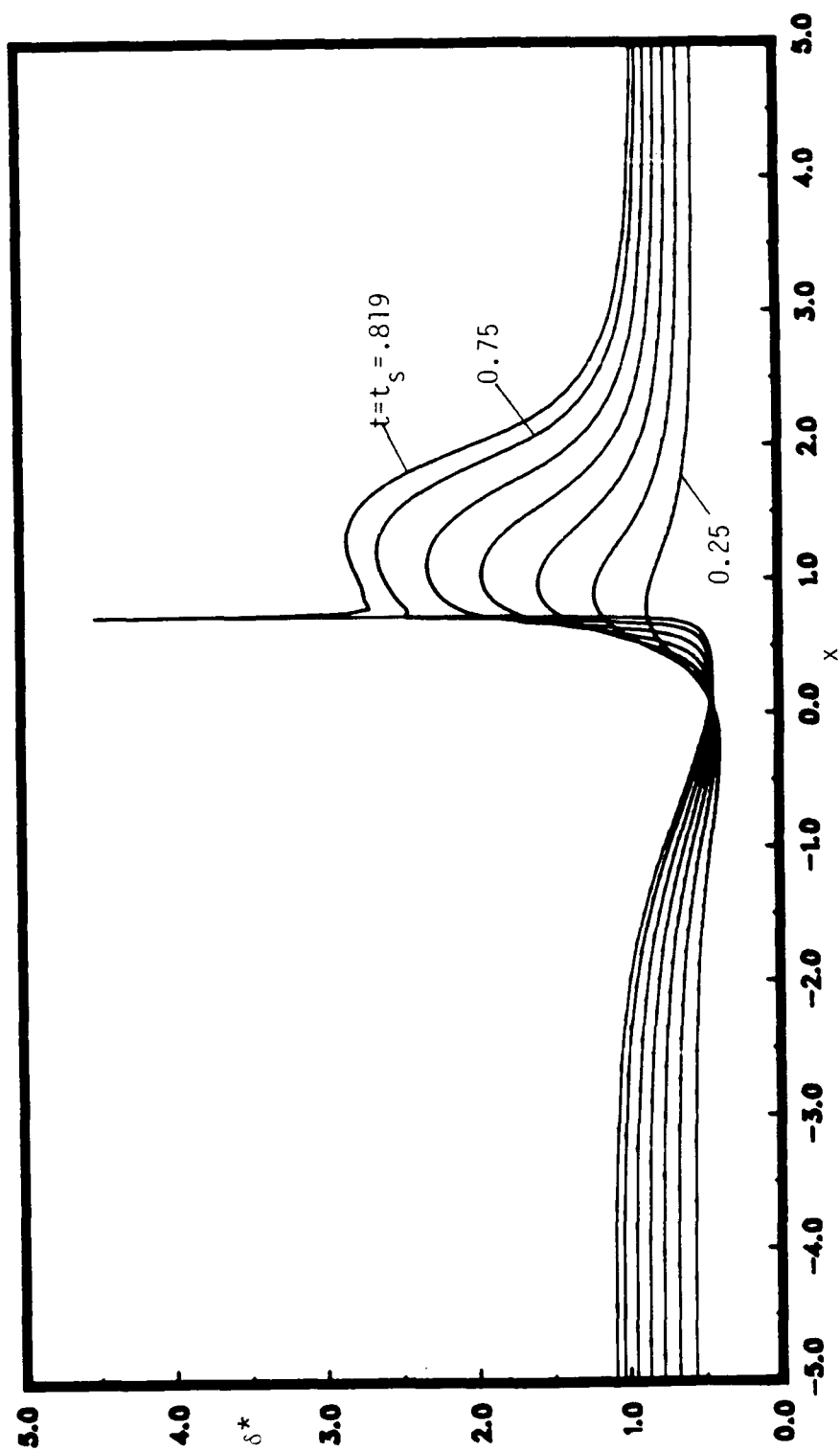
---

<sup>1</sup> The displacement thickness is calculated following the procedure described in Appendix D.

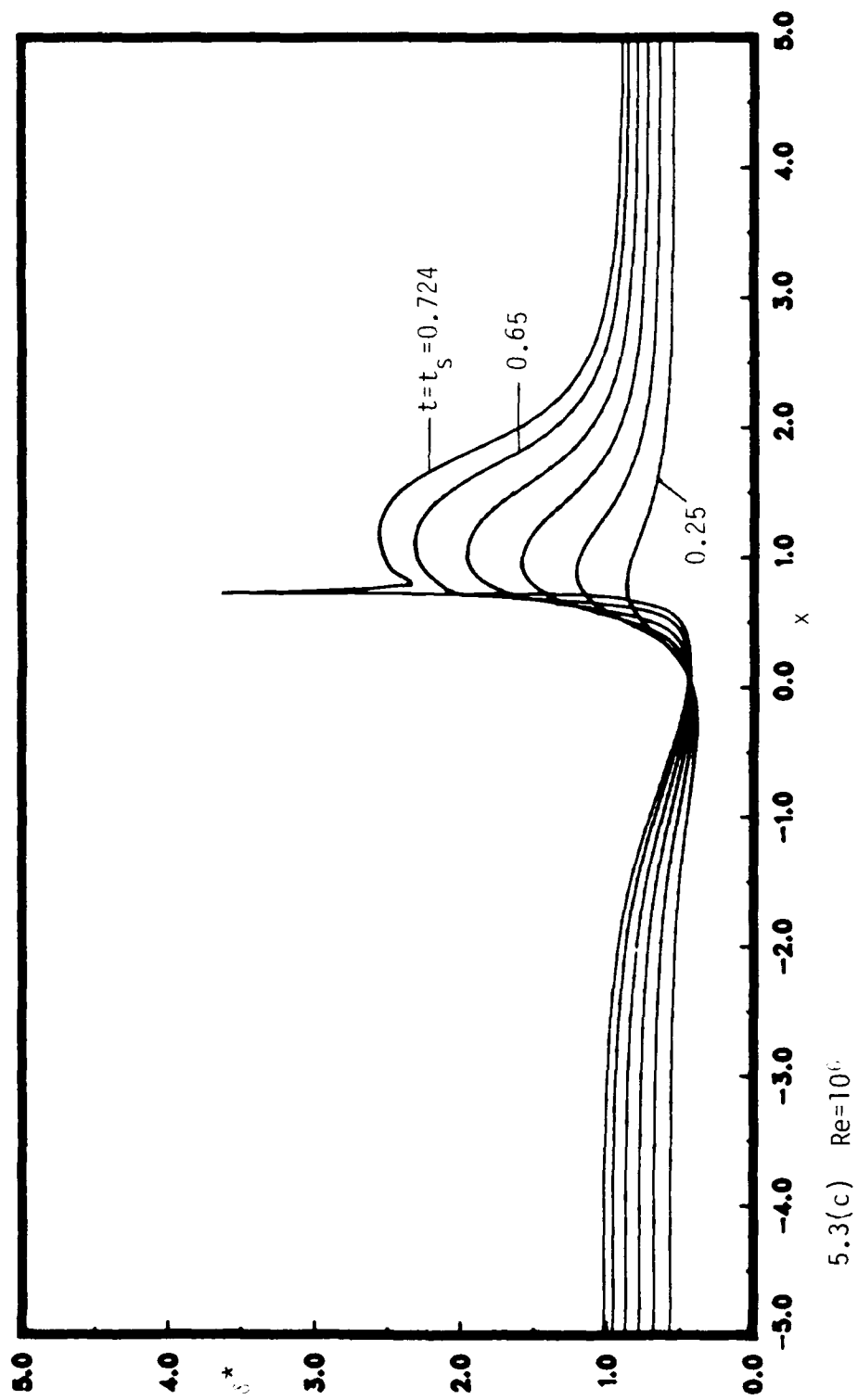


5.3(a)  $Re = 10^8$

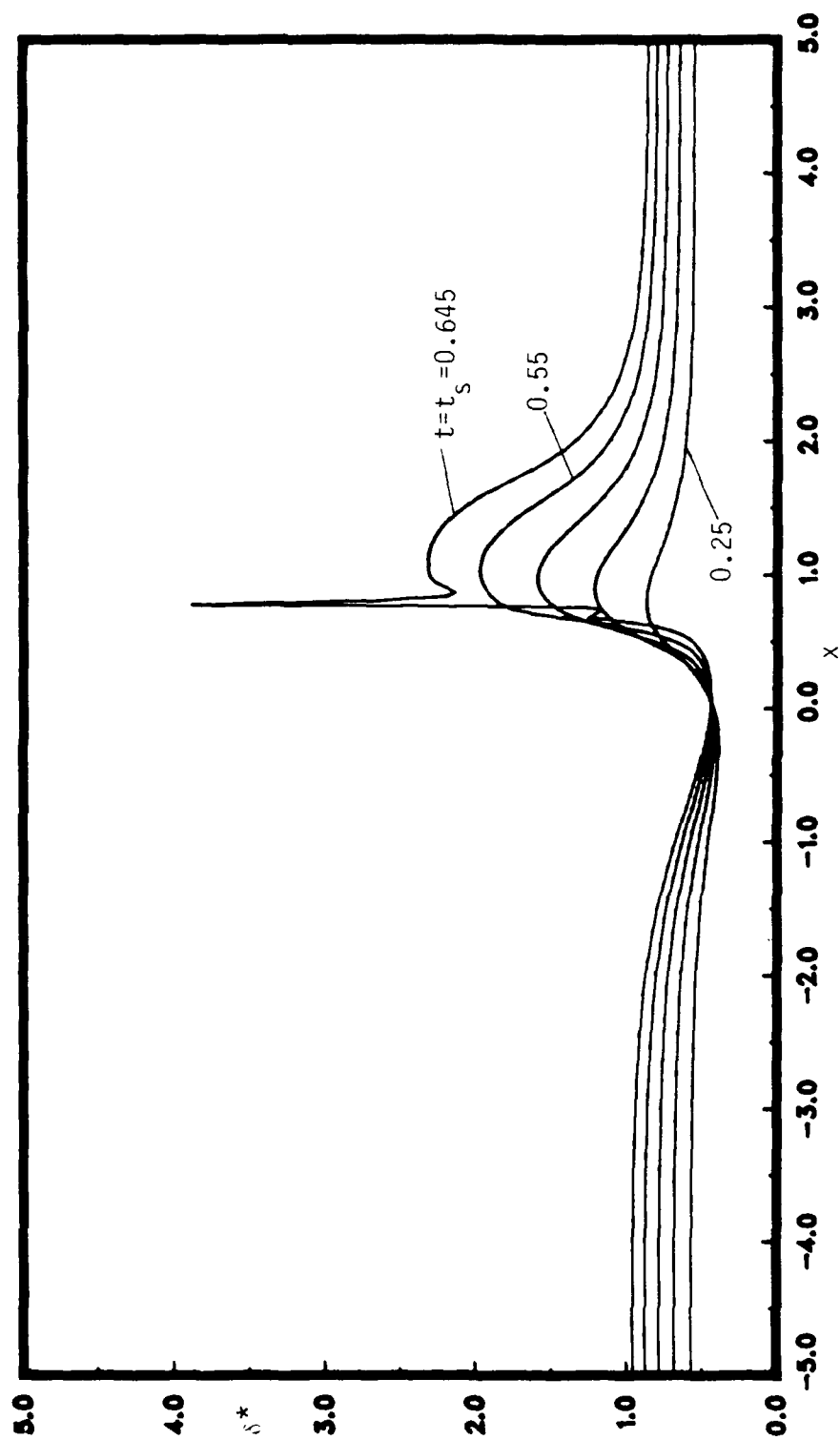
Figure 5.3. Temporal evolution of displacement thickness  $\delta^*$ , at times  $t_0 = 0.25, (0.10), t_s$ ; the results are plotted in the laboratory reference frame.



5.3(b)  $Re=10^7$



5.3(c)  $Re=10^6$



5.3(d)  $Re=10^5$



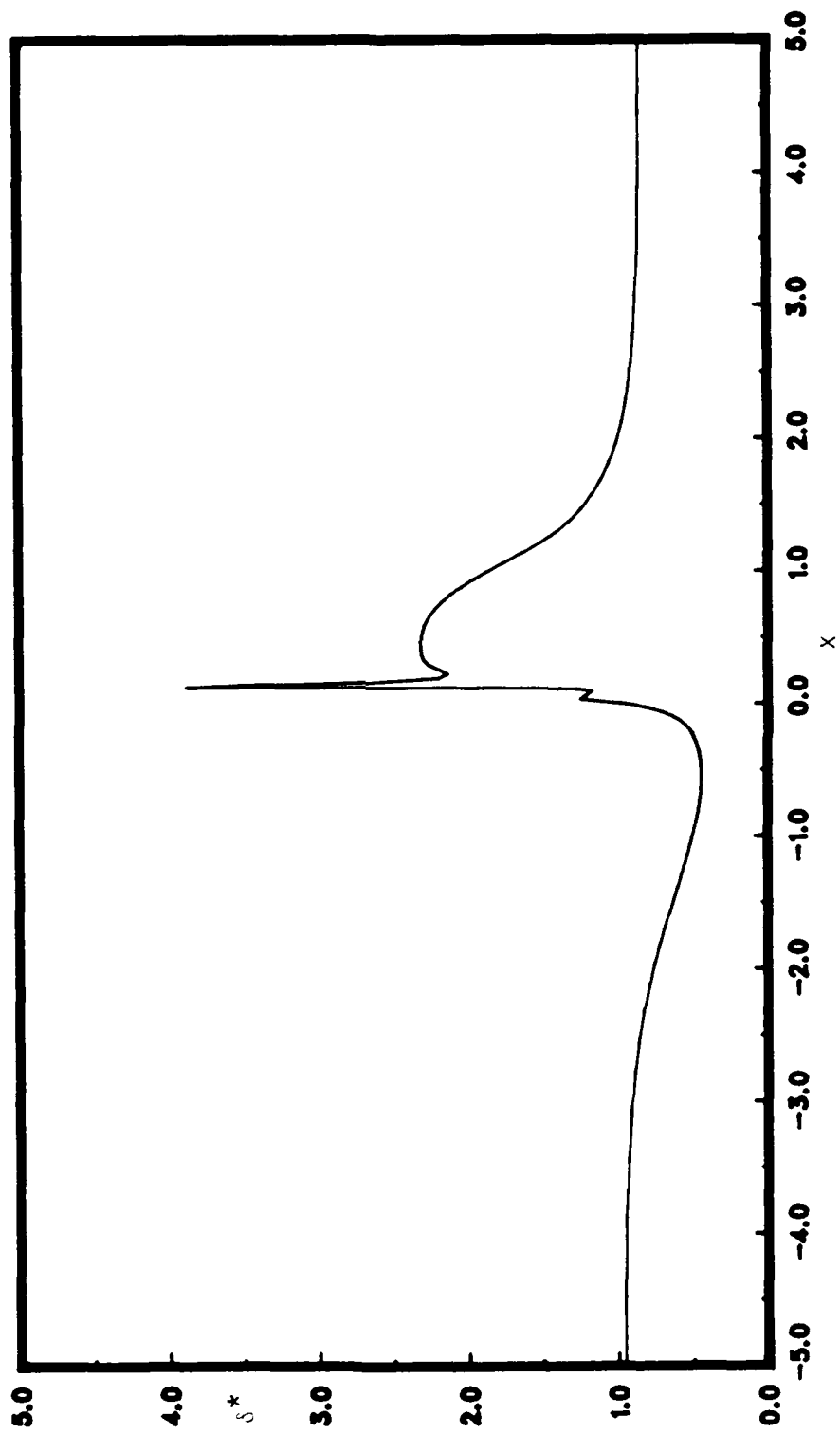


Figure 5.4. Displacement thickness at time  $t_s$  for  $Re=10^5$  in the vortex frame; note that there are two zones where an eruption is developing.

The next set of plots depict the instantaneous streamline contours in the vortex frame, and were obtained as described in Appendix D. Before considering the streamline pattern for each case of finite  $Re$  at the corresponding breakaway time  $t_s$ , it is useful to examine a representative streamline plot in figure 5.5 of the separated boundary-layer flow of the model problem, prior to the onset of interaction. The streamlines under the vortex at  $x=0$  are deflected around a growing recirculation zone. Note that at this stage the streamline plots for all Reynolds numbers look essentially the same. This is in remarkable contrast to the four streamline plots of figures 5.6, which show the streamline contours at  $t_s$  for each case of finite  $Re$ . Consider first figure 5.6(a), for  $Re=10^8$ ; the boundary-layer flow is quite smooth except near  $x_s=-.15$ , where sharp kinks occur in the streamlines at the interface between the recirculating eddy and the zone upstream and to the left. The kink in the streamlines is due to the eruptively growing interaction region on the left side of the eddy. The smooth streamlines approaching the eddy from upstream are deflected abruptly; after reaching the top of a "spike", a streamline falls almost vertically before once again becoming smooth to the right of the eruptive zone. Note that the main influence of the eruption is confined to a very narrow region near  $x_s$ . These same flow characteristics are evident in figure 5.6(b), in which streamline contours at  $t_s$  are depicted for  $Re=10^7$ . In this plot the secondary eddy is smaller than that of the  $Re=10^8$  case at  $t_s$ , mainly because the singularity occurs at an earlier stage in the flow evolution for  $Re=10^7$ . The kink in the streamline contours for the  $Re=10^7$  case is at  $x_s=-.09$ . For  $Re=10^6$  the breakdown time is earlier still at  $t_s=.724$ , and the eruption, as seen in figure 5.6(c) occurs just beneath the vortex at  $x_s=0$ . With decreasing Reynolds numbers, the flow becomes increasingly complex near the "spike". On an enlarged scale in figure 5.6(d), it may be seen that the secondary vortex (labeled "a") has split into two co-rotating vortices "a.1" and "a.2" in the interior of "a". There is also a tertiary vortex present (a

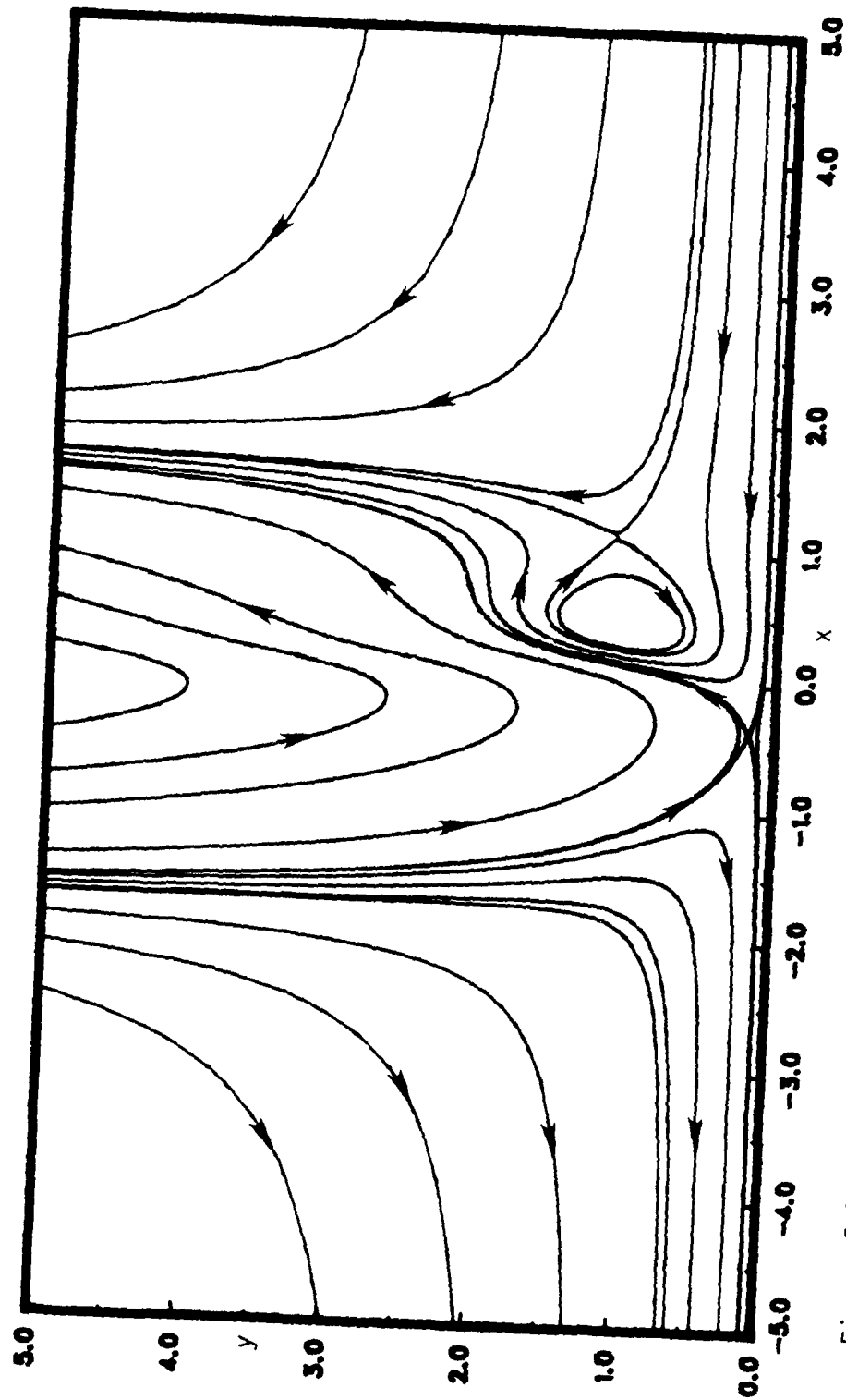
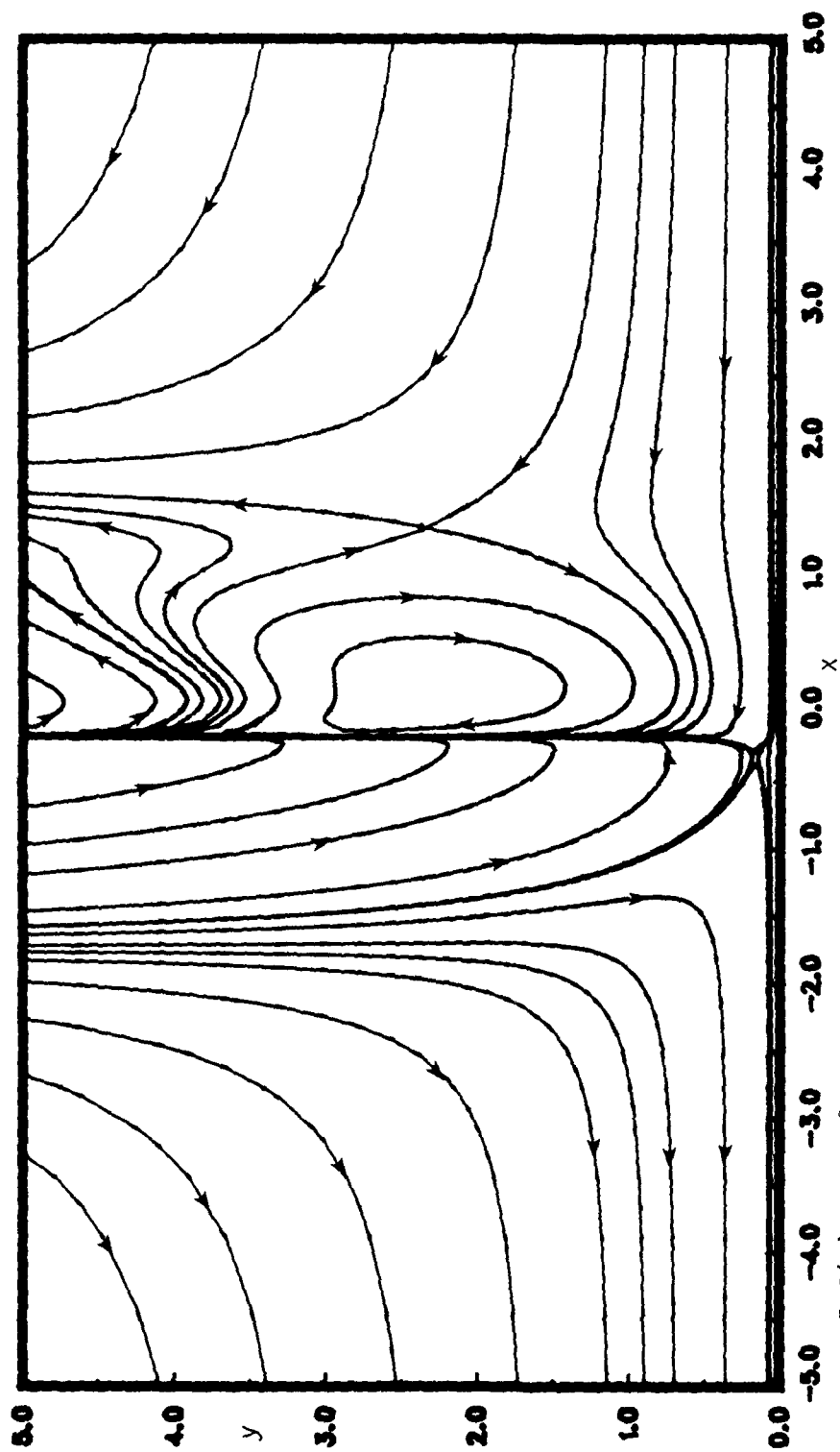
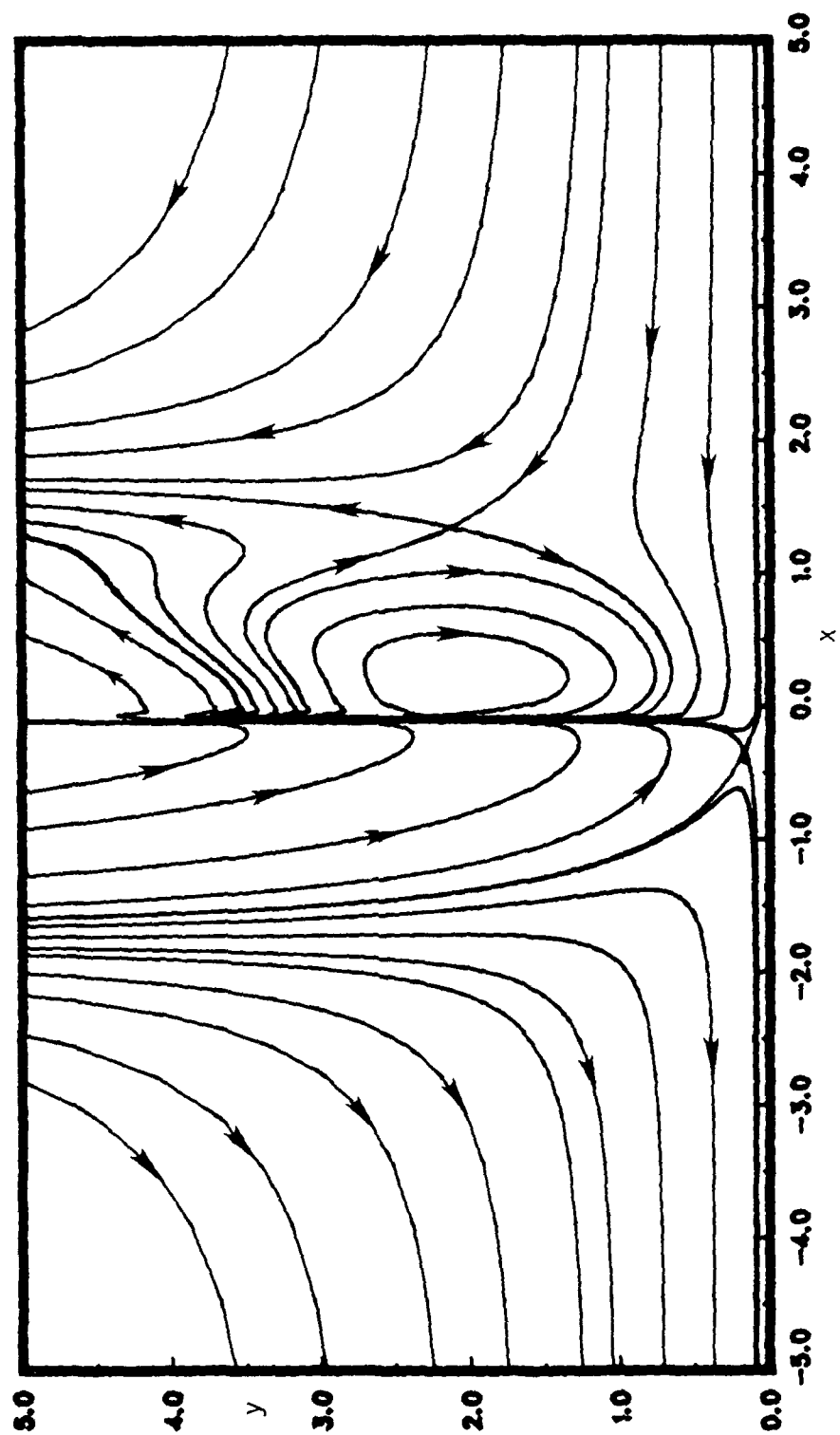


Figure 5.5. Typical streamline contours after separation and prior to breakaway  
( $Re=10^5$ ,  $t=0.45$ ).

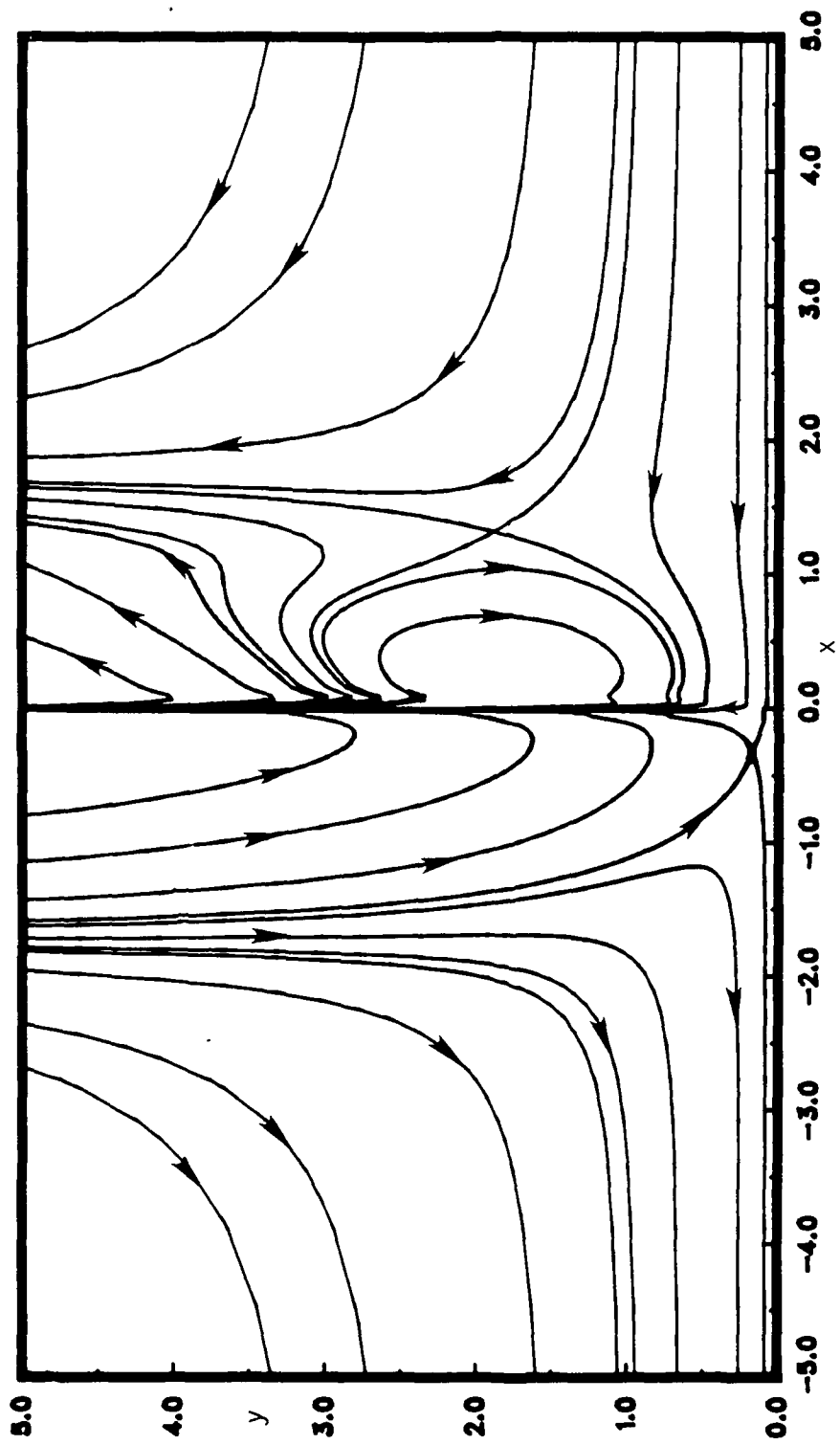


5.6(a)  $Re=10^8$

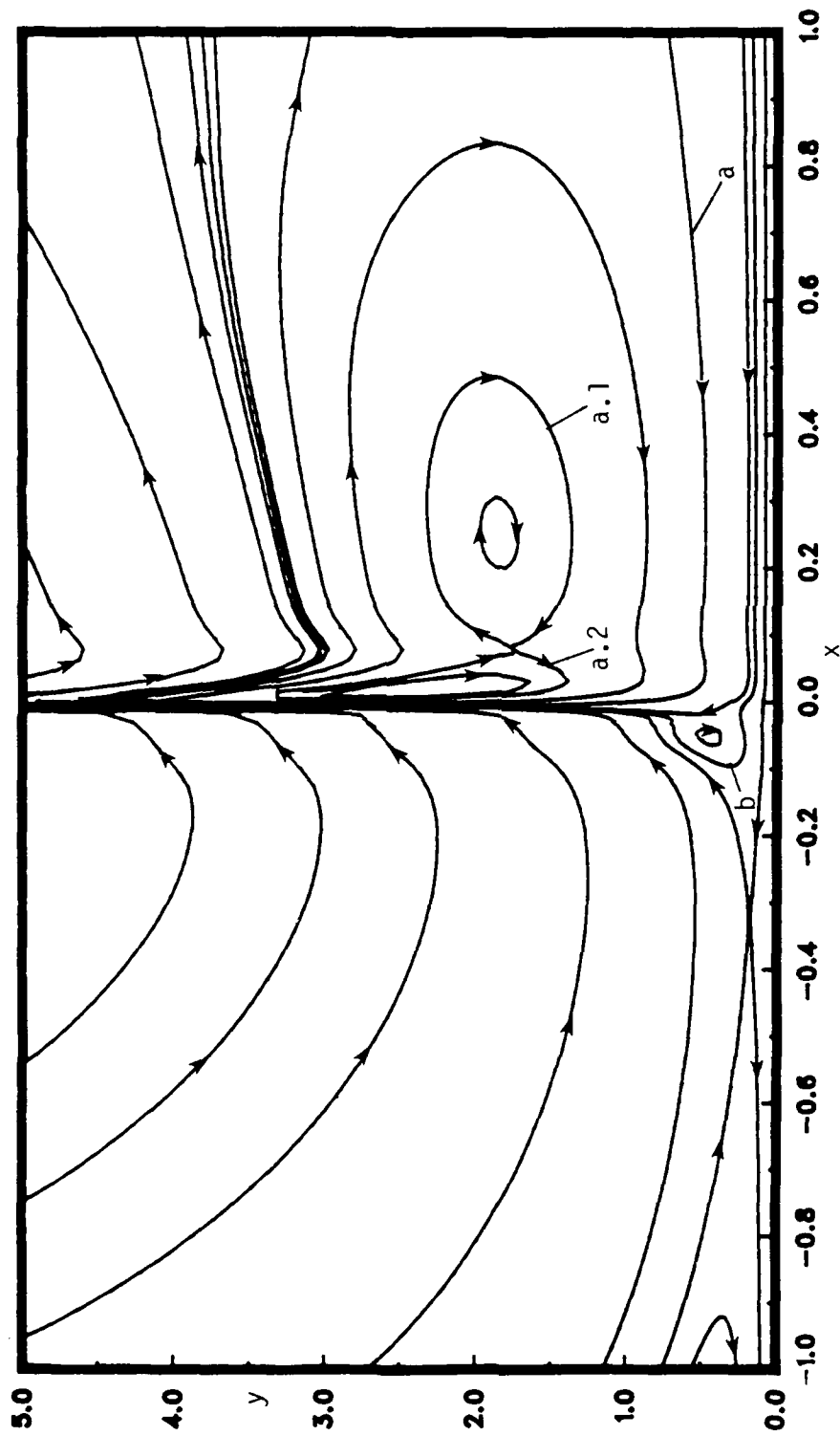
Figure 5.6. Streamlines at  $t_s$  in the vortex frame.



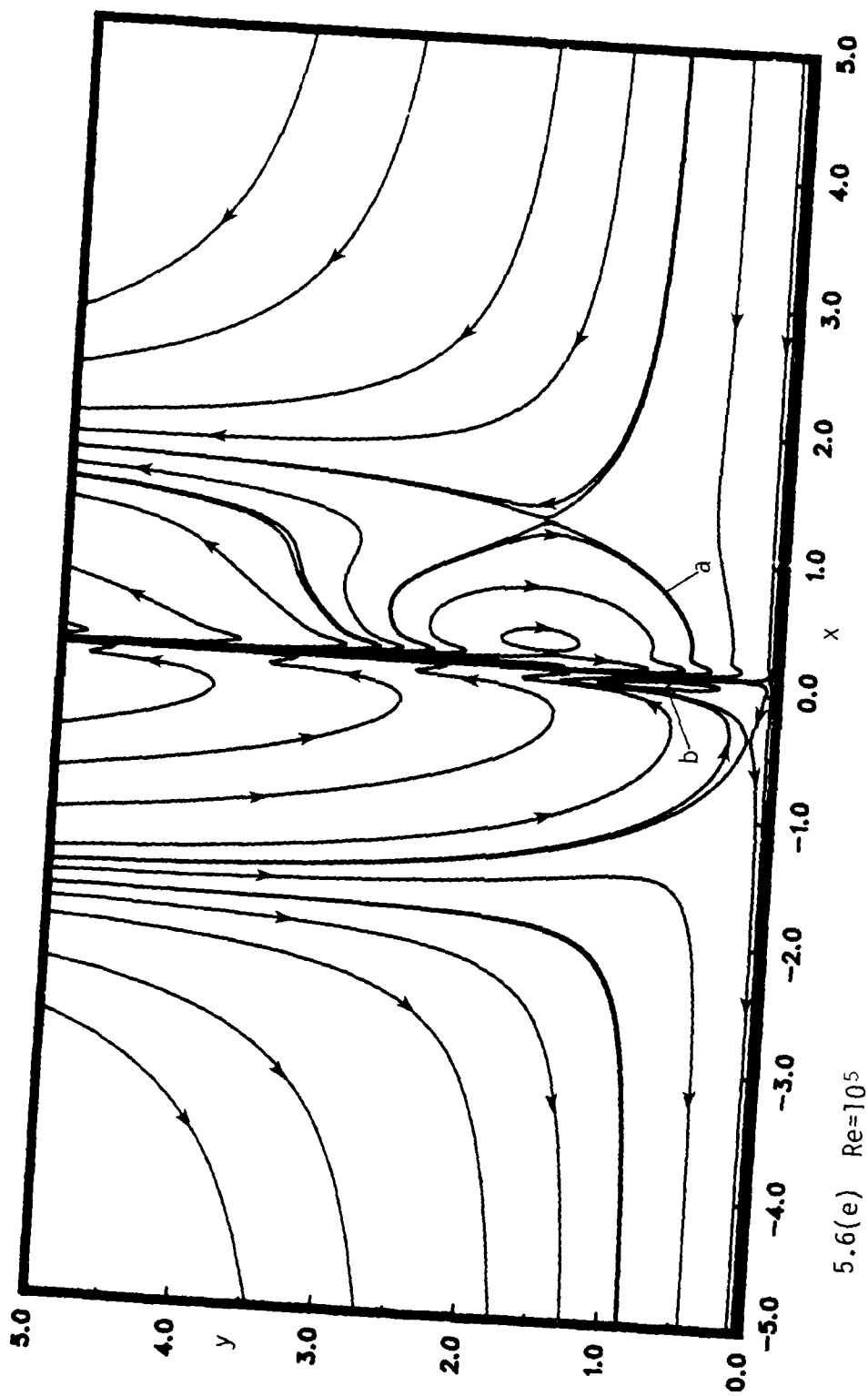
5.6(b)  $Re=10^7$



5.6(c)  $\text{Re}=10^6$

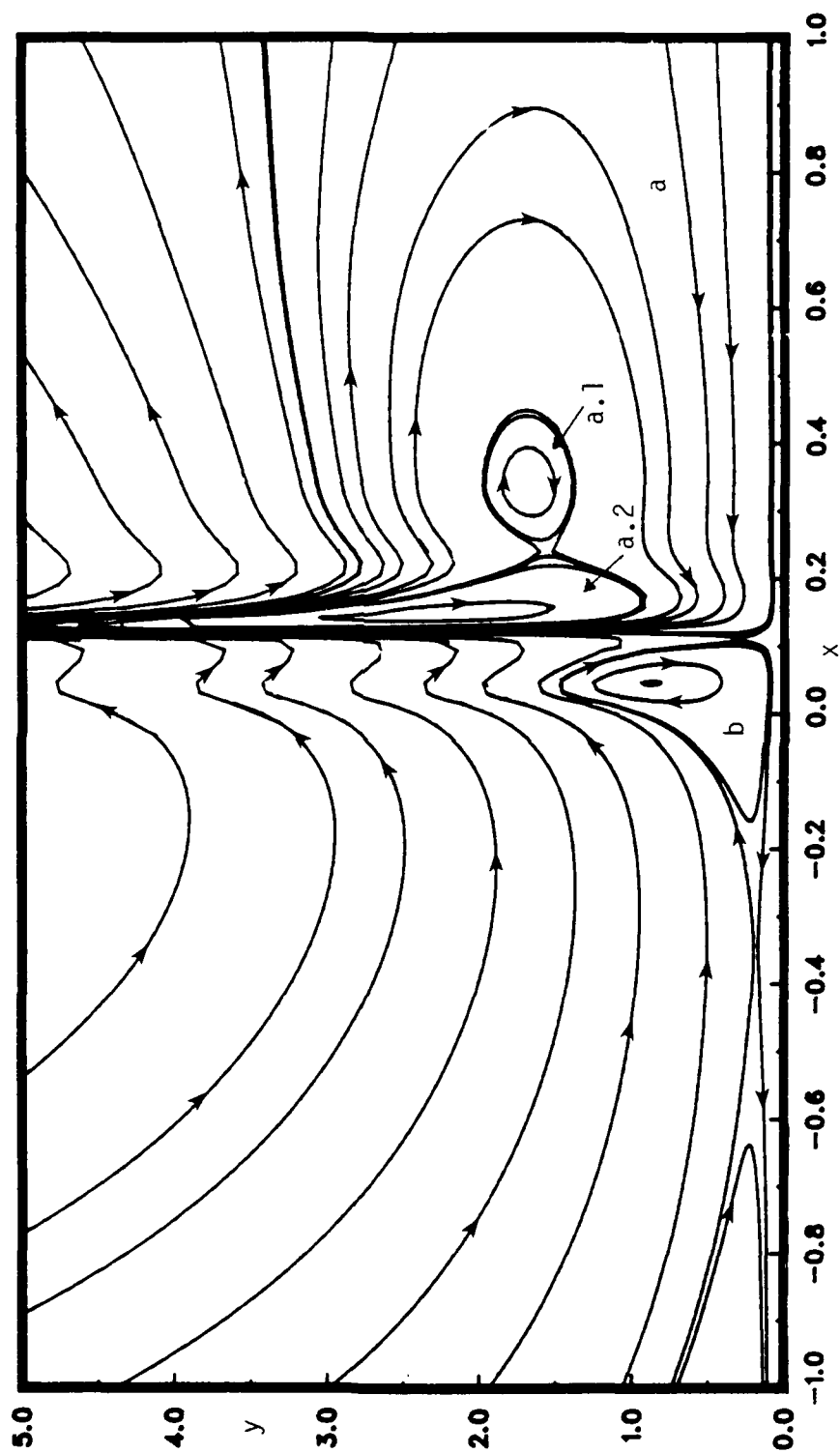


5.6(d)  $Re=10^6$  on an enlarged scale



5.6(e)  $\text{Re}=10^5$





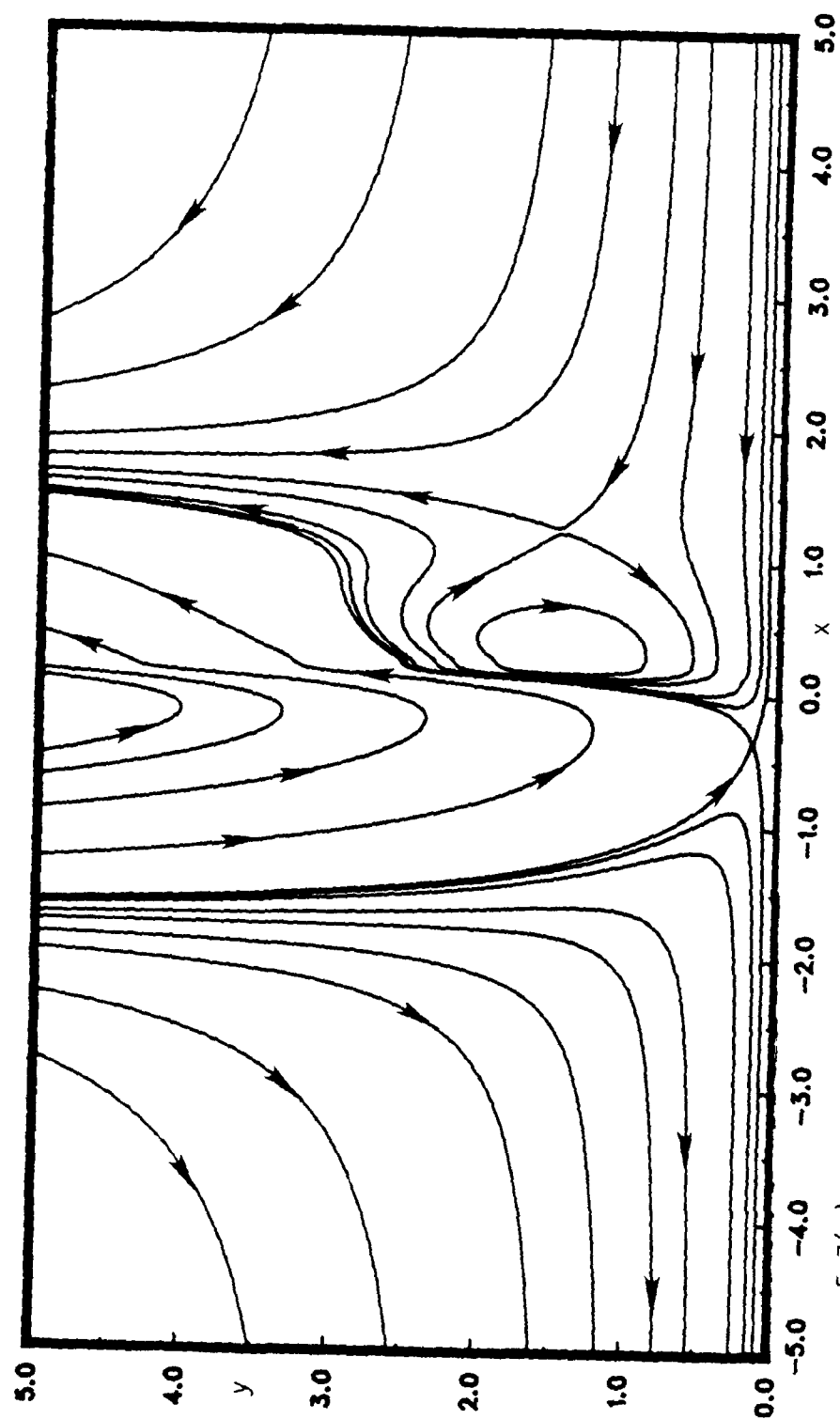
5.6(f)  $Re=10^5$  on an enlarged scale

portion of which is labeled "b" in figure 5.6(b)), which also has that same sense of rotation as the secondary eddy "a". A tertiary eddy also forms in the  $Re=10^5$  case, shown in figure 5.6(e). This plot has two distinct regions of streamline kinking: (1) the enormous streamline kink associated with the boundary-layer breakdown at  $x_s=.124$ ; and (2) a smaller kink near  $x=0$  associated with the tertiary eddy, which corresponds to the second small spike previously noted in the displacement thickness in figure 5.5. The large kink is due to boundary-layer breakdown promoted by the strong interactions at the left face of the secondary eddy, labeled "a" in figure 5.6(e). The smaller kink is due to an independent interaction that develops on the left face of a tertiary eddy, labeled "b" in figure 5.6(e); this interaction is in the process of evolving toward an eruptive state when the calculation terminates at  $t_s$ , due to the primary interaction associated with eddy "a". The vorticity sub-structure near  $x=0$  is more clearly appreciated in the magnified view of the streamline contours provided by figure 5.6(f). Here, like  $Re=10^6$ , it is interesting to note that the original secondary eddy encompasses two internal sub-eddies labeled "a.1" and "a.2". All four eddies are embedded deep in the viscous layer and have vorticity of opposite sign to the parent vortex in the inviscid flow. The formation of a tertiary eddy was also observed by Chuang and Conlisk (1989) in their interacting calculation of the vortex convected in a uniform flow above the wall. The development of a tertiary counter-rotating vortex has also been observed experimentally by Walker *et al* (1987) in their study of the impact of a vortex ring on a wall; the tertiary vortex was seen to eventually erupt from the boundary layer. In the present study for  $Re=10^5$  the tertiary eddy does interact with the outer flow; however this interaction has not quite reached the point of eruption before the singularity associated with the stronger interaction occurs with the secondary eddy "a".

The formation of the tertiary vortex, and the bifurcation of the

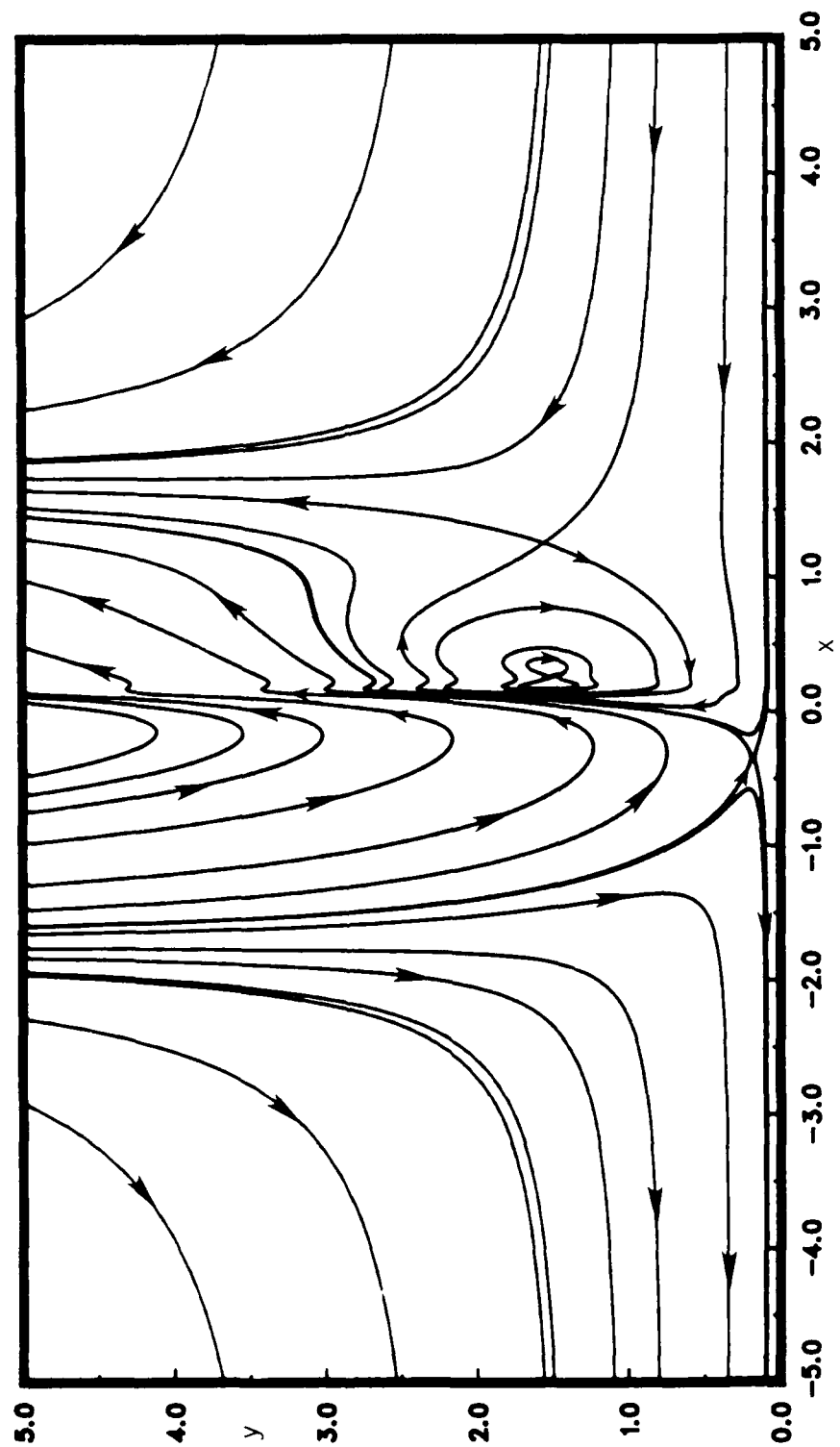
secondary eddy, are illustrated in the sequence in figures 5.7. At time  $t=0.58$  (figure 5.7(a)) the complex, bifurcated eddy structure has not yet begun to form. However, by time  $t=0.60$  (figure 5.7(b)) the internal subdivision of the secondary eddy into two sub-eddies is seen to have occurred. By time  $t=0.62$  (figures 5.7(c) and 5.7(d), on an enlarged scale) the flow patterns which immediately precede the evolution of the tertiary vortex is depicted. By  $t=0.63$  the tertiary vortex has formed, as seen in figures 5.7(e) and 5.7(f) on an enlarged scale.

Next, consider figure 5.8 which illustrates contours of constant vorticity  $\omega$  for the case of  $Re=10^8$  at  $t_s$ . The singularity forms on the zero-vorticity line. The nature of the vorticity field for the  $Re=10^8$  case at  $t_s$  is quite similar to that of the limit problem (figure 4.5(d)), as are the vorticity fields for the  $Re=10^7, 10^6$  cases. However, the vorticity field for the  $Re=10^5$  case is somewhat more complex because this case has two distinct regions of strong interaction. To illustrate the evolution of the vorticity field for the  $Re=10^5$  case consider figures 5.9, which depicts the vorticity field at successive times between  $t=.58$  and  $t_s=.645$ . The very orderly and smooth contours of  $\omega$  at  $t=.58$ , depicted in figure 5.9(a), scarcely prefigure the impending eruption at  $t_s=.645$ . At time  $t=0.60$ , shown in figure 5.9(b), the inverted "V" pattern observed in the limit problem (c.f. §4.4) has begun to form. The spike in the vorticity contours is first seen in the plot corresponding to  $t=0.62$ , shown in figure 5.9(c); this spike heralds the onset of the breakdown associated with the secondary vortex. Figure 5.9(d) illustrates the vorticity fields at  $t=0.63$ . The tertiary eddy is formed by time  $t\sim 0.63$ , and in the next plot (figure 5.9(e)), at time  $t=0.64$  the first hint of vorticity-line kinks associated with the interaction near the tertiary eddy are visible. The vorticity field at  $t_s$  shown in figure 5.9(f). The vorticity contours now have a very distinct kink just to the left of the eruption zone at  $x_s=.125$ , and these are due to the interaction

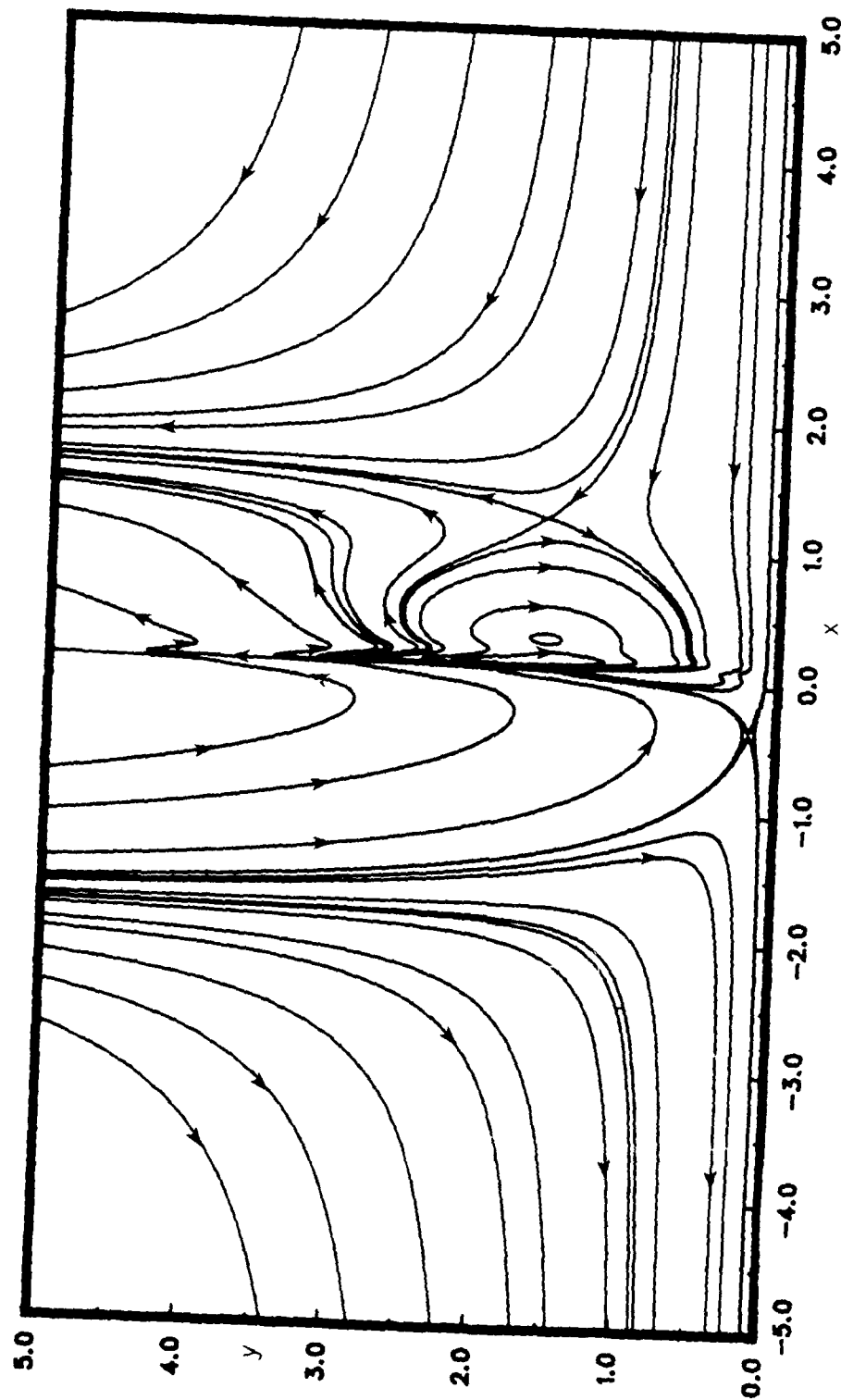


5.7(a)  $t=0.58$

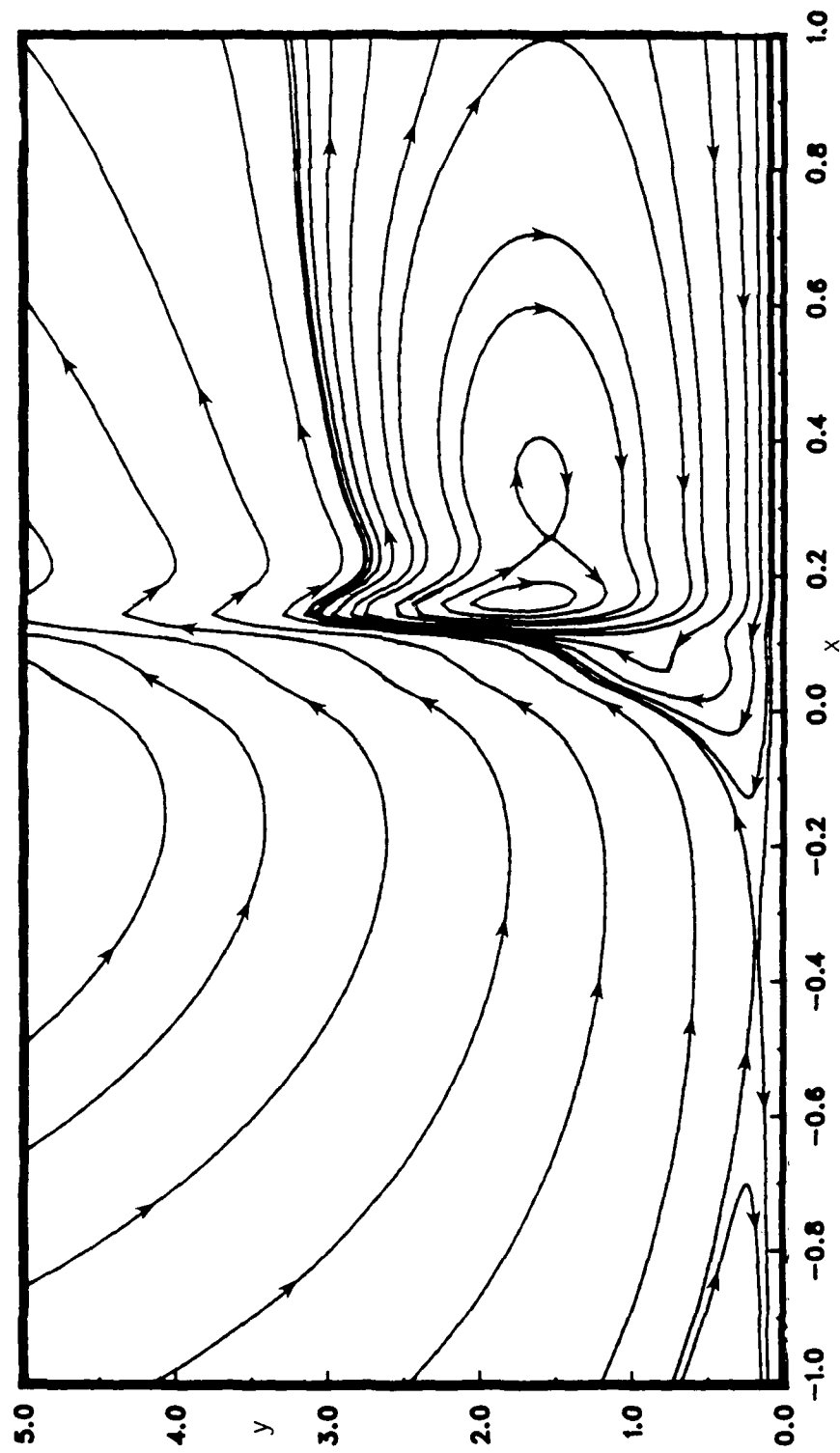
Figure 5.7. Temporal evolution of streamline contours for  $Re=10^5$ .



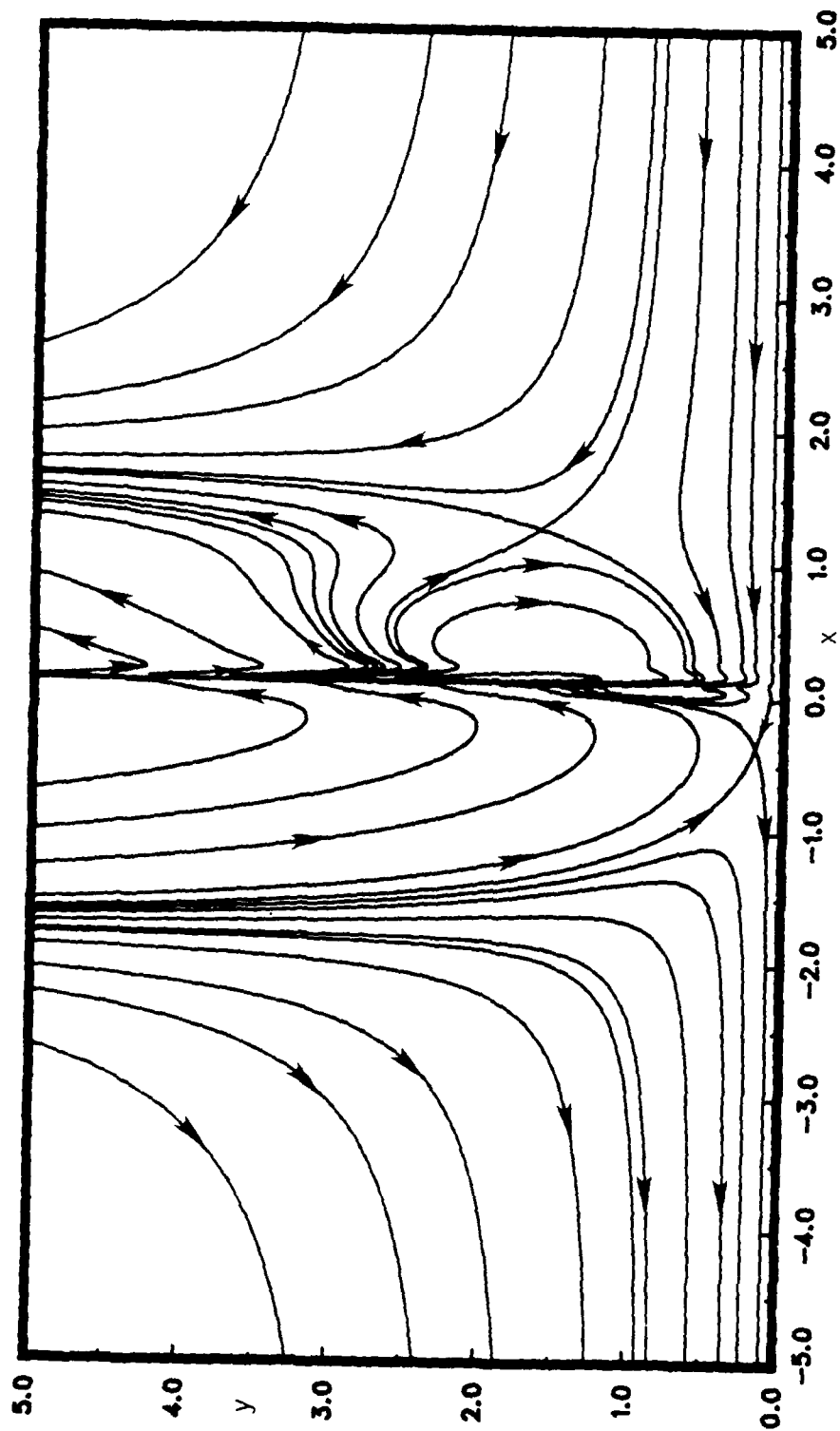
5.7(b)  $t=0.60$



5.7(c)  $t=0.62$

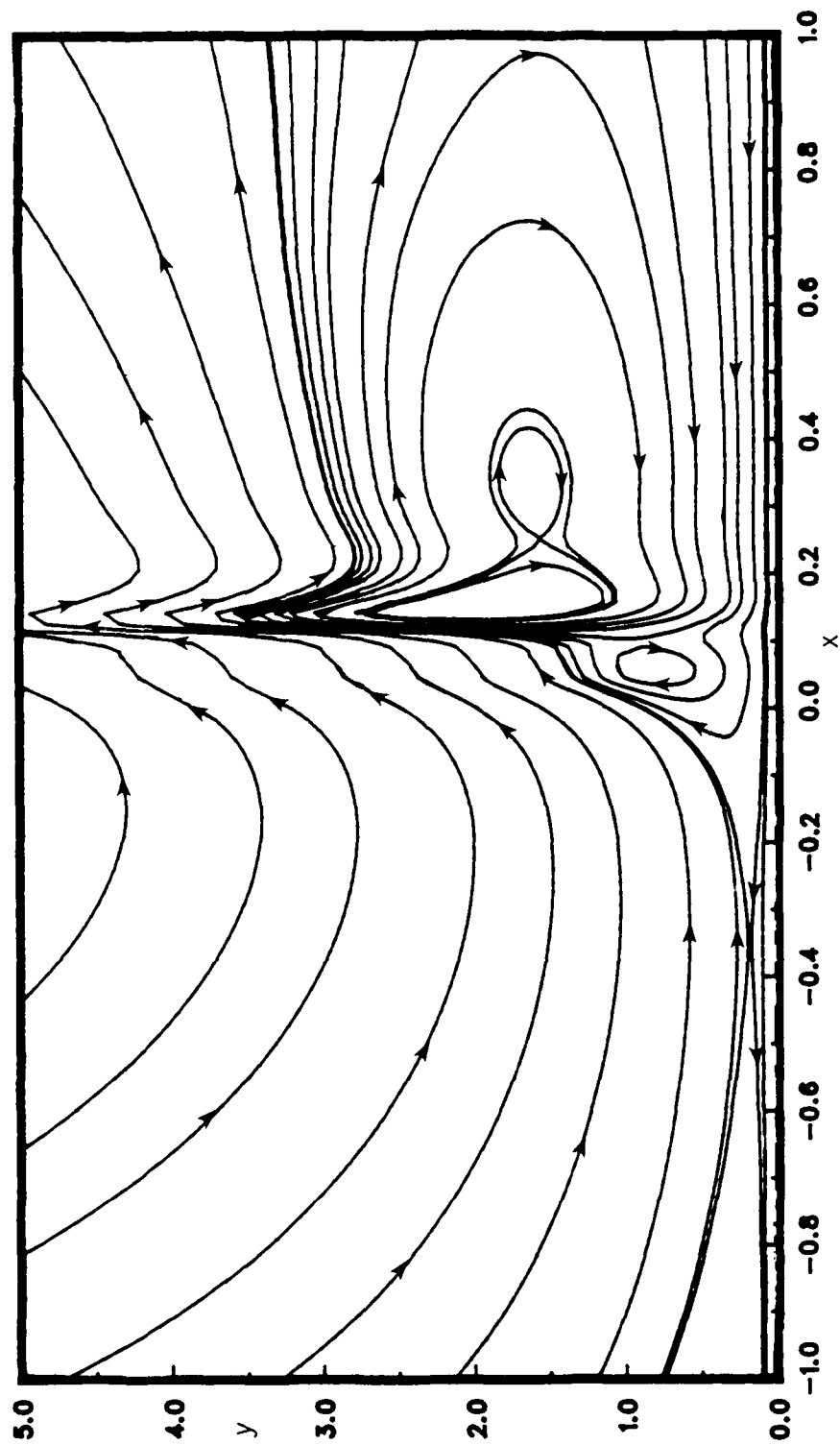


5.7(d)  $t=0.62$  on an enlarged scale



5.7(e)  $t=0.63$





5.7(f)  $t=0.63$  on an enlarged scale; the stagnation point at  $(0.1, 1.0)$  is difficult to plot.

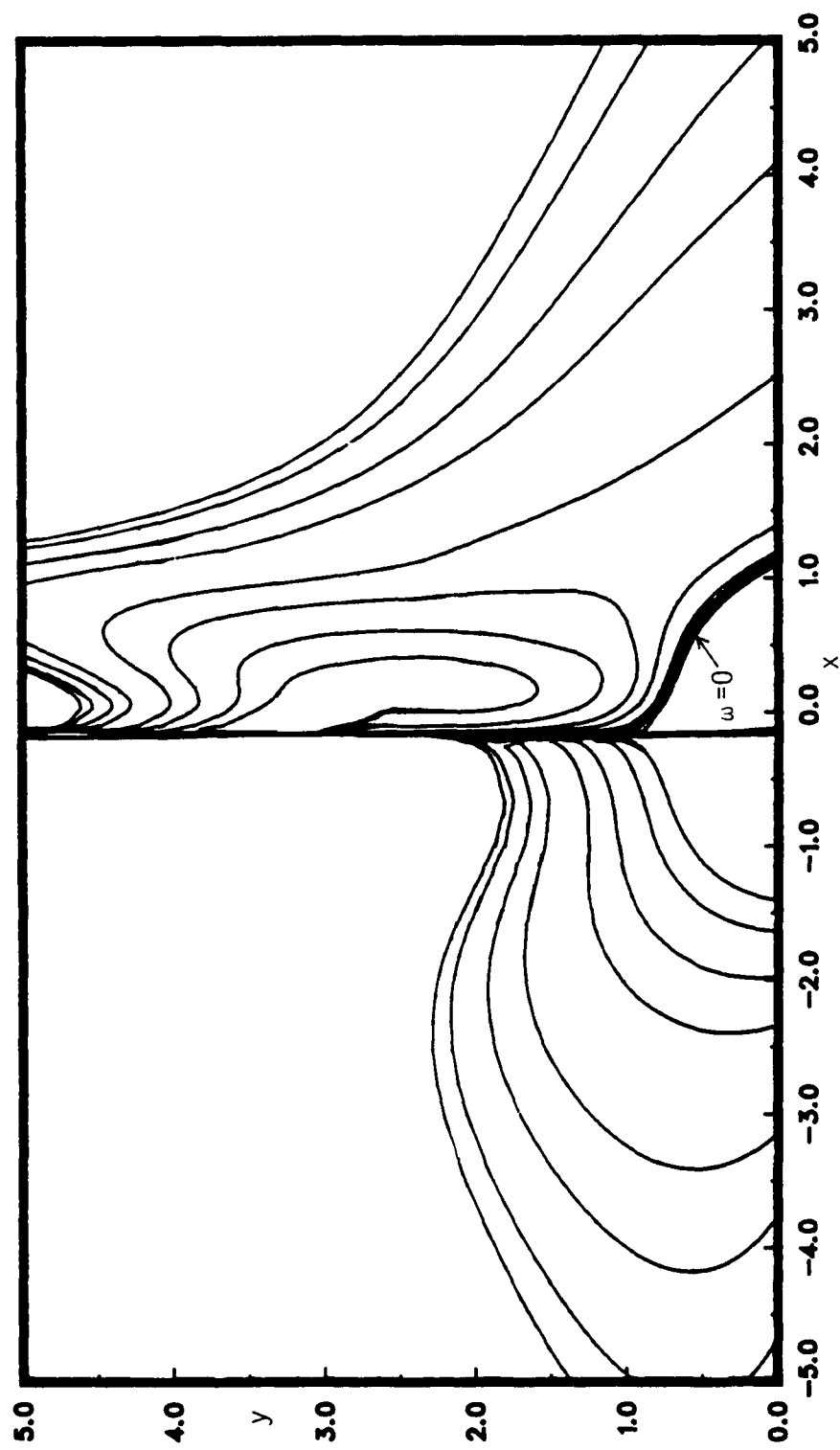


Figure 5.8. Vorticity field at breakthrough time  $t_s$ , for  $Re=10^8$ .

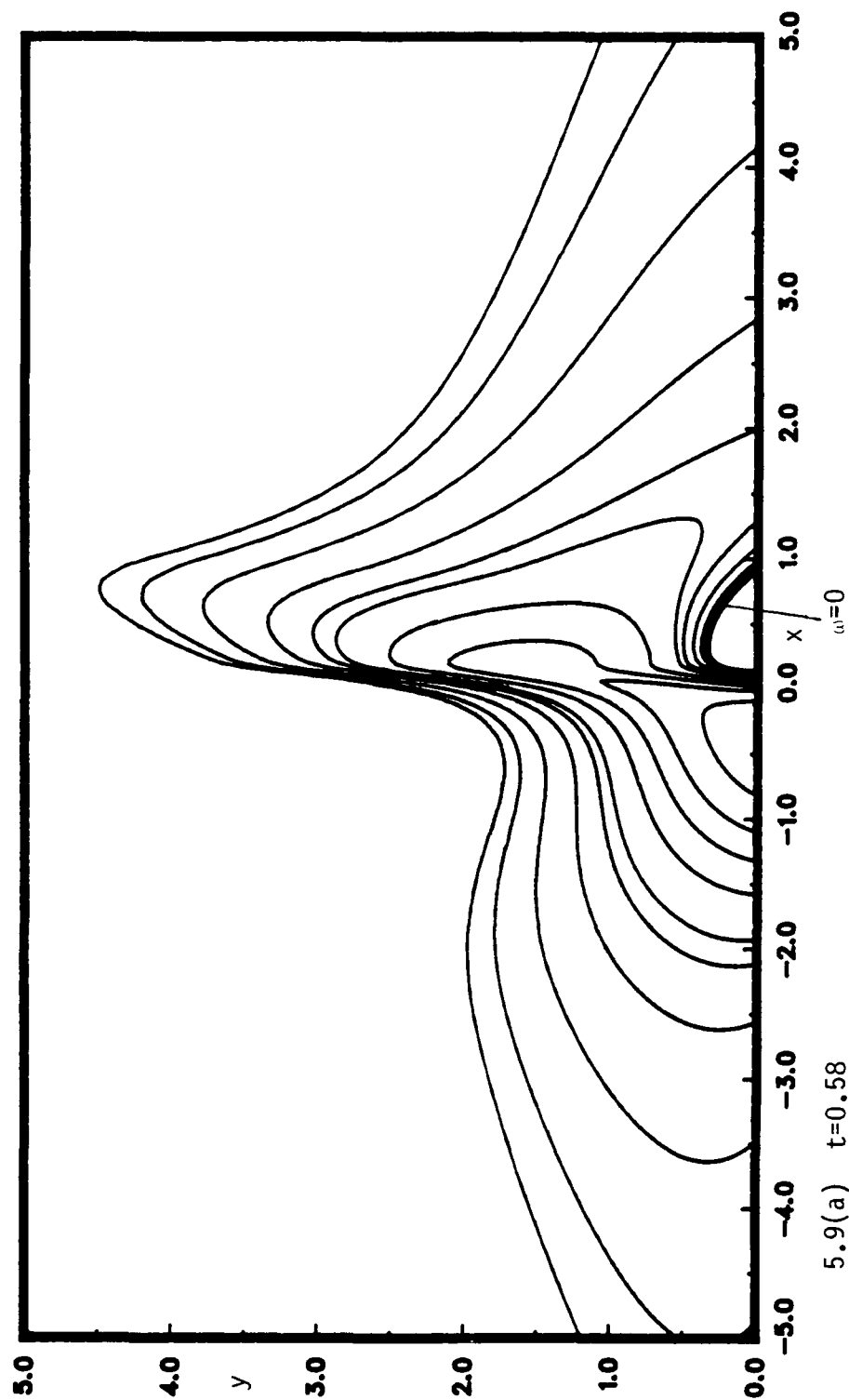
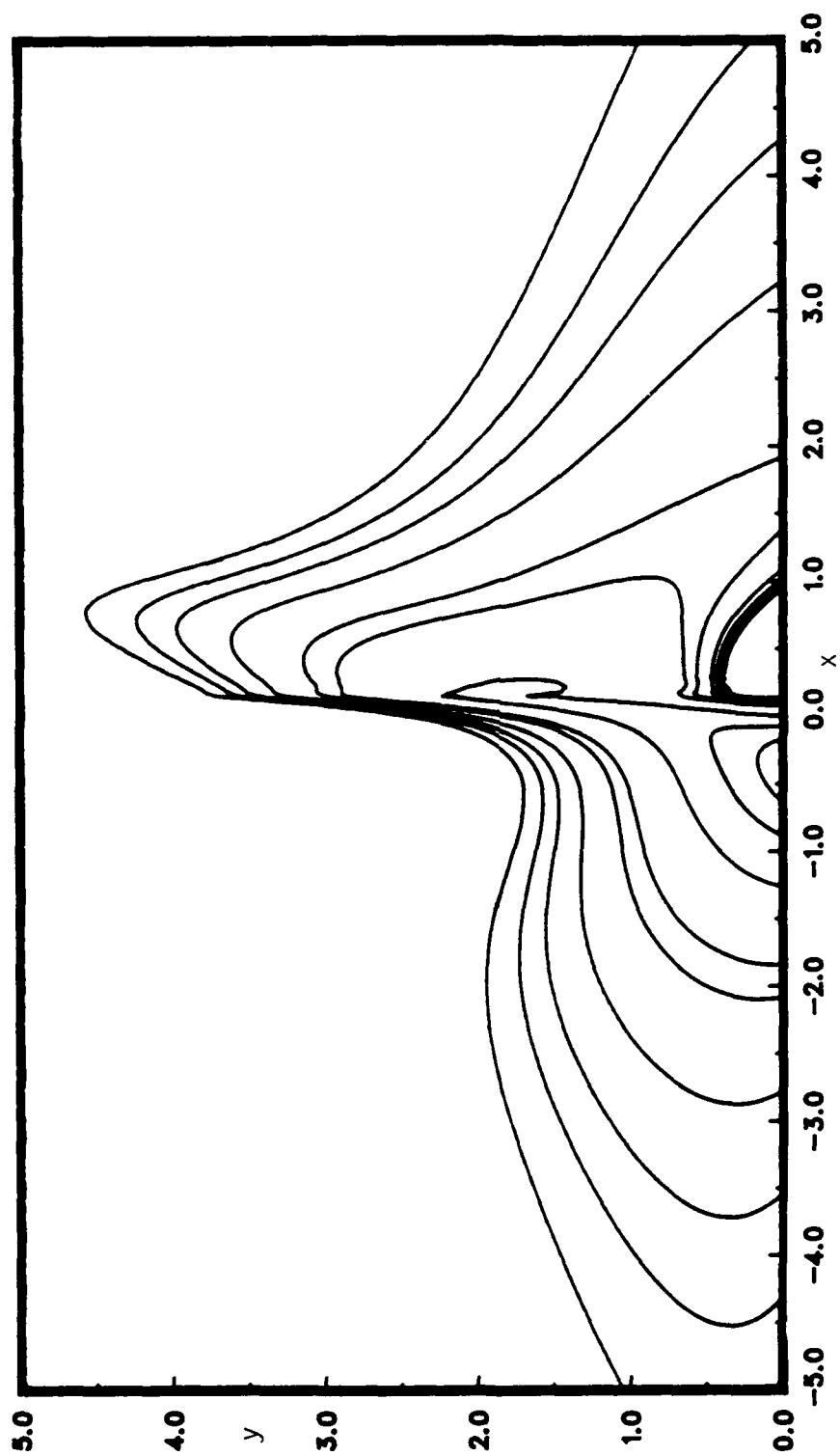
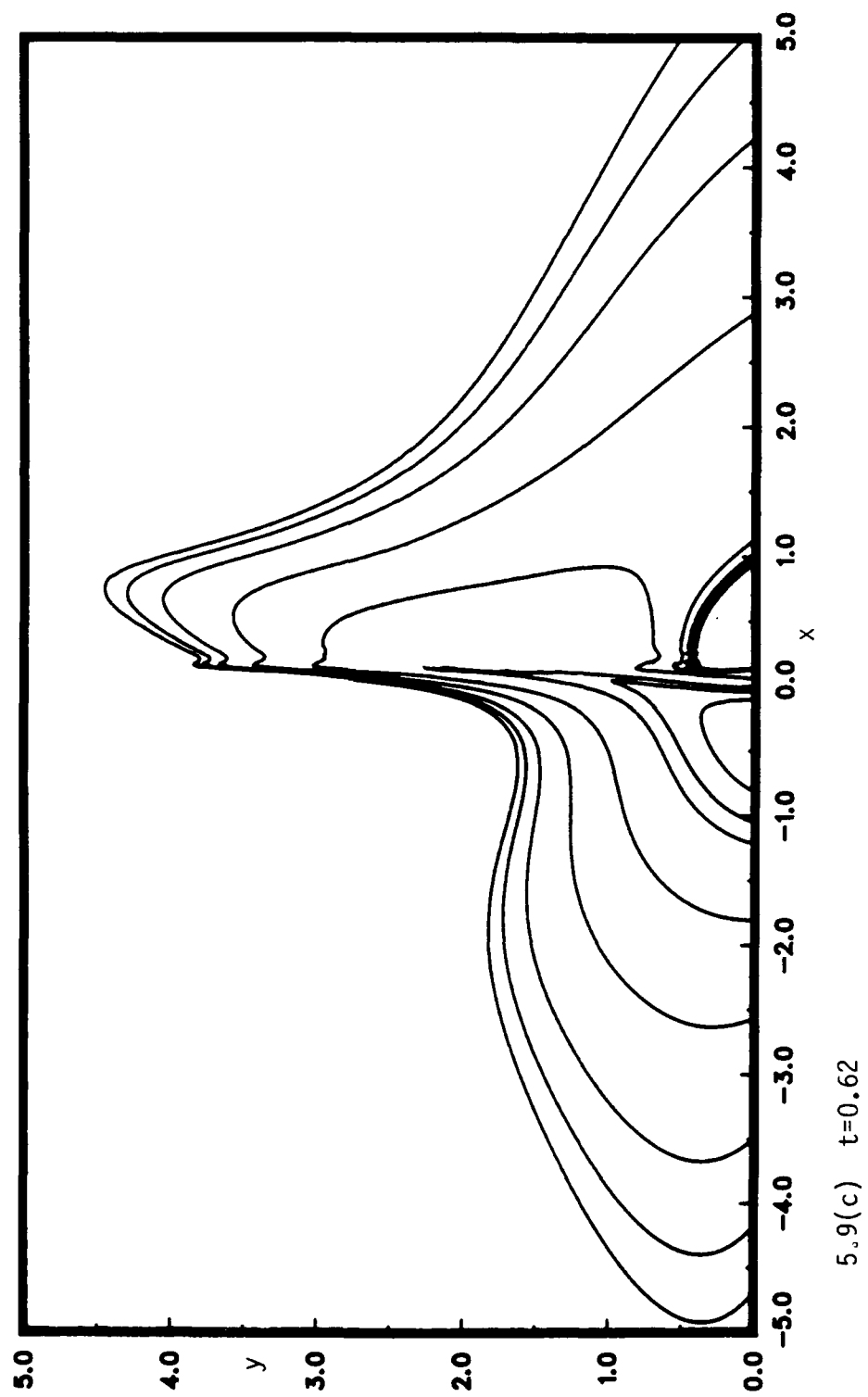
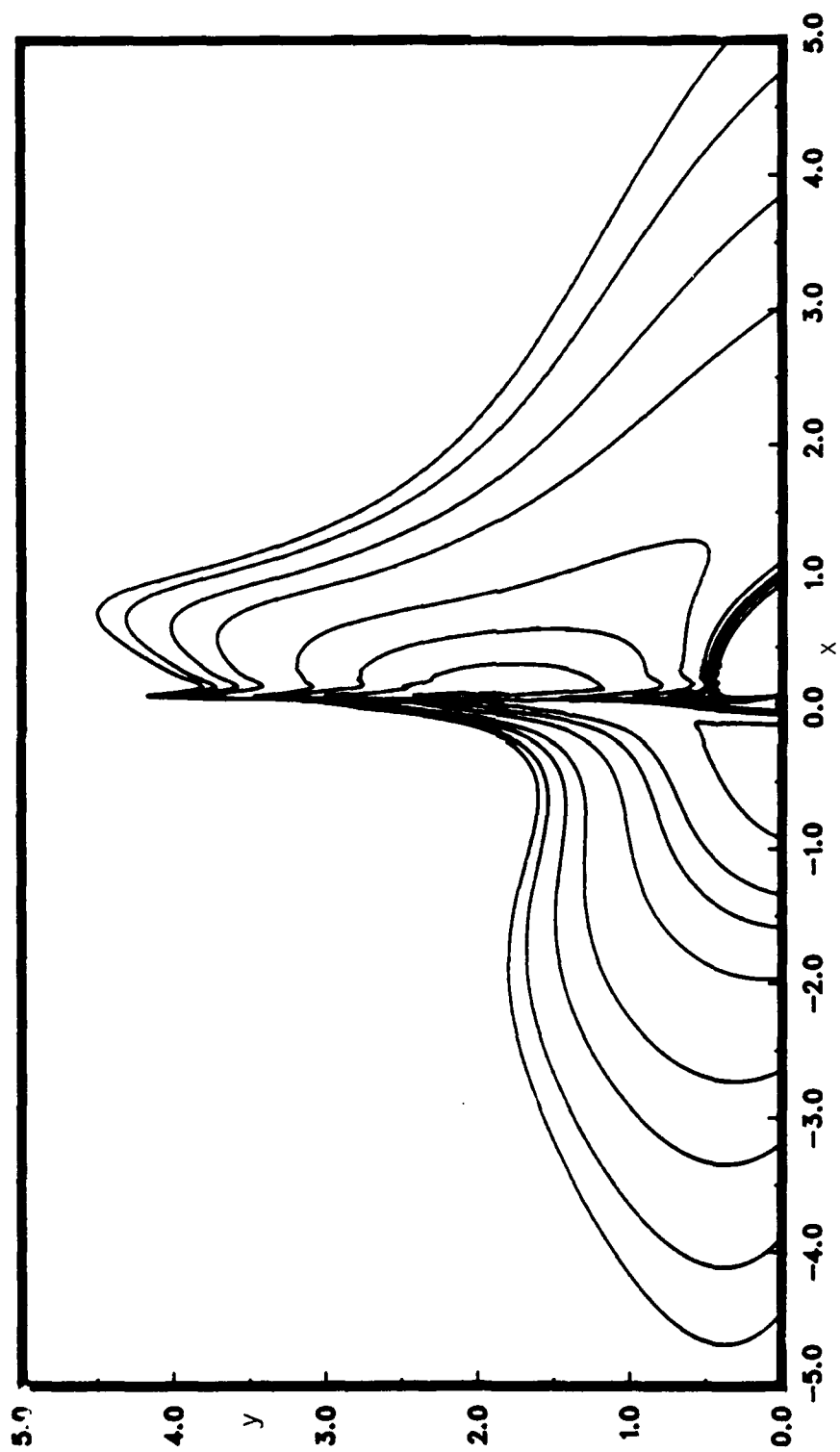


Figure 5.9. Vorticity field for  $Re=10^5$  at successive times.

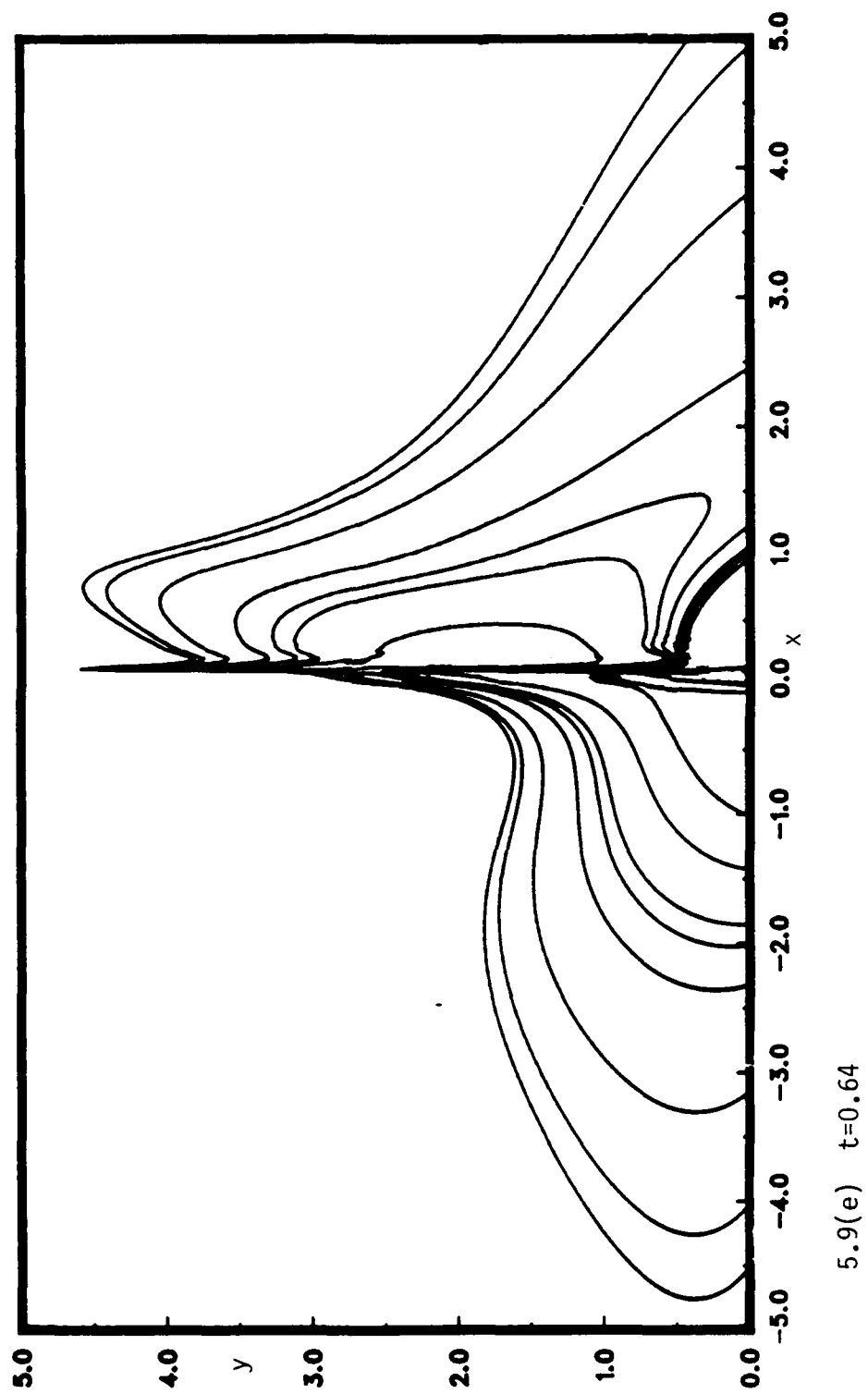


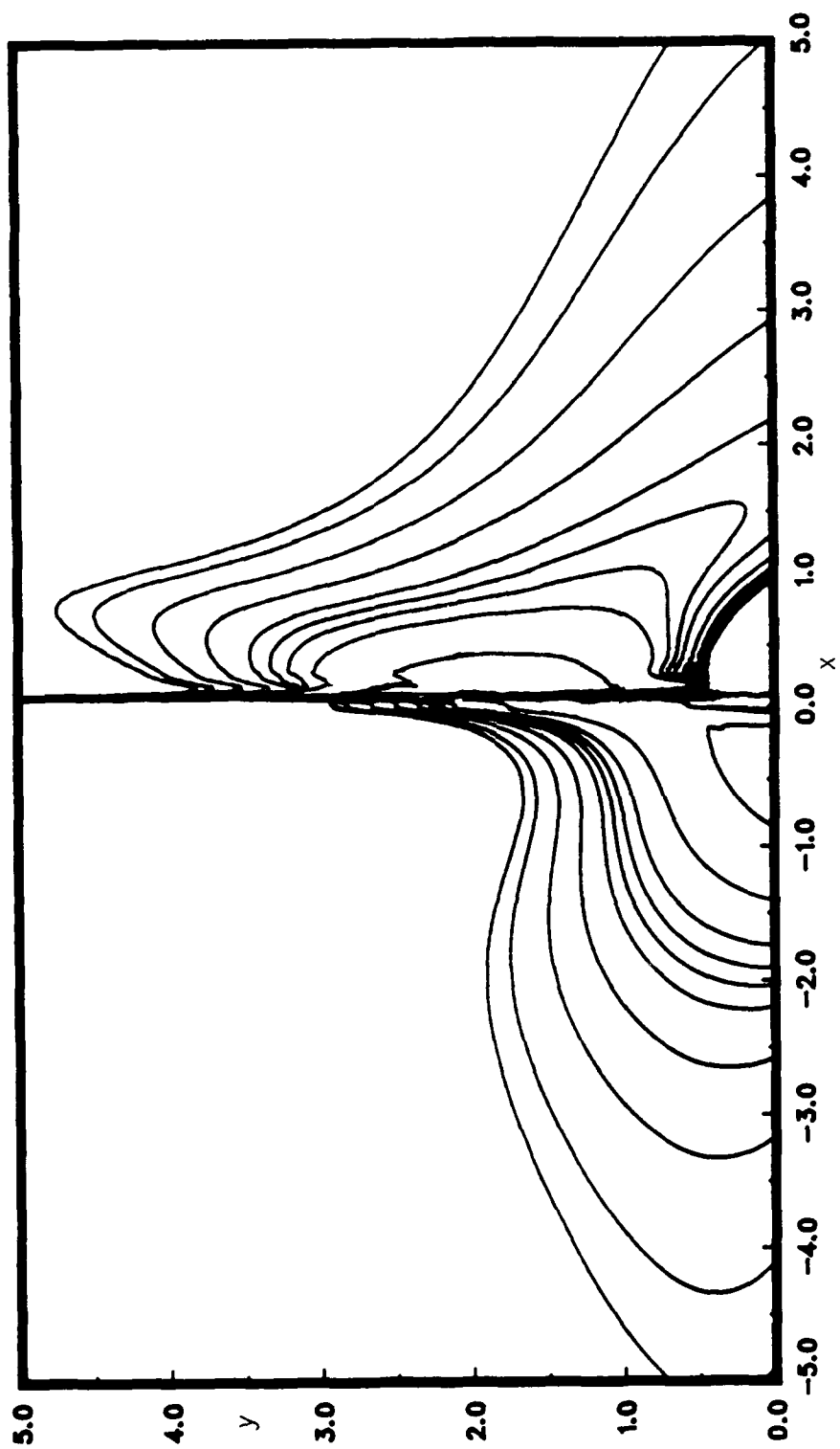
5.9(b)  $t=0.60$





5.9(d)  $t=0.63$



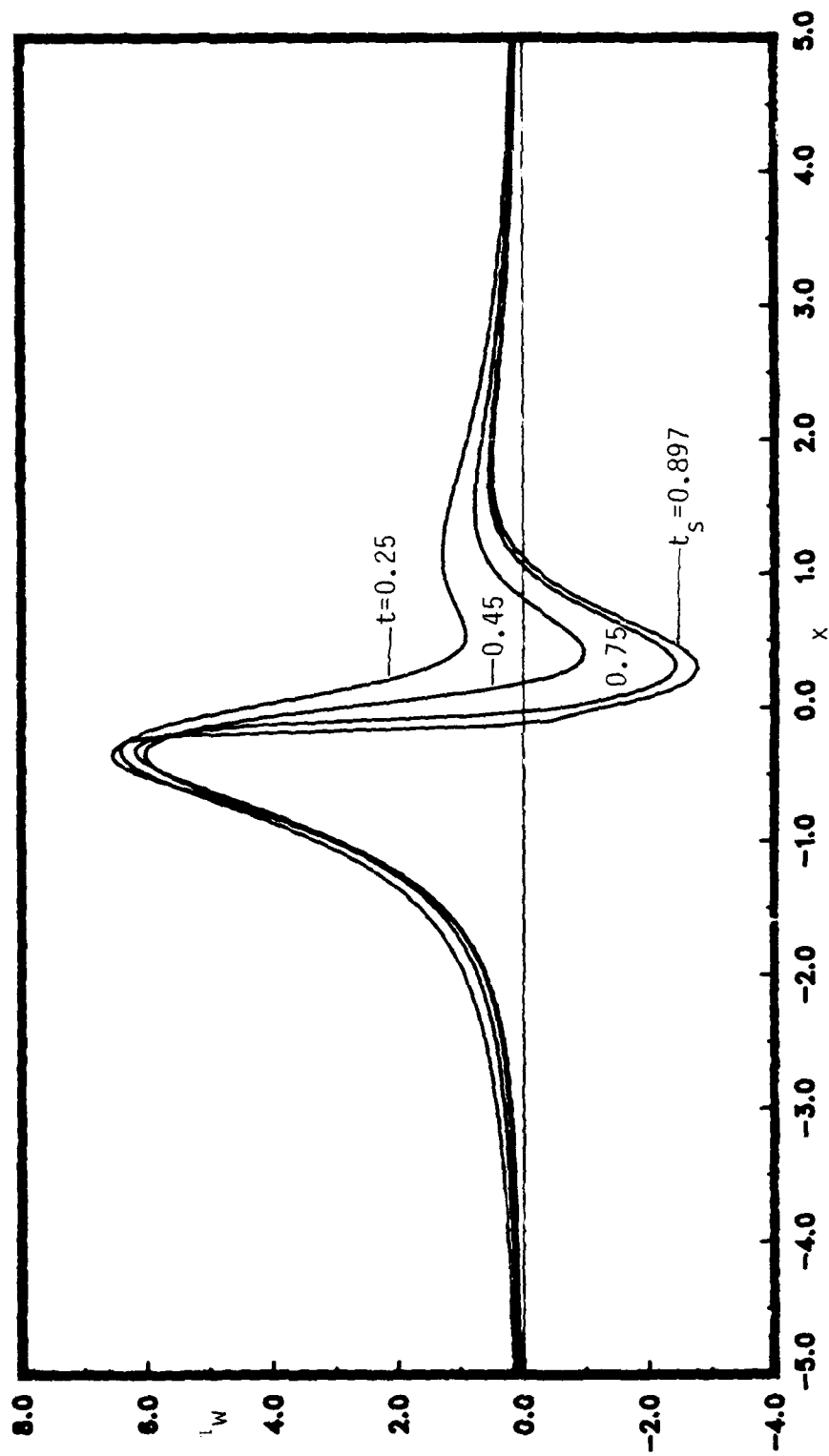


5.9(f)  $t=t_s=0.645$



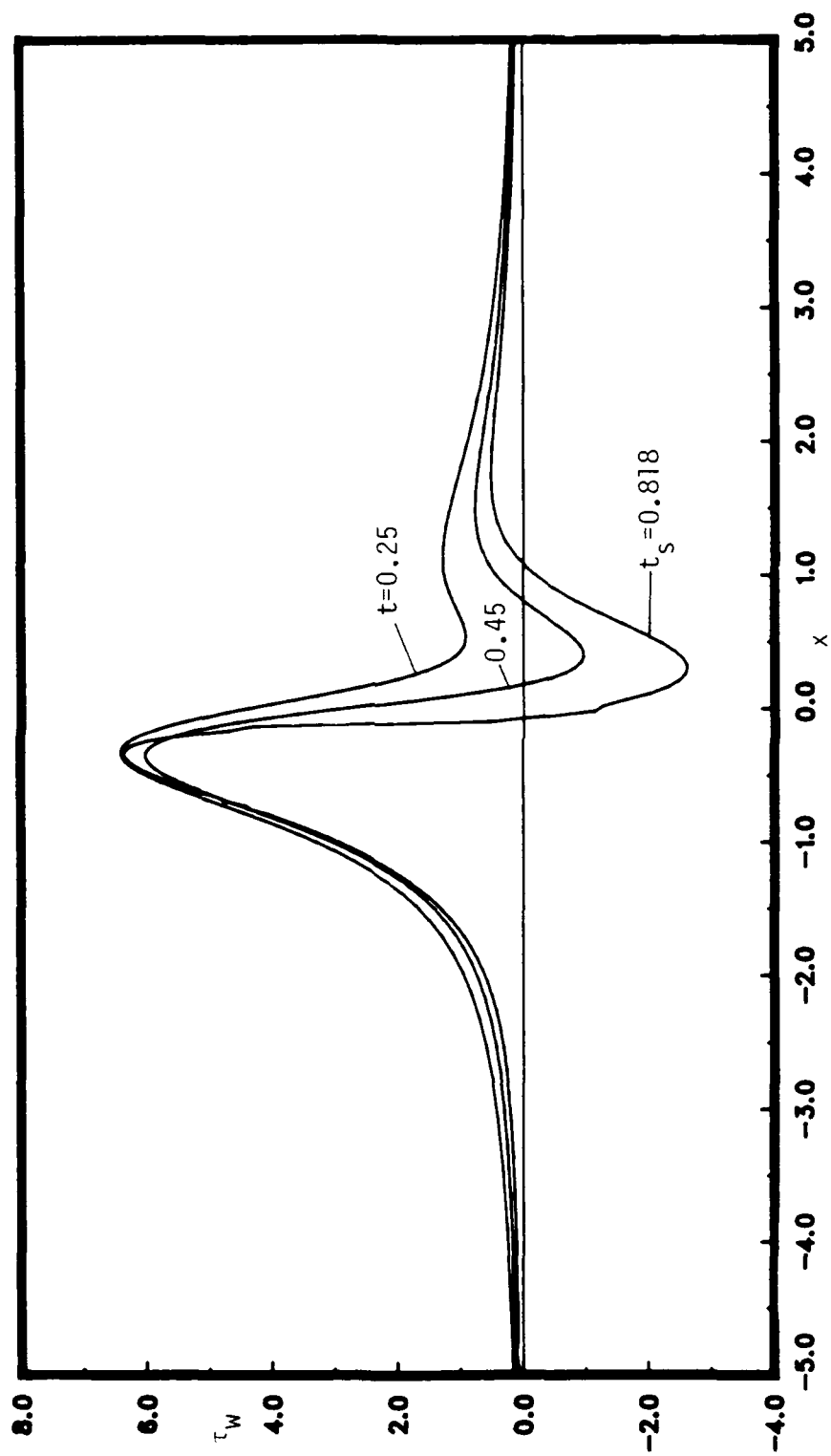
of the tertiary eddy with the outer flow.

Finally, consider the temporal evolution of the wall shear  $\tau_w$  for each case of finite  $Re$ , which was computed using the method described in Appendix D. Figures 5.10 illustrates the temporal evolution of  $\tau_w$  for  $Re=10^8, 10^7, 10^6$ , and  $10^5$  at select times including the singularity time  $t_s$ . In all cases the evolution of the wall shear is identical to that associated with the limit problem except when interaction is significant near  $t=t_s$ ; in particular the final result at  $t_s$  in figures 5.10 may be observed to depart quite radically from the limit distribution near  $x=x_s$ . Recall that the wall shear was regular in the limit problem in the neighborhood of  $x_s$  (c.f. §4.3). In figures 5.10(a) to 5.10(d) each case of finite  $Re$  has been plotted on the same vertical scale and it may be inferred that the wall shear develops a singularity at  $x_s$  on the curve corresponding to  $t_s$ . It is also evident that the amplitude of the singular perturbation of the wall shear becomes larger as  $Re$  decreases, as follows: (1) for  $Re=10^8$  in figure 5.10(a), the singularity is barely noticeable; (2) for  $Re=10^7$  in figure 5.10(b), it appears as a small distortion; (3) the singularity is quite dramatic at  $Re=10^6$  (figure 5.10(c)) , and (4) goes off scale in the  $Re=10^5$  curves depicted in figure 5.10(d). The wall shear at  $t_s$  is depicted in figure 5.11 for the  $Re=10^5$  case on a extended vertical scale from that of figures 5.10; it is seen that the amplitude of the perturbation is an order of magnitude greater than the local value of the wall shear. These results support the theoretical prediction of Smith (1988) who argues that, while the limit problem wall shear remains regular at  $x_s$ , the wall shear (in zone I, figure 2.9) for the fully-interacting case can develop a singularity (c.f. §2.7).

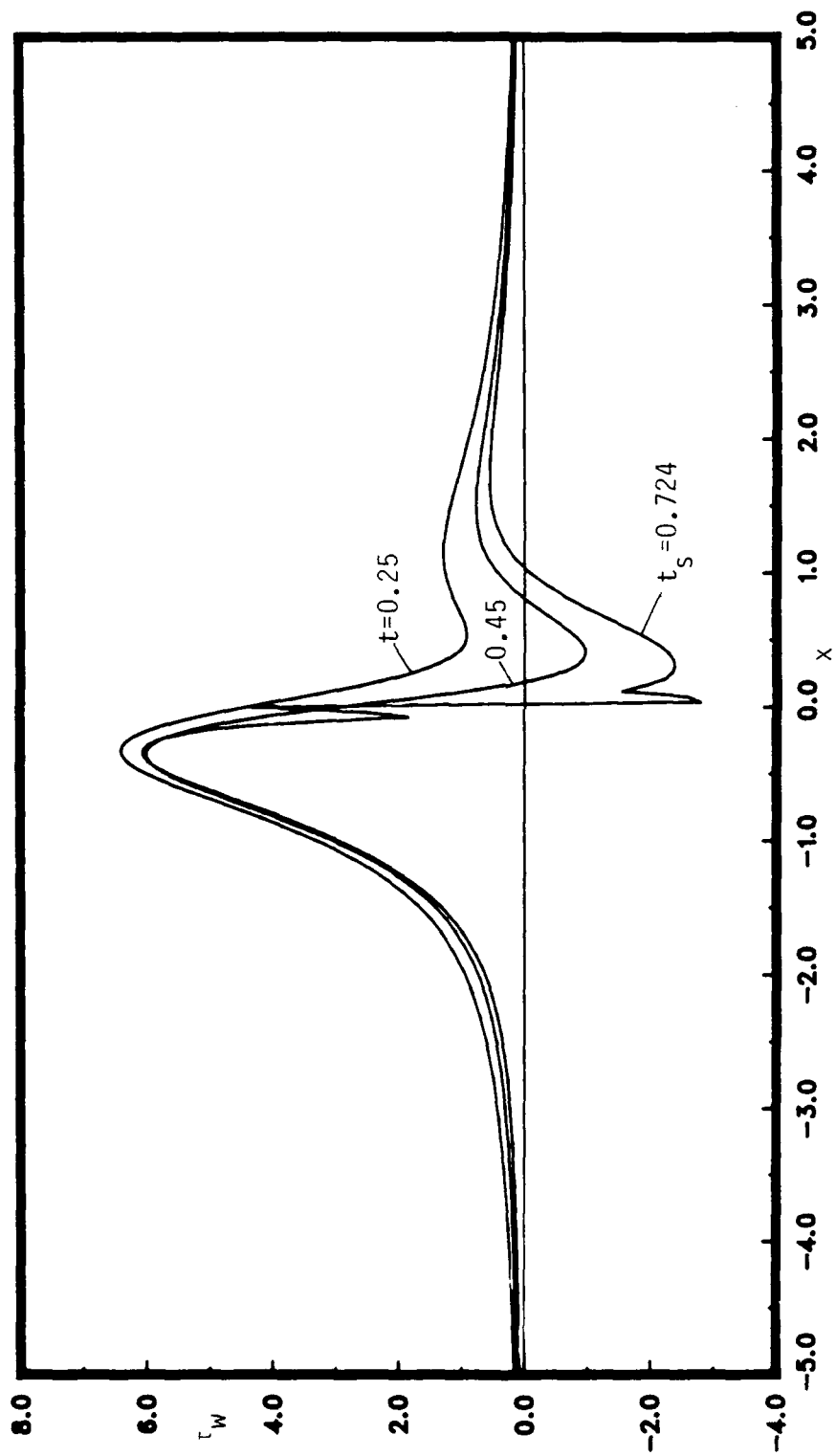


5.10(a)  $Re=10^8$

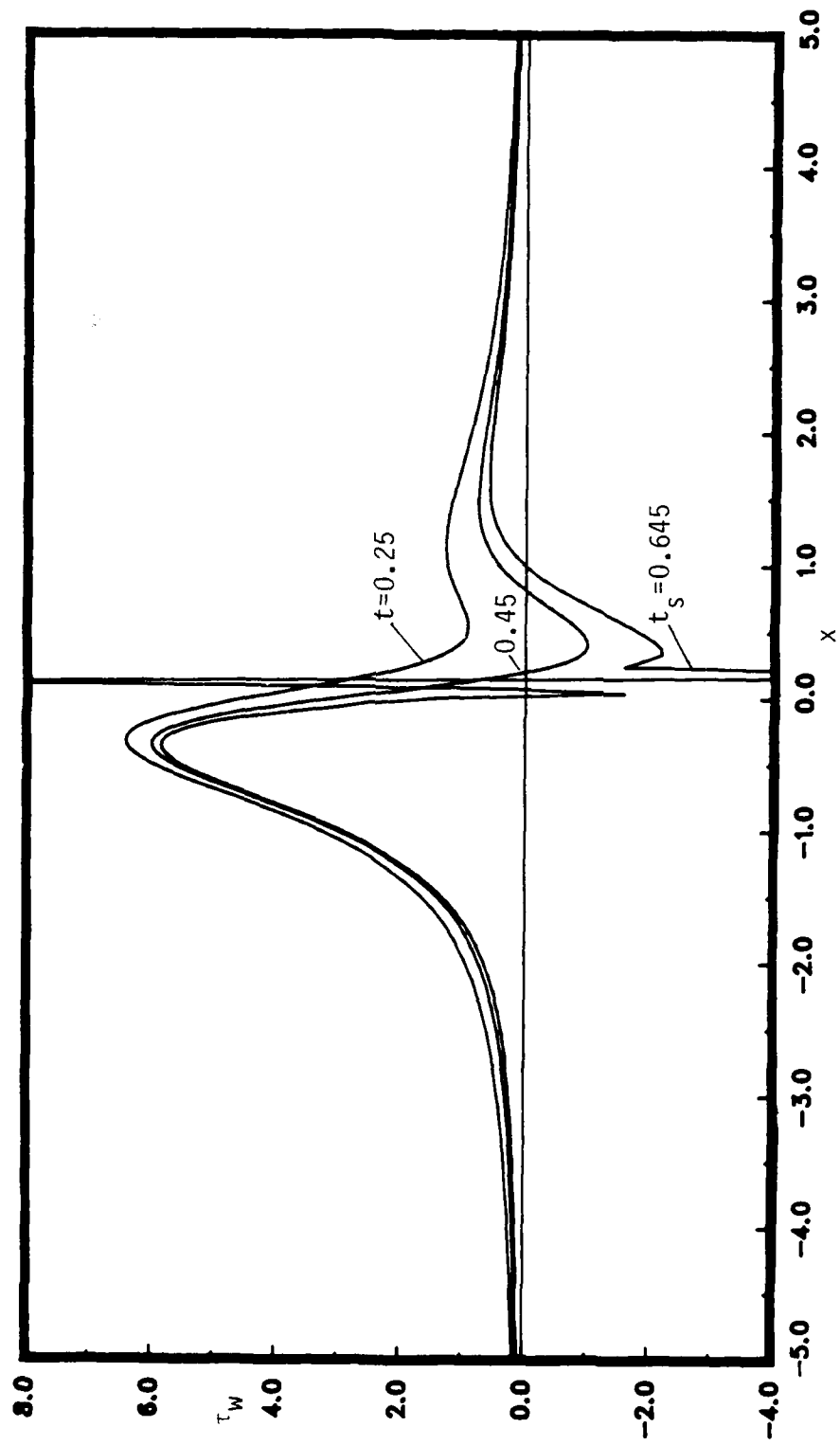
Figure 5.10. Temporal evolution of wall shear, at  $Re=10^8$ ,  $10^7$ ,  $10^6$  and  $10^5$ .



5.10(b)  $Re=10^7$



5.10(c)  $Re=10^6$



5.10(d)  $Re=10^5$

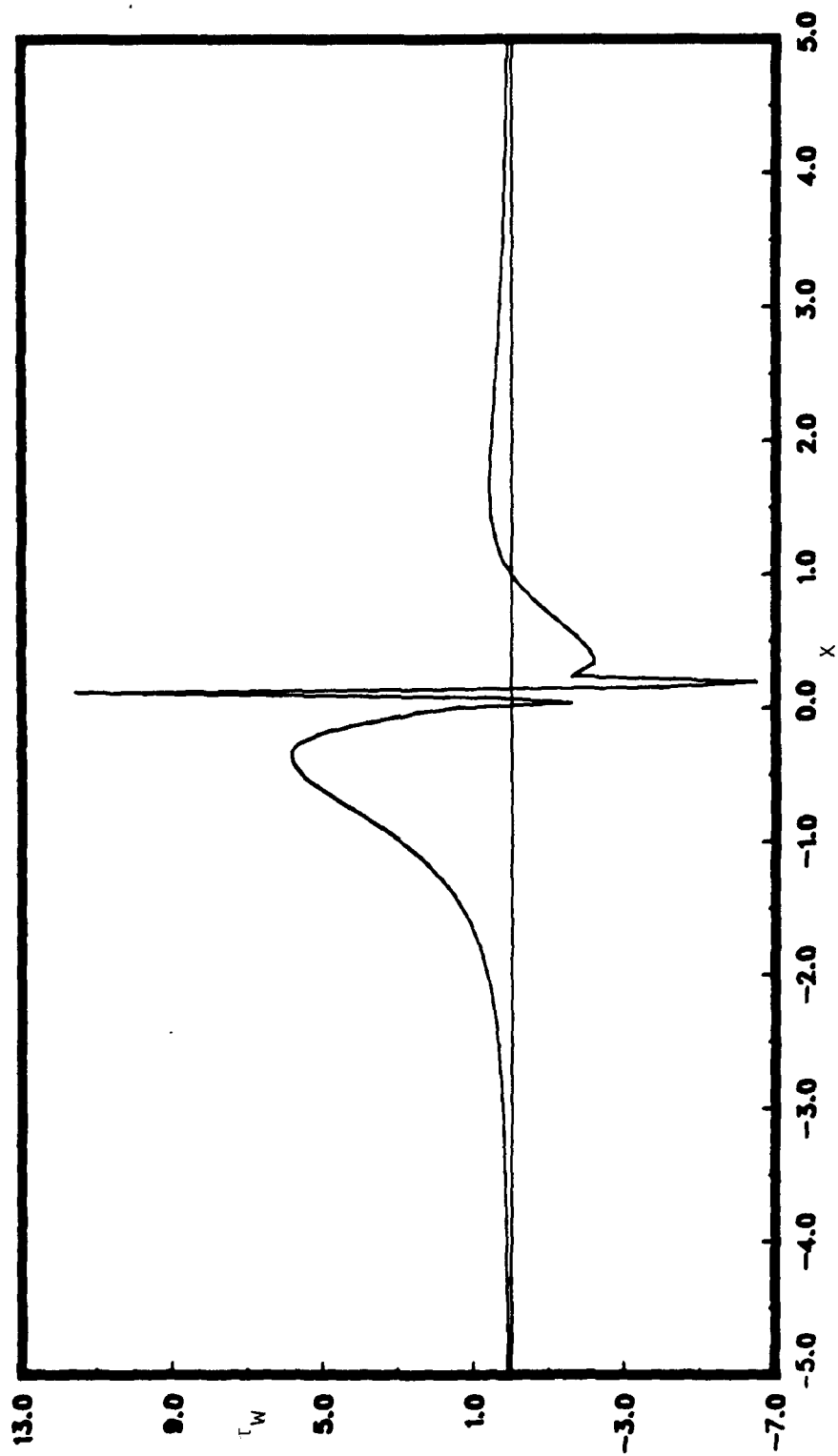
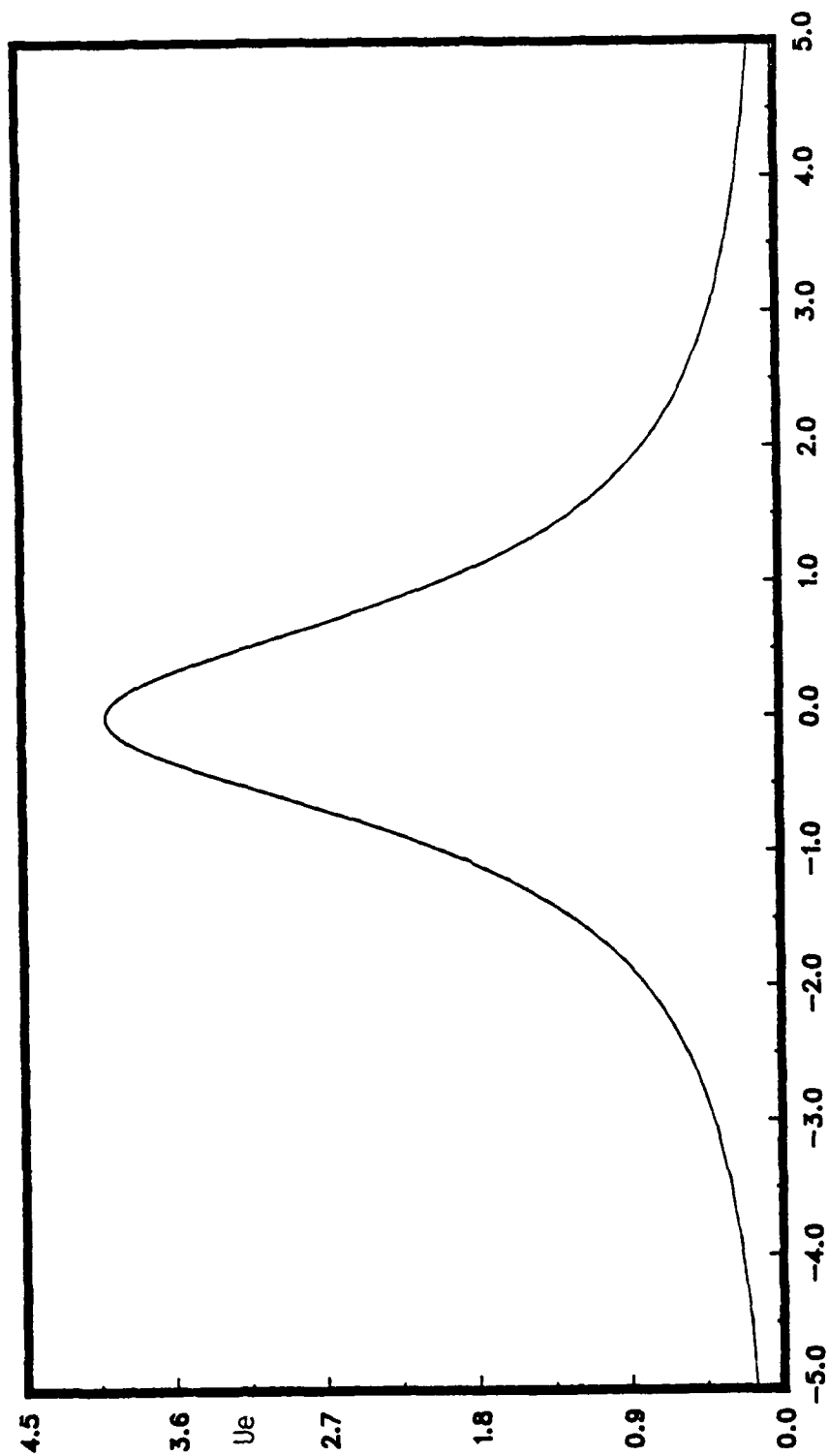


Figure 5.11. Wall shear for  $Re=10^5$ , at  $t_s$ .

#### 5.4 The External Flow Development as $t \rightarrow t_s$

For the limit problem, the inviscid flow is steady in a frame of reference moving with the vortex; in the interacting problem the external flow is unsteady due to the effect of the thickening boundary layer. However, the unsteady inviscid solution at finite  $Re$  is essentially the same as in the limit problem until strong interaction begins to propel the flow near  $x_s$  into an eruptive state. During the period just prior to the evolution of a singularity, the external flow deviates from the limit-case solution only in a very narrow region centered on  $x_s$  (which is consistent with the development of the boundary-layer flow discussed in §5.3). In this section distributions which characterize the inviscid flow at the boundary-layer edge will be examined at time  $t_s$ . The external flow distributions described here appear to indicate that the interactive boundary-layer assumption that  $V_d = O(1)$  (c.f. §1.4) breaks down rather dramatically.

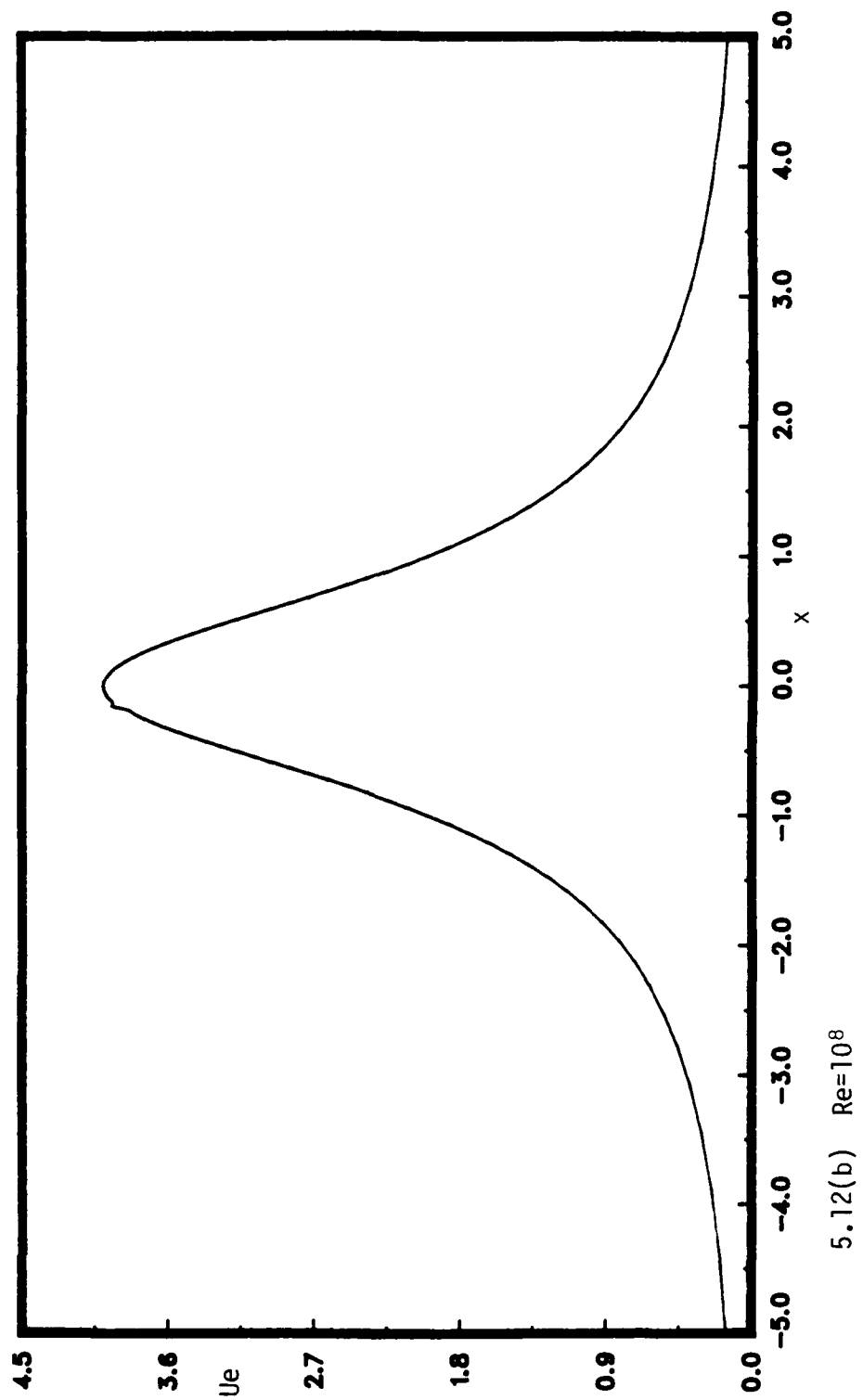
The instantaneous mainstream velocity, as viewed by an observer in the laboratory frame near the wall, is  $U_e$  and is depicted in figures 5.12, first for the limit problem and then for the four cases of finite  $Re$  at  $t_s$ . The steady limit-problem distribution for  $U_e$  (equation (3.7)), is given for comparative purposes in figure 5.12(a). For the interacting calculations  $U_e$  was computed from equation (3.128) and figures 5.12(b) to 5.12(e) depict  $U_e$  for the respective cases of  $Re = 10^8, 10^7, 10^6, 10^5$  at  $t_s$ . The only deviation from the limit problem is easily identified in each case and occurs at  $x_s$ . It should be noted that the magnitude of the departure of the interacting  $U_e$  curves from the limit-problem curve increases with decreasing  $Re$ . It is also of interest to note that there are two "spikes" in figure 5.12(e), which corresponds to the case  $Re = 10^5$ . In this figure the large spike to the right is associated with

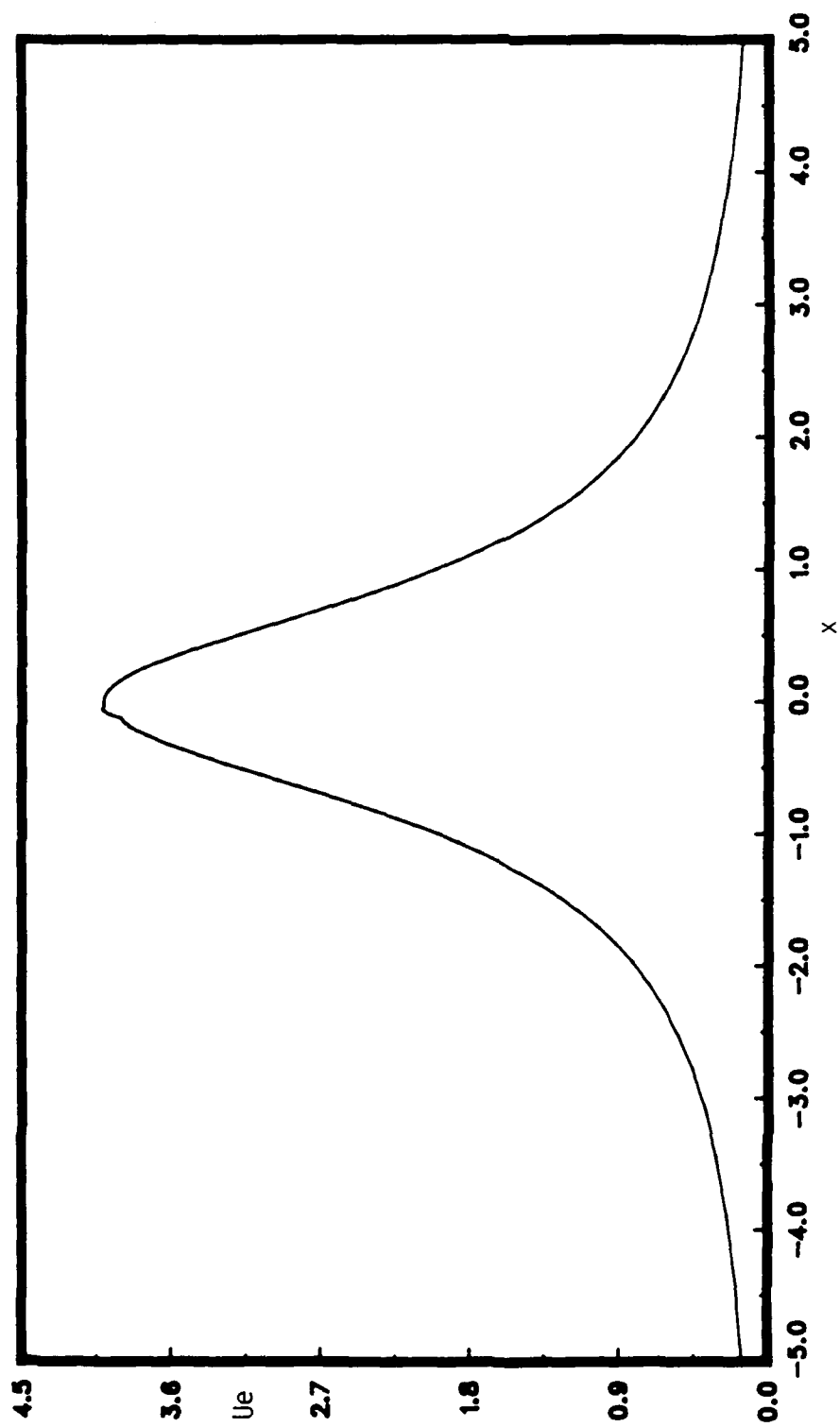


5.12 (a) limit problem  $Re \rightarrow \infty$

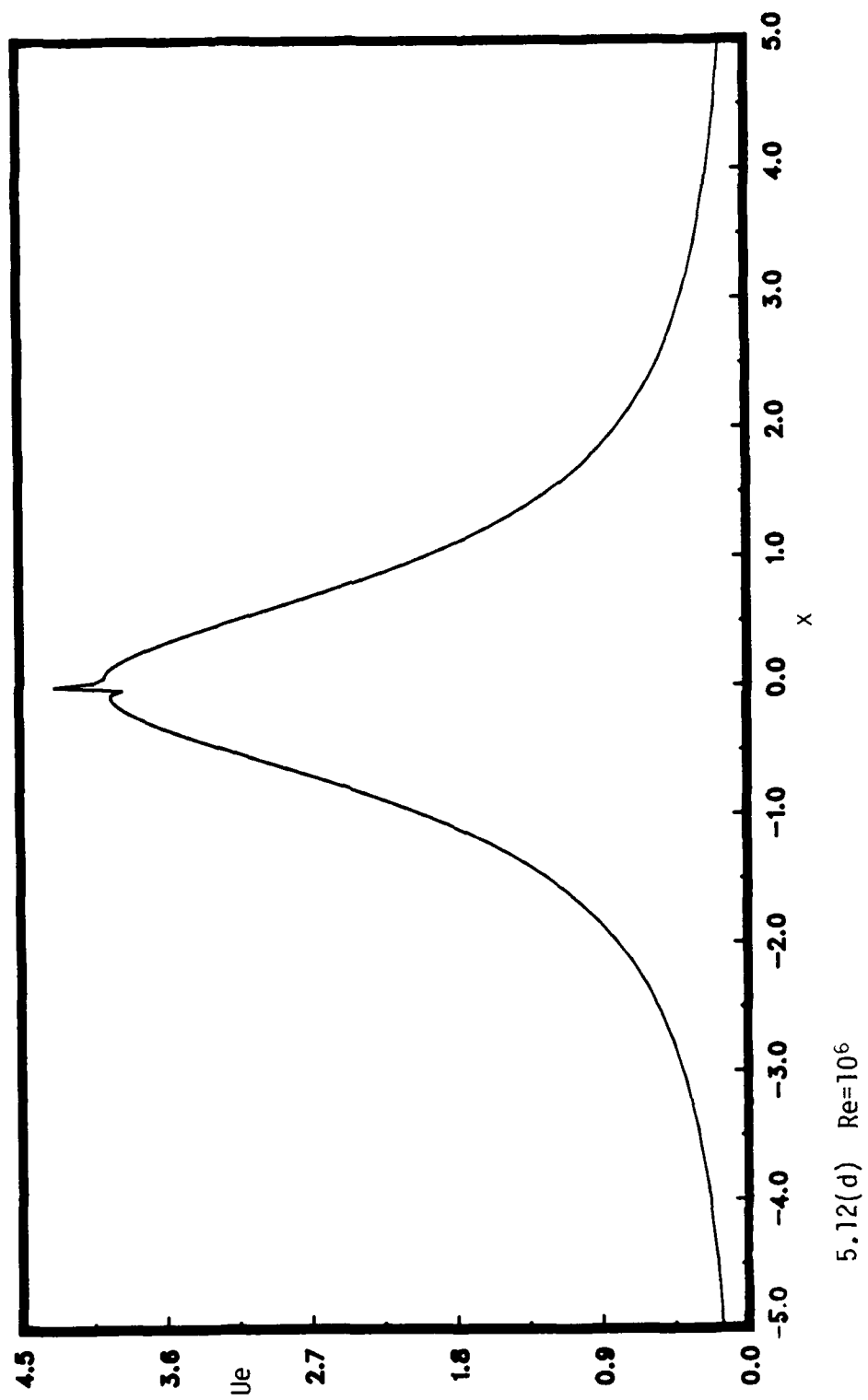
Figure 5.12. Mainstream velocity in the laboratory frame, at  $t_s$ .

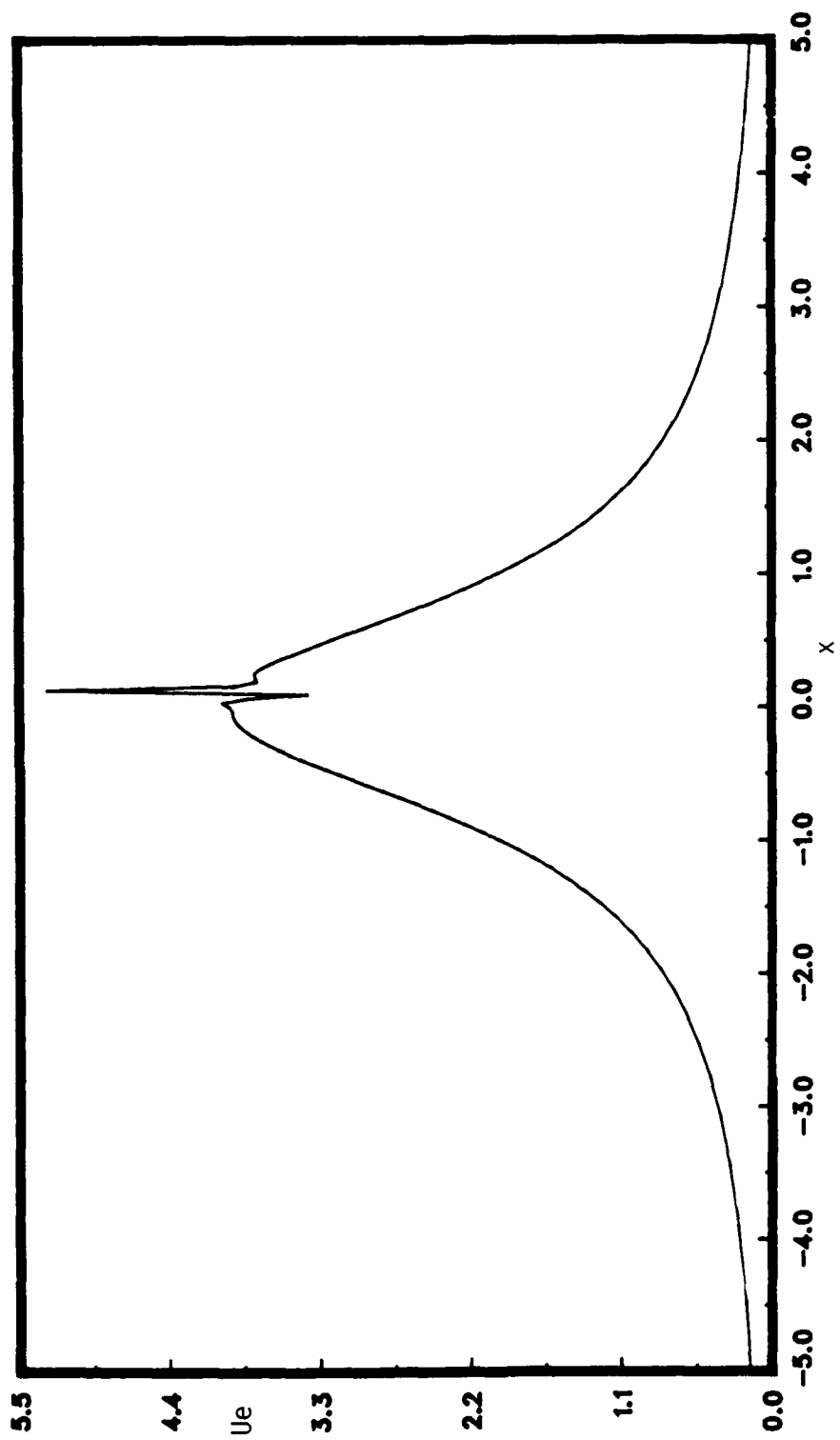






5.12(c)  $Re=10^7$





5.12(e)  $Re=10^5$

1

breakdown singularity that occurs in the interaction zone adjacent to the secondary eddy labeled "a" in figure 5.6(e); the smaller spike to the left near  $x=0$  corresponds to the interaction zone associated with the tertiary eddy labeled "b" in figure 5.6(e).

The next quantity that shall be considered is the dynamic pressure  $P=p-p_\infty$  both for the limit problem and the four fully-interacting cases at finite  $Re$ ; here  $p_\infty$  is the pressure at infinity. Generally, the quantity  $P$  is not directly computed in the unsteady boundary-layer calculations. However, it is a physical quantity of interest and was computed here to compare the behavior predicted for the breakdown of interacting boundary-layer theory by Smith (1988). The dynamic pressure for the limit problem ( $Re \rightarrow \infty$ ) is

$$P(x) = -\frac{1}{2}((Ue-1)^2 - 1), \quad (5.1)$$

where the  $Ue$  distribution for the limit problem is steady and is given by equation (3.7). The solution for  $P$  in the interacting problems is

$$P(x,t) = -\frac{1}{2}((Ue - U_v)^2 - U_v) - \int_{-\infty}^x \frac{\partial Ue}{\partial t} dx; \quad (5.2)$$

Since  $\partial Ue/\partial t$  is known at equally-spaced node points in the transformed variable  $\hat{x}$  the integral term of equation (5.2) is most conveniently integrated<sup>2</sup> in transformed space using the trapezoid rule from

---

2

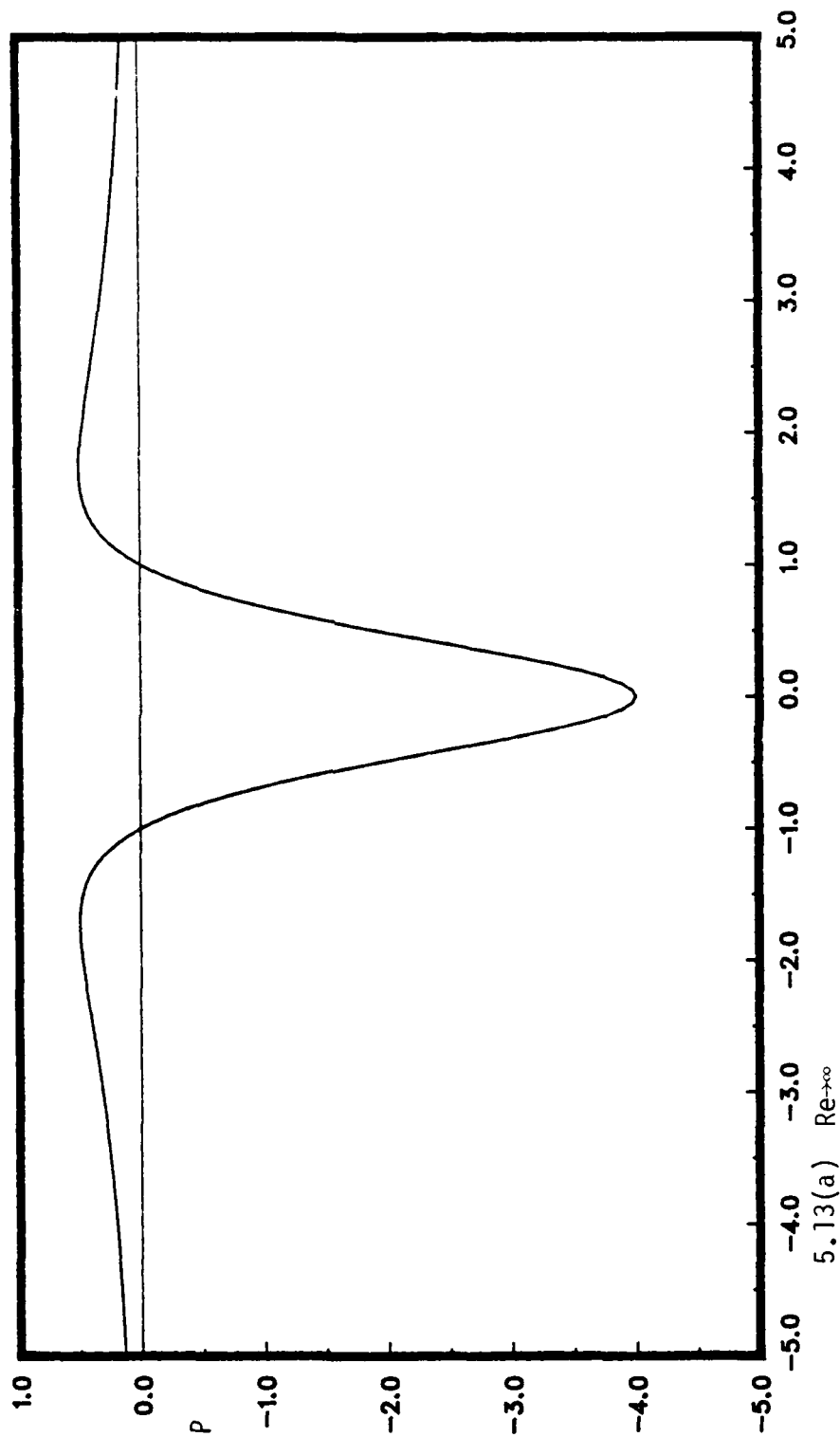
In equation (5.3)  $Ue_0(\hat{x})$  is a steady function that arises from transformation (3.51), and  $\hat{x}(x)$  is given by equation (3.50). The quantities  $Ue$ ,  $U_v$  and  $\partial Ue/\partial t$  are all unsteady in the interacting case and are computed as follows:  $Ue$  from equation (3.173),  $U_v$  from equation (3.168), and  $\partial Ue/\partial t$  by evaluating  $(Ue - Ue^*)/\Delta t$  at each node location in  $\hat{x}$ ; here the asterisk indicates the value in the prior time plane.

$$P(x,t) = -\frac{1}{2}((Ue-U_v)^2 - U_v) - 2\pi \int_{\hat{x}(x)}^2 \frac{\partial Ue}{\partial t} \frac{d\hat{x}}{Ue_0(\hat{x})}. \quad (5.3)$$

Curves of dynamic pressure are shown for both the limit problem and the four interacting cases in figures 5.13. A plot of the steady limit case pressure is presented in figure 5.13(a) as a basis of comparison, while figures 5.13(b) to 5.13(d) correspond to the pressure field at  $t_s$  for  $Re=10^8$ ,  $10^7$ , and  $10^6$ . The analysis of Smith (1988) indicates that  $P$  is  $O((x-x_s)^{1/3})$  near  $x=x_s$ , and this does not appear to be inconsistent with the  $Re=10^8$  case and, perhaps, the  $Re=10^7$  case. However, a "spike" has developed in the pressure curve for the  $10^6$  case, which suggests that a strong irregularity has developed in the pressure distribution. The spike is also found in the pressure field for  $Re=10^5$ , and the abrupt nature of its formation may be seen in figures 5.14 which depicts  $P$  at two times,  $t_s - 0.015$  and  $t_s$ . The most significant contribution to eruptive spike in the pressure field is  $\partial Ue/\partial t$ , because this distribution exhibits a high degree of spatial and temporal variation near  $x_s$ , as  $t \rightarrow t_s$ . Contours of  $\partial Ue/\partial t$  are given in figures 5.15 for the interacting calculations (note that this distribution is identically zero in the limit problem). In the interacting problems, the distribution  $\partial Ue/\partial t$  is negligible throughout the majority of the calculation up until very close to  $t_s$ , when it exhibits tremendous streamwise variation near  $x_s$ . The irregular character of  $\partial Ue/\partial t$  at  $t_s$  is very evident in the four plots of figures 5.15 for  $Re=10^8, 10^7, 10^6$  and  $10^5$  respectively. These curves are essentially zero everywhere but near  $x_s$ , where they develop a very large spike.

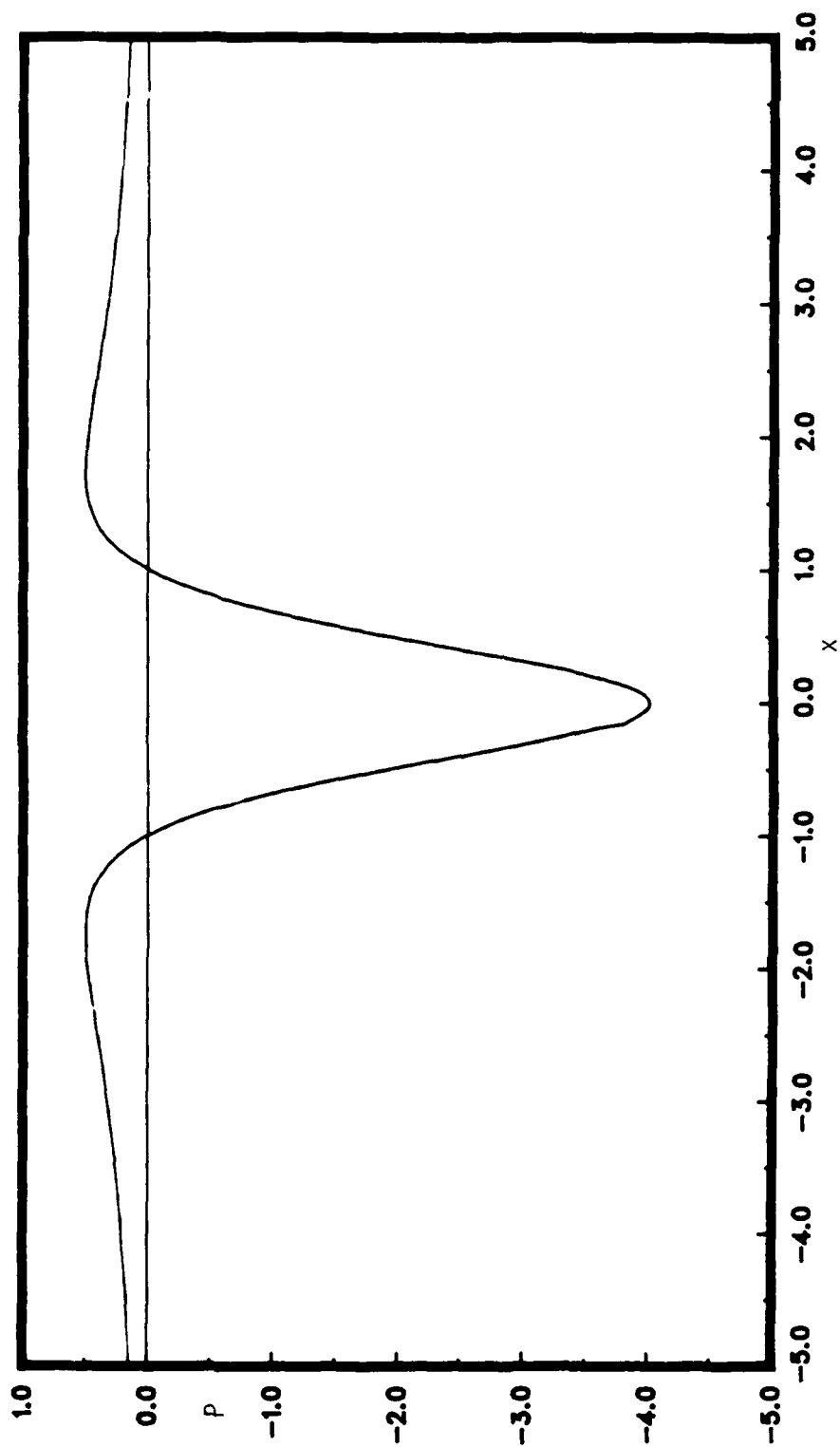
The pressure gradient term, for the model problem is given by

$$-\frac{dp}{dx} = \frac{\partial(Ue)}{\partial x}(Ue-U_v) + \frac{\partial(Ue)}{\partial t}, \quad (5.4)$$



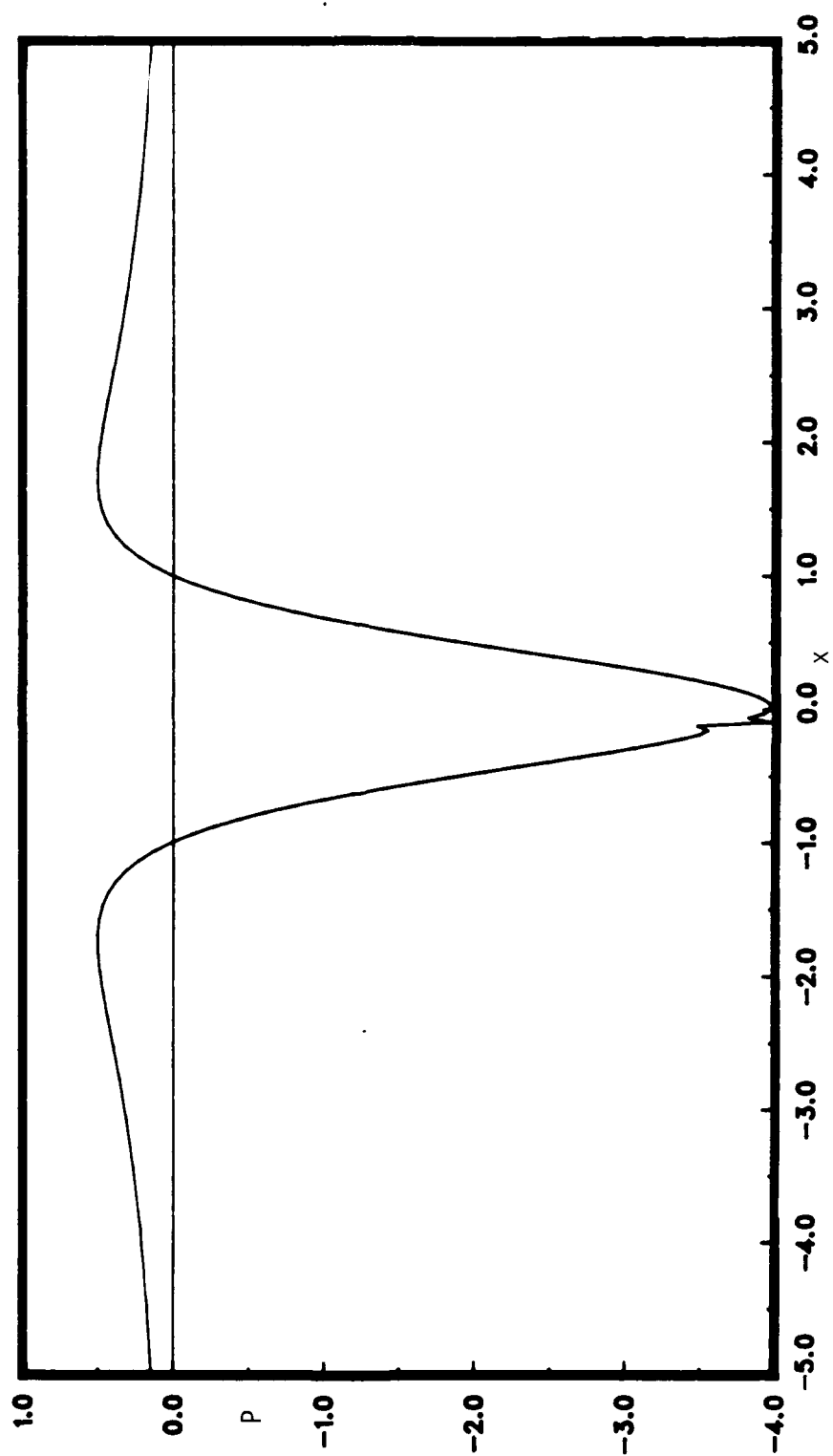
5.13(a)  $Re \rightarrow \infty$

Figure 5.13. Dynamic pressure at  $t_s$  for the limit problem and the interacting cases  $Re=10^8$ ,  $10^7$  and  $10^6$ .

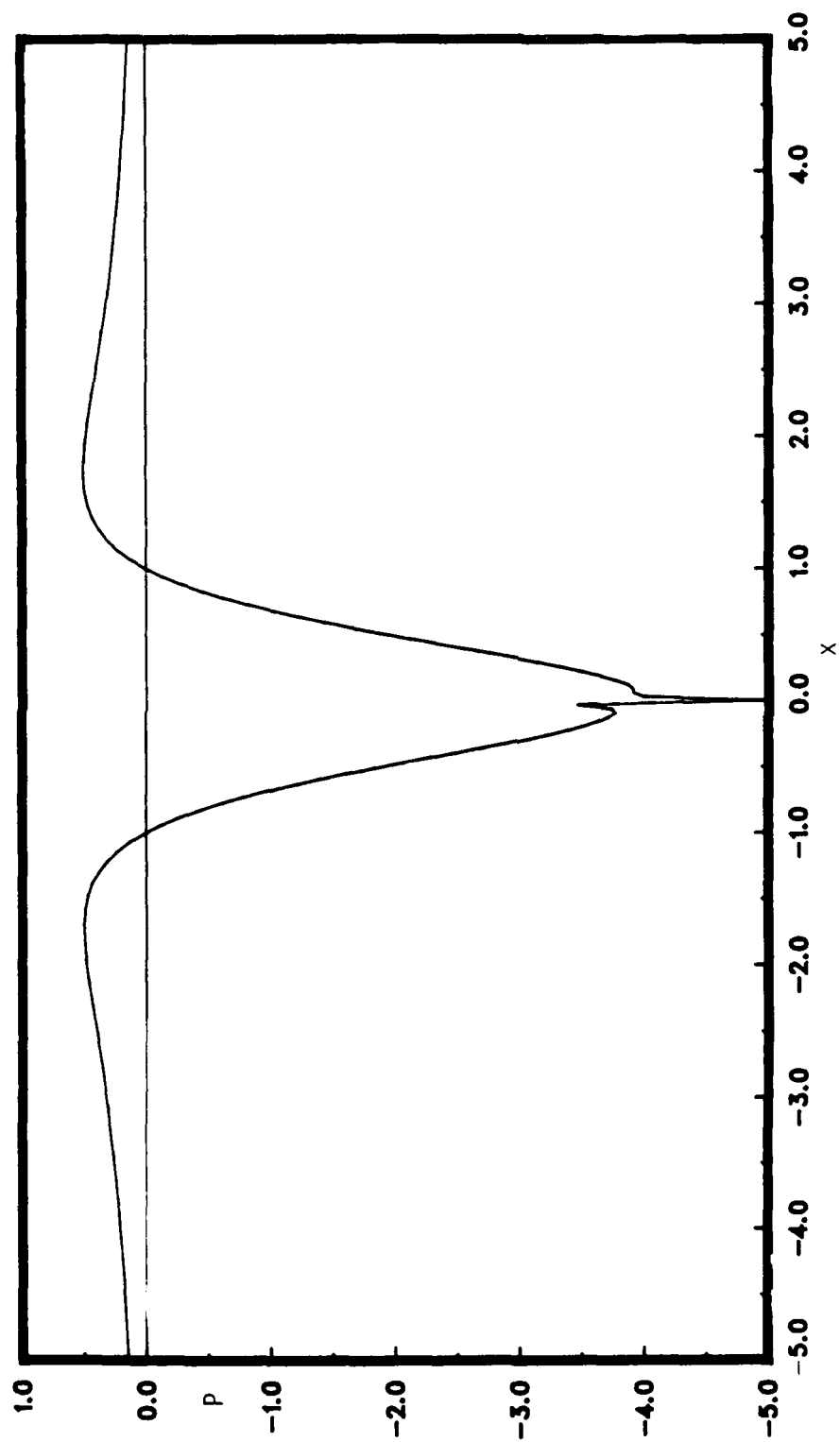


5.13(b)  $\text{Re}=10^8$  (note the small distortion near  $x_S=-0.15$ )

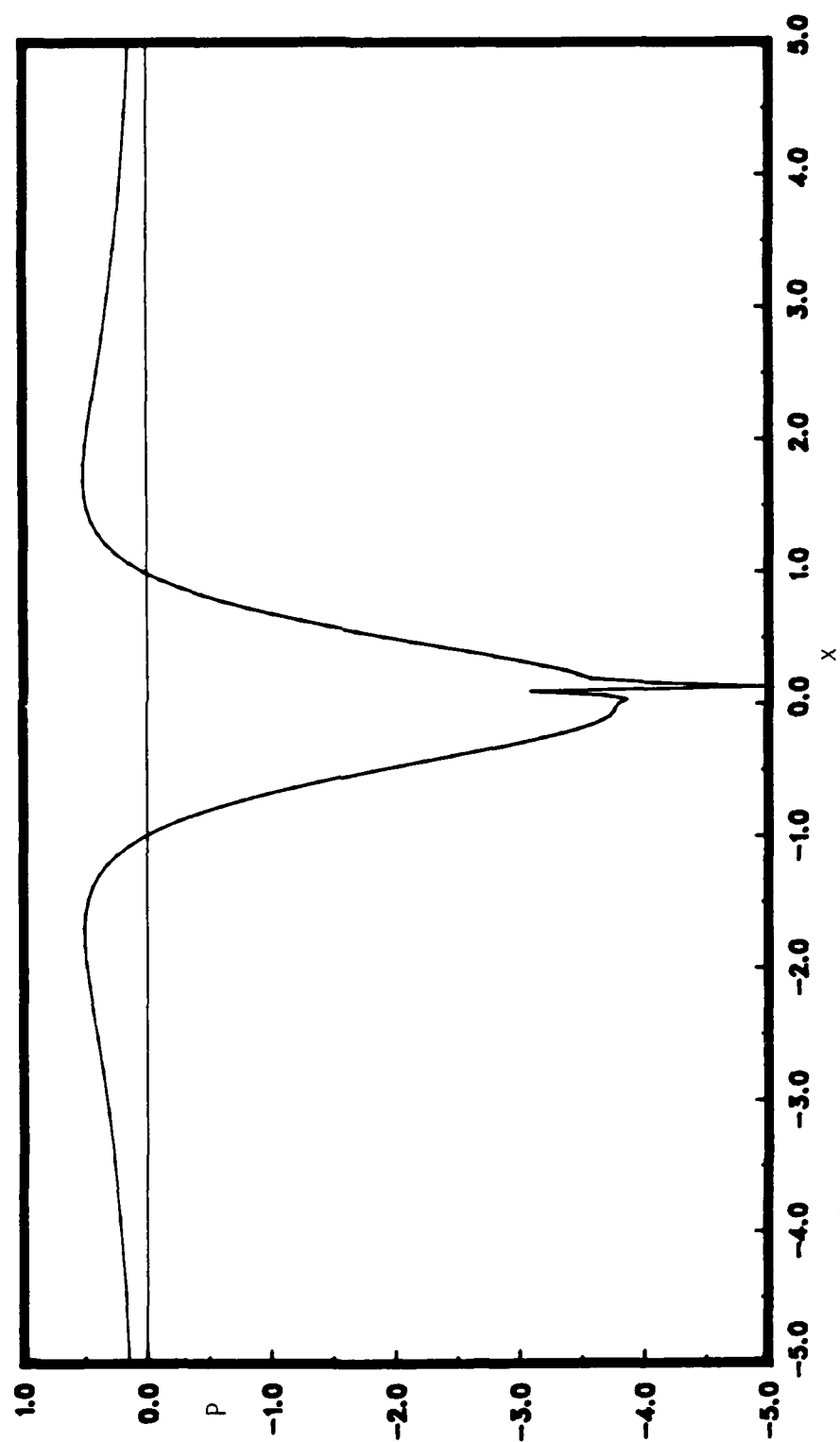




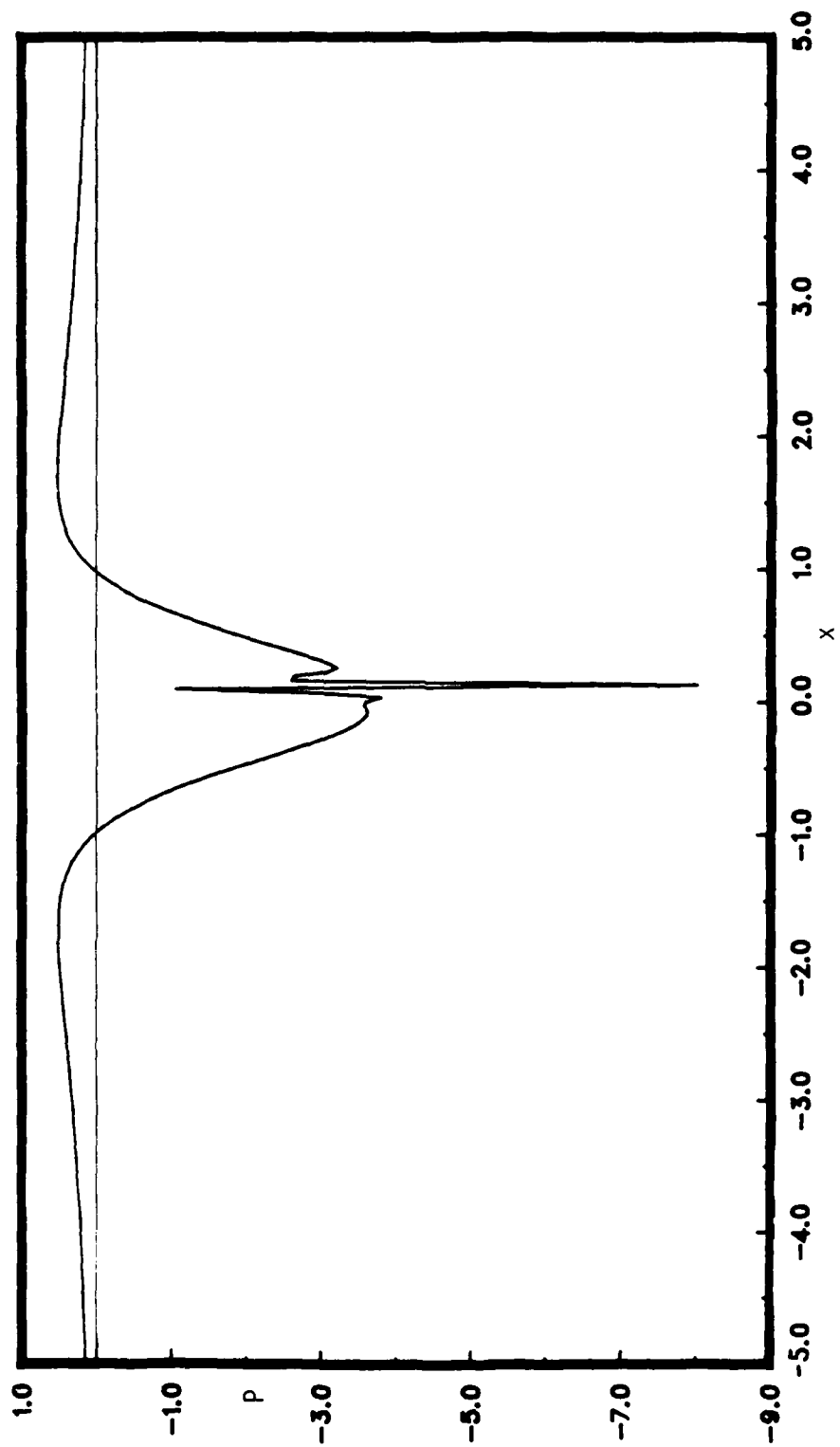
5.13(c)  $Re=10^7$



5.13(d)  $\text{Re}=10^6$



5.14(a) at  $t_s - 0.015$   
 Figure 5.14. Dynamic pressure for  $Re = 10^5$  as  $t \rightarrow t_s$ .



5.14(b) at  $t_s$

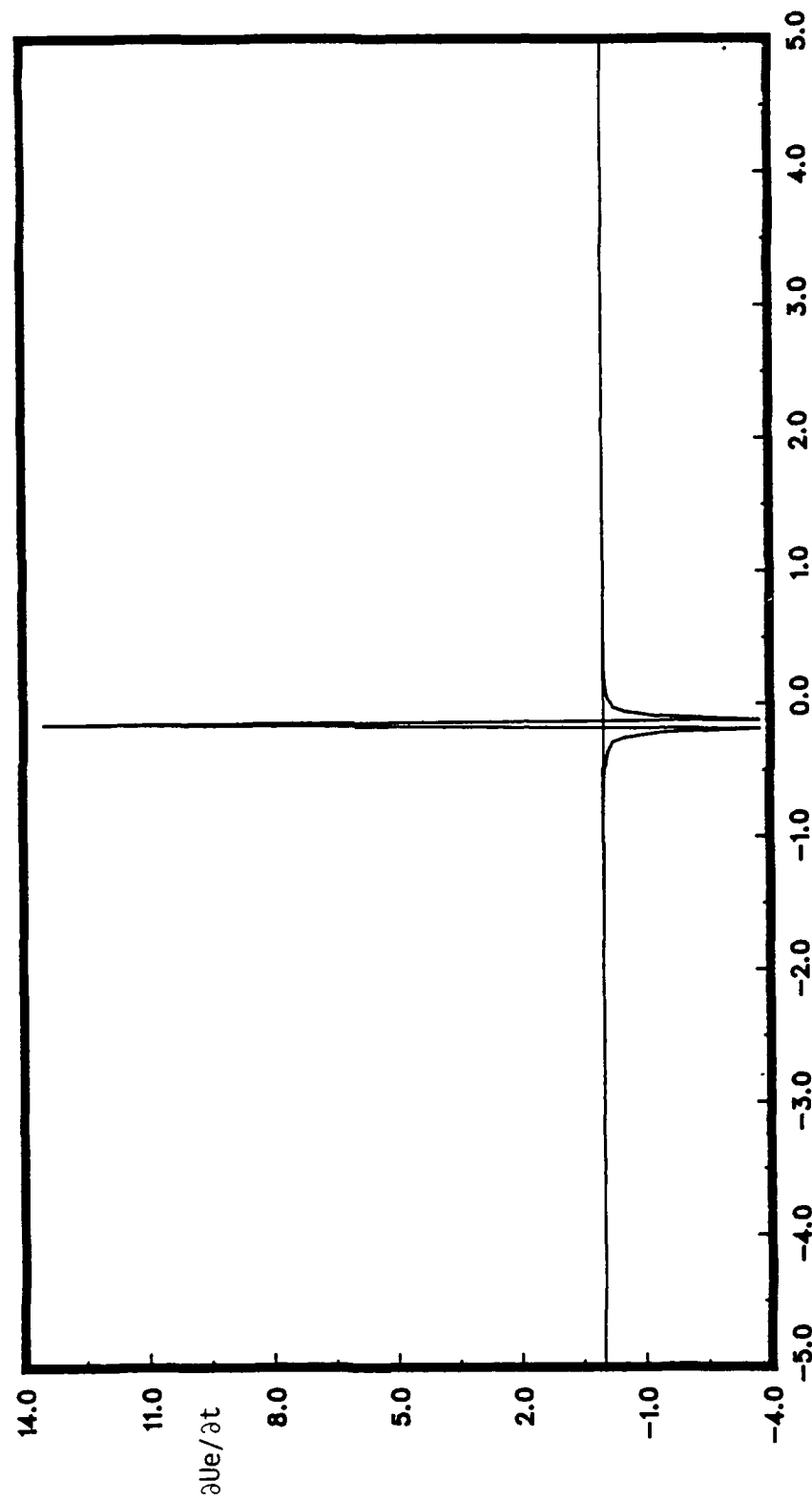
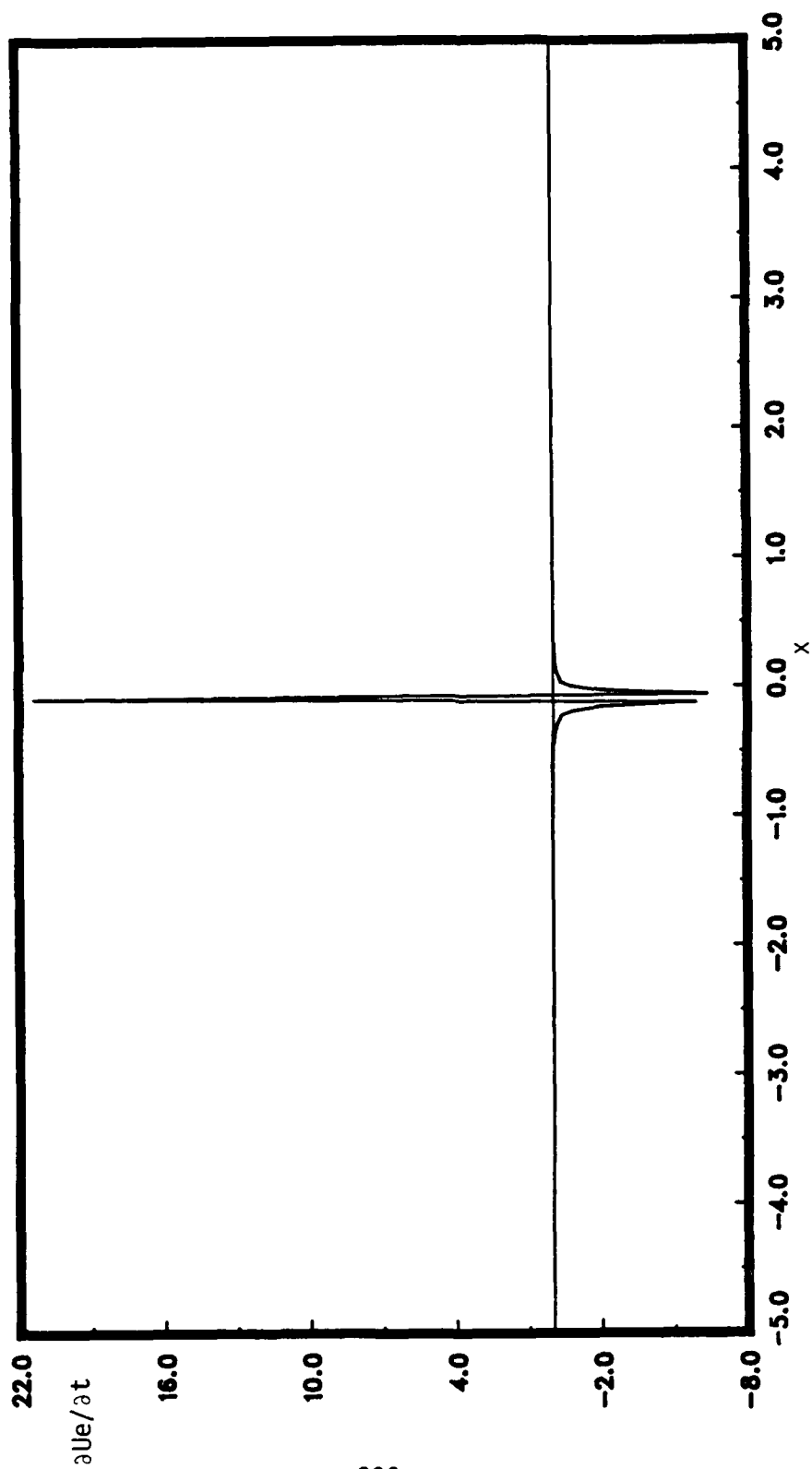
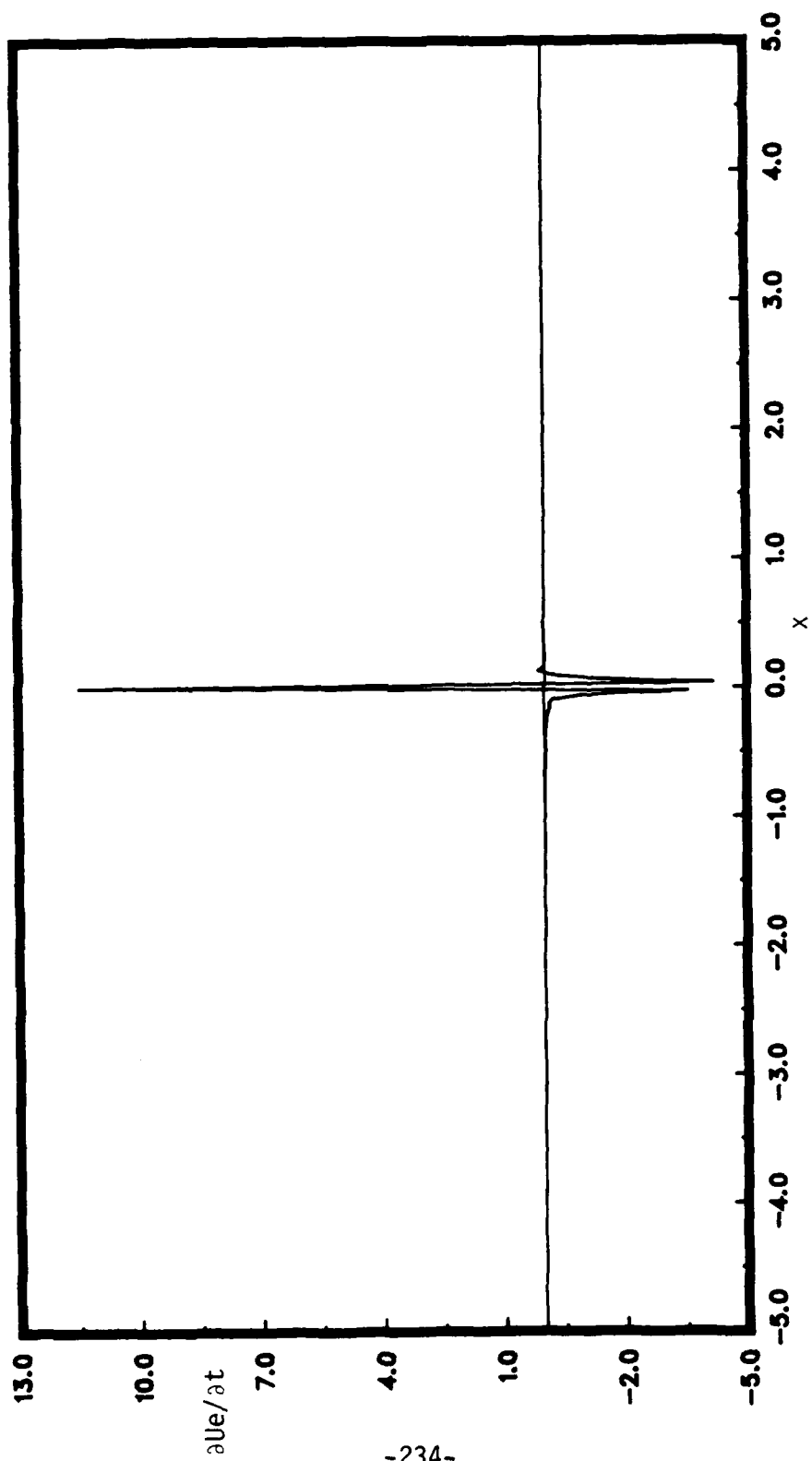


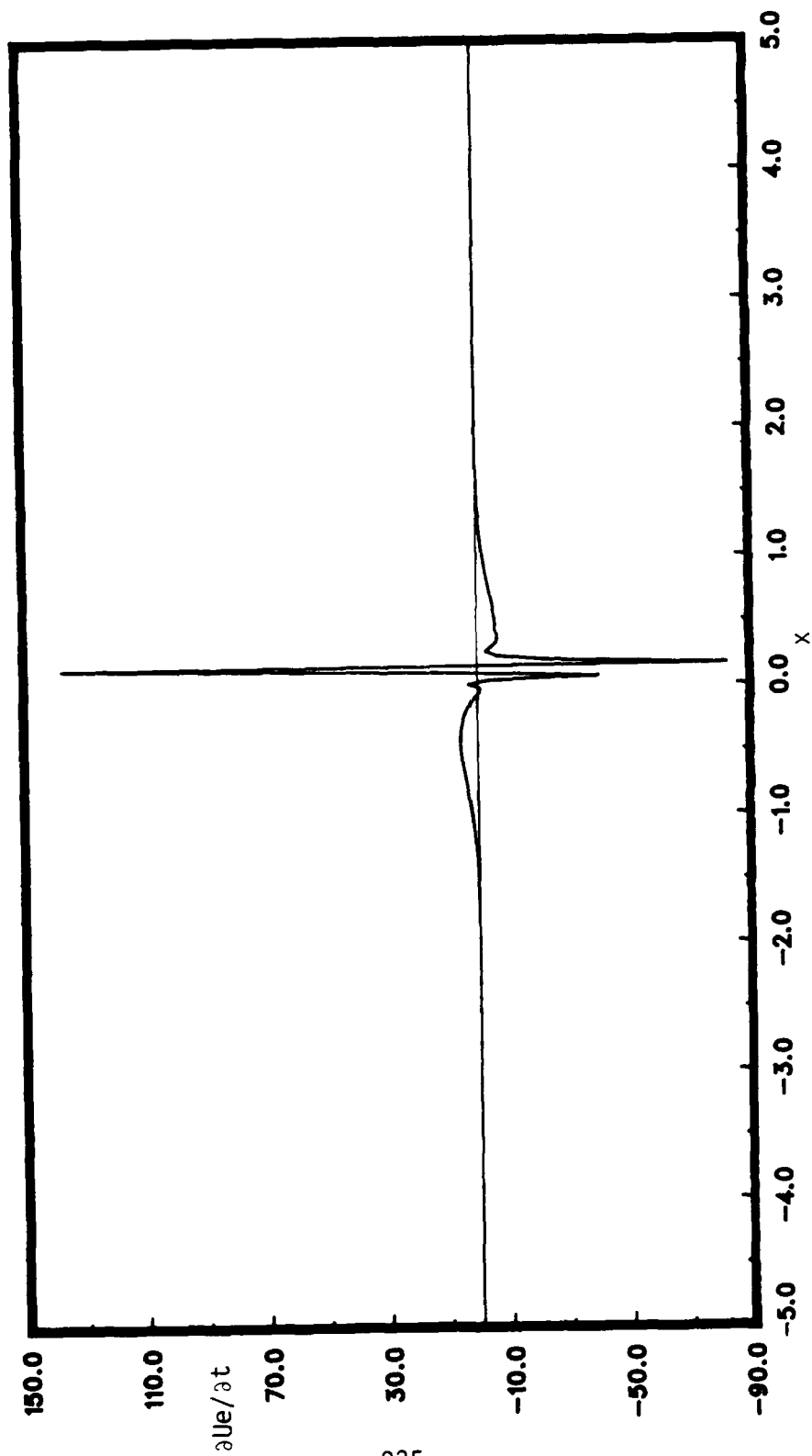
Figure 5.15. Curves of  $\partial u / \partial t$  at time  $t_s$ .



5.15(b)  $Re=10^7$



5.15(c)  $\text{Re}=10^6$



5.15(d)  $Re=10^5$



is of particular interest, since this distribution forces the unsteady boundary-layer flow evolution. The theory of Smith (1988) predicts that  $dp/dx$  is  $O((x-x_s)^{-2/3})$  as  $t \rightarrow t_s$  and the plots of figures 5.16 of the pressure gradient certainly do suggest that a singularity develops in the interacting cases, although a close confirmation of the  $O(x-x_s)^{-2/3}$  behavior is difficult to establish. In all of the interacting cases, the singularity is centered on  $x_s$  and consists of a large positive spike and a somewhat shorter negative spike. The distribution for  $Re=10^5$  is shown at two times,  $t_s-0.015$  and  $t_s$ , in figures 5.17(a) and 5.17(b), to illustrate the strong growth in the pressure spike. Note that the vertical scale has changed from figure 5.17(a) to 5.17(b) to accommodate the substantial growth. At this stage the local values of pressure gradient near  $x=x_s$  are much larger than the original pressure gradient induced by the vortex.

Finally, the scaled boundary-layer displacement velocity  $V_d$ , defined by equation (3.121), is plotted in figures 5.18. To gain an appreciation for the scale of  $V_d$  this quantity has been divided by  $\sqrt{Re}$  so that the actual magnitude of the displacement velocity is displayed; so scaled,  $V_d Re^{-1/2}$  for the limit problem is identically zero for all  $x$ . The quantity plotted in figures 5.18,  $(V_d/\sqrt{Re})$ , is assumed to be  $O(Re^{-1/2})$  in interacting boundary-layer theory. The results in figures 5.18 indicate that this assumption becomes invalid as  $t \rightarrow t_s$ . The curves of  $V_d/\sqrt{Re}$  for each case of finite  $Re$  have an almost identical shape, but  $V_d$  increases in amplitude as  $Re$  is decreased. Figure 5.18(d) again indicates that there are two independent interactions taking place for  $Re=10^5$ : the maximum value of  $V_d$  associated with the breakaway singularity is near  $x_s$  is about 0.40, while that associated with the tertiary eddy at near  $x=0$  has a positive maximum of about 0.04. In all cases the maximum value of  $V_d$  is two to three orders of magnitude greater than  $Re^{-1/2}$ .

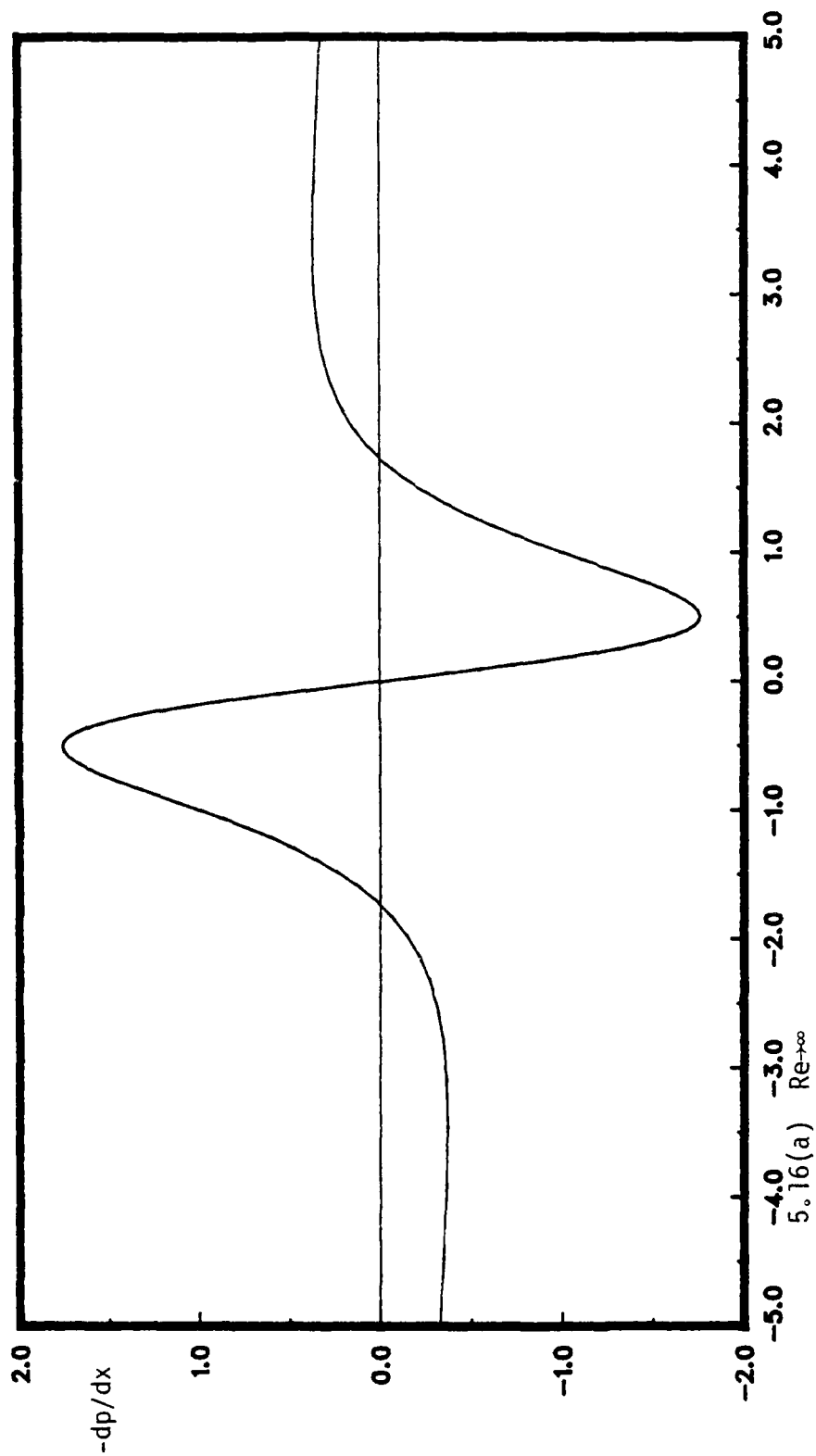
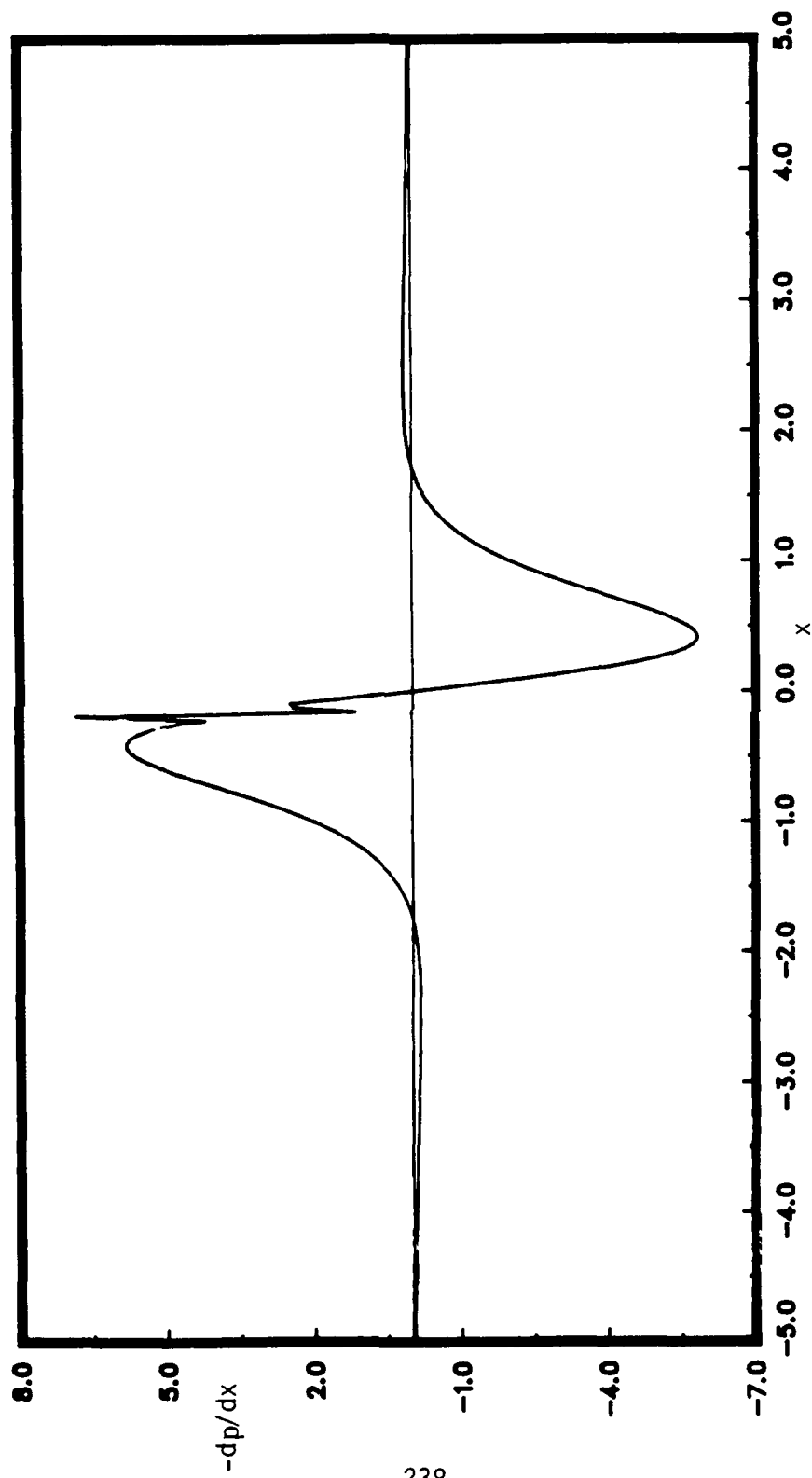
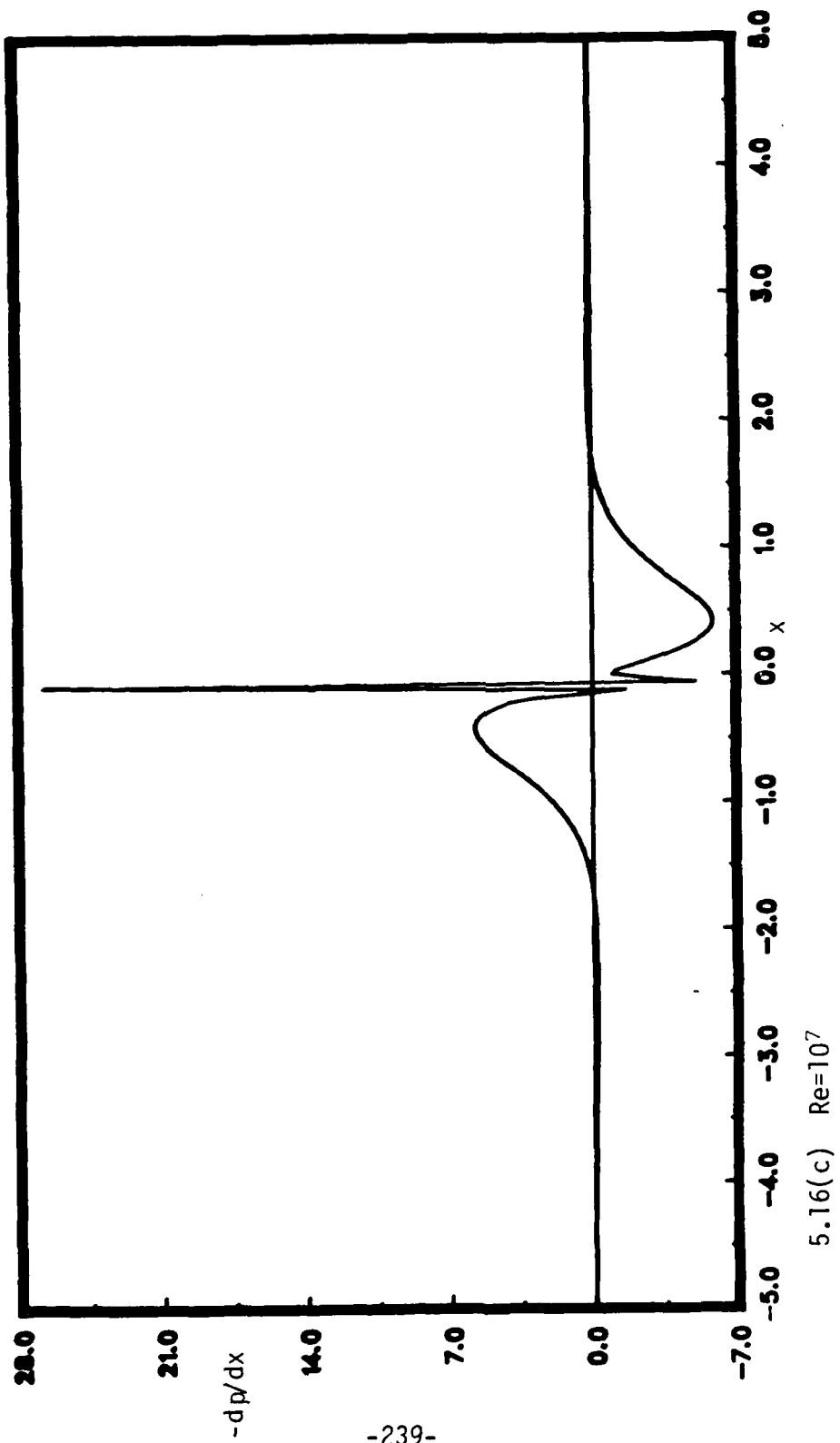
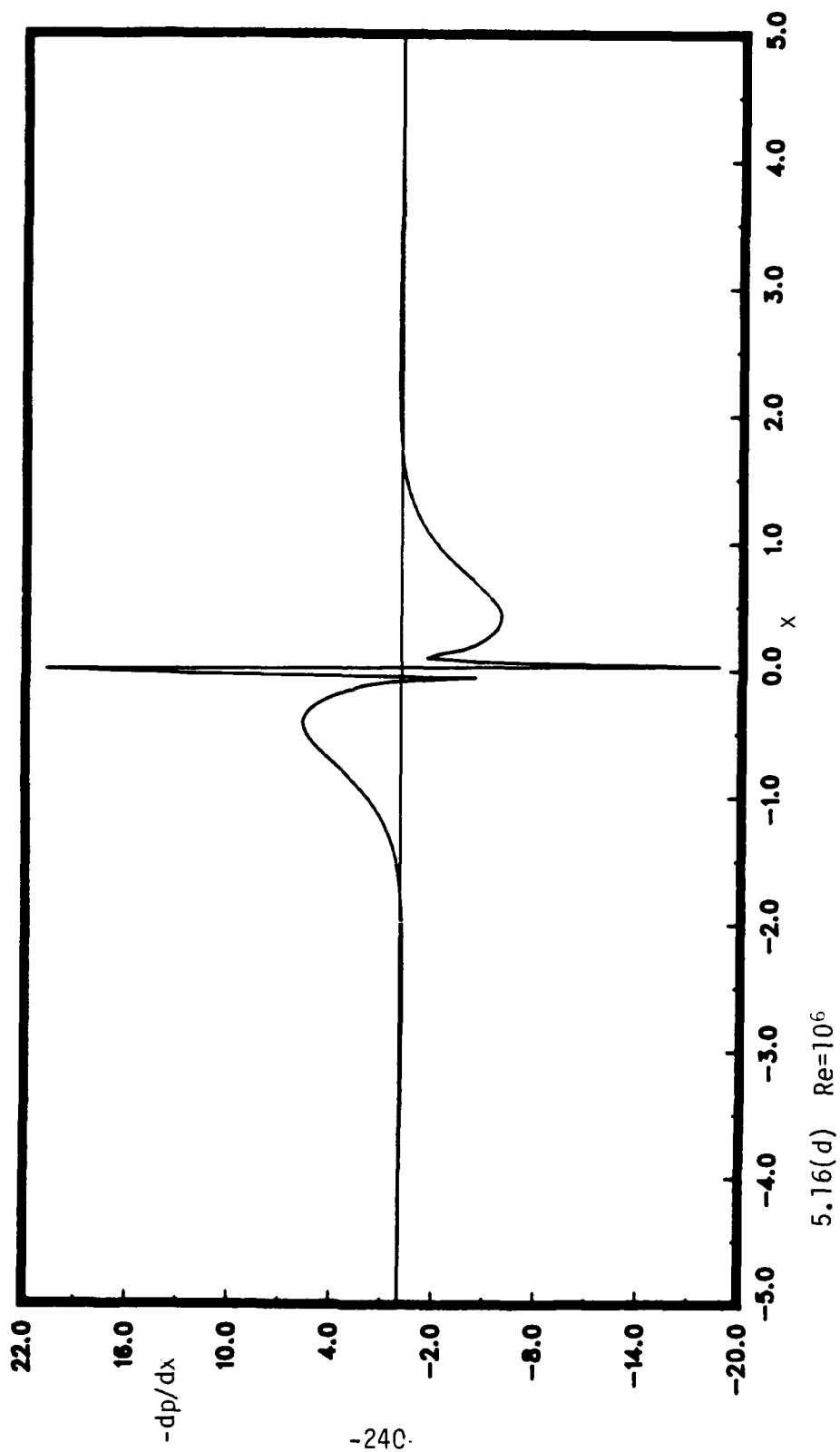


Figure 5.16. Pressure gradient at time  $t_s$ , for the limit problem and the fully interacting cases  $Re=10^8$ ,  $10^7$  and  $10^6$ .



5.16(b)  $Re=10^8$





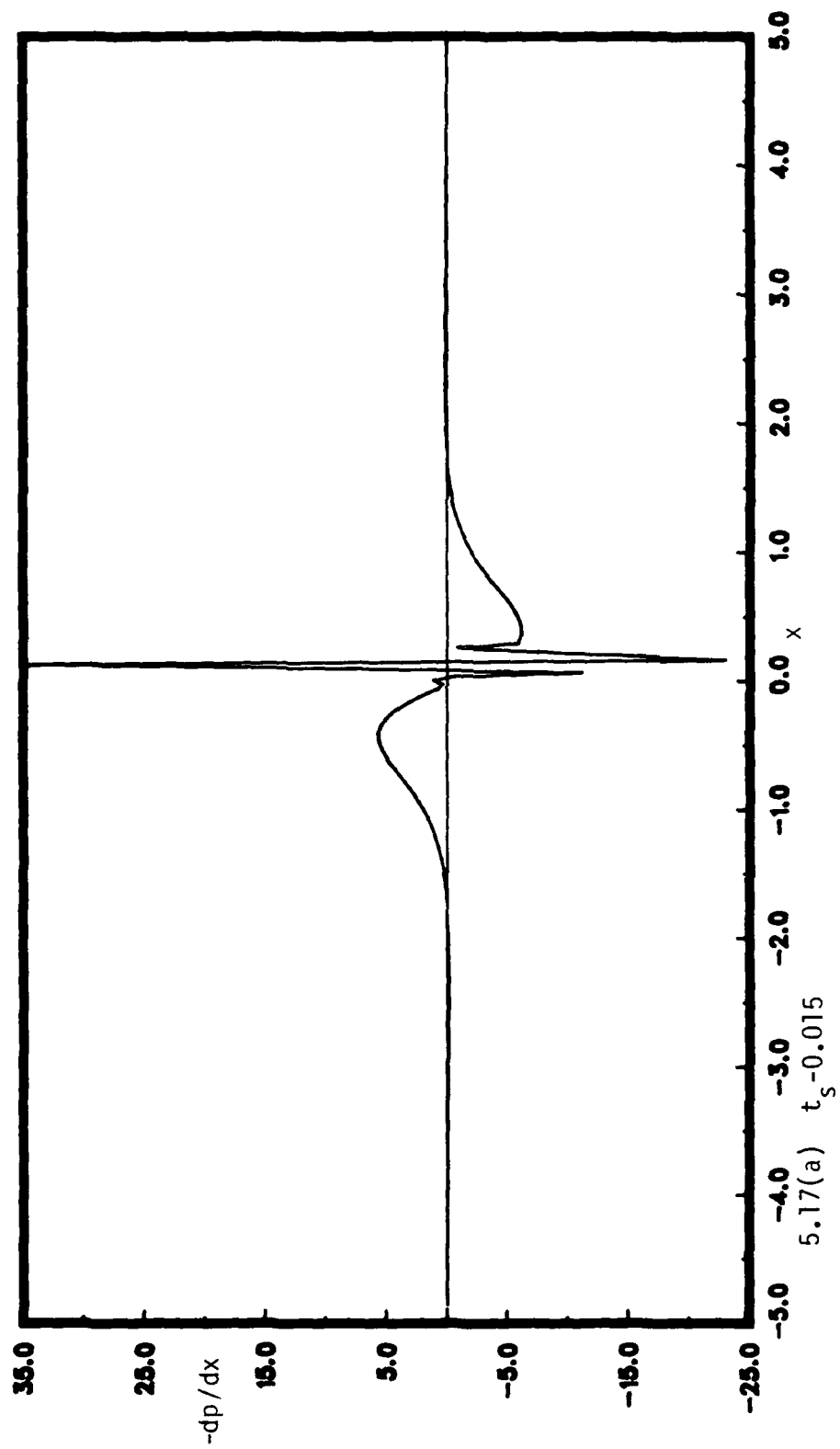
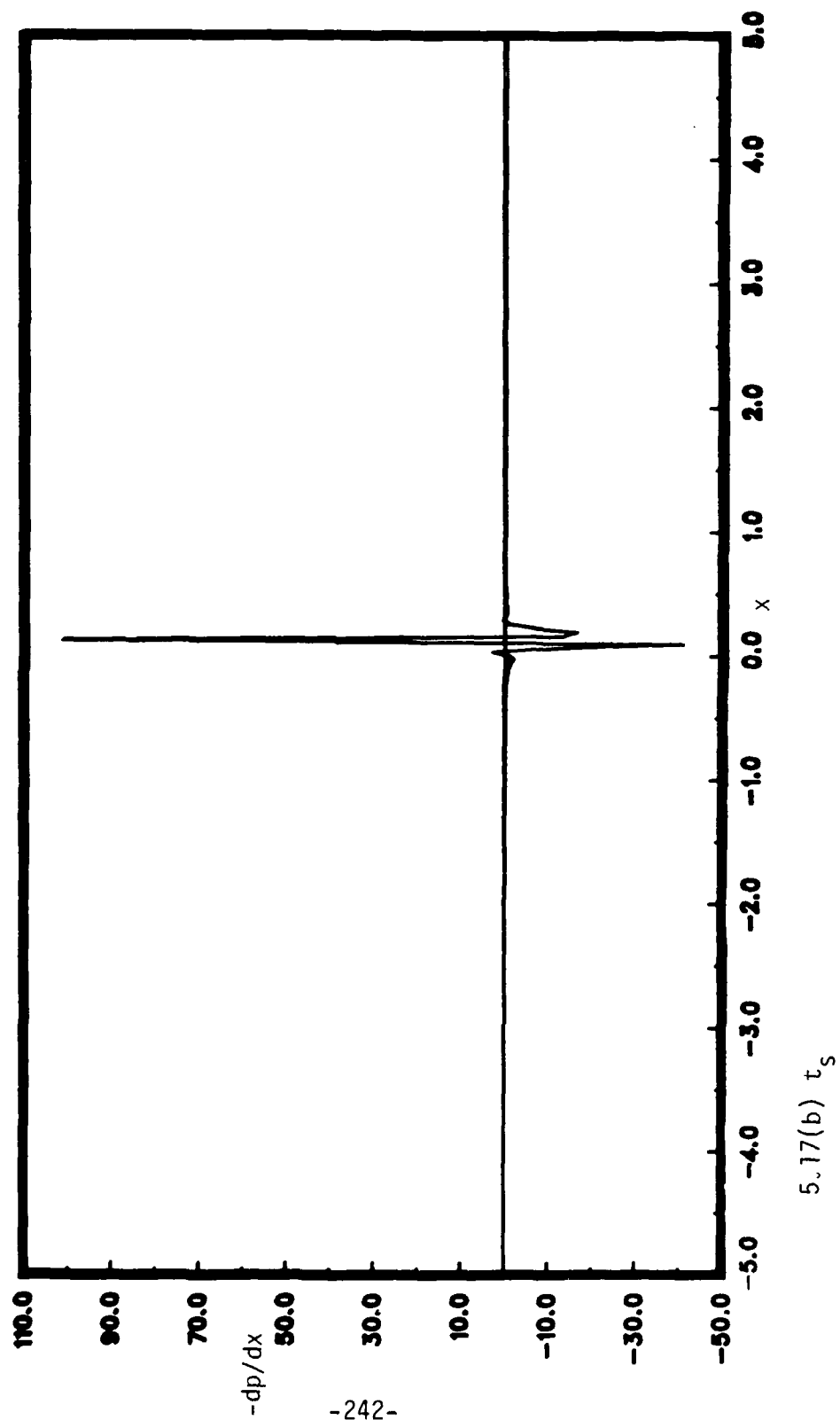
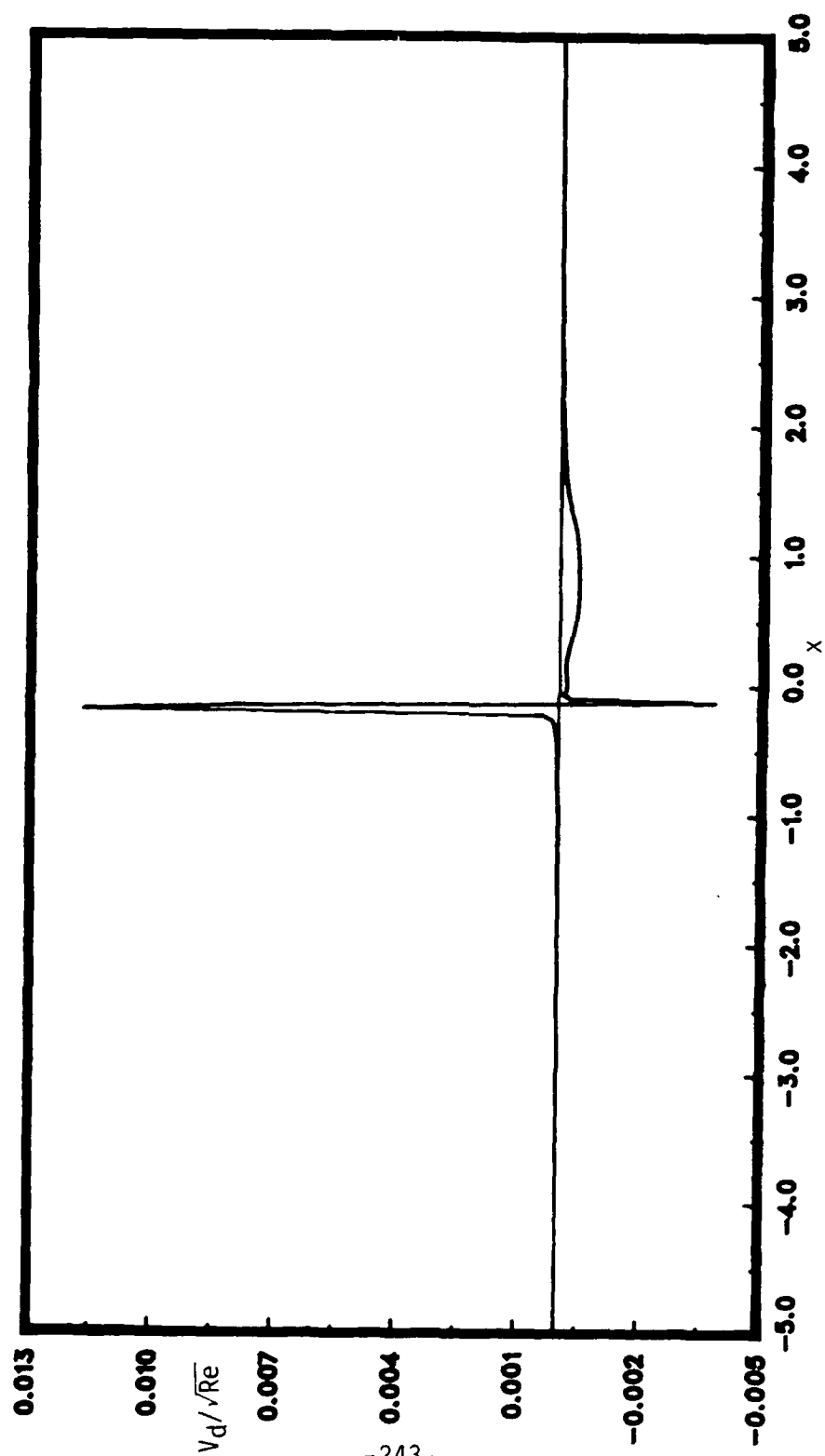


Figure 5.17. Temporal evolution of pressure gradient as  $t \rightarrow t_s$ ,  $Re=10^5$ .

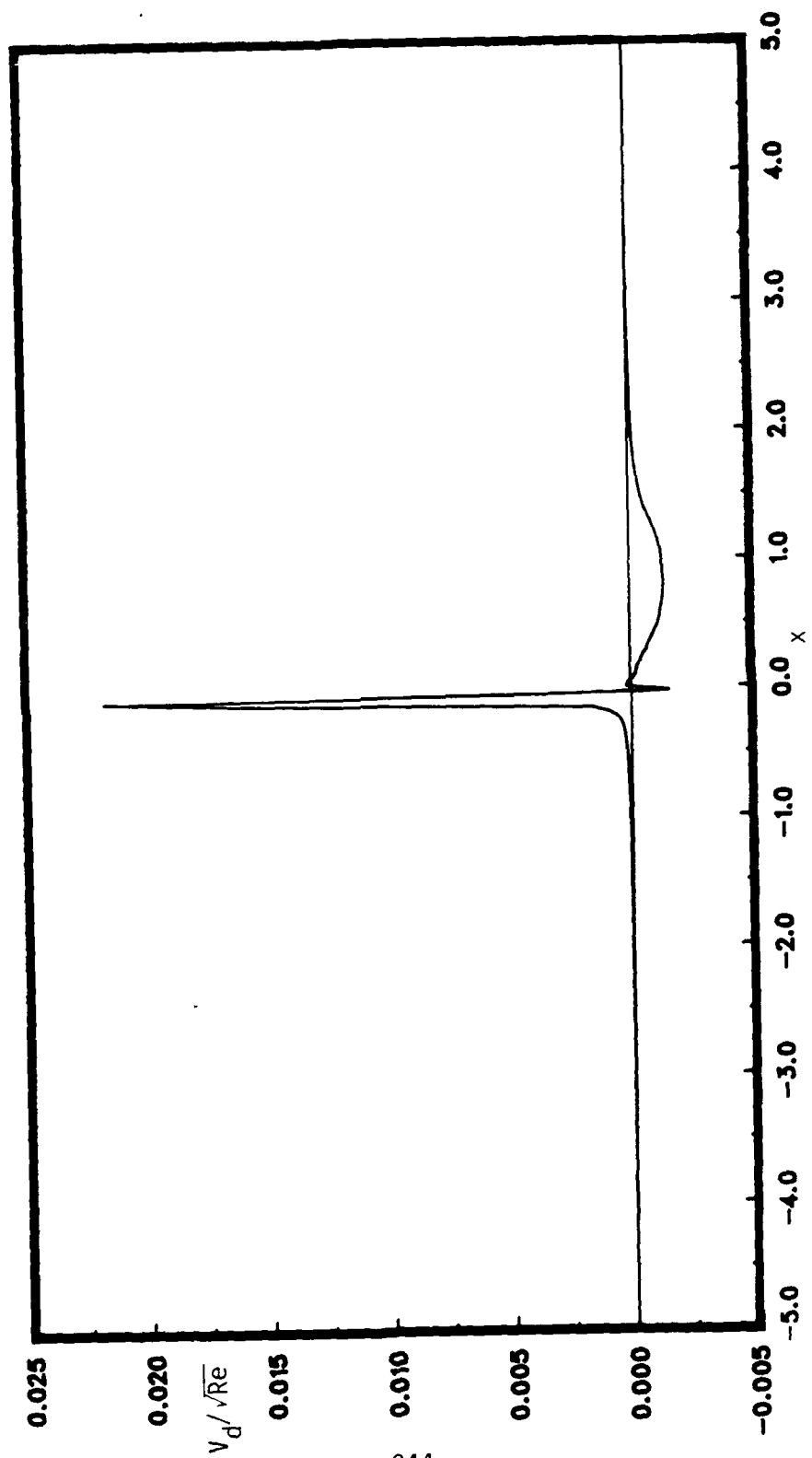




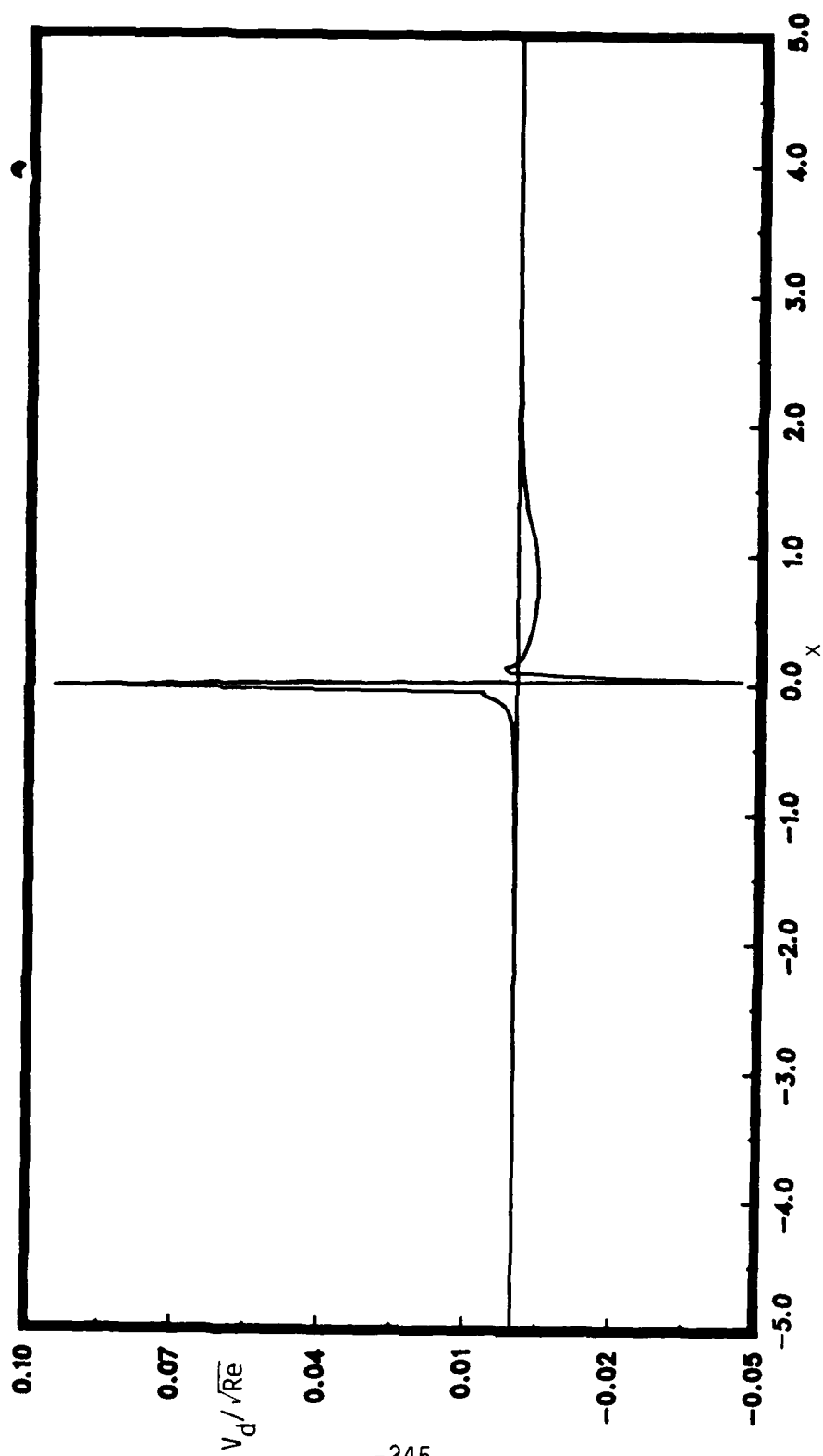
5.18(a)  $Re=10^8$

Figure 5.18. Induced displacement velocity at time  $t_s$ .

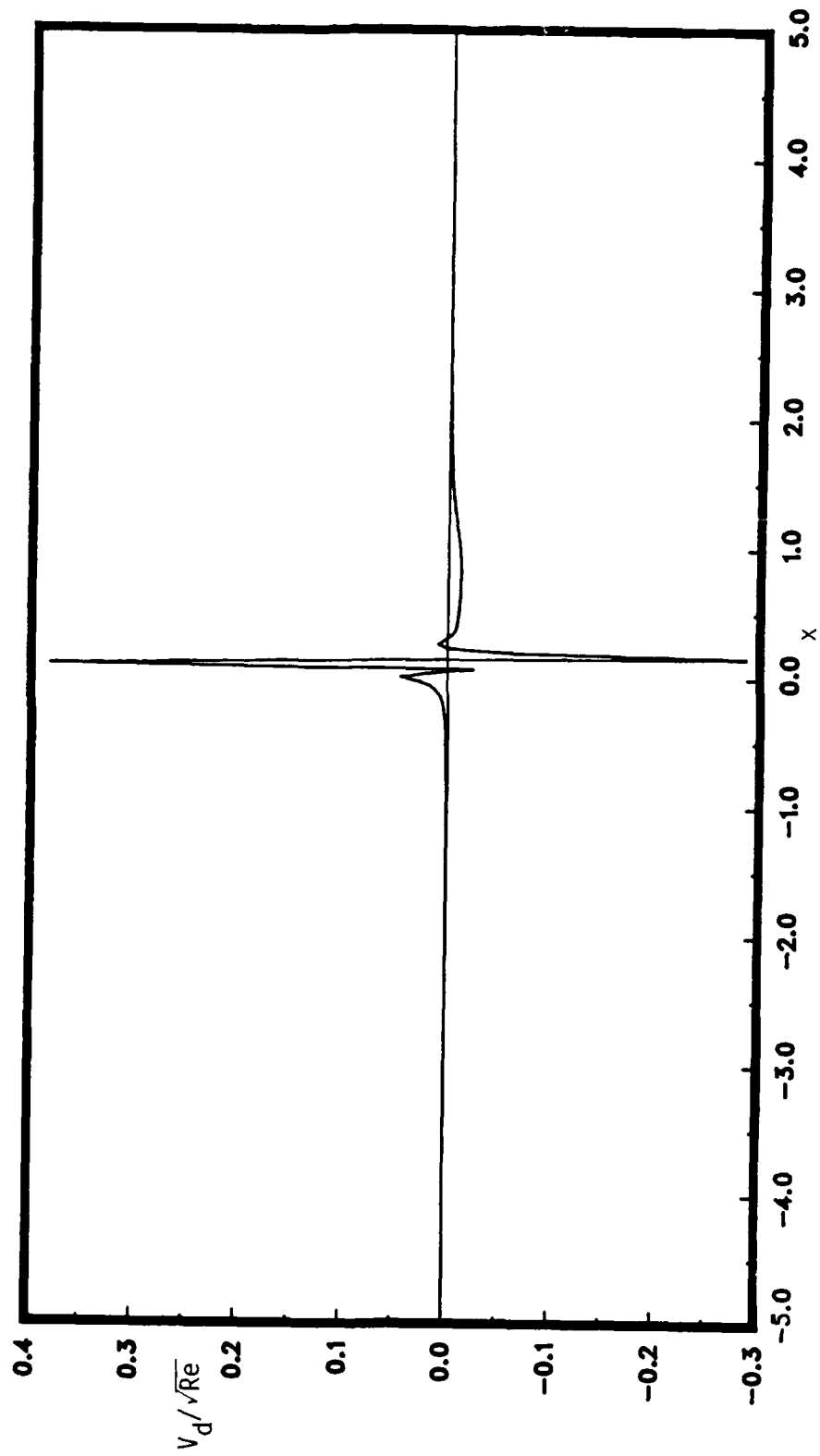




5.18(b)  $Re=10^7$



5.18(c)  $Re=10^6$



5.18(d)  $Re=10^5$

### 5.5 The Streamwise and Temporal Scales for the First Interactive State

The purpose of this section is to show that the interacting boundary-layer results are quantitatively, as well as qualitatively, consistent with the temporal and streamwise scales derived by Elliott, Cowley and Smith (1983) for the first interactive state (c.f. §2.6). In the first interactive state a multi-structured region (depicted in figure 2.7) appears as a vertical spike-like region on a scale where  $x=O(1)$ . The interacting results of this study are in qualitative agreement with the Reynolds-number dependent time and length scales proposed by Elliott, Cowley and Smith (1983); for example, the spike in the displacement thickness (and hence the streamwise scale of the first interactive state) increases with decreasing  $Re$ . In addition, the time between the onset of strong interaction and ultimate boundary-layer breakdown also decreases as  $Re$  decreases (see table 5.1). However, it is possible to make a somewhat stronger quantitative comparison with the predicted asymptotic results and this is carried out in this section.

The governing equations for the first interactive state, formulated by Elliott, Cowley and Smith (1983), are given in equations (2.35) to (2.39); scaled streamwise and temporal variables of this state are reproduced here from equations (2.32) and (2.33) viz.

$$t_1 = Re^{2/11}(t-t_s), \quad X_1 = Re^{3/11}((x-x_s) - K(t_s-t)), \quad (5.5)$$

where the subscript (1) indicates variables which are  $O(1)$  in the first interactive state. The numerical problem associated with the first interactive state is complex and has not yet been solved. However, as discussed in §2.6, the first interactive state is expected to terminate in a singularity; accordingly,

in the following discussion let  $t_{ls}$  and  $X_{ls}$  be the time and spatial location of this singularity. The quantity  $t_{ls}$  is related to the breakdown times of the interactive boundary-layer problem by

$$t_{ls} = Re^{2/11}(t_s(Re) - t_s(\infty)), \quad (5.6)$$

where  $t_s(Re)$  is the breakdown time at a finite value of  $Re$ , and  $t_s(\infty)$  is the breakdown time for the limit problem. The tabulated data in table 5.1 for  $t_s(Re)$ ,  $Re$ , and  $t_s(\infty)$  was used to carry out a regression analysis which confirmed the  $(2/11)$  scale in  $Re$ , and estimated the value of  $t_{ls}$ . The analysis was carried out as follows. Let  $t_{ls}' = (-t_{ls})$ , then algebraic manipulation of equation (5.6) gives

$$\log(t_s(\infty) - t_s(Re)) = \log(t_{ls}') - 2/11 \cdot \log(Re). \quad (5.7)$$

The regression (i.e. a least squares curve fit) was carried out on the equation

$$\log(t_s(\infty) - t_s(Re)) = \hat{a} + \hat{b} \cdot \log(Re), \quad (5.8)$$

using the data in table 5.1. The estimated values for  $\hat{a}$  and  $\hat{b}$  using this approach are

$$\hat{a} = 1.21 \pm .36, \quad \hat{b} = -.190 \pm .024. \quad (5.9)$$

Since  $(2/11) = 0.182$ , the estimate for the slope  $\hat{b}$  indicates that the interaction time scale of this study is in close agreement with the time scale predicted by Elliott, Cowley and Smith (1983). The intercept  $\hat{a}$  may be used to estimate  $t_{ls}$  by

$$t_{1s} = -e^{\hat{a}}; \quad (5.10)$$

and thus the best estimate for  $t_{1s}$  is

$$t_{1s} = -3.4, \quad (5.11)$$

for which ninety-five percent confidence interval is  $-4.8 < t_{1s} < -2.3$ . The length of time from the onset of strong interaction to the boundary layer breakdown,  $(t_s(\text{Re}) - t_{0i}(\text{Re}))$ , also scales as  $\text{Re}^{2/11}$ , as predicted by the analysis of Elliott *et al* (1983). A regression on the equation

$$\log(t_s(\text{Re}) - t_{0i}(\text{Re})) = \hat{e} + \hat{f} \cdot \log(\text{Re}), \quad (5.12)$$

was used to obtain the estimates

$$\hat{e} = -5.84 \pm .63, \quad \hat{f} = 0.185 \pm .041. \quad (5.13)$$

The computed  $\hat{f}$  closely confirms the predicted theoretical value  $(2/11) = 0.182$ .

It is also of interest to compare the streamwise eruptive zone which is expected to be  $O(\text{Re}^{-3/11})$ , as predicted by the asymptotic theory of Elliott, Cowley and Smith (1983). The values of the breakdown locations  $x_s(\infty)$  and  $x_s(\text{Re})$  are given in table 5.1 and represent distances from the origin in a reference frame moving with the vortex. In order to make a comparison with the theoretical results consider a laboratory reference frame in which the origin corresponds to the instantaneous location of the vortex at  $t_s(\infty)$ . For the cases at finite  $\text{Re}$  the vortex is assumed to pass the same location at  $t_s(\text{Re})$ . In the laboratory frame the velocity of the singularity is given by

$$U_e(x_s(Re)) \cdot U_s = U_v - K. \quad (5.14)$$

Note that the vortex velocity, which is  $U_v = 1 + O(Re^{-1/2})$ , is close to being constant throughout the integrations.<sup>3</sup> The analysis of Elliott, Cowley and Smith (1983) suggests that

$$x_s(Re) - x_s(\infty) + U_{e_s} U_s (t_s(\infty) - t_s(Re)) = O(Re^{-3/11}). \quad (5.15)$$

A least-squares regression of the equation

$$\log((x_s(Re) - x_s(\infty)) - (U_{e_s} U_s)(t_s(Re) - t_s(\infty))) = \hat{c} + \hat{d} \cdot \log(Re), \quad (5.16)$$

generated the regression estimated values

$$\hat{c} = 3.05 \pm .23, \quad \hat{d} = -.295 \pm .015. \quad (5.17)$$

Since  $(3/11) = 0.273$ , the value computed for the slope  $\hat{d}$  is in close agreement to the scale predicted by Elliott, Cowley and Smith (1983).

---

<sup>3</sup>In the limit problem the vortex velocity is constant ( $U_v = 1$ ). Although unsteady in the interacting problems, it deviates from the limit problem only by  $O(Re^{-1/2})$ . During the interacting calculation  $U_v$  increases monotonically from  $U_v(0) = 1$  to:  $U_v(t_s) = 1.000$  for  $Re = 10^8$ ,  $U_v(t_s) = 1.001$  for  $Re = 10^7$ ,  $U_v(t_s) = 1.001$  for  $Re = 10^6$ ,  $U_v(t_s) = 1.004$  for  $Re = 10^5$ .

## 5.6 Breakdown of the Conventional Interactive Approach

Smith (1988) has shown that a singularity can form in the solution of the boundary-layer equations using the conventional interacting approach. In this study all interacting calculations developed a singularity in finite time, and the purpose of this section is to compare the present results with specific details predicted by Smith (1988). As discussed in §2.7, Smith (1988) shows that, in a conventional interacting boundary-layer calculation, a three-zone structure will emerge at  $t \rightarrow t_s$  consisting of an inviscid interaction region sandwiched between a viscous shear layer near the wall and a non-linear critical layer above. The breakdown of the conventional interactive approach can be of a "moderate" or "severe" type (Smith, 1988). For "moderate" breakdown, Smith (1988) indicates that the temporal behavior of the wall shear  $\tau_w$  is  $O(t_s - t)^{-1/4}$  near  $x = x_s$  as indicated in equation (2.31); in addition the predicted behavior for the maximum value of pressure gradient and normal velocity near  $x = x_s$  are given by equation (2.58) and (2.59) and are  $O(t_s - t)^{-1}$ . In the first part of this section, regression analyses of the present results will be described in an effort to confirm the predicted behavior of  $\tau_w$ ,  $v_{\max}$  and  $(dp/dx)_{\max}$ . In the second part of this section, a qualitative comparison is made between the velocity field near  $x = x_s$  computed in this study and the three-tier structure described by Smith (1988).

Three regression studies of the temporal evolution (within the interaction zone) of wall shear, pressure gradient, and normal velocity were carried out using data computed in the terminal stages of each interacting case. As  $t \rightarrow t_s$ , the  $\hat{x}$  location corresponding to the point of minimum gradient,  $\hat{x}_M$ , moves toward  $\hat{x} = \hat{x}_s$ , the location of the singularity. Values of  $\tau_w$ ,  $(dp/dx)$  and  $v$  were evaluated at  $\hat{x}_M$  over a number of time steps as  $t \rightarrow t_s$ ; these temporal



records were then fitted using least squares analysis to determine how the appropriate quantity behaved as the singularity evolved. Smith (1988) shows that the wall shear, in a conventional interacting boundary-layer calculation, should develop a quarter-power time dependence according to equation (2.51), which is repeated here,

$$\tau_w(\hat{x}_s) = c(t_s - t)^{-1/4} \quad \text{as } t \rightarrow t_s. \quad (5.18)$$

The prediction of a wall shear singularity is qualitatively confirmed by the results of this study, as may be seen in figures 5.10; however, a quantitative comparison is also possible. At each time step in the terminal stages of the calculations,  $\tau_w$  was estimated from the mesh point whose streamwise location was closest to  $\hat{x}_M$ . A least squares curve fit, one for each value of Re was carried out using the regression equation  $\tau_w(\hat{x}_M, t) = c(t_s - t)^b$ , and table 5.2 summarizes the results of these studies. The value of b is consistently close to -0.25 for all values of Re considered; in view of the small standard error in each case these results support the theoretical prediction of Smith (1988) and suggest that the model problem of this study experiences what Smith has termed a "moderate" boundary-layer breakdown.

Re	$t_s$	interval	$\log( c )$	b
$10^8$	0.8965	[0.819, $t_s$ )	$-0.391 \pm 0.065$	$-0.252 \pm 0.016$
$10^7$	0.8185	[0.805, 0.816]	$-0.778 \pm 0.174$	$-0.253 \pm 0.035$
$10^6$	0.7240	[0.680, $t_s$ )	$-0.295 \pm 0.092$	$-0.263 \pm 0.022$
$10^5$	0.6445	[0.634, $t_s$ )	$0.892 \pm 0.127$	$-0.234 \pm 0.032$

Table 5.2. Summary of regression study for temporal behavior of wall shear near  $\hat{x}_s$ ;  $\tau_w = O(t_s - t)^b$ ; values of  $t_s$  for each Re are given in table 5.1.

The predicted behavior for the maximum pressure gradient near  $x=x_s$  is given by equation (2.58) which is repeated here,

$$-\frac{dp}{dx}(\hat{x}_s) = c(t_s - t)^{-1} \quad \text{as } t \rightarrow t_s. \quad (5.19)$$

At each time step in the terminal stages of the interacting calculation, the pressure gradient was computed from equation

$$-\frac{dP}{dx}(\hat{x}_M) = \left( (U_e - U_v) \frac{\partial U_e}{\partial x} + \frac{\partial U_e}{\partial t} \right) \Big|_{x(\hat{x}_M)}, \quad (5.20)$$

where again  $\hat{x}_M$  denotes the  $\hat{x}$  position of the minimum gradient (as  $t \rightarrow t_s$ ,  $\hat{x}_M \rightarrow \hat{x}_s$ ). A regression on the pressure gradient was carried out on the equation  $-dP(\hat{x}_M, t)/dx = c(t_s - t)^b$  for each finite Reynolds number case, and the results are summarized in table 5.3. Again, broad agreement with the

theory of Smith (1988) (which predicts  $b=-1$ ) is obtained. Note however that the quantitative evidence is not overwhelming strong. The theoretical prediction of  $b=-1$  is within the ninety-five percent confidence intervals of the cases for  $Re=10^8$ ,  $10^7$  and  $10^6$ , but there is a rather large standard error. The only case in which the relative error is low,  $Re=10^5$ , suggests a much larger value for  $b$  which inconsistent with Smith's (1988) description of moderate boundary layer breakdown. Unfortunately, both  $dp/dx$  and  $V_d$  are difficult to evaluate with a great deal of accuracy as  $t \rightarrow t_s$ , and this may be the reason for the apparent discrepancy.

Re	$t_s$	interval	$\log(c)$	$b$
$10^8$	0.8965	[0.855, 0.890]	$-1.43 \pm 1.03$	$-0.778 \pm 0.278$
$10^7$	0.8185	[0.813, $t_s$ )	$-3.85 \pm 0.97$	$-1.06 \pm 0.61$
$10^6$	0.7240	[0.710, $t_s$ )	$-2.39 \pm 1.69$	$-1.11 \pm 0.33$
$10^5$	0.6445	[0.623, $t_s$ )	$-17.6 \pm 2.9$	$-4.64 \pm 0.70$

Table 5.3. Summary of regression study for temporal behavior of pressure gradient near  $x=x_s$ ;  $dp/dx=O(t_s-t)^b$ .

A regression study of the temporal growth in  $v_{max}$  was also carried out in the same manner as the studies on wall shear and pressure gradient. The quantity  $V_d(\hat{x}_M)$ , where  $V_d$  is the induced displacement velocity given by equation (3.121), was used to estimate  $v_{max}$  in the strong interaction zone. The  $V_d$  equation (3.121) may be computed in the transformed  $\hat{x}$  coordinates

using transformation law (3.51), from<sup>4</sup>

$$V_d(\hat{x}_M) = \left( -\frac{Ue_0}{2\pi} \left( \delta^* \frac{\partial Ue}{\partial \hat{x}} + Ue \frac{\partial \delta^*}{\partial \hat{x}} \right) \right) \Big|_{\hat{x}_M}. \quad (5.21)$$

The theoretical prediction (2.59) is repeated here, viz.

$$V_d(\hat{x}_s) = c \cdot (t_s - t)^{-1} \quad \text{as } t \rightarrow t_s. \quad (5.22)$$

A regression study for each case was carried out on the equation  $V_d(\hat{x}_M, t) = c(t_s - t)^b$  and the results are summarized in table 5.4. The theoretical value is  $b = -1$  and again the present results are in reasonable agreement with Smith (1988). Note however that the standard error is somewhat large for these estimates in table 5.4.

---

4

The value of  $\delta^*$  at  $\hat{x}_s$  was computed in a procedure which determines  $\hat{x}_s$  using a bisection search of  $\delta^*$  to find  $\delta^*_{\max}$ . This procedure also gives  $\delta^*$  at  $(\hat{x}_s + \epsilon)$  and  $(\hat{x}_s + 2\epsilon)$ ; the slope of  $\delta^*$  at  $\hat{x}_s$  was then evaluated using the second-order forward-difference expression

$$\frac{\partial \delta^*}{\partial \hat{x}} = \frac{-3\delta^*(\hat{x}_s) + 4\delta^*(\hat{x}_s + \epsilon) - \delta^*(\hat{x}_s + 2\epsilon)}{2\epsilon}.$$

The value  $\epsilon$  is equal to the interval size of the final iterate of the bisection-search procedure for  $\delta^*_{\max}$ ;  $\epsilon$  is halved at every iterate and its magnitude and depends on how many iterates are required to isolate the "spike". Consequently,  $\epsilon$  has no minimum value, but the maximum value is  $\epsilon = \Delta \hat{\xi}/4$ , where  $\Delta \hat{\xi}$  is the streamwise discretization interval of both the inner and outer unsteady calculations.

Re	$t_s$	interval	$\log(c)$	b
$10^8$	0.8965	[0.855, 0.890]	$-2.81 \pm 1.07$	$-1.24 \pm 0.31$
$10^7$	0.8185	[0.810, $t_s$ )	$-1.55 \pm 0.53$	$-0.957 \pm 0.094$
$10^6$	0.7240	[0.669, $t_s$ )	$-0.823 \pm 0.974$	$-1.03 \pm 0.18$
$10^5$	0.6445	[0.6405, $t_s$ )	$-0.53 \pm 1.32$	$-0.94 \pm 0.21$

Table 5.4. Summary of regression study for temporal behavior of  $v_{\max}$ ;  $V_d(\bar{x}_s) = O(t_s - t)^b$ .

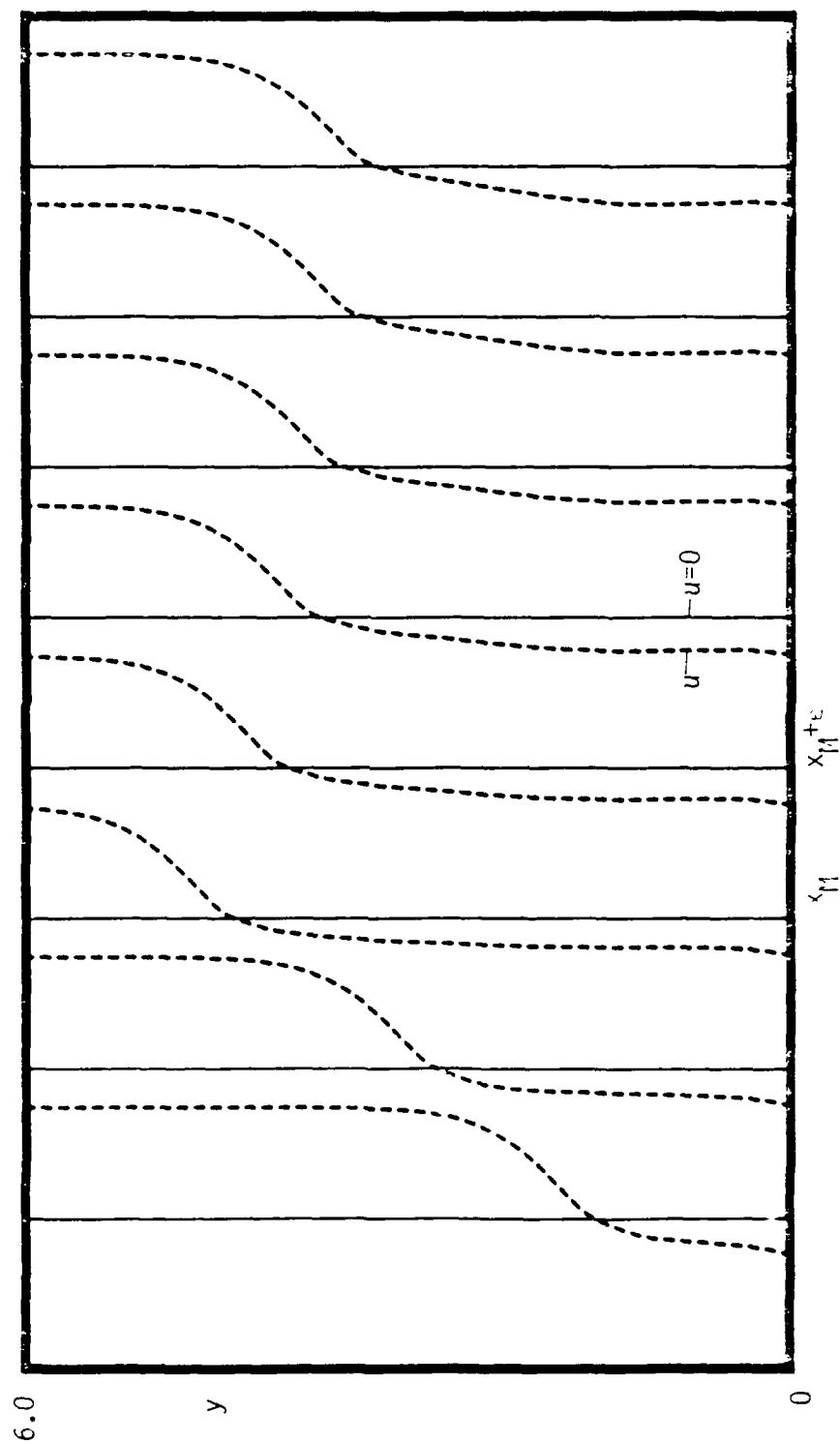
Two aspects of the regression analysis should be noted. First, the regressions were carried out on time intervals in which the regression quantity ( $V_d$ ,  $\tau_w$ , or  $dp/dx$ ) had a well-defined trend. Generally, this interval included the very terminal stages of the calculation up to  $t_s$ , but in a few individual cases the interval was truncated at a time slightly before  $t_s$  because the data beyond this time was somewhat erratic. Such cases are indicated in tables 5.2 to 5.4 wherever the last point in the time interval is not  $t_s$ . A second very important point is that, in all cases, the value of "b" is very sensitive to the value  $t_s$ ; a change in  $t_s$  of as little as 0.001 can change the value of "b" by as much as thirty percent.

Next, the velocity profiles near  $x_s$  of the present results will be plotted in order to compare with the three-tier structure that Smith (1988) predicts will form during interacting boundary-layer calculations as  $t \rightarrow t_s$ . This three-zone

structure is depicted schematically in figure 2.9, and consists of an inviscid zone sandwiched between two shear layers (an upper critical layer and a viscous layer at the wall). The governing equations for the inviscid zone (equations (2.44) and (2.45)) suggest that the streamwise velocity in this region should exhibit a significant streamwise dependence, in contrast to the limit problem ( $Re \rightarrow \infty$ ), where the velocity profiles near  $x_s$  are essentially uniform.

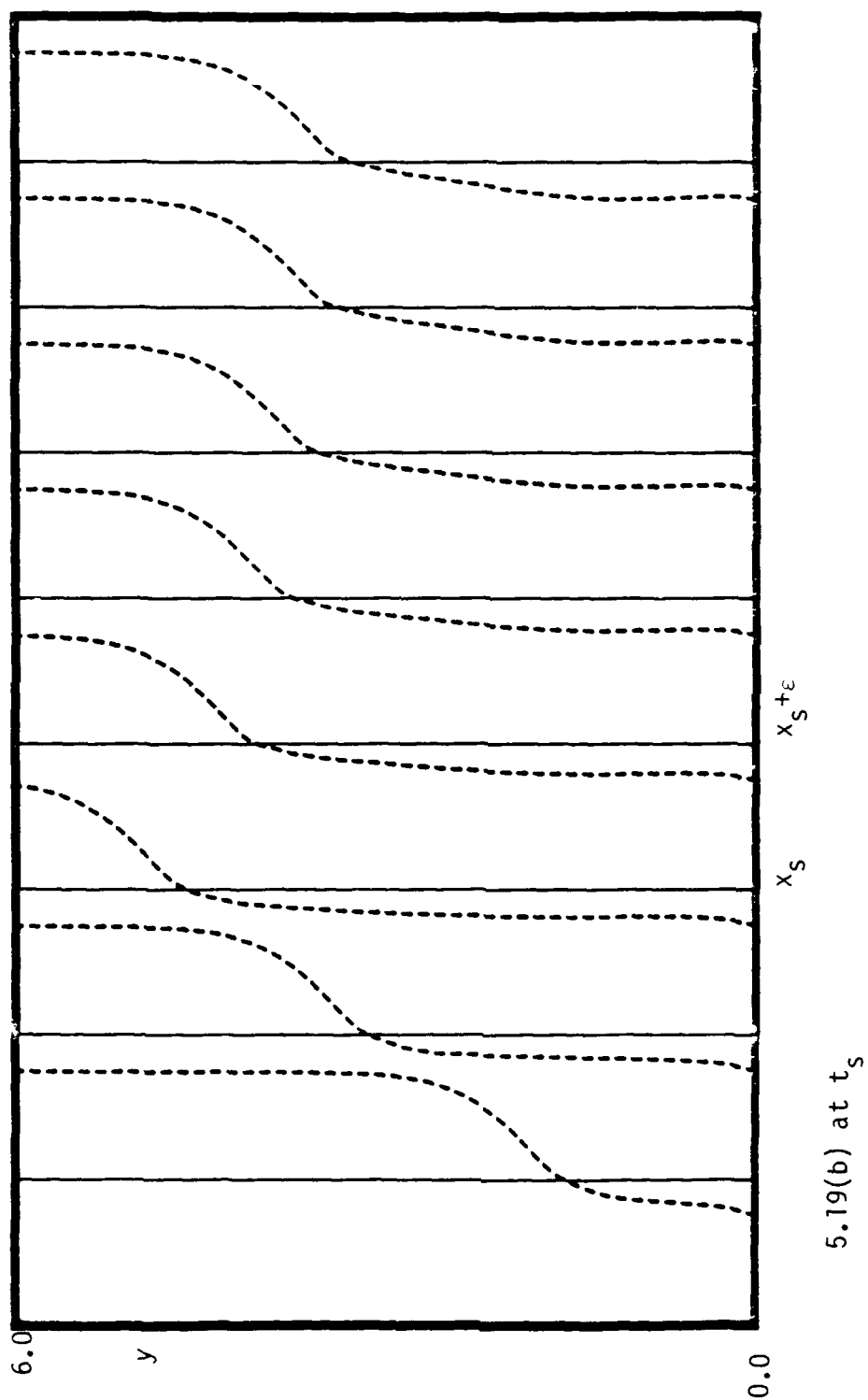
Figure 5.19 depicts velocity contours for the  $Re=10^8$  near  $x_s$  at times  $t_s-0.004$  and  $t_s$ . Note that in these figures, as well as in figures 5.20 to 5.22,  $x_M$  denotes the current estimate of the point of minimum gradient in  $x$  for times  $t < t_s$  (as discussed in Appendix E). Thus  $x_M$  for  $t < t_s$  denotes a streamwise location which is moving toward  $x=x_s$  and arrives there at  $t=t_s$ . Because the Reynolds number is very large, it is not surprising that this figure has essentially the same character as the terminal solution in the limit problem  $Re \rightarrow \infty$ . The middle inviscid region (unlike the schematic shown in figure 2.9) is seen to be somewhat asymmetric. In the interval between figures 5.19(a) and 5.19(b) it may be confirmed upon close comparison that the main changes in the velocity profiles occur near  $x_s$ , where the greatest normal growth has occurred. The velocity profiles in the middle of these plots are fairly flat but do exhibit a slight amount of curvature.

Figures 5.20(a) to 5.20(c) depict velocity profiles for  $Re = 10^7$  at times  $t_s-0.01$ ,  $t_s-0.005$  and  $t_s$ . The interaction zone starts to form at  $t_s-0.01$ , as is indicated in figure 5.20(a), and by  $t_s$  it is well-established. The velocity profiles for the  $Re=10^7$  case, like those of the  $Re=10^8$  case, have a very slight curvature. In addition, a very slight kink has developed near the top of the zone where the profiles are flat; this is evidence of the evolution of a critical shear layer near the top of the inviscid zone, as suggested by Smith (1988).

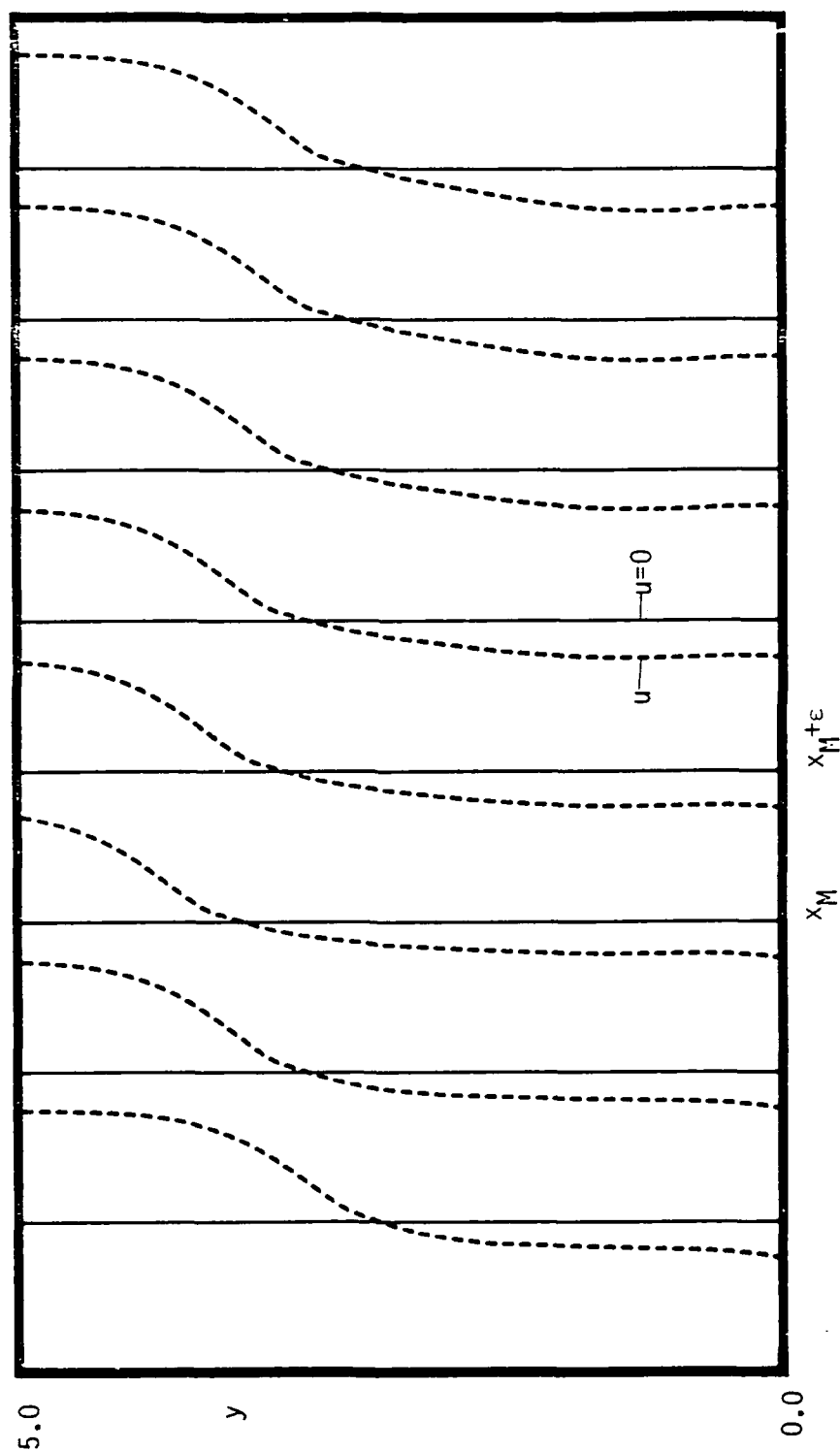


5.19(a) at  $t_s - 0.004$

Figure 5.19. Velocity profiles at equally spaced intervals near  $x_s$  for  $Re=10^8$ ;  $\epsilon = 2.09 \cdot 10^{-3}$ .

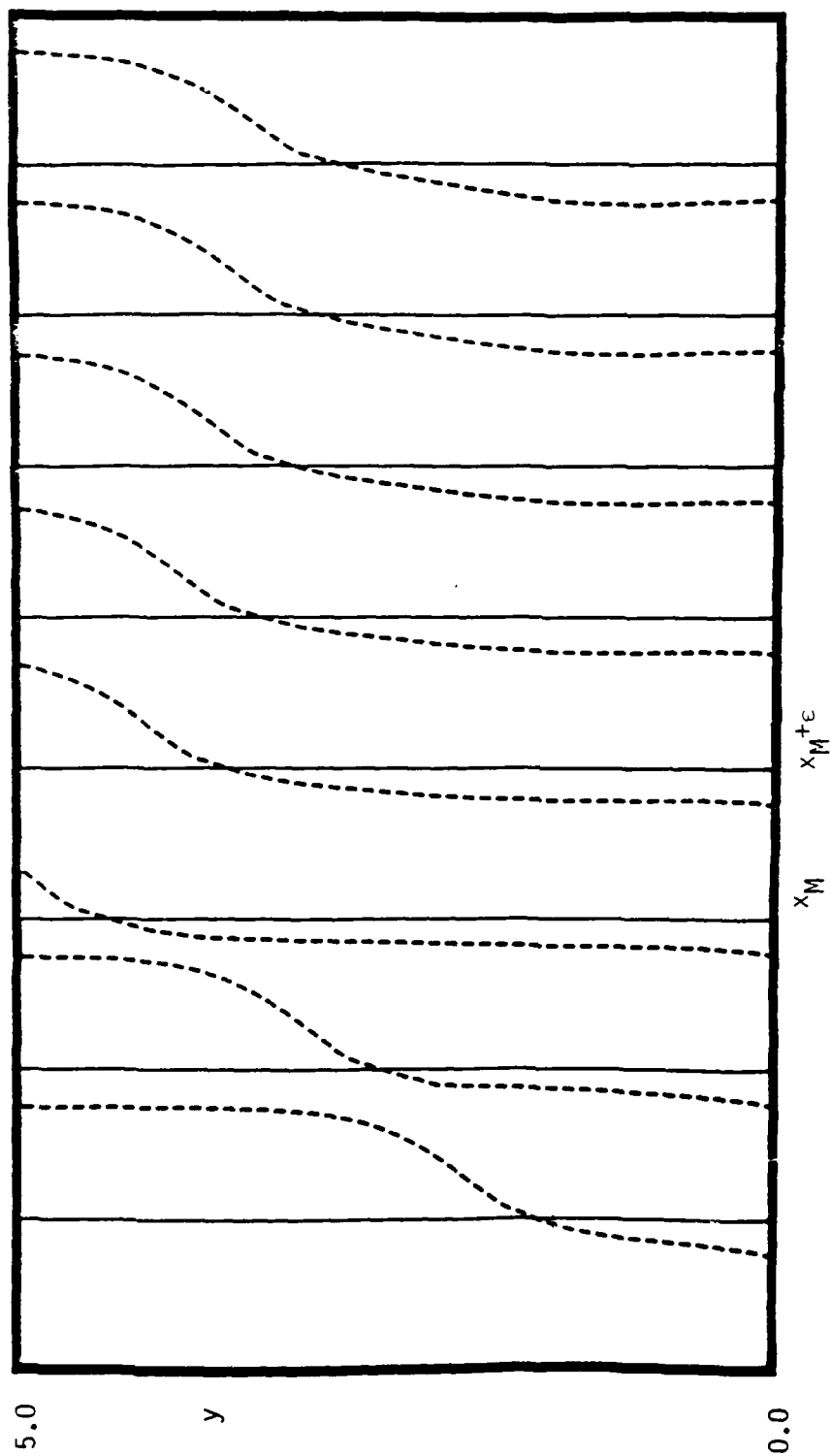




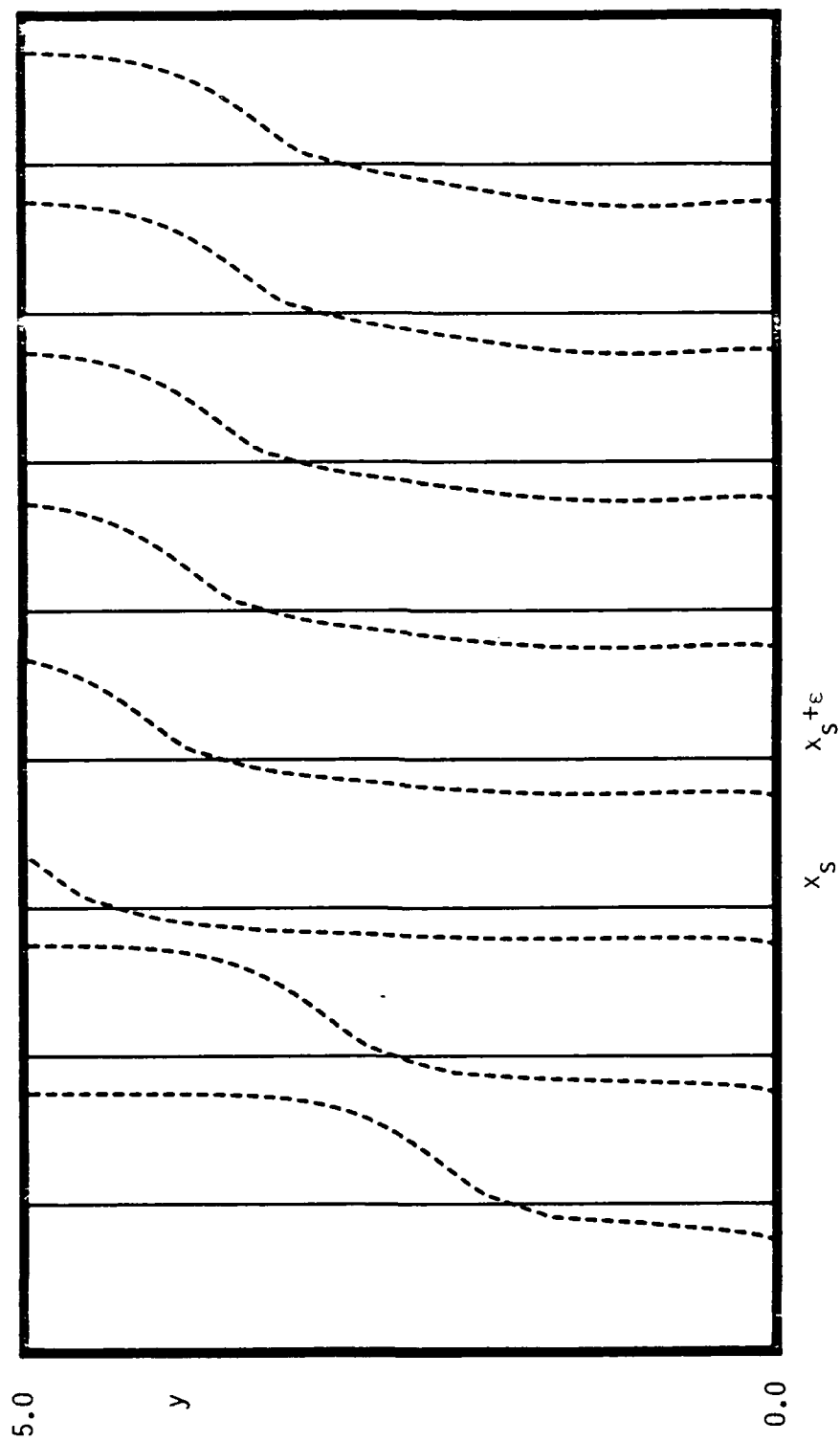


5.20(a) at  $t_s - 0.01$

Figure 5.20. Velocity profiles near  $x_s$  for  $Re=10^7$ ;  $\epsilon = 2.09 \cdot 10^{-3}$ .



5.20(b) at  $t_s - 0.005$

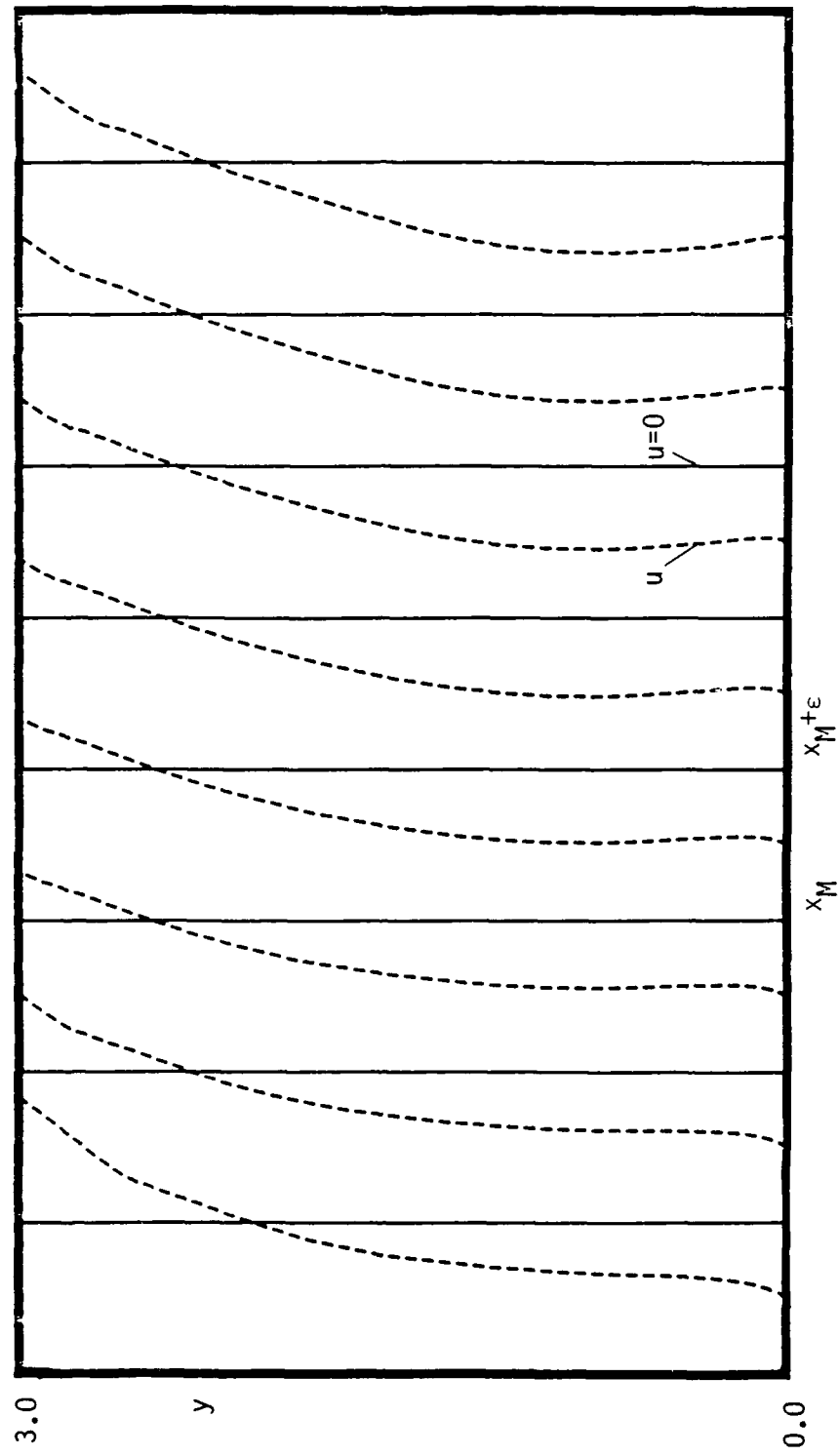


5.20(c) at  $t_s$

The narrowing of the interaction zone is also evident in this sequence of figures.

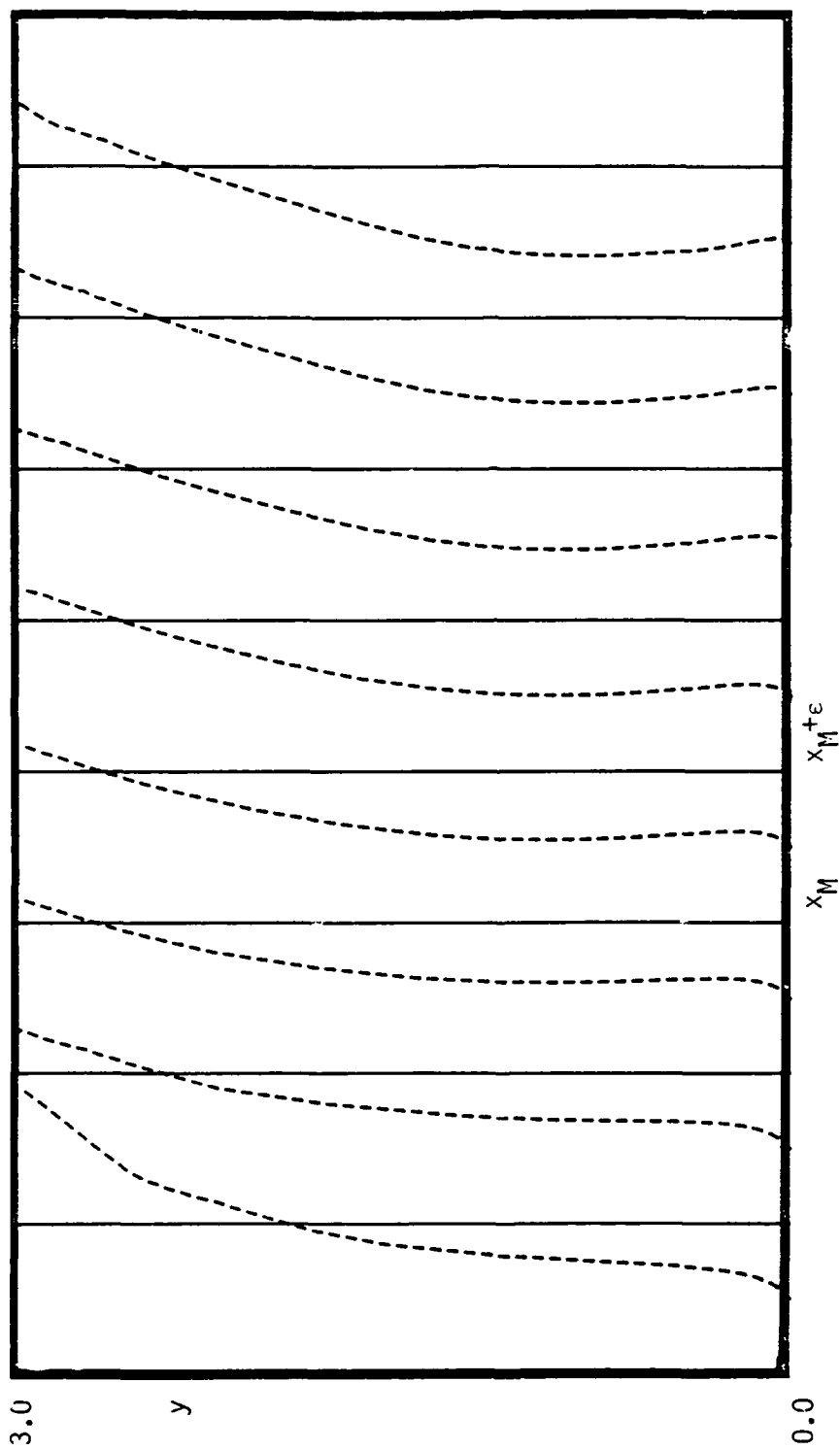
The velocity profiles for the  $Re=10^6$  case are quite bowed, as may be seen in figure 5.21, which again correspond to times  $t_s-0.01$ ,  $t_s-0.005$  and  $t_s$ . This indicates that the vorticity distribution in the central region is very non-uniform. The change in the profiles from figures 5.21(a) to 5.21(b) is rather insignificant, but the development from  $t_s-0.005$  to  $t_s$  is fairly dramatic. The velocity profiles to the left of  $x_s$  have prominent kinks suggestive of a shear layer, and the upper portion of these profiles has changed from moderate negative values of velocity to large positive values. This abrupt change in the sign of these velocity profiles suggests that the inviscid region is focussing rapidly.

The case  $Re=10^5$  case bears the most qualitative resemblance to the three-zone structure proposed by Smith (1988), and is shown in figures 5.22. Figure 5.22(a) depicts the velocity profiles near  $x_s$  at  $t_s-0.025$ . Although the time of this plot is quite close to the breakdown time, there is no feature in any one of these profiles which differentiates one from another. The three-zone region starts to form at  $t_s-0.015$ , shown in figure 5.22(b). Both the upper and lower shear layers may be seen in this plot, and the velocity profiles in the central region have the characteristic bowed appearance of the  $Re=10^6$  case profiles. In figure 5.22(c), shown at time  $t_s-0.005$ , the inviscid region is seen to narrow and focus as the velocity contours to the left of  $x_s$  take on large positive values of velocity. By time  $t_s$ , depicted in figure 5.22(d), there is a considerable degree of streamwise variation in the velocity contours in zone II.

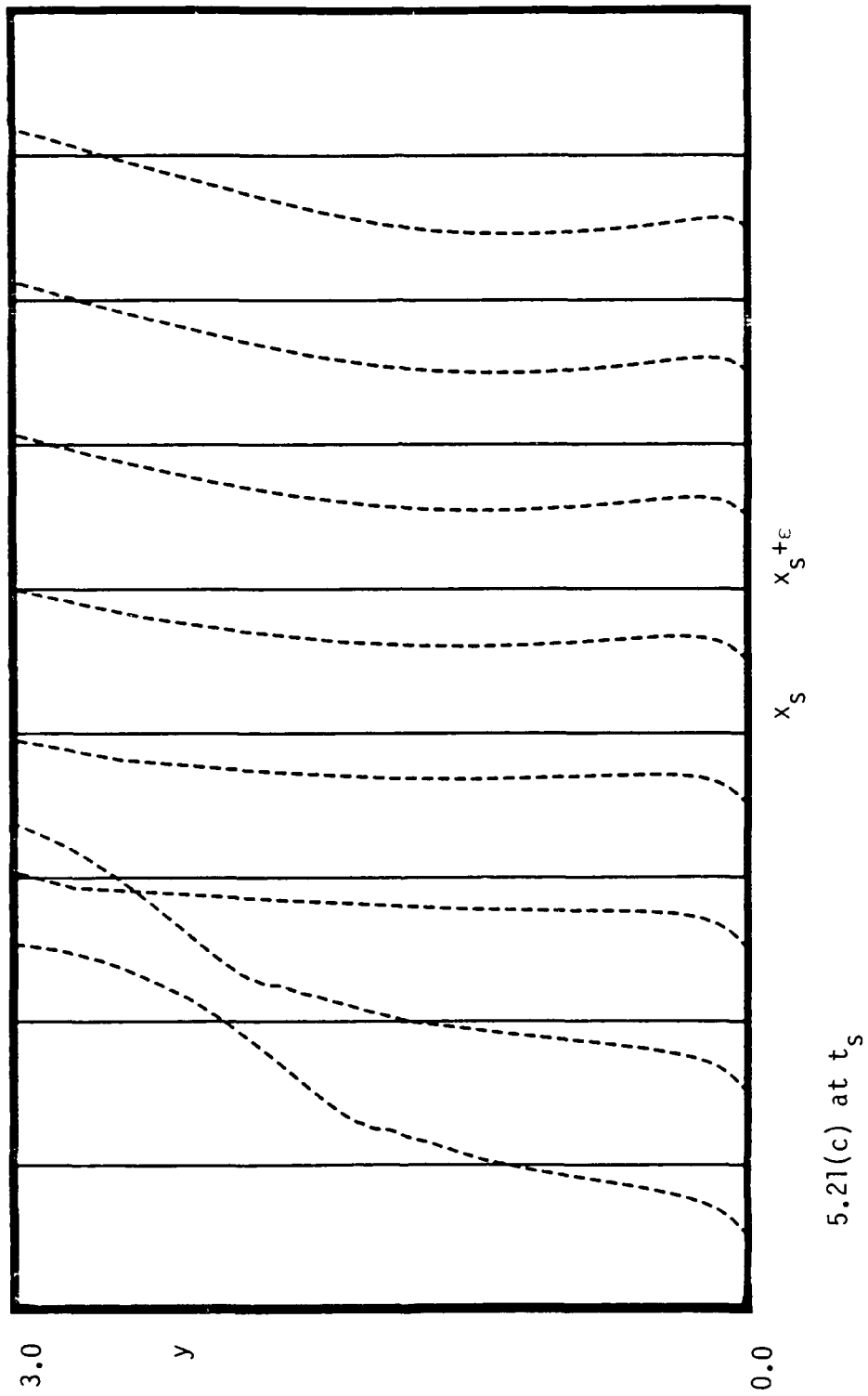


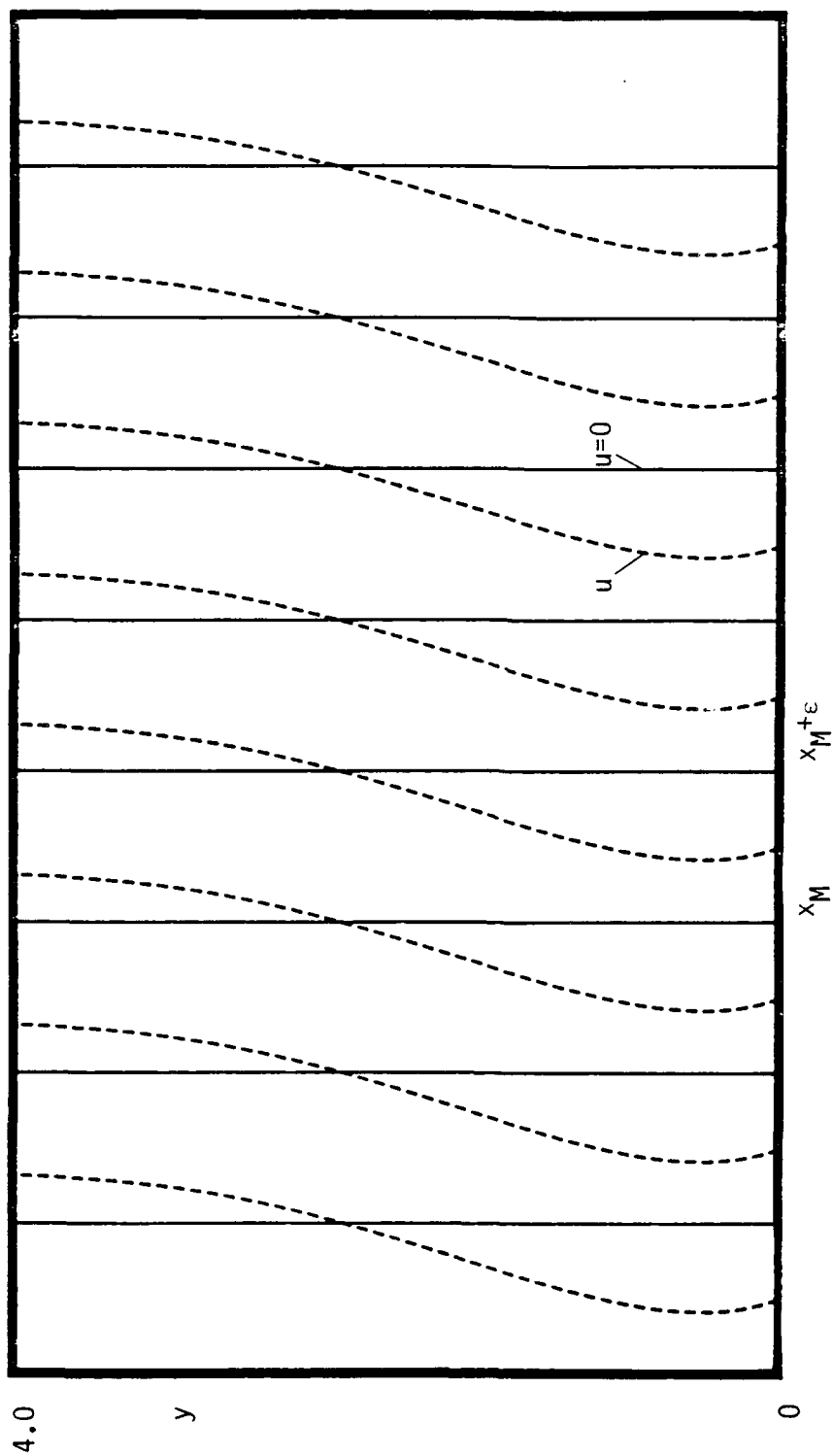
5.21(a) at  $t_s - 0.01$

Figure 5.21. Velocity profiles near  $x_s$  for  $\text{Re}=10^6$ ;  $\varepsilon = 2.09 \cdot 10^{-3}$ .



5.21(b) at  $t_s - 0.005$

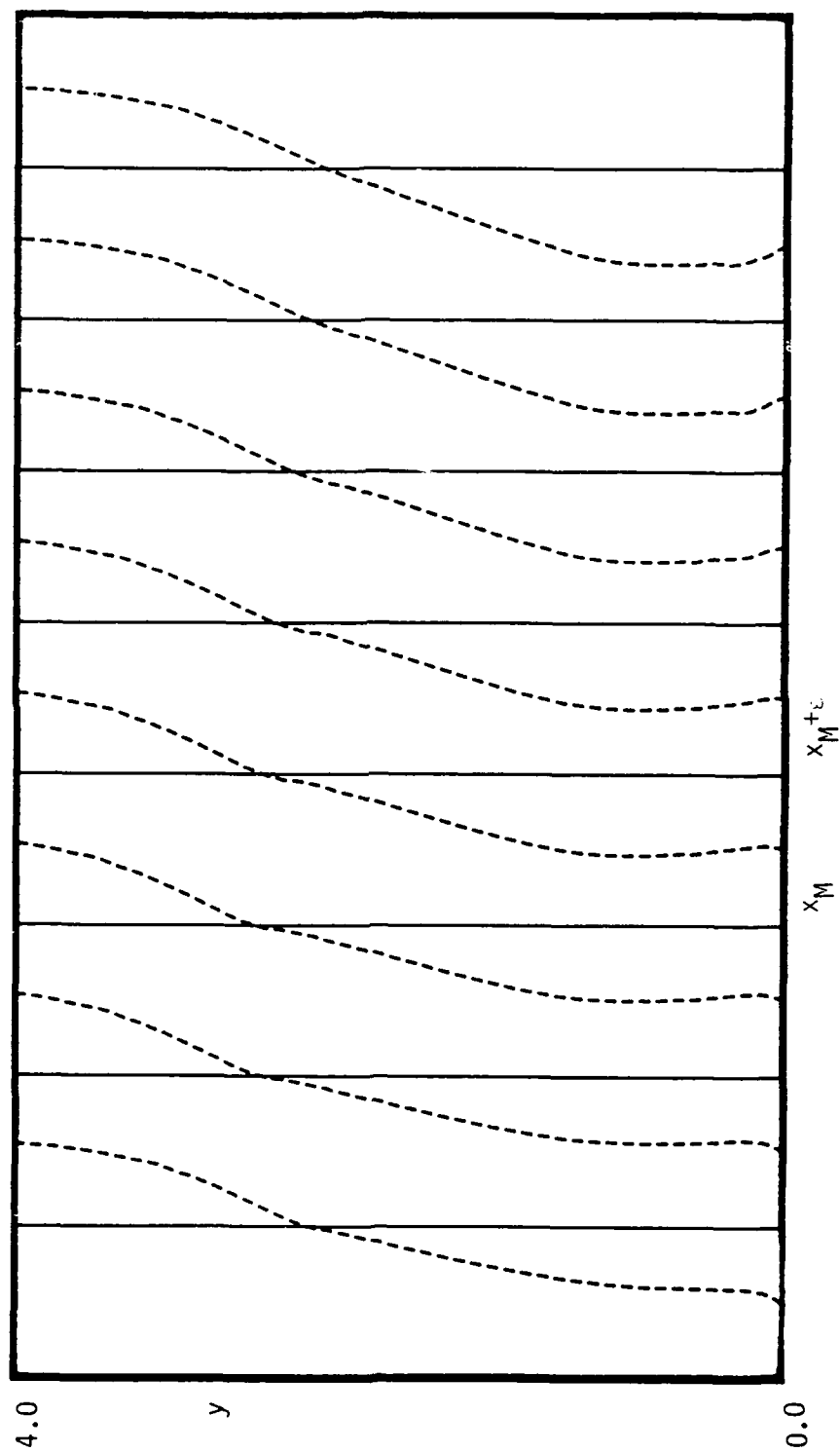




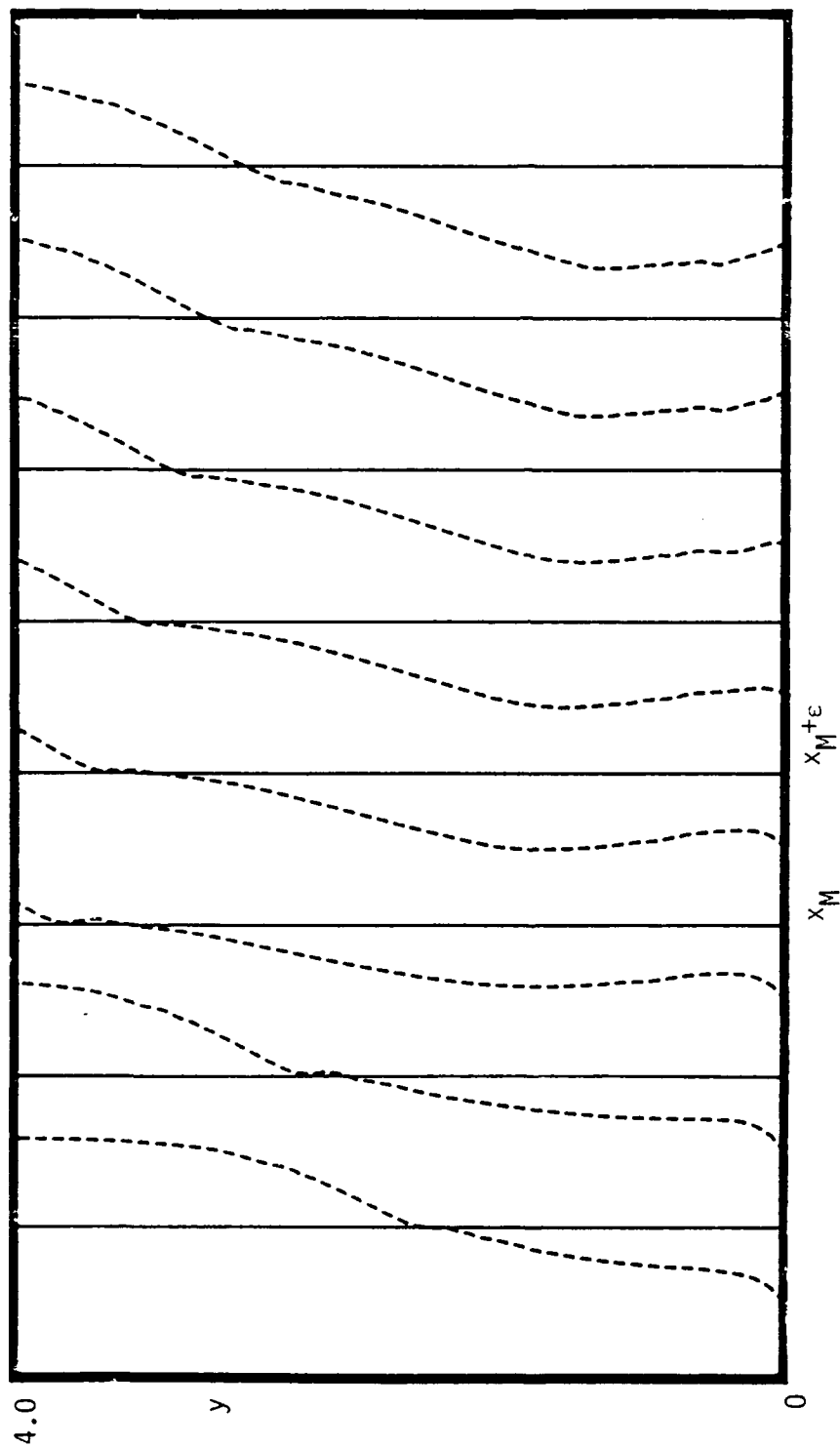
5.22(a) at  $t_s - 0.025$

Figure 5.22. Velocity profiles near  $x_s$  for  $Re=10^5$ ;  $\epsilon = 4.53 \cdot 10^{-3}$ .

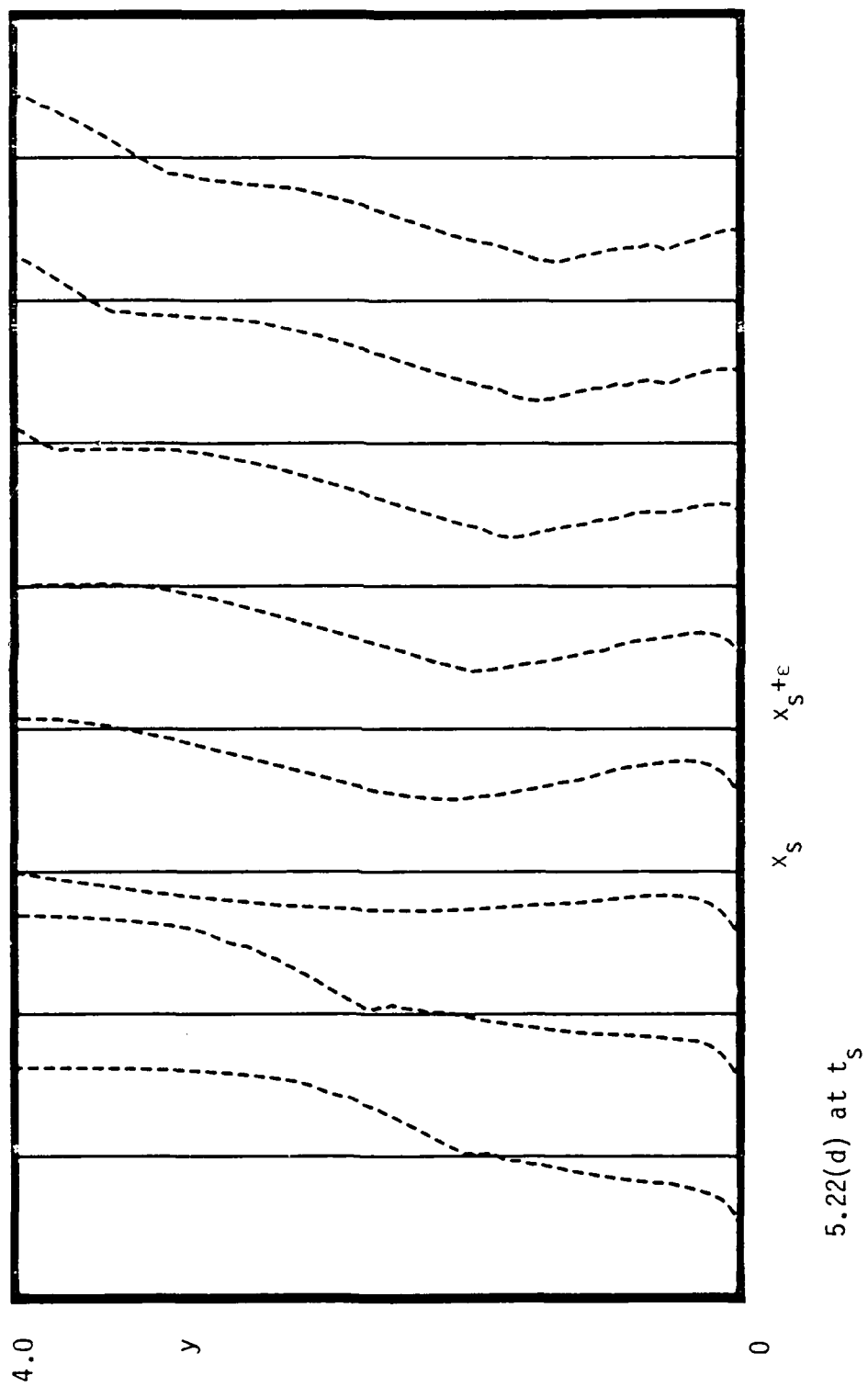




5.22(b) at  $t_s - 0.015$



5.22(c) at  $t_s - 0.005$



## 5.7 Summary

The present results tend to strongly support the asymptotic study of Smith (1988) on the breakdown of the interacting boundary-layer procedure. The following aspects of this breakdown have been found in the present calculated results:

- (1) Interacting calculations of unsteady separation develop boundary-layer breakdown in finite time (c.f. Table 5.1).
- (2) The Reynolds number-dependent scalings of the first interactive stage proposed by Elliott, Cowley and Smith (1983), have been confirmed (c.f. §5.5).
- (3) The wall shear, as  $t \rightarrow t_s$ , is singular at  $x=x_s$  for the interacting problem (see figures 5.10, 5.11); it is regular for the limit problem (figure 4.6).
- (4) The wall shear at  $x_s$  is  $O(t_s - t)^{-1/4}$ , as  $t \rightarrow t_s$  (c.f. Table 5.2).
- (5) The pressure gradient at  $x_s$  is  $O(t_s - t)^{-1}$ , as  $t \rightarrow t_s$  (c.f. Table 5.3).
- (6) The displacement velocity at  $x_s$  is  $O(t_s - t)^{-1}$ , as  $t \rightarrow t_s$  (c.f. Table 5.4).
- (7) The velocity profiles near  $x=x_s$  exhibit pronounced non-uniform vorticity in the interacting problem (figures 5.19-5.22); in the limit problem the velocity profiles are uniform (figure 4.10).

There is a discrepancy between the present results and the behavior predicted by Smith (1988) for the dynamic pressure distributions of the  $Re=10^5, 10^6$  cases at time  $t_s$ . Both cases developed a spike in  $P$  as  $t \rightarrow t_s$ . However, as  $t \rightarrow t_s$ , the pressure distribution for the lower values of  $Re$  is becoming extremely complex and it is likely that the results for the external flow quantities may suffer from significant numerical error near  $x_s$ . In the last stages of the integrations, as  $t \rightarrow t_s$ , the flow develops very rapidly near  $x=x_s$ . Furthermore,

the assumptions used to derive the governing equations (e.g., that  $V_d$  is  $O(1)$ ) and to develop the algorithm (e.g., that  $\partial U_e / \partial t$  is  $O(1)$ ) rapidly become invalid near  $x_s$  in this phase. Consequently, the evaluation method for dynamic pressure  $P$  should not be regarded as being precise near  $x_s$  as  $t \rightarrow t_s$ . In principle further algorithm refinements for the last stages of the calculation might be made in an effort to more accurately compute  $P(x_s)$  as  $t \rightarrow t_s$ ; such refinements would be rather difficult and were not carried out here. Overall, the results of this study are in substantial agreement with Smith (1988).

## 6. CONCLUSIONS

A number of significant results have been obtained in this study which will now be discussed:

(1) For the limit problem  $Re \rightarrow \infty$ , it has been demonstrated in Chapter 4 that (for the model problem) a singularity evolves in the boundary-layer solution at finite time. The structure of this singularity is identical to that found in the numerical solution of the boundary-flow past an impulsively-started circular cylinder (Van Dommelen, 1981). As the boundary-layer erupts, the singular region is moving in a direction opposite to that of the local inviscid flow; consequently, this is a case of what Van Dommelen (1981) refers to as "upstream-slipping separation". The numerical results are in agreement with the asymptotic structure of the terminal boundary-layer solution found by Elliott, Cowley and Smith (1983). Those studies suggest that a generic terminal state can emerge for the limit problem  $Re \rightarrow \infty$  for unsteady boundary layers developing in an adverse pressure gradient; as the eruption develops, the local boundary-layer flow "forgets" the nature of the external pressure distribution which triggered the formation of a zero-vorticity line and thereby initiated the process. The present results support this idea and the same terminal state as for the impulsively-started cylinder is reached here, even though the external pressure distribution induced by the moving vortex is quite different.

(2) The interacting boundary-layer results show that a singularity develops in the solution at finite time. Consequently, the utility of conventional interacting boundary-layer methods is believed to be limited to computing unsteady separation up to the onset of interaction with the external flow, and no farther. This conclusion is in agreement with the recent theory of Smith (1988) who shows that breakdown can occur at finite time in any conventional interacting boundary-layer formulation. It is a variance with

the conclusions of three recent studies (Henkes and Veldman, 1987; Cebeci, 1988; Riley and Vasantha, 1989) which indicate that the use of conventional interacting boundary-layer concepts relaxes the singularity (known to occur in the limit problem). This apparent discrepancy may be partly due to the common use of first-order numerical schemes for evaluating the Cauchy integral term in the interaction condition; this type of approach was first tried in this study and was found to effectively smear out important details near the point of eruption. In a fourth recent study, Chuang and Conlisk (1989) used a second-order method for the Cauchy integral but eventually encountered severe numerical instability which was attributed to a "singularity". A further difficulty with the aforementioned studies is that they were all carried out using an Eulerian formulation, for the boundary-layer problem. It is evident that such methods cannot properly resolve the flow field as an eruption starts to develop, because the streamwise extent of the erupting zone narrows progressively and ultimately reaches a stage wherein adequate numerical resolution using a fixed mesh in the Eulerian frame is impossible. In principle, some type of time-dependent adaptive mesh algorithm could be developed in an Eulerian formulation, in which the mesh is changed at each time step in order to pack the grid points into the erupting zone. However, by and large, previous studies in the Eulerian formulation used a fixed mesh and did not resolve the intense variations that develop as  $t \rightarrow t_s$ . The present numerical results are the first to carry out interacting boundary-layer integrations using a Lagrangian formulation for the boundary layer, and are able to accurately resolve the erupting flow up to the point of the formation of the singularity.

(3) The present interacting boundary-layer integrations are the first to confirm the Reynolds number dependence of the first stage of interaction described in the theoretical analysis of Elliott, Cowley and Smith (1983). As the boundary layer first starts to evolve into interaction, it does so over a local streamwise extent  $O(Re^{-3/11})$  and on a time scale  $O(Re^{-2/11})$ ; these values have been shown to be closely consistent with the present results.

(4) The effects of interaction relieve the singularity that occurs in the limit problem  $Re \rightarrow \infty$ , but only for a brief period. The recent results show that for the model problem a singularity develops in the interacting boundary-layer solution at finite time, for all  $Re$  considered. This is consistent with the recent theoretical study by Smith (1988). The qualitative features of the present solutions as  $t \rightarrow t_s$ , near  $x_s$ , are in agreement with the three-tier structure predicted by Smith (1988). In addition, it has been possible to obtain quantitative comparisons with the asymptotic theory (Smith, 1988) which suggests that as  $t \rightarrow t_s$  and  $x = x_s$ : (i) the wall shear is singular and  $O(t_s - t)^{-1/4}$ , and (ii) the maximum vertical velocity  $v_{\max}$  and the pressure gradient  $(dp/dx)_{\max}$  are  $O(t_s - t)^{-1}$ . The present numerical results closely confirm the scaling for the wall shear and are generally consistent with the predicted behavior for  $v_{\max}$  and the pressure gradient. Note that of the three quantities, calculation of the wall shear is believed to be the most accurate in the present approach; the values of  $v_{\max}$  and  $(dp/dx)_{\max}$  near  $x = x_s$  are difficult to compute precisely as  $t \rightarrow t_s$ . Overall, the recent results are considered to be a very close confirmation of the asymptotic theory.

(5) The interacting boundary-layer results for the model problem indicate that, rather than delay the onset of interaction (as has been suggested by some authors), interaction promotes and hastens the breakdown of the boundary-layer solution. The limit problem  $Re \rightarrow \infty$  develops a singularity at finite time  $t_s(\infty) \approx 0.989$ . For  $Re$  large but finite, the breakdown time  $t_s(Re)$  is always less than  $t_s(\infty)$  and decreases with decreasing Reynolds number (c.f. Table 5.1).

(6) With decreasing  $Re$ , the boundary-layer flow appears to develop into a more mature state (than the limit problem) before breakdown occurs and to develop complex flows near the surface. These effects include: (i) bifurcation of the secondary boundary-layer eddy into several substructures, and (ii) the evolution of a tertiary eddy, which has been observed in a variety of experiments.



(7) A stable and robust upwind-downwind ADI (alternating-direction-implicit) method has been developed in this study. The method has been applied here to the solution of the Lagrangian boundary-layer equations but should have wide applicability to *unsteady flow problems in two-dimensions*, either in an Eulerian boundary-layer problem or in solutions of the full Navier-Stokes equations. The method is believed to be particularly effective in flow problems having strong convective effects such as were encountered in this study. Note that the method was developed here because the conventional Beam and Warming (1978) algorithm failed to accurately track the solution once strong updrafts began to occur.

(8) The Lagrangian formulation (originally due to Van Dommelen, 1981) is believed to be a very effective approach for dealing with the strongly eruptive flows of interest in this study. Thus far, it is the only approach which has succeeded in accurately tracking a separating boundary-layer all the way to breakdown. However, the method is not without problems and it was necessary to exercise caution during the course of the integrations. As previously discussed, the method evaluates the  $x$  particle positions as well as their streamwise velocities  $u$ ; both quantities are regular and never become large. In an Eulerian calculation when  $v$  or  $\partial u / \partial x$  become locally large it becomes progressively difficult to obtain convergence of the numerical scheme at each time step and eventually the numerical scheme fails; these failures are a very clear signal that a inherent problem has occurred in the computational algorithm. By contrast, the Lagrangian computation continues to produce distributions of  $x$  and  $u$ , and to converge even in situations where substantial error had developed in the solution. For example, it seems to always be possible to extend the integrations for  $x, u$  (in the limit problem) beyond  $t=t_s$ , even though the  $y$  position develops a singularity at  $t_s$  and all computations beyond  $t_s$  are meaningless. Another problem was also encountered in the present study. As  $t$  approaches  $t_s$  the flow field begins to evolve rapidly and unless the time step progressively decreased, the number of iterations was observed to increase substantially. It is relatively easy to program a time step

reduction based on the number of iterations at each time step; however this simple algorithm was not entirely satisfactory. Once the number of iterations started to increase, the difficulty was found to originate at a time several time steps earlier in the calculation, where irregular behavior would develop in the contours of constant  $u$ . In the present problem this irregular behavior always initiated near the stagnation point closest to the wall; this point may be noted near  $x = -0.40$  in figure 4.3(b), for example, where the instantaneous streamlines form a saddle point. In order to trace the onset of the problem, it was necessary to plot contours of constant  $u$  at time steps back from where the increase in iterations was noted. The integration was then restarted with a reduced time step from a point where the constant  $u$  contours were smooth. This graphical procedure is somewhat tedious, but an automated way of reducing the time step proved elusive in the present study. Unfortunately, the nature of the Lagrangian procedure is such that no obvious warning is given as the calculation starts to deviate from the true solution.

(9) The second-order algorithm developed for the Cauchy principal-value integrals on infinite domains is believed to be a very effective and accurate method.

Finally, it is of interest to address the question of future research in this area. It has been previously remarked that, in the latter stages of the interacting boundary-layer integrations, the numerical methods used to evaluate the pressure may be somewhat in error as the displacement thickness "spike" develops. It is these errors which may be associated with the slight discrepancy between the present results and Smith's (1988) asymptotic theory. In principle the procedures used to evaluate the external flow quantities could be refined. However, since the algorithms necessarily involve trying to compute the deviations (both time and streamwise) of a rapidly evolving displacement thickness spike, the numerical difficulties are nontrivial. Moreover, this route is not considered to be a profitable one, particularly if the objective is to extend the integrations further into interaction. The present

method allows a calculation up to the point of interaction; in order to relieve the interaction singularity that develops it is necessary to incorporate some additional features of the Navier-Stokes equations in the interacting boundary-layer formulation. At present, it is believed that the effects of normal pressure variations *must* be included in order to extend the computations beyond the point reached in this study.

## REFERENCES

- Abramowitz, M. & Stegun, I., (1965), Handbook of Mathematical Functions, Dover, New York.
- Acarlar, M.S. & Smith, C.R. (1984), "An Experimental Study of Hairpin-Type Vortices as a Potential Flow Structure of Turbulent Boundary Layers". AFOSR Rep. FM-5, Dept. Mech. Eng. & Mech., Lehigh University.
- Acarlar, M.S. & Smith, C.R. (1987a), "A Study of Hairpin Vortices in a Laminar Boundary Layer. Part 1. Hairpin Vortices Generated by a Hemisphere Protuberance", *J. Fluid Mech.* 175, pp. 1-41.
- Acarlar, M.S. & Smith, C.R. (1987b), "A Study of Hairpin Vortices in a Laminar Boundary Layer. Part 2. Hairpin Vortices Generated by Fluid Injection", *J. Fluid Mech.* 175, pp. 43-83.
- Bar-Lev, M. & Yang, H.T. (1975), "Initial Flow Field over an Impulsively-started Circular Cylinder", *J. Fluid Mech.* 72, pp. 625-647.
- Beam, R.M. & Warming, R.F. (1978), "An Implicit Factored Scheme for the Compressible Navier-Stokes Equations", *AIAA J.* 16, pp. 393-402.

Belcher, R.J., Burggraf, O.R., Cooke, J. C., Robins, A.J. & Stewartson, K. (1972), Recent Research on Unsteady Boundary Layers, Laval University Press, Quebec, pp.1444-1466.

Blasius, H. (1908), "Grenzschichten in Flüssigkeiten mit kleiner Reibung", Z. Math. Phys. 56, pp.1-37.

Bouard, R., & Coutenceau, M. (1980), "Early Stage Development of the Wake behind an Impulsively Started Cylinder of  $40 < Re < 10,000$ ", J. Fluid Mech. 101, pp.583-607.

Brotherton-Ratcliffe, R.V. & Smith, F.T. (1987), "Complete Breakdown of an Unsteady Interacting Boundary Layer (over a Surface Distortion or on a Liquid Layer)", Mathematika 34, pp.86-100.

Brown, S.N., Cheng, H.K. & Smith, F.T. (1988), "Nonlinear Instability and Break-up of Separated Flow", J. Fluid Mech. 193, pp.191-216.

Burggraf, O.R. & Duck, P.W. (1982), "Spectral Computation of Triple Deck Flows", Proceedings of Symposium on Numerical and Physical Aspects of Aerodynamic Flow, (ed. T.Cebeci), Long Beach, California.

Burggraf, O.R., Rizzetta, D., Werle, M.J. & Vatsa, V.N. (1979), "Effect of Reynolds Number on Laminar Separation of a Supersonic Stream", AIAA J. 17, pp.336-343.

Carter, J. E., & Wornam, S.F. (1975), "Forward Marching Procedure for Separated Boundary-layer Flows", AIAA J. 13, pp.1101-1103.

- Cebeci, T. (1978), "An Unsteady Laminar Boundary Layer with Separation and Reattachment", *AIAA J.* 16, pp.1305-1036.
- Cebeci, T. (1979), "The Laminar Boundary Layer on a Circular Cylinder Started Impulsively from Rest", *J. Comp. Phys.* 31, pp.153-172.
- Cebeci, T. (1986), "Unsteady Boundary Layers with an Intelligent Numerical Scheme", *J. Fluid Mech.* 163, pp.129-140.
- Cebeci, T. (1988), "Separation and Reattachment near the Leading Edge of a Thin Oscillating Airfoil", *J. Fluid Mech.* 188, pp.253-274.
- Chuang, F.S. & Conlisk, A.T. (1989), "Effect of Interaction on the Boundary Layer Induced by a Convected Rectilinear Vortex", *J. Fluid Mech.* 200, pp. 337-365.
- Collins, W.M. & Dennis, S.C.R. (1973a), "The Initial Flow past an Impulsively Started Circular Cylinder", *Quart. J. Mech. App. Math.* 26, pp.53-75.
- Collins, W.M. & Dennis, S.C.R. (1973b), "Flow past an Impulsively Started Circular Cylinder", *J. Fluid Mech.* 60, pp. 105-127.
- Cowley, S.J. (1983), "Computer Extension and Analytic Continuation of Blasius Expansion for Impulsive Flow past a Circular Cylinder", *J. Fluid Mech.* 135, pp.389-405.

- Davis, R.L. & Carter, J.E. (1984), "Analysis of Airfoil Transitional Separation Bubbles", paper 84-1613 presented at AIAA meeting, June, 1984.
- Doligalski, T.L. & Walker, J. D.A. (1984), "Boundary Layer Induced by a Convected Two-dimensional Vortex", *J. Fluid Mech.* 139, pp.1-28.
- Ece, M.C., Walker, J. D.A. & Doligalski, T.L. (1984), "The Boundary Layer on an Impulsively Started Rotating and Translating Cylinder", *Phys. Fluids* 23, pp.1077-1089.
- Edwards, D.E. & Carter, J. E. (.985), "Viscous-inviscid Interaction Analysis of Transonic Shock Induced Separated Flow Including Normal Pressure Gradients", paper 85-0371 presented at the 23rd Aerospace Sciences Meeting, January, 1985, Reno, Nevada.
- Elliott, J. W., Cowley, S.J. & Smith, F.T. (1983), "Breakdown of Boundary Layers: (i) on Moving Surfaces; (ii) in Self-similar Unsteady Flow; (iii) in Fully Unsteady Flow", *Geophy. Astrophys. Fluid Dynamics* 25, pp.77-138.
- Ersoy, S. & Walker, J. D.A. (1985), "Viscous Flow Induced by Counter-rotating Vortices", *Phys Fluids* 28, pp.2687-2698.
- Ersoy, S. & Walker, J. D.A. (1986), "Flow Induced at a Wall by a Vortex Pair", *AIAA J.* 24, pp.1597-1605.
- Francis, M.S. & Keesee, J. E. (1985), "Airfoil Dynamic Stall Performance with Large Amplitude Motions", *AIAA J.* 23, pp. 1653-1659.

- Goldstein, S. (1930), "Concerning Some Solutions of the Boundary-layer Equations in Hydrodynamics", *Proc. Camb. Phil. Soc.* 26, pp.1-30.
- Goldstein, S. (1948), "On Laminar Boundary-layer Flow Near a Point of Separation", *Quart. J. Mech. App. Math.* 1, pp.43-69.
- Goldstein, S. & Rosenhead, L. (1936), "Boundary Layer Growth", *Proc. Camb. Phil. Soc.* 32, pp.392-401.
- Gradshteyn, I.S. & Rhyzik, I.M. (1965), Tables of Integrals, Series and Products. Academic Press, New York.
- Harvey, J. K. & Perry, F.J. (1971), "Flowfield Produced by Trailing Vortices in the Vicinity of the Ground", *AIAA J.* 9, pp.1659-1660.
- Henkes, R.A.W.M. & Veldman, A.E.P. (1987), "On the Breakdown of the Steady and Unsteady Interacting Boundary-layer Description", *J. Fluid Mech.* 179, pp.513-529.
- Hon, T.L. & Walker, J. D.A. (1987), "An Analysis of the Motion and Effects of Hairpin Vortices", AFOSR Rep. FM-11, Dept. Mech. Eng. & Mech., Lehigh University.
- Honji, H. & Taneda, S. (1969), "Unsteady Flow past a Circular Cylinder", *J. Phys. Soc. Japan* 27, pp.1668-1677.
- Kim, H.T., Kline, S.J. & Reynolds, W.C. (1971), "The Production of Turbulence near a Smooth Wall in a Turbulent Boundary Layer", *J. Fluid Mech.* 50, pp.133-160.



- Kline, S.J., Reynolds, W.C., Schroub, F.A. & Runstadler, P.W. (1967), "Structure of Turbulent Boundary Layers", *J. Fluid Mech.* **30**, pp.741-773.
- McAlister, K.W. & Carr, L.W. (1978), "Water Tunnel Visualizations of Dynamic Stall", *Nonsteady Fluid Dynamics* (ed. D.E.Crow & J. A. Miller). AMSE, New York, pg.103.
- McCroskey, W.J., Carr, L.W. & McAlister, K.W. (1976), "Dynamic Stall Experiments on Oscillating Airfoils", *AIAA J.* **14**, pg.57.
- Messiter, A.F. (1970), "Boundary-layer Flow Near the Trailing Edge of a Flat Plate", *SIAM J. App. Math.* **18**, pp.241-257.
- Milne-Thomson, L.M. (1962), *Theoretical Hydrodynamics*, MacMillan, London.
- Moore, F.K. (1958), "On the Separation of the Unsteady Boundary Layer", *Boundary Layer Research* (ed. H.G.Görtler), Springer, Berlin, pp.296-311.
- Napolitano, M., Werle, M.J. & Davis, R.T. (1978), "Numerical Solution of the Triple-deck Equations for Supersonic and Subsonic Flow past a Hump", David Taylor Naval Shipyard Research and Development Center report AFL78-6-42.
- Peridier, V.J. & Walker, J. D.A. (1988), "An Algorithm for Unsteady Flows with Strong Convection", NASA technical memorandum 100828, ICOMP-88-5, NASA Lewis Research Center.

- Proudman, I. & Johnson, K. (1962), "Boundary-layer Growth near a Rear Stagnation Point", *J. Fluid Mech.* 12, pp.161-168.
- Riley, N. (1975), "Unsteady Laminar Boundary Layers", *SIAM Rev.* 17, pp.282.
- Riley, N. & Vasantha, R. (1989), "Unsteady High Reynolds Number Flows", *J. Fluid Mech.*, (to appear).
- Robins, A.J. & Howarth, J. A. (1972), "Boundary-layer Development at a Two-dimensional Rear Stagnation Point", *J. Fluid Mech.* 56, pp.161-171.
- Rothmayer, A.P. (1985), A Study of High Reynold Number Laminar Separation. Ph.D dissertation, U. of Cincinnati.
- Rothmayer, A.P. & Smith, F.T. (1985), "Large-Scale Separation and Hysteresis in Cascades", *Proc. R. Soc. Lond. A* 402, pp.83-108.
- Rott, N. (1956), "Unsteady Viscous Flow in the Vicinity of a Stagnation Point", *Quart. Appl. Math.* 13, pp 444-451.
- Sears, W.P. & Telionis, D.P. (1971), "Unsteady Boundary-layer Separation", Recent Research on Unsteady Boundary Layers. Laval University Press, Quebec, pp.404-447.
- Sears, W.P. & Telionis, D.P. (1975), "Boundary-layer Separation in Unsteady Flow", *SIAM J. App. Math.* 28, pp.215-235.

- Smith, F.T. (1979), "Laminar Flow past a Bluff Body: the Separation, Reattachment, Eddy Properties and Drag", *J. Fluid Mech.* 92, pp.171-205.
- Smith, F.T. (1982), "On the High Reynolds Number Theory of Laminar Flows", *IMA J. App. Math.* 28, pp.207-281.
- Smith, F.T. (1985), "A Structure for Laminar Flow past a Bluff Body at High Reynolds Number", *J. Fluid Mech.* 155, pp.175-191.
- Smith, F.T. (1988), "Finite-time Breakup Can Occur in Any Unsteady Interacting Boundary Layer", *Mathematika* 35, pp.256-273.
- Smith, F.T., Sykes, R.I. & Brighton, P.W.M. (1977), "A Two-dimensional Boundary Layer Encountering a Three-dimensional Obstacle", *J. Fluid Mech.* 83, pp.163-176.
- Stewartson, K. (1958), "On Goldstein's Theory of Laminar Separation", *Quart. J. Mech. App. Math.* 11, pp.399-410.
- Stewartson, K. (1969), "On the Flow Near the Trailing Edge of a Flat Plate - II", *Mathematika* 16, pp.106-121.
- Swearingen, J. D. & Blackwelder, R.F. (1987), "The Growth and Breakdown of Streamwise Vortices in the Presence of a Wall", *J. Fluid Mech.* 182, pp.255-290.
- Taneda, S. (1977), "Visual Study of Unsteady Separated Flow Around Bodies", *Prog. Aerospace Sci.* 17, pp.287-348.

- Ta Phuoc Loc, & Bouard, R. (1985), "Numerical Solution of the Early Stage of the Unsteady Viscous Flow Around a Circular Cylinder: a Comparison with Experimental Visualization and Measurements", J. Fluid Mech. 160, pp.93-117.
- Van Dommelen, L.L. (1981), Unsteady Boundary-layer Separation, Ph.D dissertation, Cornell University.
- Van Dommelen, L.L. & Shen, S.F. (1980), "The Spontaneous Generation of the Singularity in a Separating Boundary Layer", J. Comp. Phys. 38, pp. 125-140.
- Van Dommelen, L.L. & Shen, S.F. (1982), "The Genesis of Separation", Proceedings of Symposium on Numerical and Physical Aspects of Aerodynamic Flow, (ed. T.Cebeci), Long Beach, California, pp. 283-311.
- Van Dommelen, L.L. & Shen, S.F. (1985), "The Flow at a Rear Stagnation Point is Eventually Determined by Exponentially Small Values of Velocity", J. Fluid Mech. 157, pp.1-26.
- Vatsa, V.N. & Carter, J. E. (1984), "Analysis of Airfoil Leading-edge Separation Bubbles", AIAA J. 22, pp.1697-1704.
- Walker, J. D.A. (1978), "The Boundary Layer Due to Rectilinear Vortex", Proc. R. Soc. Lond. A 359, pp.167-188.
- Walker, J. D.A., Smith, C.R., Doligalski, T.L. & Cerra, A.W. (1987), "Impact of a Vortex Ring on a Wall", J. Fluid Mech. 181, pp.99-140.

Walker, J. D.A, Abbott, D.E., Sharnhorst, R.K. & Weigand, G. G. (1989),  
"Wall-layer Model for Velocity Profile in Turbulent Flows", AIAA J.  
27, pp 140-149.

Williams, III, J.C. (1977), "Incompressible Boundary-layer Separation",  
Ann. Rev. Fluid Mech. 9, pp.113-144.

## APPENDIX A

### Lagrangian Variables

Consider a flow for which the velocity field is known at some initial instant at  $t=t_0$ ; let  $(\xi, \eta)$  be the Cartesian coordinates describing the location of individual fluid particles at  $t_0$ . In Lagrangian variables, a fluid particle is distinguished by its initial position  $(\xi, \eta)$  and the time it has moved along its subsequent trajectory in the flow field; the dependent variables are the particle positions

$$x = x(\xi, \eta, t), \quad y = y(\xi, \eta, t), \quad (\text{A.1})$$

and the initial conditions are

$$x = \xi, \quad y = \eta, \quad \text{at } t=t_0. \quad (\text{A.2})$$

The boundary-layer equations in Eulerian coordinates are given by equations (1.10) and (1.14) and may be written in the form

$$\frac{Du}{Dt} = \frac{\partial Ue}{\partial t} + Ue \frac{\partial Ue}{\partial x} + \frac{\partial^2 u}{\partial y^2}, \quad (\text{A.3})$$

with the associated equation of continuity (1.11)

$$\frac{\partial u}{\partial x} + \frac{\partial v}{\partial y} = 0. \quad (\text{A.4})$$

Here  $\frac{Du}{Dt}$  denotes the substantive derivative and the left side of equation (A.3) corresponds to the acceleration of a fluid particle; in Lagrangian coordinates this term becomes  $\frac{\partial u}{\partial t}$  where

$$u \equiv \frac{Dx(\xi, \eta, t)}{Dt} = \frac{\partial x}{\partial t} \quad (\text{A.5})$$

is the time-rate of change of the particle streamwise position. The first two terms on the right side of equation (A.3) correspond to the pressure gradient. In general, the pressure may be regarded as a known function of  $x$  and  $t$  which

is impressed across the boundary layer; as a specific fluid particle moves through the boundary layer its streamwise location  $x(\xi, \eta, t)$  changes and thus it experiences a corresponding change in pressure.

To determine the form of the viscous term (the last term on the right side of equation (A.3)) consider the general transformation

$$x = x(\xi, \eta, t), y = y(\xi, \eta, t), \quad (\text{A.6})$$

for which

$$\left. \begin{aligned} \frac{\partial}{\partial x} &= \frac{\partial \xi}{\partial x} \frac{\partial}{\partial \xi} + \frac{\partial \eta}{\partial x} \frac{\partial}{\partial \eta} , \\ \frac{\partial}{\partial y} &= \frac{\partial \xi}{\partial y} \frac{\partial}{\partial \xi} + \frac{\partial \eta}{\partial y} \frac{\partial}{\partial \eta} . \end{aligned} \right\} \quad (\text{A.7})$$

To determine expressions for the partial derivatives  $(\xi_x, \xi_y, \eta_x, \eta_y)$ , each of equations (A.7) are taken to operate on  $x$  and  $y$  successively to obtain the identities

$$\left. \begin{aligned} \frac{\partial}{\partial x} (x) &= \frac{\partial \xi}{\partial x} \frac{\partial x}{\partial \xi} + \frac{\partial \eta}{\partial x} \frac{\partial x}{\partial \eta} = 1, \\ \frac{\partial}{\partial x} (y) &= \frac{\partial \xi}{\partial x} \frac{\partial y}{\partial \xi} + \frac{\partial \eta}{\partial x} \frac{\partial y}{\partial \eta} = 0, \\ \frac{\partial}{\partial y} (y) &= \frac{\partial \xi}{\partial y} \frac{\partial y}{\partial \xi} + \frac{\partial \eta}{\partial y} \frac{\partial y}{\partial \eta} = 1, \\ \frac{\partial}{\partial y} (x) &= \frac{\partial \xi}{\partial y} \frac{\partial x}{\partial \xi} + \frac{\partial \eta}{\partial y} \frac{\partial x}{\partial \eta} = 0 . \end{aligned} \right\} \quad (\text{A.8})$$

These equations may be regarded as a set of four linear equations for the partial derivatives of  $\xi$  and  $\eta$  and the solution is:

$$\left. \begin{aligned} \xi_x &= \frac{1}{J} \frac{\partial y}{\partial \eta} , & \xi_y &= -\frac{1}{J} \frac{\partial x}{\partial \eta} , \\ \eta_x &= -\frac{1}{J} \frac{\partial y}{\partial \xi} , & \eta_y &= \frac{1}{J} \frac{\partial x}{\partial \xi} , \end{aligned} \right\} \quad (\text{A.9})$$

where  $J$  is the Jacobian of the transformation defined by

$$J(x,y; \xi,\eta) = \begin{vmatrix} x_\xi & x_\eta \\ y_\xi & y_\eta \end{vmatrix} = \frac{\partial x}{\partial \xi} \frac{\partial y}{\partial \eta} - \frac{\partial x}{\partial \eta} \frac{\partial y}{\partial \xi} . \quad (A.10)$$

The transformations for the partial derivatives then become

$$\left. \begin{aligned} \frac{\partial}{\partial x} &= \frac{1}{J} \left\{ \frac{\partial y}{\partial \eta} \frac{\partial}{\partial \xi} - \frac{\partial y}{\partial \xi} \frac{\partial}{\partial \eta} \right\} , \\ \frac{\partial}{\partial y} &= \frac{1}{J} \left\{ \frac{\partial x}{\partial \xi} \frac{\partial}{\partial \eta} - \frac{\partial x}{\partial \eta} \frac{\partial}{\partial \xi} \right\} , \end{aligned} \right\} \quad (A.11)$$

which hold for any transformation of the form (A.6); the mapping is made specific by substitution of equations (A.11) into the continuity equation (A.4) to obtain

$$\frac{1}{J} \left\{ \frac{\partial u}{\partial \xi} \frac{\partial y}{\partial \eta} - \frac{\partial u}{\partial \eta} \frac{\partial y}{\partial \xi} - \frac{\partial v}{\partial \xi} \frac{\partial x}{\partial \eta} + \frac{\partial v}{\partial \eta} \frac{\partial x}{\partial \xi} \right\} = 0 . \quad (A.12)$$

In Lagrangian coordinates the velocity components ( $u,v$ ) are the time rate of change of the particle coordinates, viz.

$$u = \frac{\partial x}{\partial t}, \quad v = \frac{\partial y}{\partial t}, \quad (A.13)$$

and substitution in equation (A.12) yields

$$\frac{1}{J} \frac{\partial}{\partial t} \left\{ \frac{\partial x}{\partial \xi} \frac{\partial y}{\partial \eta} - \frac{\partial x}{\partial \eta} \frac{\partial y}{\partial \xi} \right\} = \frac{1}{J} \frac{\partial J}{\partial t} = 0 . \quad (A.14)$$

Consequently the Jacobian is invariant in time and substitution of the initial conditions (A.2) into equations (A.10) yields

$$J \equiv 1 . \quad (A.15)$$

This is the mathematical statement of conservation of mass in Lagrangian coordinates; the implication is that, while a fluid particle may undergo considerable deformation as it moves through the flow, the area of the particle is conserved.

The streamwise momentum equation (A.3) and equation (A.5) comprise



a set of two coupled unsteady equations for the dependent variables  $x(\xi, \eta, t)$ ,  $u(\xi, \eta, t)$ , viz.

$$\frac{\partial u}{\partial t} = \frac{\partial U_e}{\partial t} + U_e \frac{\partial U_e}{\partial x} + \left\{ \frac{\partial x}{\partial \xi} \frac{\partial}{\partial \eta} - \frac{\partial x}{\partial \eta} \frac{\partial}{\partial \xi} \right\}^2 u, \quad (\text{A.16})$$

$$\frac{\partial x}{\partial t} = u. \quad (\text{A.17})$$

Computation of a flow in Lagrangian variables always involves a time-dependent integration (even for flows which are steady in the Eulerian frame), since the motion of individual fluid particles is being computed. A specific fluid particle is distinguished by its initial position in the flow field, and the initial conditions for equations (A.16), (A.17) are given by equations (A.2).

It is worthwhile to note that equations (A.16) and (A.17) do not involve the normal coordinate  $y(\xi, \eta, t)$  or the normal velocity  $v(\xi, \eta, t)$ ; this feature of the boundary-layer equations in Lagrangian coordinates is particularly important for unsteady boundary-layer flows which ultimately develop an eruptive character. For such flows (c.f. §1.3) the normal velocity distribution, as well as the boundary-layer thickness, will become large locally as the boundary layer develops strong updrafts. In a boundary-layer calculation procedure where the pressure distribution in the external flow is taken to be prescribed, the boundary-layer solution ultimately develops a singularity in  $v$  as the eruption begins to build. Generally, unsteady boundary-layer calculation methods based on Eulerian variables have not been successful in adequately resolving the flow field as a boundary layer becomes eruptive. On the other hand, in Lagrangian variables, the boundary-layer flow solution is computed by calculating the development of the streamwise particle positions  $x(\xi, \eta, t)$  and the tangential velocity  $u(\xi, \eta, t)$ ; both of these quantities remain regular for all time even for flows which develop into a local eruption.

At any fixed value of  $t$ , the normal distance  $y(\xi, \eta, t)$  of a fluid particle from the wall may be calculated by the integration of the continuity equation.

In Lagrangian variables, this equation follows from equations (A.10) and (A.15) viz.

$$\frac{\partial x}{\partial \xi} \frac{\partial y}{\partial \eta} - \frac{\partial x}{\partial \eta} \frac{\partial y}{\partial \xi} = 1. \quad (\text{A.18})$$

If it is assumed that the streamwise particle positions  $x(\xi, \eta, t)$  are known at any time  $t$  (through numerical integration of equations (A.16) and (A.17), for example), then it may be observed that equation (A.18) is a first order linear partial differential equation for  $y(\xi, \eta, t)$ ; it may be solved by the method of characteristics and the subsidiary equations are

$$\frac{d\eta}{x_\xi} = -\frac{d\xi}{x_\eta} = \frac{dy}{1}. \quad (\text{A.19})$$

In view of the no-slip condition, fluid particles which are located on the wall at some initial instant remain on the wall at known values of  $x$ ; starting from  $y=0$  the numerical integration of equations (A.19) produces the characteristic curves as well as the values of  $y$  along the characteristics. These curves are the characteristics of the differential operator,

$$\mathcal{L} = \frac{\partial x}{\partial \xi} \frac{\partial}{\partial \eta} - \frac{\partial x}{\partial \eta} \frac{\partial}{\partial \xi}, \quad (\text{A.20})$$

and since  $\mathcal{L}(x) = \frac{d}{dy}(x) = 0$ , the characteristics are curves of constant  $x$ . These characteristic curves have the following physical interpretation. At some initial instant the values of  $x$  are given by equation (A.2) and the characteristics are vertical lines; one such curve is shown schematically in figure A.1. As time increases, the fluid particles move and a characteristic curve at a subsequent time is also shown in figure A.1; both characteristics start at the same point on the wall since fluid particles there do not move (in view of the no-slip condition). The solid line represents the initial location of all fluid particles (at  $t=t_0$ ) which have now arrived at a constant value of

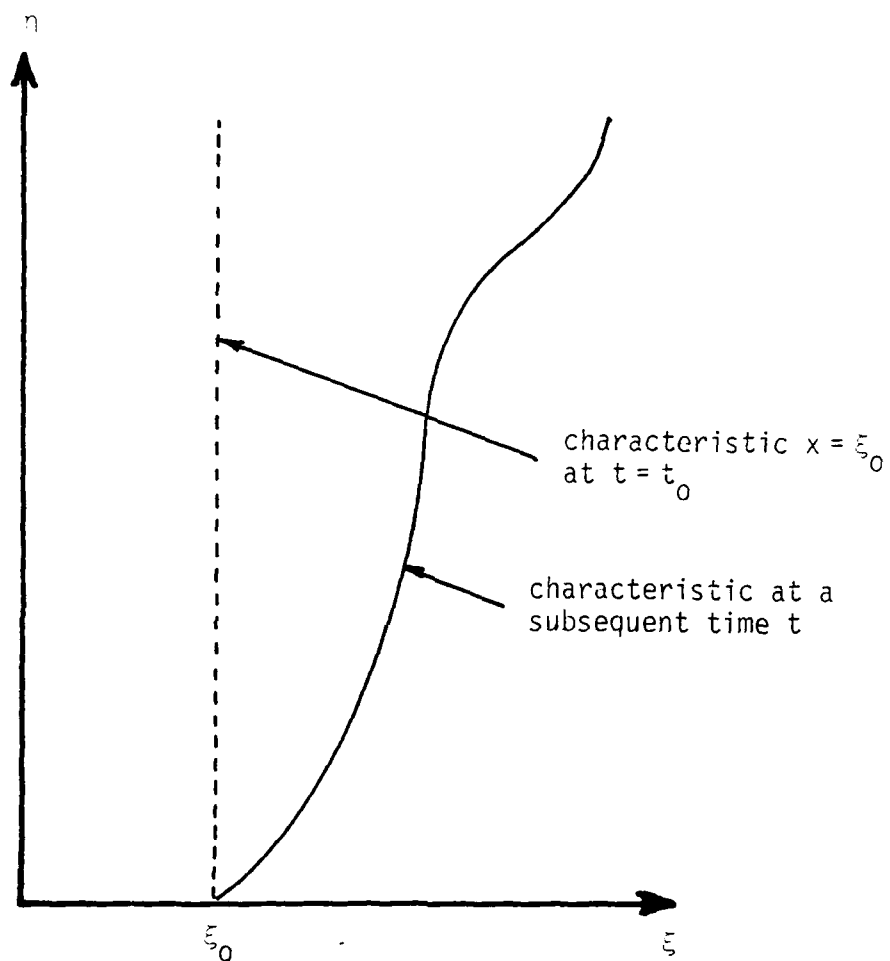


Figure A.1. Schematic diagram of characteristic  $x = \text{constant}$  in the  $\xi, \eta$  plane.

$x=\xi_0$ ; in the example depicted in figure A.1 the fluid particles have experienced a drift from right to left in the interval between  $t_0$  and  $t$ , with the greatest displacement occurring in the upper part of the boundary layer.

The solution of equation (A.19) may be written

$$y(\xi_p, \eta_p, t) = \int_{\text{wall}}^{(\xi_p, \eta_p)} \frac{ds}{\sqrt{x_\xi^2 + x_\eta^2}}, \quad (\text{A.21})$$

where the integral is along a characteristic  $x(\xi, \eta, t)=\text{constant}$ , starting at the wall and passing through the point  $(\xi_p, \eta_p)$ ; this expression gives the normal distances from the wall of a fluid particle which started at  $x=\xi_p, y=\eta_p$  at the instant  $t=t_0$ . It is evident from this expression that if a stationary point develops in the  $x(\xi, \eta, t)$  distribution at some time  $t=t_s$ , viz.

$$\frac{\partial x}{\partial \xi} = \frac{\partial x}{\partial \eta} = 0 \quad \text{at } (\xi, \eta, t)=(\xi_s, \eta_s, t_s), \quad (\text{A.22})$$

then equation (A.21) shows that a singularity has evolved in the boundary-layer solution. In physical terms, fluid particles which lie on a characteristic (of constant  $x$ ) passing through the point  $(\xi_s, \eta_s)$  will be located an infinite distance from the wall (on the boundary-layer scale). In addition, fluid particles lying on constant  $x$  trajectories close to  $(\xi_s, \eta_s)$  will be located at very large distances from the wall. It is worthwhile to note that the development of a singularity always occurs somewhere on the zero-vorticity line; the vorticity is defined by  $\omega = -(\partial u / \partial y)$  in Eulerian variables and in the Lagrangian frame,

$$\omega = - \left( \frac{\partial x}{\partial \xi} \frac{\partial u}{\partial \eta} - \frac{\partial x}{\partial \eta} \frac{\partial u}{\partial \xi} \right). \quad (\text{A.23})$$

It may be observed from equation (A.23) that if a stationary point in  $x$  occurs, the vorticity must be zero as well.

## APPENDIX B

### Numerical Methods for the Eulerian Boundary-layer Equations

In this study the coupled unsteady boundary-layer equations in the Eulerian frame (3.27) were integrated forward in time using a standard method based on the Crank-Nicolson approximation (Walker, 1978). The finite difference expressions are developed in this appendix. Assume that the solution for  $U(\xi, \eta, t)$  and  $\bar{\Psi}(\xi, \eta, t)$  is known in a previous time plane at  $t=t^*$ , and the objective is to compute these distributions in the current time plane at  $t=(t^*+\Delta t)$ . First, consider the momentum equation (3.27) for the Eulerian formulation which is

$$4t \frac{\partial U}{\partial t} = T \frac{\partial^2 U}{\partial \zeta^2} + P \frac{\partial U}{\partial \zeta} + WU + Q \frac{\partial U}{\partial x} + \Gamma; \quad (\text{B.1})$$

here the coefficients  $T$ ,  $P$ ,  $W$ ,  $Q$  and  $\Gamma$  are specified by equations (3.28). Note that  $P$ ,  $W$  and  $Q$  are functions of  $U$ , and that the governing equation is therefore nonlinear in  $U$ . In the Crank-Nicolson approximation method all terms in equation (B.1) are approximated midway between the current and previous time planes at  $t=\bar{t}$ , where  $\bar{t}=(t^*+t)/2$ . If  $U(\bar{x}, \bar{\zeta}, t)$  at  $t^*$  and  $t$  is denoted by  $U^*$  and  $U$  respectively, then the time-derivative term in (B.1) may be approximated at  $\bar{t}$  using the central difference expression

$$\overline{4t \frac{\partial U}{\partial t}} = 4\bar{t} \left( \frac{U - U^*}{\Delta t} \right) + O(\Delta t)^2, \quad (\text{B.2})$$

which, as indicated, is second-order accurate. All other terms of equation (B.1) may be approximated at  $\bar{t}$  simply by averaging the appropriate quantities in the current and previous time planes; for example

$$\bar{U} = \frac{U + U^*}{2}, \quad \bar{P} = \frac{P + P^*}{2}. \quad (\text{B.3})$$

Since  $U(\hat{x}, \hat{\zeta})$  is unknown at this stage, the previous iterate of  $U$  (which is taken to be  $U^*$  at the first iteration) is used to approximate the coefficients  $\bar{P}$ ,  $\bar{W}$  and  $\bar{Q}$  at any stage; the approximation for these coefficients improves with each iteration. The Crank-Nicolson approximation to equation (B.1) may be written,

$$\begin{aligned} 8\bar{t} \cdot U - \Delta t \left( \bar{T} \frac{\partial^2 U}{\partial \hat{\zeta}^2} + \bar{P} \frac{\partial U}{\partial \hat{\zeta}} + \bar{W} U + \bar{Q} \frac{\partial U}{\partial \hat{x}} \right) = \\ 8\bar{t} \cdot U^* + \Delta t \left( \bar{T} \frac{\partial^2 U^*}{\partial \hat{\zeta}^2} + \bar{P} \frac{\partial U^*}{\partial \hat{\zeta}} + \bar{W} U^* + \bar{Q} \frac{\partial U^*}{\partial \hat{x}} \right) + 2\Delta t \bar{f}. \end{aligned} \quad (B.4)$$

The terms involving the known values  $U^*$  have been placed on the right side of equation (B.4).

The finite-difference equations are obtained by defining a two-dimensional uniform mesh in the  $(\hat{x}, \hat{\zeta})$  space with spacings  $(\Delta \hat{x}, \Delta \hat{\zeta})$  respectively, and then approximating the spatial derivative operators with conventional central-difference expressions. Let  $i, j$  denote an arbitrary point in the mesh consisting of the intersection of the  $i$ th line of constant  $\hat{x}$  and the  $j$ th line of constant  $\hat{\zeta}$ . For convenience, the Southwell notation is used wherein values at the pivotal point  $i, j$  are denoted by a subscript 0, and the surrounding points by 1, 2, 3, 4 according to

$$U_{i,j} = U_0, \quad U_{i+1,j} = U_1, \quad U_{i,j+1} = U_2, \quad U_{i-1,j} = U_3, \quad U_{i,j-1} = U_4. \quad (B.5)$$

The resulting approximation to equation (B.4) at any interior node is second-order accurate and is given by

$$\begin{aligned}
8\bar{t}U_0 - \Delta t \left( \bar{T}_0 \frac{U_2 - 2U_0 + U_4}{\Delta \hat{\zeta}^2} + \bar{P}_0 \frac{U_2 - U_4}{2\Delta \hat{\zeta}} + \bar{W}_0 U_0 + \bar{Q}_0 \frac{U_1 - U_3}{2\Delta \hat{x}} \right) = \\
8\bar{t}U_0^* + \Delta t \left( \bar{T}_0 \frac{U_2^* - 2U_0^* + U_4^*}{\Delta \hat{\zeta}^2} + \bar{P}_0 \frac{U_2^* - U_4^*}{2\Delta \hat{\zeta}} + \bar{W}_0 U_0^* + \bar{Q}_0 \frac{U_1^* - U_3^*}{2\Delta \hat{x}} \right) \\
+ 2\Delta t \bar{\Gamma}_0.
\end{aligned} \tag{B.6}$$

The nonlinear set of difference equation defined by equation (B.6) was solved by using point-by-point iterative sweeps of the mesh in which the functional coefficients  $\bar{P}_0$ ,  $\bar{T}_0$ , etc., were updated at each iteration. To accomplish this, at each node the unknown value  $U_0 = U_{i,j}$  was written as a linear sum of adjacent unknown nodal quantities and the known nodal quantities in the previous time plane, viz.

$$U_0 = \frac{1}{\alpha_0} \left( \sum_{k=1}^4 \alpha_k U_k + \sum_0^4 \beta_k U_k^* + 2\Delta t \bar{\Gamma}_0 \right), \tag{B.7}$$

where

$$\begin{aligned}
\alpha_0 &= \theta \left( 2(\Delta \hat{x}) \bar{T}_0 - (\Delta \hat{x})(\Delta \hat{\zeta})^2 \bar{W}_0 \right) + 8\bar{t}, \\
\alpha_1 &= \theta \left( (\Delta \hat{\zeta})^2 \bar{Q}_0 / 2 \right), \quad \alpha_2 = \theta \left( (\Delta \hat{x}) \bar{T}_0 + (\Delta \hat{x})(\Delta \hat{\zeta}) \bar{P}_0 / 2 \right), \\
\alpha_3 &= -\alpha_1, \quad \alpha_4 = \theta \left( (\Delta \hat{x}) \bar{T}_0 - (\Delta \hat{x})(\Delta \hat{\zeta}) \bar{P}_0 / 2 \right), \\
\beta_0 &= -\theta \left( 2(\Delta \hat{x}) \bar{T}_0 - (\Delta \hat{x})(\Delta \hat{\zeta})^2 \bar{W}_0 \right) + 8\bar{t}, \\
\beta_1 &= \alpha_1, \quad \beta_2 = \alpha_2, \quad \beta_3 = \alpha_3, \quad \beta_4 = \alpha_4,
\end{aligned} \tag{B.8}$$

$$\theta = (\Delta t) / \left( (\Delta \hat{x})(\Delta \hat{\zeta})^2 \right).$$

To complete one iterate, equation (B.7) was systematically applied at every node using Gauss-Seidel iteration.

It may be seen from the second of equations (3.27) that the solution for the streamfunction  $\bar{\Psi}(\hat{x}, \hat{\zeta}, t)$  at any time depends on the distribution  $U(\hat{x}, \hat{\zeta}, t)$  at that time. After each iteration for  $U$  was computed, new values of  $\bar{\Psi}$  were

obtained by integrating

$$\frac{\partial \bar{\Psi}}{\partial \hat{\zeta}} = \frac{1}{Z(\hat{\zeta})} U, \quad (\text{B.9})$$

on lines of  $\hat{x}_i = \text{constant}$ , starting from the wall and using a method based on Simpson's rule. To illustrate this approach designate successive values of  $\hat{\zeta}$  in the mesh by  $\hat{\zeta}_0=0$ ,  $\hat{\zeta}_1=\Delta\hat{\zeta}$ ,  $\hat{\zeta}_2=2\Delta\hat{\zeta}$ , ...,  $\hat{\zeta}_j=j\Delta\hat{\zeta}$ , ... . Then at  $\hat{\zeta}=0$

$$\bar{\Psi}_{i,0}=0, \quad (\text{B.10})$$

since  $\bar{\Psi}$  is taken to be zero at the wall (c.f. equation 3.18). The value of  $\bar{\Psi}$  at the first line of points from the wall was calculated using a special starting formula, which is based on a forward-difference expression that is accurate to  $O((\Delta\hat{\zeta})^5)$ , which is the same level of error that is associated with Simpson's rule; the formula is

$$\bar{\Psi}_{i,1} = \left(\frac{\Delta\hat{\zeta}}{24}\right) \left(9\frac{U_{i,0}}{Z_0} + 19\frac{U_{i,1}}{Z_1} - 5\frac{U_{i,2}}{Z_2} + \frac{U_{i,3}}{Z_3}\right), \quad (\text{B.11})$$

where  $U_{i,j}=U(\hat{x}_i, \hat{\zeta}_j)$  and  $Z_j=Z(\hat{\zeta}_j)$ . The remaining nodal values of  $\bar{\Psi}_{i,j}$  on a line of constant  $\hat{x}_i$ , for  $j \geq 2$  were calculated using the standard Simpson's rule, viz.

$$\bar{\Psi}_{i,j} = \left(\frac{\Delta\hat{\zeta}}{3}\right) \left(\frac{U_{i,j-2}}{Z_{j-2}} + 4\frac{U_{i,j-1}}{Z_{j-1}} + \frac{U_{i,j}}{Z_j}\right) + \bar{\Psi}_{i,j-2}. \quad (\text{B.12})$$



## APPENDIX C

### Algorithm for the Cauchy Integral

A second-order accurate procedure for calculating a Cauchy principal-value integral at a specific point  $x_i$  is described in §3.8; here  $x_i$  shall be referred to as the field-point. The integral is evaluated as the sum of two parts consisting of the main portion  $S(x_i)$ , and a contribution  $L(x_i)$  due to the asymptotic behavior of the integrand as  $|x| \rightarrow \infty$ . The derivation of the procedure and the terms associated with the model problem is the topic of §3.8; the purpose of this appendix is to obtain the constant coefficients in the series expansion of  $L_i$  and  $S_i$ .

The quantity  $S_i$ , defined by equation (3.145), is the main contribution to the Cauchy integral from the interval  $[-R, +R]$  transformed onto the finite interval  $[\Delta\hat{x}/2, 2-\Delta\hat{x}/2]$ . The series approximation for  $S_i$  is given by equation (3.147) and the constant coefficients, reproduced from equations (3.148)-(3.149) are,

$$\alpha_{i,j} = (\Delta\hat{x}) \cdot \int_{-1/2}^{+1/2} \frac{d\mu}{\sin(\frac{\pi}{2}\{r_{i,j} - (\Delta\hat{x})\mu\})}, \quad (C.1)$$

$$\beta_{i,j} = (\Delta\hat{x})^2 \cdot \int_{-1/2}^{+1/2} \frac{\mu \cdot d\mu}{\sin(\frac{\pi}{2}\{r_{i,j} - (\Delta\hat{x})\mu\})}, \quad (C.2)$$

where  $r_{i,j} = (\hat{x}_i - \hat{x}_j)$ . The solution for the leading order coefficient  $\alpha_{i,j}$  may be obtained in closed form and is

$$\alpha_{i,j} = \frac{1}{\pi} \log \left( \frac{\sin(\pi \cdot r_{i,j}/2) + \sin(\pi \cdot \Delta\hat{x}/4)}{\sin(\pi \cdot r_{i,j}/2) - \sin(\pi \cdot \Delta\hat{x}/4)} \right)^2. \quad (C.3)$$

The second-order coefficient  $\beta_{i,j}$  cannot be solved in closed form. However, it is easily confirmed that  $\beta_{i,j}$  is significant only for  $r_{i,j} = O(\Delta\hat{x})$ , and for small  $r_{i,j}$

the denominator of equation (C.2) may be approximated to  $O(\Delta\hat{x}^3)$ , viz.

$$\sin\left(\frac{\pi}{2} \cdot \Delta\hat{x} \cdot (i-j-\mu)\right) \approx \frac{\pi(\Delta\hat{x})}{2}(i-j-\mu). \quad (C.4)$$

Integration of equation (C.2) gives

$$\beta_{ij} = -\frac{1}{\pi} \left( 2 \cdot (\Delta\hat{x}) + r_{ij} \cdot \log\left(\frac{r_{ij} - \Delta\hat{x}/2}{r_{ij} + \Delta\hat{x}/2}\right)^2 \right). \quad (C.5)$$

For  $r_{ij}$  large, it may be shown that  $\beta_{ij} \sim \pi(\Delta\hat{x})^3 \cot(\pi r_{ij}/2) / (24 \cdot \sin(\pi r_{ij}/2))$ . Table C.1 summarizes the coefficients  $\alpha_{ij}$  and  $\beta_{ij}$  in the vicinity of the field-point  $x_i$  for the three different mesh discretizations used in this study. At any field-point the coefficient of the first order term,  $\alpha_{ij}$ , is identically zero. In contrast, the coefficient of the second order term,  $\beta_{ij}$ , is a maximum at the field-point; this indicates that there is a significant contribution to the Cauchy integral at the field-point  $\hat{x}_i$  from the second-order term associated with  $\beta_{ij}$ . Note that in a first-order method,  $H$  is assumed constant throughout each interval; this type of method implicitly takes  $\beta_{ij}=0$ .

The quantity  $L_i$  is the contribution to the Cauchy integral from the two exterior intervals,  $(-\infty, -R]$  and  $[+R, +\infty)$ , defined by equation (3.143); the series approximation for  $L_i$  is given by (3.155). When  $x_i \neq 0$  the constant coefficients are defined as

$$a_{i,k} = \frac{1}{\pi x_i^k} \int_{+R/x_i}^{+\infty} \frac{d\tau}{\tau^k(1-\tau)}, \quad (C.6)$$

$$b_{i,k} = \frac{1}{\pi x_i^k} \int_{+\infty}^{-R/x_i} \frac{d\tau}{\tau^k(1-\tau)}, \quad (C.7)$$

as given in equation (3.156). Here,  $R$  is the constant given by (3.144). Equations (C.6) and (C.7) may be solved in closed form from the general

$(i-j)\Delta\hat{x}$	N=60		N=100		N=200	
	$\alpha_{ij}$	$\beta_{ij}$	$\alpha_{ij}$	$\beta_{ij}$	$\alpha_{ij}$	$\beta_{ij}$
$-10\Delta\hat{x}$	-0.0677	0.0000	-0.0648	0.0000	-0.0640	0.0000
$-9\Delta\hat{x}$	-0.0744	0.0000	-0.0718	0.0000	-0.0710	0.0000
$-8\Delta\hat{x}$	-0.0829	0.0000	-0.0805	0.0000	-0.0799	0.0000
$-7\Delta\hat{x}$	-0.0939	0.0000	-0.0918	0.0000	-0.0913	0.0000
$-6\Delta\hat{x}$	-0.1087	0.0001	-0.1070	0.0000	-0.1065	0.0000
$-5\Delta\hat{x}$	-0.1297	0.0001	-0.1283	0.0000	-0.1279	0.0000
$-4\Delta\hat{x}$	-0.1615	0.0001	-0.1604	0.0001	-0.1601	0.0000
$-3\Delta\hat{x}$	-0.2154	0.0002	-0.2145	0.0001	-0.2143	0.0001
$-2\Delta\hat{x}$	-0.3260	0.0005	-0.3254	0.0003	-0.3253	0.0001
$-1\Delta\hat{x}$	-0.6998	0.0024	-0.6995	0.0013	-0.6994	0.0006
0	0.0000	-0.0244	0.0000	-0.0127	0.0000	-0.0064
$1\Delta\hat{x}$	0.6998	0.0024	0.6995	0.0013	0.6994	0.0006
$2\Delta\hat{x}$	0.3260	0.0005	0.3254	0.0003	0.3253	0.0001
$3\Delta\hat{x}$	0.2154	0.0002	0.2145	0.0001	0.2143	0.0001
$4\Delta\hat{x}$	0.1615	0.0001	0.1604	0.0001	0.1601	0.0000
$5\Delta\hat{x}$	0.1297	0.0001	0.1283	0.0000	0.1279	0.0000
$6\Delta\hat{x}$	0.1087	0.0001	0.1070	0.0000	0.1065	0.0000
$7\Delta\hat{x}$	0.0939	0.0000	0.0918	0.0000	0.0913	0.0000
$8\Delta\hat{x}$	0.0829	0.0000	0.0805	0.0000	0.0799	0.0000
$9\Delta\hat{x}$	0.0744	0.0000	0.0718	0.0000	0.0710	0.0000
$10\Delta\hat{x}$	0.0677	0.0000	0.0648	0.0000	0.0640	0.0000

Table C.1. Cauchy integral coefficients for nodes near the field point  $\hat{x}_i$ . N corresponds to the number of intervals in each of the three meshes used in this study. Here,  $\alpha_{ij}$  is the coefficient of  $H_j$ ,  $\beta_{ij}$  is the coefficient of  $H_j'$ , and  $\Delta\hat{x}=2/N$ .

solution of the indefinite integral

$$\int \frac{d\tau}{\tau^k(1-\tau)} = \sum_{j=1}^{k-1} \frac{-1}{(k-j)\tau^{(k-j)}} + \frac{1}{2} \log\left(\frac{\tau}{1-\tau}\right)^2. \quad (C.8)$$

(See Gradshteyn and Ryzik, 2.117[4].) Using this expression, it is possible to derive  $a_{i,k}$  and  $b_{i,k}$  to any order  $k$  that is required, and the first five are tabulated below:

$$a_{i,1} = \frac{1}{x_i} \cdot \frac{1}{2\pi} \cdot \left( +\log\left(\frac{x_i-R}{R}\right)^2 \right), \quad (C.9)$$

$$b_{i,1} = \frac{1}{x_i} \cdot \frac{1}{2\pi} \cdot \left( -\log\left(\frac{x_i+R}{R}\right)^2 \right),$$

$$a_{i,2} = \frac{1}{x_i^2} \cdot \frac{1}{2\pi} \cdot \left( \frac{2 \cdot x_i}{R} + \log\left(\frac{x_i-R}{R}\right)^2 \right),$$

$$b_{i,2} = \frac{1}{x_i^2} \cdot \frac{1}{2\pi} \cdot \left( \frac{2 \cdot x_i}{R} - \log\left(\frac{x_i+R}{R}\right)^2 \right),$$

$$a_{i,3} = \frac{1}{x_i^3} \cdot \frac{1}{2\pi} \cdot \left( \frac{x_i}{R} \cdot \left(2 + \frac{x_i}{R}\right) + \log\left(\frac{x_i-R}{R}\right)^2 \right),$$

$$b_{i,3} = \frac{1}{x_i^3} \cdot \frac{1}{2\pi} \cdot \left( \frac{x_i}{R} \cdot \left(2 - \frac{x_i}{R}\right) - \log\left(\frac{x_i+R}{R}\right)^2 \right),$$

$$a_{i,4} = \frac{1}{x_i^4} \cdot \frac{1}{2\pi} \cdot \left( \frac{x_i}{R} \cdot \left(2 + \frac{x_i}{R} \cdot \left(1 + \frac{2x_i}{3R}\right)\right) + \log\left(\frac{x_i-R}{R}\right)^2 \right),$$

$$b_{i,4} = \frac{1}{x_i^4} \cdot \frac{1}{2\pi} \cdot \left( \frac{x_i}{R} \cdot \left(2 - \frac{x_i}{R} \cdot \left(1 - \frac{2x_i}{3R}\right)\right) - \log\left(\frac{x_i+R}{R}\right)^2 \right),$$

$$a_{i,5} = \frac{1}{x_i^5} \cdot \frac{1}{2\pi} \cdot \left( \frac{x_i}{R} \cdot \left(2 + \frac{x_i}{R} \cdot \left(1 + \frac{x_i}{R} \cdot \left(\frac{2}{3} + \frac{1x_i}{2R}\right)\right)\right) + \log\left(\frac{x_i-R}{R}\right)^2 \right),$$

$$b_{i,5} = \frac{1}{x_i^5} \cdot \frac{1}{2\pi} \cdot \left( \frac{x_i}{R} \cdot \left(2 - \frac{x_i}{R} \cdot \left(1 - \frac{x_i}{R} \cdot \left(\frac{2}{3} - \frac{1x_i}{2R}\right)\right)\right) - \log\left(\frac{x_i+R}{R}\right)^2 \right), \quad \text{for } x_i \neq 0.$$

Note that  $a_{i,k}$  and  $b_{i,k}$  are only evaluated for interior nodes, and from the

definition of  $R$  in equation (3.144),

$$\left| \frac{x_i}{R} \right| < 1. \quad (C.10)$$

For the special case of  $x_i=0$ ,  $a_{i,k}$  and  $b_{i,k}$  may be solved for all  $k$  from equation (3.157) and are

$$a_{i,k} = \frac{-1}{\pi \cdot k \cdot R^k} \quad b_{i,k} = \frac{(-1)^k}{\pi \cdot k \cdot R^k}, \quad \text{for } x_i=0. \quad (C.11)$$

## APPENDIX D

### Evaluation of the Physical Quantities from Lagrangian Data

The physical quantities that are computed directly, in the Lagrangian formulation of the boundary-layer problem of this study, are the transformed streamwise particle positions  $\hat{x}(\hat{\xi}, \hat{\eta}, t)$  and the normalized velocity  $U(\hat{\xi}, \hat{\eta}, t)$  defined by equation (3.48). In this appendix, the numerical procedures used to compute the following quantities are described: (1) the normal distance  $\hat{y}(\hat{\xi}, \hat{\eta}, t)$  of each fluid particle from the wall; (2) the displacement thickness  $\delta^*(\bar{x}, t)$ ; (3) the stream-function  $\Psi(\bar{x}, \bar{y}, t)$ ; (4) the vorticity  $\omega(\bar{x}, \bar{y}, t)$ ; and (5) the wall shear  $\tau_w(\bar{x}, t)$ .

#### D.1 The Normal Distance $\hat{y}(\hat{\xi}, \hat{\eta}, t)$

At any stage during the course of a boundary-layer integration, the normal distance  $y(\xi, \eta, t)$  of each fluid particle from the wall may be determined through integration of the continuity equation (1.21). The  $x$  and  $y$  variables are defined on infinite ranges, and the calculations were carried out in terms of the variables  $\hat{x}$  and  $\hat{y}$  defined by equations (3.50) and (3.53) on the finite ranges  $(0, 2)$  and  $[0, 1)$ , respectively. The discussion in this section will focus on the computation of  $\hat{y}(\hat{\xi}, \hat{\eta}, t)$  and, once this quantity is available, the corresponding value of  $y$  can be obtained by inverting the first of equations (3.53). For both the limit problem and the interacting boundary-layer calculations, the continuity equation (1.21), in the transformed variables, is

$$\left( \frac{Ue_0(\hat{\xi})}{Ue_0(\bar{x})} \frac{Z(\hat{\eta})}{Z(\bar{y})} \right) \left( \frac{\partial \hat{x}}{\partial \hat{\xi}} \frac{\partial \hat{y}}{\partial \hat{\eta}} - \frac{\partial \hat{x}}{\partial \hat{\eta}} \frac{\partial \hat{x}}{\partial \hat{\xi}} \right) = 1, \quad (D.1)$$

where  $Ue_0$  and  $Z$  are analytic functions given by (3.52) and (3.55). If, at any time  $t$ , it is assumed that  $\hat{x}(\hat{\xi}, \hat{\eta}, t)$  is known from a numerical solution of the boundary-layer equations, it is evident that equation (D.1) is a first-order

partial differential equation for  $\hat{y}$ . The characteristic curves are  $\hat{x}=\text{constant}$ , and the subsidiary equations are of the form

$$\frac{d\hat{\xi}}{A} = \frac{d\hat{\eta}}{B} = \frac{d\hat{y}}{C} = ds, \quad (\text{D.2})$$

where

$$A = -\frac{\partial \hat{x}}{\partial \hat{\eta}}, \quad B = \frac{\partial \hat{x}}{\partial \hat{\xi}}, \quad C = \frac{Ue_0(\hat{x}) Z(\hat{y})}{Ue_0(\hat{\xi}) Z(\hat{\eta})}, \quad (\text{D.3})$$

and  $s$  is a parameter along the characteristic curve  $\hat{x}=\text{constant}$ . Note that the characteristics at the start of the integration, at  $t=t_0$ , start out as vertical straight lines (c.f. figure 4.2(a)), but at all subsequent times are curves in  $(\hat{\xi}, \hat{\eta})$  space which are to be determined during the course of the integration of equation (D.2).

Generally, the integration of equation (D.2) may be started at the wall at time  $t$  for some selected value of  $\hat{\xi}$ . Fluid particles located on the wall at the start of the problem stay on the surface, but are convected to the left in the frame of reference moving with the vortex. For the limit problem

$$x = \xi - (t - t_0) \quad \text{for } \eta=0, t > t_0, \quad (\text{D.4})$$

which fixes  $x$  for a specific choice of  $\xi$  at time  $t$ ; values of the transformed variables  $\hat{x}, \hat{\xi}$  are readily obtained from equations (3.50). For the interacting boundary-layer integrations the vortex moves with a *non-uniform* velocity  $U_v(t)$ , and  $x$  on the wall may be obtained through numerical integration of

$$\frac{dx}{dt} = -U_v(t), \quad x=\xi \text{ at } t=t_0, \quad (\text{D.5})$$

where  $\eta=0$  and  $t > t_0$ . Consequently, for a specific fluid particle on the wall (i.e. a specified value of  $\hat{\xi}$ ), the corresponding value of  $x$  may be calculated from either (D.4) or (D.5). However, a simpler procedure may be used to find

$\hat{x}$ , which may be understood with reference to figure D.1. The broken lines in this figure represent the mesh lines in  $(\hat{\xi}, \hat{\eta})$  and, at any time  $t$ , values for  $\hat{x}(\hat{\xi}, \hat{\eta}, t)$  and  $U(\hat{\xi}, \hat{\eta}, t)$  are known at all nodes in the mesh from the numerical solution of the boundary-layer problem described in §3.6. Consider the selection of a specific location on the wall at  $\hat{\xi}^0$ , as indicated in figure D.1; since  $\hat{x}(\hat{\xi}, \hat{\eta}, t)$  is known at the mesh points on either side, a linear interpolation readily produces the value of  $\hat{x}$  corresponding to this particular contour. An integration of equations (D.2) may then be initiated along the contour starting from the initial conditions

$$\hat{\xi} = \hat{\xi}^0, \hat{y} = 0, \hat{\eta} = 0, \text{ at } s = 0. \quad (\text{D.6})$$

Integration of equation (D.2) was accomplished using a predictor-corrector algorithm that moves one step at a time, generating both the sequence of points along the characteristic as shown in figure D.1 and the corresponding values of  $\hat{y}$ . Assume that the process has reached the  $k$ th point on the contour at  $(\hat{\xi}^k, \hat{\eta}^k)$  where  $\hat{y} = \hat{y}^k$ , and that the object is to find the next point  $(\hat{\xi}^{k+1}, \hat{\eta}^{k+1})$  and  $\hat{y}^{k+1}$ . It is first necessary to decide how far to step along the contour. It follows from equation (D.2) that the arc length along the contour in a single step is approximated by

$$\Delta s \sqrt{(A^k)^2 + (B^k)^2}, \quad (\text{D.7})$$

when  $(\hat{\xi}, \hat{\eta})$  change by an amount  $\Delta \hat{\xi}$ ,  $\Delta \hat{\eta}$  respectively; here  $A^k$  and  $B^k$  denote the values of  $A$  and  $B$  at the  $k$ th point on the contour. In the present study, the change in arc length along each constant  $\hat{x}$  contour was taken to be equal to the mesh spacing  $\Delta \hat{\xi}$  used in the Lagrangian boundary-layer integrations, viz.

$$\Delta s = \frac{\Delta \hat{\xi}}{\sqrt{(A^k)^2 + (B^k)^2}}. \quad (\text{D.8})$$



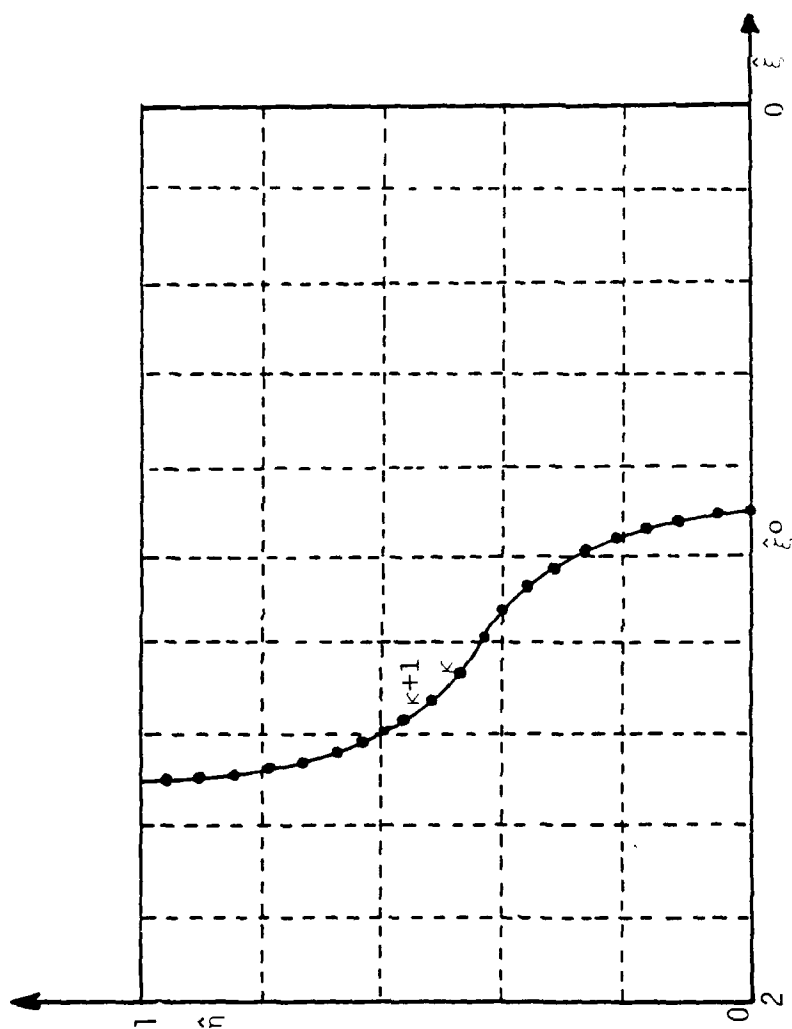


Figure D.1. Schematic diagram of integration along a characteristic  $\hat{x} = \text{constant}$ .

The selection restricts the step size along the contour to reasonably small values and insured an accurate evaluation of  $\hat{y}$ .

The values of  $\hat{\xi}^{k+1}$ ,  $\hat{\eta}^{k+1}$  and  $\hat{y}^{k+1}$  were first predicted by the algorithm

$$\left. \begin{aligned} \hat{\xi}_p^{k+1} &= \hat{\xi}^k + A^k \Delta s, \\ \hat{\eta}_p^{k+1} &= \hat{\eta}^k + B^k \Delta s, \\ \hat{y}_p^{k+1} &= \hat{y}^k + C^k \Delta s, \end{aligned} \right\} \quad (D.9)$$

where  $A^k$ ,  $B^k$  and  $C^k$  were obtained using a process of bivariate linear interpolation that will be described subsequently. With these estimates for  $\hat{\xi}^{k+1}$ ,  $\hat{\eta}^{k+1}$  and  $\hat{y}^{k+1}$ , the values of  $A^{k+1}$ ,  $B^{k+1}$  and  $C^{k+1}$  were computed and the corrector was applied, viz.

$$\left. \begin{aligned} \hat{\xi}_c^{k+1} &= \hat{\xi}^k + \frac{1}{2}(A^k + A^{k+1})\Delta s, \\ \hat{\eta}_c^{k+1} &= \hat{\eta}^k + \frac{1}{2}(B^k + B^{k+1})\Delta s, \\ \hat{y}_c^{k+1} &= \hat{y}^k + \frac{1}{2}(C^k + C^{k+1})\Delta s. \end{aligned} \right\} \quad (D.10)$$

In practice, the step size  $\Delta s$  was small enough so that iterating the corrector had no effect on the computed results. The algorithm is second-order accurate. As indicated in figure D.1, the calculation proceeds in a step-by-step manner and must eventually terminate at  $\hat{\eta}=1$ . Generally, the step-size along the contour must be reduced systematically to a smaller value than indicated by equation (D.8) in order that the calculation terminate exactly at  $\hat{\eta}=1$ , where  $\hat{y}=1$ .

To evaluate the right side of equations (D.9) and (D.10), it is necessary to be able to compute the coefficients A, B, and C in equations (D.3) at any location in the  $(\hat{\xi}, \hat{\eta})$ -plane. Suppose an evaluation at  $(\hat{\xi}^k, \hat{\eta}^k)$  is required and let  $(i,j)$  be the index of the closest mesh point in the sense that

$$\hat{\xi}_i \leq \hat{\xi}^k, \hat{\eta}_j \leq \hat{\eta}^k; \quad (D.11)$$

then,

$$\hat{\xi}^k = \hat{\xi}_i + p\Delta\hat{\xi}, \hat{\eta}^k = \hat{\eta}_j + q\Delta\hat{\eta}, \quad (D.12)$$

where  $p$  and  $q$  are positive numbers which lie between 0 and 1 and are computed from

$$p = \frac{(\hat{\xi}^k - \hat{\xi}_i)}{\Delta\hat{\xi}}, q = \frac{(\hat{\eta}^k - \hat{\eta}_j)}{\Delta\hat{\eta}}. \quad (D.13)$$

If  $D$  represents any of  $A$ ,  $B$ , or  $C$ , the bivariate linear interpolation formula is

$$D^k = D(\hat{\xi}_i + p\Delta\hat{\xi}, \hat{\eta}_j + q\Delta\hat{\eta}) = (1-p)(1-q)D_{i,j} + \\ p(1-q)D_{i+1,j} + q(1-p)D_{i,j+1} + pqD_{i+1,j+1}. \quad (D.14)$$

Here, the subscripts denote evaluations of  $D$  on the four corners of the grid cell containing the point  $(\hat{\xi}^k, \hat{\eta}^k)$ . The quantities  $A$  and  $B$  involve first derivatives of  $\hat{x}$  and were evaluated at all points in the mesh using second-order accurate central difference formulae. The evaluation of  $C$  in equation (D.3) is straightforward since  $Z$  and  $Ue_0$  are analytic functions.

## D.2 The Stream-function $\Psi(\hat{x}, \hat{y}, t)$

A stream-function  $\Psi$  is defined in terms of the velocity  $u$  in a frame of reference moving with the vortex by

$$u = \frac{\partial \Psi}{\partial y}, \quad (D.15)$$

and  $u$  is defined in terms of the normalized velocity  $U$  by equation (3.48)

which is repeated here, viz.

$$u(\xi, \eta, t) = Ue(x, t) U(\xi, \eta, t) - U_v(t). \quad (D.16)$$

If a subsidiary stream-function  $\tilde{\psi}$  is defined by

$$U = \frac{\partial \tilde{\psi}}{\partial y} \quad (D.17)$$

it follows that

$$\Psi(x, y, t) = Ue(x, t) \tilde{\psi}(x, y, t) - y U_v(t), \quad (D.18)$$

since both  $\Psi$  and  $\tilde{\psi}$  vanish on the wall. The subsidiary stream-function  $\tilde{\psi}$  is obtained by integration of equation (D.17) along a line of constant  $x$ . In terms of the transformed variables  $(\hat{x}, \hat{y})$

$$\tilde{\psi}(\hat{x}, \hat{y}, t) = \int_0^{\hat{y}} U(\hat{\xi}, \hat{\eta}, t) \bigg|_{\hat{x}=\text{constant}} \frac{d\alpha}{Z(\alpha)}, \quad (D.19)$$

where, from (3.53) and (3.55)

$$\hat{y} = \frac{2}{\pi} \arctan(y), \quad Z(\hat{y}) = \frac{2}{\pi} \cos^2\left(\frac{\pi}{2} \hat{y}\right). \quad (D.20)$$

In section (D.1) a step-by-step integration procedure to find  $\hat{y}$  all along a contour of constant  $\hat{x}$  was described, in which values of  $\hat{y}$  (namely,  $\hat{y}^k$ ) were computed at points  $(\hat{\xi}^k, \hat{\eta}^k)$  along a contour  $\hat{x}=\text{constant}$  (c.f. figure D.1). The integral in equation (D.19) was evaluated using the trapezoid rule during the integration along the  $\hat{x}=\text{constant}$  contour, according to the recursion relation

$$\tilde{\psi}^{k+1} = \tilde{\psi}^k + \frac{1}{2} \frac{(U^k + U^{k+1})(\hat{y}^{k+1} - \hat{y}^k)}{Z\{(\hat{y}^k + \hat{y}^{k+1})/2\}} \quad (D.21)$$

for  $k=1,2, \dots$ , and where  $\tilde{\psi}^0=0$ . Here,  $U^k$  denotes  $U(\hat{\xi},\hat{\eta},t)$  evaluated at  $(\hat{\xi}^k,\hat{\eta}^k)$  and was computed from the values of  $U$  in the Lagrangian mesh using the bivariate linear interpolation formula (D.14). The stream-function  $\Psi$  is easily evaluated from equation (D.18) for a given value of  $\hat{y}$  (using the first of equations (D.20)). This completes the general description of how  $\Psi$  may be evaluated at various  $\hat{y}$  locations all along a curve  $\hat{x}=\text{constant}$ .

In order to plot the instantaneous streamlines, which are lines of constant  $\Psi$ , it is generally desirable to compute  $\Psi$  at a number of points in a rectangular mesh. The common procedure in a contour plotting routine is to search through the mesh for values of  $\Psi=\text{constant}$ , and to use interpolation to calculate points on a specific streamline. In the present study, the same mesh discretization that was used to compute  $U$  and  $\hat{x}$  on the  $(\hat{\xi},\hat{\eta})$  mesh was used to define a similar mesh in  $(\hat{x},\hat{y})$ ; this is arbitrary and either a coarser or finer mesh could be adopted to compute and plot the streamlines. Using the step-by-step procedure just described to integrate along a contour  $\hat{x}=\text{constant}$  in  $(\hat{\xi},\hat{\eta})$ -space, the specific values of  $\hat{x}=\text{constant}$  in the grid were chosen; as the calculation proceeded up the characteristic, values of  $\Psi$  were computed by interpolation at the specific  $\hat{y}$  locations in the grid. A systematic sweep of the  $(\hat{x},\hat{y})$  mesh was used to determine the coordinates  $(\hat{x},\hat{y})$  associated with a value  $\Psi=\text{constant}$ . A contour-plotting routine then organized these coordinates into a trajectory to plot the streamline associated with the particular value  $\Psi=\text{constant}$ .

### D.3 The Displacement Thickness $\delta^*(x,t)$

The displacement thickness  $\delta^*$  is defined with respect to the velocity distribution in the laboratory frame of reference, according to

$$\delta^*(\bar{x}, t) = \int_0^{\infty} \left\{ 1 - \frac{u + U_v(t)}{Ue(\bar{x}, t)} \right\} dy. \quad (D.22)$$

Using equation (D.16), it follows that

$$\delta^*(\bar{x}, t) = \int_0^{\infty} \left\{ 1 - U(\hat{\xi}, \hat{\eta}, t) \right\} dy, \quad (D.23)$$

$\bar{x} = \text{constant}$

where it is emphasized that the integration in equation (D.23) is along a constant  $\bar{x}$  contour in the  $(\hat{\xi}, \hat{\eta})$  plane. From (D.17) it follows that

$$\delta^*(\bar{x}, t) = \lim_{y \rightarrow \infty} \{y - \tilde{\psi}\}, \quad (D.24)$$

or alternatively, in the transformed variable  $\hat{y}$

$$\delta^*(\bar{x}, t) = \lim_{\hat{y} \rightarrow 1} \left\{ \tan\left(\frac{\pi}{2}\hat{y}\right) - \tilde{\psi}(\bar{x}, \hat{y}, t) \right\}. \quad (D.25)$$

Consequently,  $\delta^*$  may be calculated as a limit along the characteristic as the computation approaches  $\hat{y}=1$  (c.f. figure D.1). An alternative and essentially equivalent approach that was used in the present study was to compute the integral (D.23) as the integration proceeded along the characteristic; using the trapezoid rule, the formula is

$$\delta^*(\bar{x}, t) = \sum_{k=1}^N \left\{ 1 - \frac{1}{2} \frac{(U^k + U^{k+1})(\hat{y}^{k+1} - \hat{y}^k)}{Z\{(\hat{y}^k + \hat{y}^{k+1})/2\}} \right\}, \quad (D.26)$$

where  $N$  total segments along the contour  $\bar{x} = \text{constant}$  have been assumed.

One point should be noted in connection with the calculation of  $\delta^*$ . In the early stages of the motion (c.f. figure 4.4), the displacement thickness is relatively smooth and may be well defined by computing  $\delta^*$  along a number of characteristics corresponding to the number of subdivisions in the  $\hat{\xi}$  mesh. The initial starting point of the constant  $\hat{\xi}$  contours may be selected along the

$\hat{\xi}$ -axis to produce a uniform mesh in either  $x$  or  $\hat{x}$ . In the latter stages of the integrations, when the displacement surface developed a locally intense behavior and eventually a spike, it was necessary to compute additional contours using a systematic search procedure, near  $\hat{x}=\hat{x}_s$ , in order to accurately resolve the tip of the "spike".

#### D.4 The Vorticity $\omega(\hat{x},\hat{y},t)$

The boundary-layer vorticity  $\omega$  is defined as

$$\omega = -\frac{\partial u}{\partial y}, \quad (D.27)$$

and is invariant in either the laboratory frame or in a frame moving with the vortex. In Lagrangian variables it follows from equations (A.23) and (3.48) that

$$\omega = -Ue(x,t) \left\{ \frac{\partial x}{\partial \xi} \frac{\partial U}{\partial \eta} - \frac{\partial x}{\partial \eta} \frac{\partial U}{\partial \xi} \right\}. \quad (D.28)$$

In the transformed variables defined by equations (3.50) and (3.53)

$$\omega = \left( \frac{Ue(\hat{x},t)}{Ue_0(\hat{x})} \right) \cdot Ue_0(\hat{\xi}) \cdot Z(\hat{\eta}) \cdot \left( \frac{\partial \hat{x}}{\partial \hat{\eta}} \frac{\partial U}{\partial \hat{\xi}} - \frac{\partial \hat{x}}{\partial \hat{\xi}} \frac{\partial U}{\partial \hat{\eta}} \right), \quad (D.29)$$

where  $Ue_0$  and  $Z$  are the analytic functions defined by equations (3.52) and (3.55). At any time step  $t$ , the vorticity may be readily computed at any internal mesh point  $(\hat{\xi}_i, \hat{\eta}_j)$  using standard central difference formulae to compute the derivatives of  $\hat{x}$  and  $U$ . Note that on the boundaries  $\hat{\xi}=0,2$  and  $\hat{\eta}=1$ , the vorticity is zero.

#### D.5 The Wall Shear $\tau_w(\bar{x},t)$

The wall shear is defined by

$$\tau_w(x,t) = \frac{\partial u}{\partial y} \Big|_{y=0}. \quad (D.30)$$

and is the negative of the surface vorticity. Since  $\frac{\partial x}{\partial \xi}=1$  and  $U=0$  on the wall, it follows from equation (D.28) that

$$\tau_w = Ue(x,t) \frac{\partial U}{\partial \eta} \Big|_{\eta=0}. \quad (D.31)$$

Expressing  $\tau_w$  in terms of the transformed variables, and using the fact that  $Z(0)=2/\pi$ , it follows that

$$\tau_w(\bar{x},t) = \frac{2}{\pi} Ue(\bar{x},t) \frac{\partial U}{\partial \hat{\eta}} \Big|_{\hat{\eta}=0}. \quad (D.32)$$

The derivative was evaluated using a third-order accurate forwards-difference formula which is given by

$$\frac{\partial U}{\partial \hat{\eta}} \Big|_{\hat{\eta}=0} = \frac{18 \cdot U(\hat{\xi}, \Delta \hat{\eta}) - 9 \cdot U(\hat{\xi}, 2\Delta \hat{\eta}) + 2 \cdot U(\hat{\xi}, 3\Delta \hat{\eta})}{6(\Delta \hat{\eta})}, \quad (D.33)$$

where the fact that  $U(\hat{\xi},0)=0$  has been used.



## APPENDIX E

### Determination of $x_s$ , $t_s$ , and $K$

In this appendix the method used to estimate the evolution time  $t_s$ , the streamwise location  $x_s$ , and the streamwise drift velocity  $(-K)$  of the singularity is described. The algorithm is used both for the limit problem ( $Re \rightarrow \infty$ ) and the interacting boundary-layer studies. Two characteristic features of the separation singularity are used to estimate the location and formation time. The first of these is that a singularity in the  $y$ -position occurs when a stationary point develops in the  $x(\xi, \eta, t)$  distribution (for some fixed value of  $t$ ), viz.

$$\frac{\partial x}{\partial \xi} = \frac{\partial x}{\partial \eta} = 0 \quad \text{at } (\xi_s, \eta_s, t_s). \quad (E.1)$$

Here,  $(\xi_s, \eta_s)$  identifies the fluid particle which is stretched a large vertical distance as  $t \rightarrow t_s$ . The second feature is that, in view of equations (2.16) and (E.1), the singularity must lie on the line of zero vorticity in both the limit problem and the interacting boundary-layer problem. The algorithm to identify  $t_s$  is a two-step procedure which was carried out at every time step during the course of the integration. In the first phase of the method, the norm of the gradient of  $\hat{x}$  was computed and the fluid particle  $(\xi_M, \eta_M)$  at which the norm is a minimum was identified. In the second step, the distance of  $(\xi_M, \eta_M)$  from the zero-vorticity line was computed; as  $t \rightarrow t_s$  this distance decreases monotonically to zero.

The numerical solution of the boundary-layer problem was carried out in the transformed variables  $\hat{\xi}$ ,  $\hat{\eta}$ ,  $\hat{x}$ , and  $U$  defined in equations (3.48), (3.50) and (3.53). As discussed in §4.3, it is convenient to define a gradient-norm function  $N$  by

$$N = \left( \frac{\partial \tilde{x}}{\partial \hat{\xi}} \right)^2 + \left( \frac{\partial \tilde{x}}{\partial \hat{\eta}} \right)^2. \quad (\text{E.2})$$

It is easily verified that when  $(\partial \tilde{x} / \partial \hat{\xi})$  and  $(\partial \tilde{x} / \partial \hat{\eta})$  vanish, conditions (E.1) are satisfied; thus  $N \rightarrow 0$  as a singularity evolves. However, because of discretization error and because  $N$  is non-negative, a value of  $N$  exactly equal to zero will never be produced numerically. In the present study, the location of the singularity was found by tracking the location of the minimum value of  $N$  during the course of the integration. The boundary-layer problem is calculated on a grid in  $(\hat{\xi}, \hat{\eta})$  which is uniform, with mesh spacings  $(\Delta \hat{\xi}, \Delta \hat{\eta})$  in the respective coordinate directions. Let  $(\hat{\xi}_M, \hat{\eta}_M)$  denote the location where  $N$  is a minimum at any value of  $t$  (which is not necessarily a point on the grid) and thus

$$\min(N(t)) = N(\hat{\xi}_M, \hat{\eta}_M, t). \quad (\text{E.3})$$

To find  $(\hat{\xi}_M, \hat{\eta}_M)$ , a systematic sweep of the mesh was done to evaluate  $N$  at each mesh point from equation (E.2) using standard central-difference approximations. Suppose that the minimum of  $N$  in the grid occurs at the  $(I, J)$  node. The function  $N$  was then represented as a second-order surface near  $(I, J)$  using the formula (Abramowitz and Stegun, 1965, equation 25.2.67)

$$\begin{aligned} N(\hat{\xi}_I + p\Delta\hat{\xi}, \hat{\eta}_J + q\Delta\hat{\eta}) = & \frac{q(q-1)}{2} N_{I,J-1} + \frac{p(p-1)}{2} N_{I-1,J} \\ & + \frac{p(p-2q+1)}{2} N_{I+1,J} + \frac{q(q-2p+1)}{2} N_{I,J+1} \\ & + (1+pq-p^2-q^2) N_{I,J} + (pq) N_{I+1,J+1}. \end{aligned} \quad (\text{E.4})$$

Here, the subscripts denote values of  $N$  at the corresponding points in the mesh. Suppose that the minimum occurs at

$$\hat{\xi}_M = \hat{\xi}_I + p\Delta\hat{\xi}, \quad \hat{\eta}_M = \hat{\eta}_J + q\Delta\hat{\eta}, \quad (\text{E.5})$$

where  $p$  and  $q$  are to be found. The condition that  $\mathcal{N}$  is a minimum is

$$\frac{\partial \mathcal{N}}{\partial \hat{\xi}} = \frac{\partial \mathcal{N}}{\partial \hat{\eta}} = 0. \quad (\text{E.6})$$

Differentiating (E.4) with respect to  $p$  and  $q$ , and setting the partial derivatives equation to zero, yields

$$\begin{aligned} \frac{\partial \mathcal{N}}{\partial p} = 0 = \frac{2p-1}{2} \mathcal{N}_{l-1,j} + (q-2p) \mathcal{N}_{l,j} + \frac{2(p-q)+1}{2} \mathcal{N}_{l+1,j} \\ - q \mathcal{N}_{l,j+1} + q \mathcal{N}_{l+1,j+1}, \end{aligned} \quad (\text{E.7})$$

$$\begin{aligned} \frac{\partial \mathcal{N}}{\partial q} = 0 = \frac{2q-1}{2} \mathcal{N}_{l,j-1} + (p-2q) \mathcal{N}_{l,j} + \frac{2(q-p)+1}{2} \mathcal{N}_{l,j+1} \\ - p \mathcal{N}_{l+1,j} + p \mathcal{N}_{l+1,j+1}, \end{aligned} \quad (\text{E.8})$$

which gives two simultaneous equations from which to determine  $p$  and  $q$ . The coordinates of the minimum were then found from equation (E.5) and the value of  $\mathcal{N}$  at the minimum  $\mathcal{N}_M$  from equation (E.4).

At each time step during the course of the integration, the coordinates of the minimum  $(\hat{\xi}_M, \hat{\eta}_M)$  and  $\mathcal{N}_M$  were evaluated. As  $t$  increases,  $\mathcal{N}_M$  was observed to decrease monotonically but, because of discretization error,  $\mathcal{N}_M$  never quite reaches zero. As indicated in §4.3, a good method for determining  $t_s$  is to find the value of  $t$  when the minimum in  $\mathcal{N}$  lies on the zero-vorticity line. The vorticity in Lagrangian variables is given by equation (2.16), and in terms of the transformed variables adopted in this study by equation (D.29). To locate the zero-vorticity line at any time  $t$ , the vorticity at each node in the mesh was computed using equation (D.29) using second-order accurate central difference formula for the derivatives. A set of points (or, alternatively, fluid particles  $(\hat{\xi}, \hat{\eta})_k$ ) defining the zero-vorticity line was then obtained by systematically sweeping the mesh along lines of  $\hat{\xi}_i$ , and then along lines of  $\hat{\eta}_j$ ,

problem and by equation (3.128) for the interacting problem;  $U_v$ , the vortex velocity, is unity for the limit problem and is given by equation (3.125) for the interacting problem.